IB 131-2015/069

Auslegung und Bau einer aktiven Rückströmklappe

S. Opitz

Institut für Faserverbundleichtbau und Adaptronik
Braunschweig

12 / 2015

Deutsches Zentrum
für Luft- und Raumfahrt e.V.
in der Helmholtzgemeinschaft
Institut für Faserverbundleichtbau und Adaptronik

IB 131-2015/069

Auslegung und Bau einer aktiven Rückströmklappe

Braunschweig, Dezember, 2015

Der Bericht umfasst:

159 Seiten

Institutsleiter:
Prof. Dr.-Ing. M. Wiedemann

Verfasser:
S. Opitz

Leiter der Abteilung:
Dr.-Ing. P. Wierach

Inhaltsverzeichnis

Abbildungsverzeichnis

1. Einleitung und Aufbau des Berichts

Die wesentlichen Erkenntnisse der Auslegung der Rückströmklappe wurden bereits in mehreren Veröffentlichungen dokumentiert. Diese sind dem vorliegendem Bericht angehangen (siehe Anhang A.1 - A.4). Während die grundlegenden Informationen zur Auslegung und zum Bau des Windkanalmodells in diesen Veröffentlichungen enthalten sind, umfasst dieser Bericht Ergänzungen und Details die über den publizierten Inhalt hinaus gehen. Mit Hilfe dieser zusätzlichen Erläuterungen soll der Weg von der Idee bis zum finalen Modell nachvollziehbar und reproduzierbar dargelegt werden.

An den Stellen, an denen die Ausführungen in den Veröffentlichungen keine weitere Ergänzung benötigen, wird im Bericht auf die entsprechenden Abschnitte in den Veröffentlichungen verwiesen und somit das Auffinden der relevanten Informationen erleichtert.

2. Auslegung der Rückströmklappe

Die Auslegung der Rückströmklappe beinhaltet zwei maßgebliche Aspekte:

- die aerodymnamische Auslegung und
- die strukturelle Auslegung.

Dieser Bericht fokussiert sich auf die strukturelle Auslegung und den Bau des Windkanalmodells.

2.1. Aerodynamik

Informationen zur aerodynamischen Auslegung der Klappe können folgenden Veröffentlichungen entnommen werden:

- Anhang A.1 Abschnitt: „2. Aerodynamic background and wind tunnel experiments“
- Anhang A.2 Abschnitt: „3 Experiment with a passively actuated flap“
- Anhang A.3 und Anhang A.4 jeweils in Abschnitt: „3.1. Aerodynamic design“

Für das Windkanalmodell realisiert wurde eine Klappe mit 12.5%c bei einer Position von 30%c. Der Öffnungswinkel der Klappe wurde auf 30° begrenzt (siehe auch Abschnitt 2.2.2).

2.2. Struktur

2.2.1. Feststoffgelenk

Die grundlegenden Informationen zu Aufbau und Berechnung des Feststoffgelenkes befinden sich in:

- Anhang A.1 Abschnitt: „3.1 Solid state hinge“
- Anhang A.2 Abschnitt: „4.1 Solid state hinge“

Realisiert wurde ein Feststoffgelenk mit einer Länge von 10mm. Die einzelne Mittellage aus GFK wurde in einem Verhältnis von 2:1 ausgespart um die Biegesteifigkeit zu reduzieren. Um eine ausgeprägte Welligkeit in Spannweitenrichtung zu verhindern wurden jeweils 2mm breite Steifen ausgespart und 1mm breite Verbindungen zur Anbindung der Klappe stehen gelassen. Zusätzlich wurden einzelne trockene Glasfaserrovings in Spannweitenrichtung über und unter der GFK-Mittellage verlegt um ein Ausbeulen im Bereich der Aussparungen zu verhindern (Abbildung 3.5). Der Zuschnitt erfolgte auf einem Cutter mit einer Ziehklinge. Trotz der Einstellung der Schnitttiefe kann nicht verhindert werden, dass es beim Ausschneiden der Aussparungen zu kleinen Einschnitten in die Verbindungsstege kommen kann. Um die Schwachstelle aus potentiell durchtrennten Fasern abzuschwächen, wurde die Länge der Ausschnitte auf 15mm vergrößert. Als Konsequenz liegt die Stelle an denen die Fasern durchtrennt sein könnten noch im Laminat von Klappe oder Handschuh und nicht an der Stelle des Steifigkeitssprungs (siehe auch Abbildung 3.5).

2.2.2. Winkelbegrenzung

Angaben zum Aufbau und zur Charakterisierung der Anbindung der Winkelbegrenzung können in den Veröffentlichungen:

- Anhang A.1 Abschnitt: „3.2 Angle restriction“
- Anhang A.2 Abschnitt: „4.2 Angle restriction“
- Anhang A.3 Abschnitt: „3.2. Structural design“

gefunden werden. Zur Dimensionierung der Winkelbegrenzungen wurden die 2D CFD-Simulationen herangezogen. Das maximal auftretende Moment wurde aus der maximalen Druckdifferenz zwischen Ober- und Unterseite der Klappe auf 7.6Nm abgeschätzt. Dabei wurden die Randeffekte

die zu einer Reduktion dieses Momentes führen bewusst vernachlässigt. Weiterhin wurde die konservative Annahme getroffen, dass die maximale Druckdifferenz über der gesamten Klappenfläche anliegt.
Es wurden zwei verschiedene Varianten zur Anbindung an die GFK-Struktur experimentell untersucht. Da eine Anbindung über das EPDM höhere Kräfte aufnehmen konnte wurde diese Ausführung gewählt. Aus dem Versuch in Anhang A.5 wurde die Festigkeit auf 34N pro 10mm Breite der Winkelbegrenzung festgelegt. Bei 7 Winkelbegrenzungen verteilt über die Modelspannweite mit einer Breite von jeweils 15mm die einen Abstand von 35mm zur virtuellen Scharnierachse haben, können die Winkelbegrenzungen ein Moment von ca. 12.5Nm aufnehmen.
Für die Charakterisierung wurde das verstärkende Glasfasergewebe in $\pm 45°$ Richtung eingelegt. Beim Versuch konnte beobachtet werden, dass die starke Querkontraktion dieses Aufbaus das Versagen beschleunigt. Im Model wurde daher eine $0/90°$ Ausrichtung realisiert. Zusätzlich wurden die Winkelbegrenzungen mit einem über die Winkelbegrenzung gelegtem Streifen GFK-Prepreg an der übrigen GFK-Struktur fixiert (siehe Abbildungen 3.10 bis 3.12).
Die Länge der Winkelbegrenzung, welche für die Einstellung eines bestimmten Klappenöffnungswinkels notwendig ist, kann über das Formelwerk zur Beschreibung der Klappenkinematik erfolgen (Anhang A.1 Abschnitt: „3.2 Angle restriction“ und Anhang A.2 Abschnitt: „4.2 Angle restriction“). Für das im Rahmen des Projektes STELAR gefertigte Modell betrug die freie Länge 21mm. Die Winkelbegrenzung wurde über eine Länge von 10mm an der Klappe und dem GFK-Handschuh angebunden. Die Winkelbegrenzung in der Modellmitte wurde aufgrund der dort vorgesehenen Druckmessungen in zwei Teile aufgespalten und aus der Mitte verschoben. Mit je 10mm sind die beiden Begrenzungen nah der Mitte in Summe etwas breiter als die ursprünglich vorgesehenen 15mm.

2.2.3. Aktuator Mechanismus

Der verwendete Aktuator Mechanismus basiert auf sich abstoßenden Permanentmagneten und ist in den folgenden Teilen der Veröffentlichungen beschrieben:

- Anhang A.1 Abschnitt: „4.2.1 Permanent magnets“
- Anhang A.2 Abschnitt: „5.2 Permanent magnet“
- Anhang A.3 und Anhang A.4 jeweils in Abschnitt: „3.3. Actuation“

Die Ansteuerung der Magnetsteller (Datenblatt im Anhang A.12) auf beiden Seiten des Modells wurde bislang noch nicht beschrieben. Die Ansteuerung der vier Elektromagnete erfolgt über je einen MOSFET Transistor (Datenblatt siehe Anhang A.13), der über einen Mikrocontroller (ATmega8 von ATMEL) geschaltet wird (siehe Abbildung 2.1). Für die Synchronisierung mit

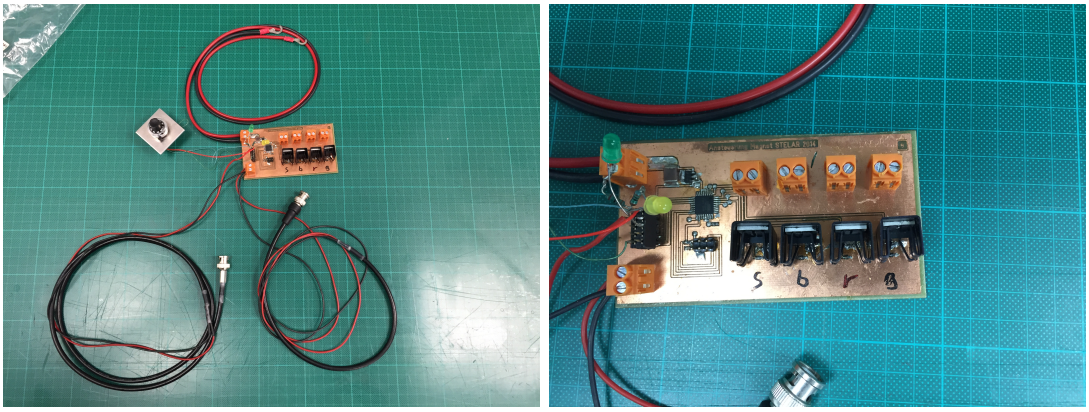

Abbildung 2.1.: Ansteuerung Elektromagnete

der Modellbewegung benötigt der Mikrocontroller eine sinusförmige Spannung die mit der Modelloszillation korreliert. Aus dieser Spannung wird bei der Initialisierung des Mikrocontrollerprogramms die Schwingfrequenz des Modells ermittelt. Im Anschluss wird die Signalspannung mit einem Schwellwert verglichen, der über ein Potentiometer eingestellt werden kann. Ist der Schwellwert erreicht, startet eine Subroutine die nach einer im Programm definierten „Wartephase“ zwei der Magnetsteller zum Öffnen der Klappe für eine ebenfalls definierte Phasendauer aktiviert um dann nach einer vorgegebenen „Öffnungsphase“ der Klappe die zwei Magnetsteller zum Schließen der Klappe zu aktivieren. Der Schaltplan die Platinenlayouts und das Ansteuerprogramm befinden sich in Anhang A.14.

3. Fertigung des Windkanalmodells

Die Fertigung aller am Institut für Faserverbundleichtbau und Adaptronik hergestellten Bauteile wird in Form eines Life Data Sheets dokumentiert und begleitet. Das Life Data Sheet für die Fertigung der Ober- und Unterschale des Windkanalmodells ist in Anhang A.6 zu finden. Die Dokumentation der Nachbearbeitung der Schalen, der Instrumentierung und der Montage erfolgt im Rahmen dieses Berichtes. Die Datenblätter der verwendeten Materialien sind den Anhängen A.7 bis A.10 zu entnehmen.

3.1. Fertigungskonzept

Verschiedene Aspekte des Fertigungskonzeptes sind in den folgenden Abschnitten der Publikationen im Anhang zu finden:

- Anhang A.1 Abschnitt: „3.3 Manufacturing concept“
- Anhang A.2 Abschnitt: „4 Structural design of the flap“
- Anhang A.3 Abschnitt: „4. MANUFACTURING CONCEPT“

3.2. Vorbereitung

Vor der Fertigung der GFK-Schalen waren einige vorbereitende Arbeiten notwendig. Diese generieren keine wissenschaftlichen Erkenntnisse und sind daher nicht in den Publikationen dokumentiert. Dieser Abschnitt dient der kurzen Beschreibung dieser unterstützenden Arbeiten.

Vorbereitung Winkelbegrenzungen

Das EPDM lag in Form einer auf 0.5mm Dicke kalandrierten Folie vor. Da die Winkelbegrenzung aus zwei Lagen EPDM besteht und zusätzlich noch einmal gefaltet wird, würde eine Verwendung des Materials in Originalstärke zu einer Aufdickung von mindestens 2mm führen. Daher wurde das Material in der Presse zwischen Distanzen von 0.1mm nochmals gepresst (siehe Abbildung 3.1). Das EPDM wurde zwischen einer Trennfolie und teflonisiertem Abreiss-

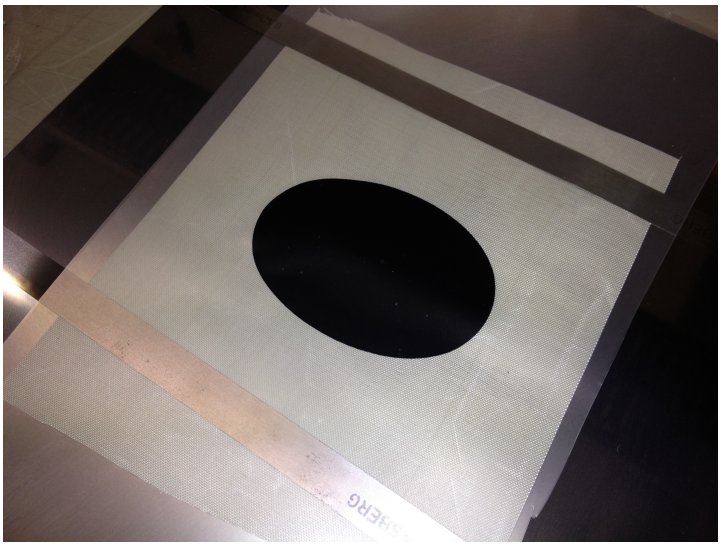

Abbildung 3.1.: Gepresstes EPDM

gewebe gepresst. Die Faserverstärkung (Glasgewebe 50g/m^2) wurde dann zwischen zwei der gepressten EPDM Folien gelegt und mit dem Messer von Hand zugeschnitten (siehe Abbildung 3.2).

Vorbereitung GFK

Der Zuschnitt aller GFK-Lagen erfolgte auf einem Cutter unter Verwendung einer Ziehklinge. Insbesondere die Aussparungen im Feststoffgelenk und die Aussparungen für die Integration der Neodymmagnete können von Hand nur mit sehr hohem Aufwand eingebracht werden.

Vorbereitung Druckmessung auf und unter der Klappe

Um später die Drücke auf und unter der Klappe messen zu können, werden im Fertigungsprozess Druckmessröhrchen integriert. Dabei muss verhindert werden, dass sich diese im Autoklavprozess mit Harz füllen. Dazu werden die Röhrchen an einer Seite irreversibel mit einem Tropfen Harz versiegelt. In das Röhrchen wurde ein eingetrennter dünner Draht geschoben, der an der nicht permanent verschlossenen Seite aus dem Röhrchen ragt. An dieser Seite wird das Röhrchen reversibel mit einem angegossenen Silikonblock verschlossen. Das Silikon wird nach der Fertigung entfernt und gibt dann einen Hohlraum frei der genutzt wird, um einen flexiblen

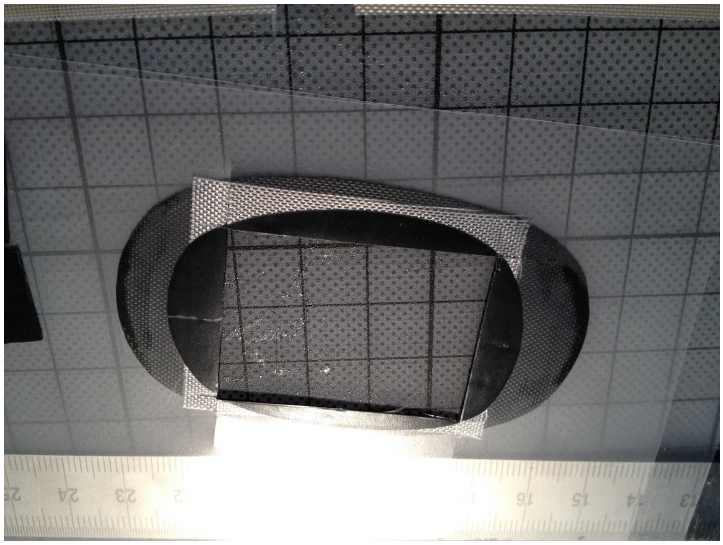

Abbildung 3.2.: Faserverstärktes EPDM

Schlauch aufzunehmen der das Röhrchen an einen Druckaufnehmer anschließt. Um den Silikonblock reproduzierbar zu formen wurden kleine Formen im 3D-Druckverfahren herstgestellt (siehe Abbildung 3.3).

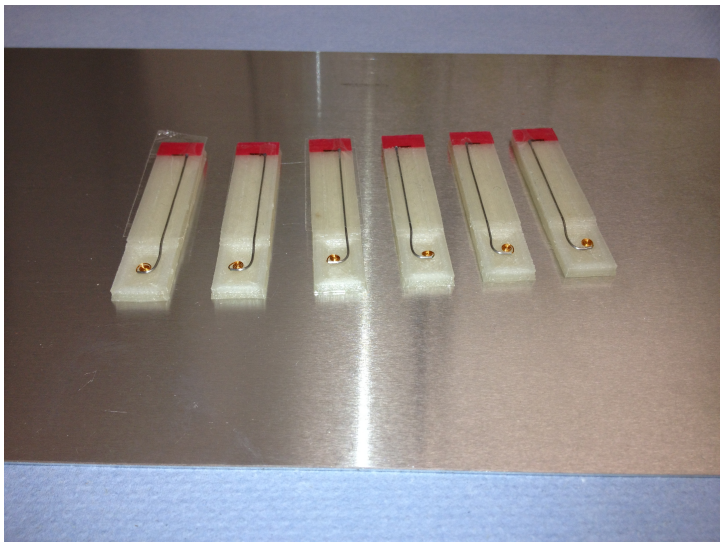

Abbildung 3.3.: Vorbereitete Druckmessröhrchen

3.3. Bau der Schalen

Anhand der folgenden Bilder wird der Ablauf beim Bau der Schalen beschrieben. Die Reihenfolge der Laminatablage und der weiteren Arbeitsschritte können ebenfalls dem LDS entnommen werden (siehe Abschnitt A.6). Zunächst wurden die Formen poliert, gesäubert und eingetrennt. Anschließend wurde ein Lineal in die Form geklebt das als Anlegekante für die Ablage des Klappenlaminates dient (siehe 3.4). Abbildung 3.5 zeigt einen Ausschnitt des Laminates nach

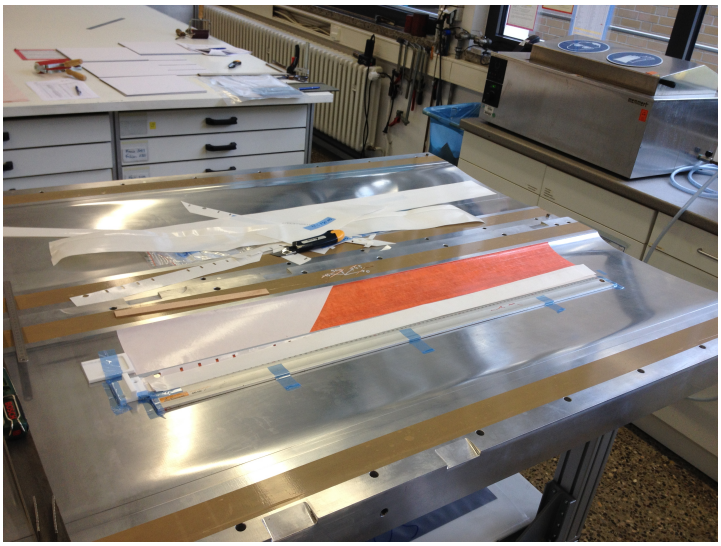

Abbildung 3.4.: Bau der Schalen

der Ablage der Mittellage der Klappe. Zu erkennen sind die Aussparungen für die Magnete

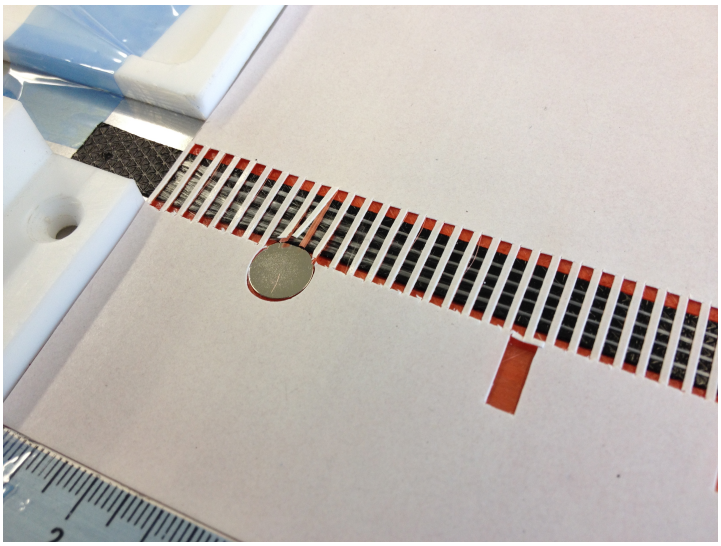

Abbildung 3.5.: Feststoffgelenk mit zusätzlicher Faserverstärkung gegen Beulenbildung

und die Aussparungen im Feststoffgelenk sowie die trockenen GFK-Rovings um Beulenbildung

im Bereich der Aussparungen zu vermindern. Nach jeder abgelegten Lage wurden die Magnete und die Druckröhrchen in die Aussparungen eingelegt um trotz des leichten Versatzes der Einzellagen die spätere Montage garantieren zu können. Nachdem das Laminat der Klappe ab-

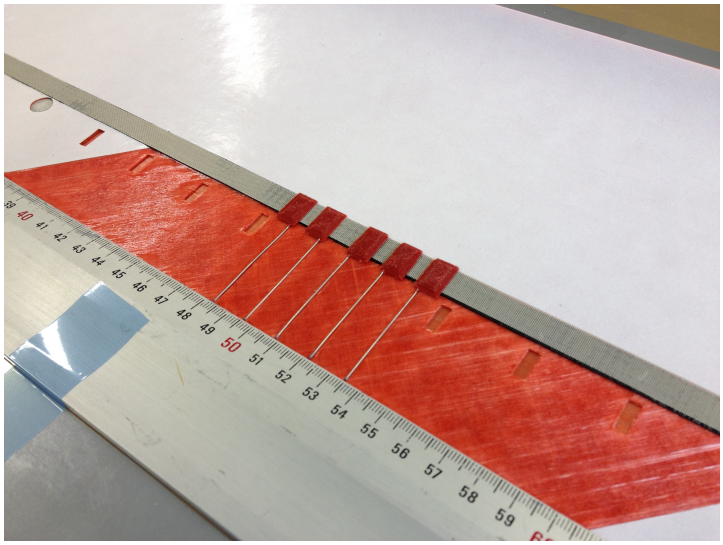

Abbildung 3.6.: Integration der Druckröhrchen

gelegt wurde, wurden die Druckröhrchen eingelegt (siehe Abbildung 3.6) und anschließend mit einer Zusatzlage GFK-Prepreg abgedeckt. Zwischen den Silikonklötzchen der Druckröhrchen und dem EPDM wurde ein Streifen teflonisiertes Abreißgewebe eingelegt.
Nach dem Einlegen der Magnete (siehe Abbildung 3.7) für die Klappenöffnung (rechteckig) und die Messung des Klappenwinkels mit Hall-Effekt-Sensoren (rund), wurden alle Magnete mit einem gut zu drapierendem trockenem Glasgewebe abgedeckt (siehe Abbildung 3.8). Dieses

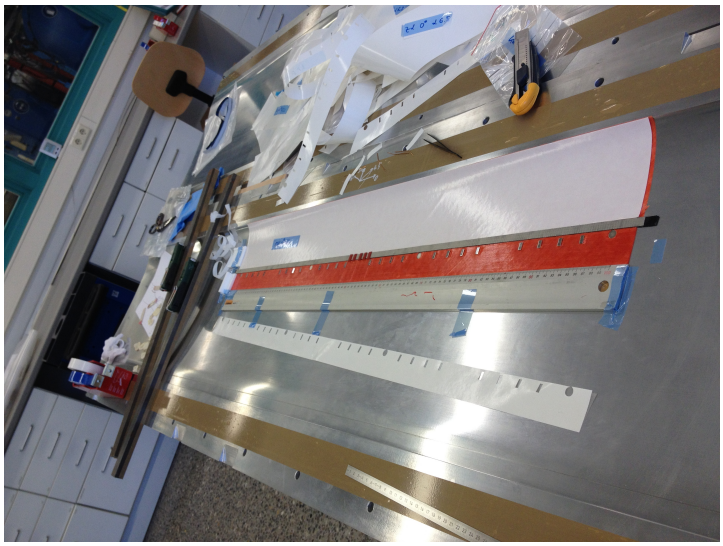

Abbildung 3.7.: Einlegen der Magnete

trockene Gewebe wird im Prozess mit überschüssigem Harz des GFK-Prepregs getränkt.

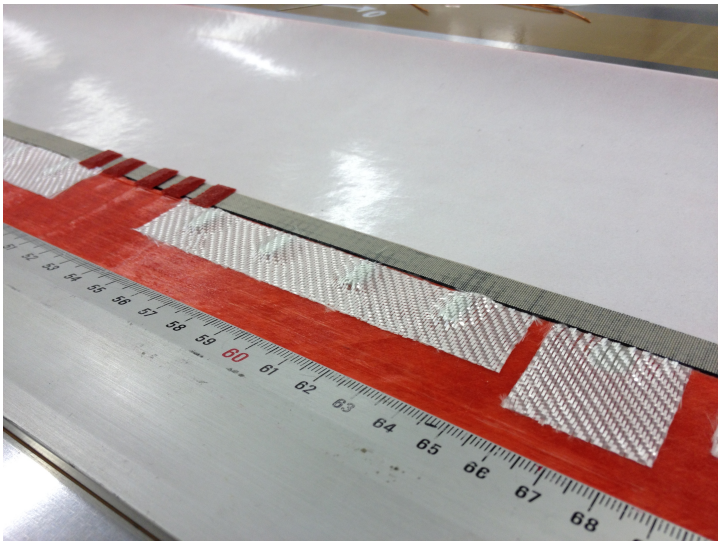

Abbildung 3.8.: Abdecken der Magnete mit trockenem Glasgewebe

Anschließend erfolgt die Ablage einer Trennfolie damit sich dich Klappe später öffnen kann (siehe Abbildung 3.9). Um die Anbindung der Winkelbegrenzung an die Klappenstruktur zu

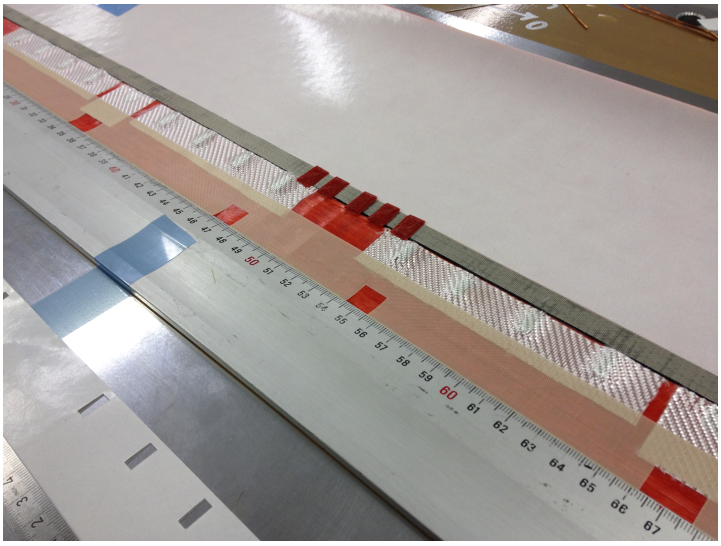

Abbildung 3.9.: Trennfolie mit Aussparungen für Winkelbegrenzung

gewährleisten wurde auch diese Trennfolien auf dem Cutter mit Aussparungen versehen.
In diese Aussparungen werden dann im nächsten Arbeitsschritt die vorbereiteten Winkelbegrenzungen eingelegt (siehe Abbildung 3.10). Ein kleiner Prepregstreifen dient der zusätzlichen Anbindung des Winkelbegrenzung an die Klappenstruktur.
Es folgt das in Abbildung 3.11 dargestellte Falten der Winkelbegrenzungen. Ein in teflonisiertes Abreißgewebe eingeschlagener Kupferdraht definiert den Knickradius und durch die Trennung

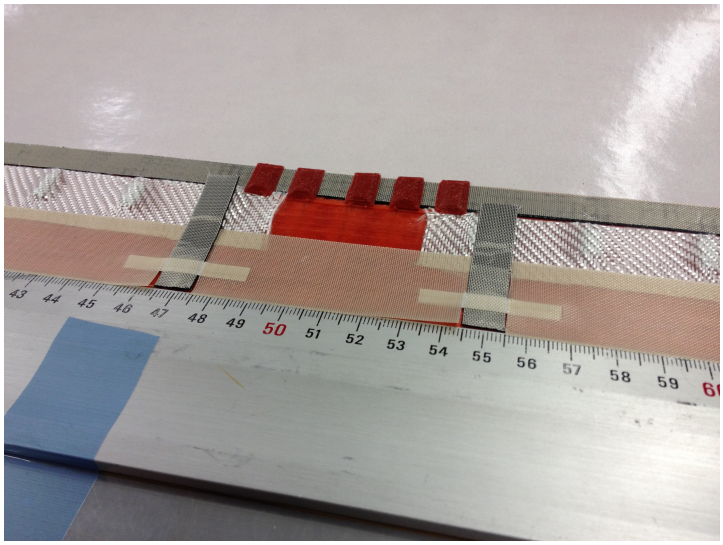

Abbildung 3.10.: Einlegen Winkelbegrenzung und Fixierung mit Prepregstreifen

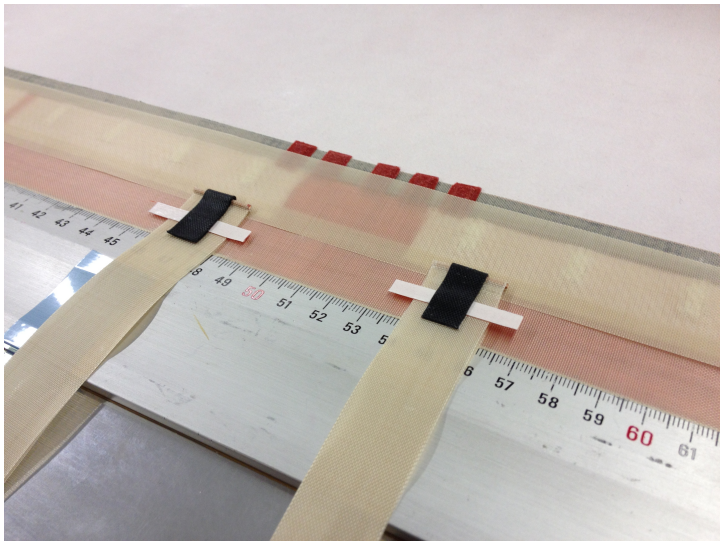

Abbildung 3.11.: Falten der Winkelbegrenzung und zusätzliche Trennfolie unter der Klappe

zwischen Ober- und Unterseite des Elastomers wird die spätere Öffnung ermöglicht. Die Abreißgewebestreifen werden auf die benötigte Länge gekürzt. Eine zusätzliche Lage teflonisiertes Abreißgewebe trennt den vorderen Teil der Klappe von der Handschuhstruktur. Die getrennte Ausführung der Trennlagen erleichterte die genaue Positionierung der Winkelbegrenzungen. In den Abbildung 3.11 und 3.12 ebenfalls zu erkennen sind die kurzen Prepregstreifen, die die Winkelbegrenzungen zusätzlich am Handschuh fixieren. Bevor die erste durchgehende Lage GFK-Prepreg abgelegt wird, muss noch wie in Abbildung 3.12 dargestellt, der vordere Teil der Winkelbegrenzung mit teflonisiertem Abreißgewebe abgedeckt werden.

Nach der Ablage des Laminates erfolgt der Vakuumaufbau und das Bauteil wird im Auto-

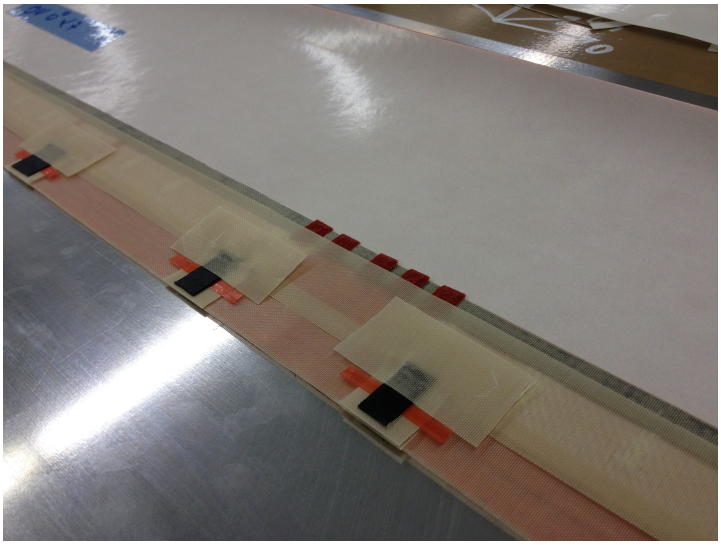

Abbildung 3.12.: Klappe mit Winkelbegrenzung direkt vor Ablage der ersten durchgehenden GFK-Lage

klaven gemäß dem im Life Data Sheet angegeben Zyklus ausgehärtet bzw. vulkanisiert (siehe Anhang A.6). Abbildung 3.13 zeigt die Oberschale des Windkanalmodells unmittelbar nach

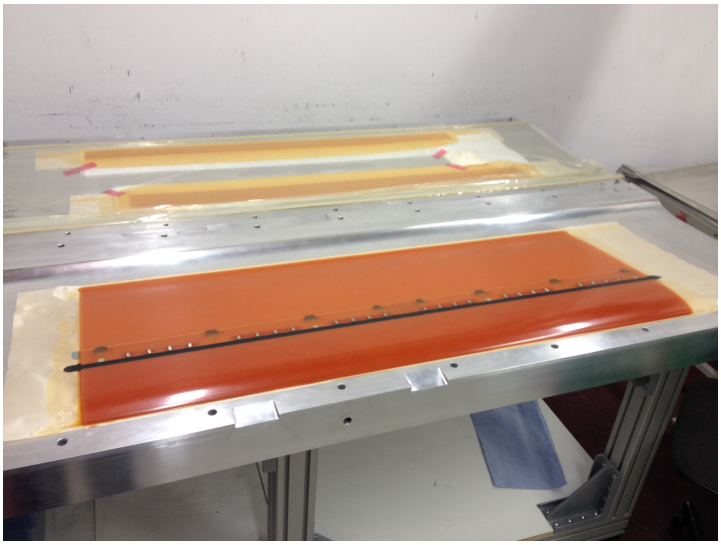

Abbildung 3.13.: Oberschale nach Entformen

dem Entformen des Bauteils.

3.4. Bearbeitung der Halbschalen

Für die weitere Bearbeitung der Schalen mussten diese wieder in der Form fixiert werden. Da das GFK der Schale und das Aluminum der Form unterschiedliche thermische Ausdehnungskoeffizienten haben, war dies nicht ohne weiteres möglich. Die Markierung zur Abtrennung der Hinterkante wurde händisch weggeschliffen. Dadurch konnte die Schale leicht zur Vorderkanten geschoben und besser in der Form fixiert werden.
Der im Fertigungskonzept beschriebene Dummy wurde mit Trennfolie beklebt und ebenfalls in die Form gelegt. Die seitlichen Enden wurden mit einer zurechtgeschnittenen Kopierfolie, Heißklebepistole und einem thixotropen, langsam härtendem Epoxidklebstoff abgedichtet (Loctite Hysol). Nachdem die seitliche Abdichtung durchgehärtet war, wurde er Hohlraum zwischen Schale und Dummy mit einem langsam härtendem Gießharz gefüllt (Datenblatt siehe Anhang A.9). Wichtig war, dass entstehende Gießharzblock über die Trennebene hinausragt. Dazu wurde eine Wulst aus Heißkleber als Barriere auf der vorher mit Packband abgeklebten Form aufgetragen.
Mit Hilfe des in Abbildung 3.14 dargestellten Fräsgestells wurde die Trennebene von Ober- und Unterseite der Schale gefräst. Weiterhin wurden mit diesem Werkzeug die Nut für die Führung

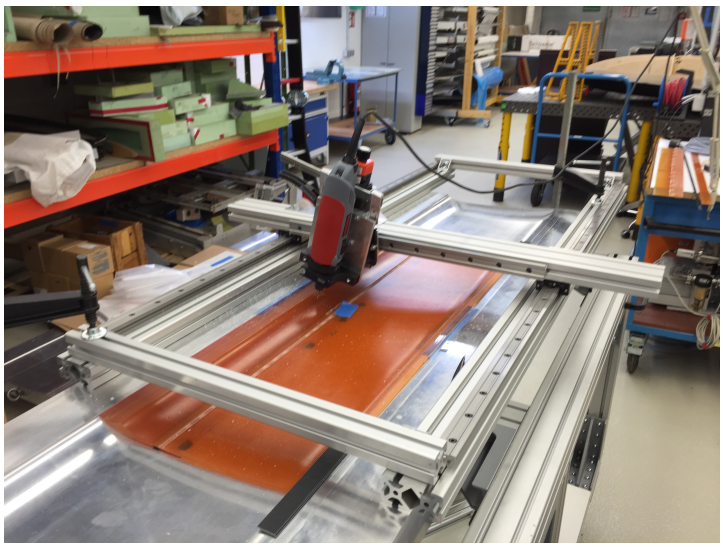

Abbildung 3.14.: Fräsgestell zur Nachbearbeitung der Trennebene und Einbringung von Nuten und Bohrungen

der Schubstange der Aktuatorik und die Kanäle für Kabel und Referenzdruckleitungen der Sensorik gefräst sowie die Durchführungen der Druckmessbohrungen gebohrt. Um die Form nicht zu beschädigen wurde die Schale zum Bohren mit Distanzen in der Form fixiert.

3.5. Instrumentierung

Die Positionen der durchzuführenden Druckbohrungen wurden mit Hilfe von Klebemarkierungen in die Schale übertragen. Um die Schale immer wieder in der gleichen Position auf das Modell legen zu können, wurden zunächst Anschläge an der Hinterkante des GFK-Handschuhs mit doppelseitigem Klebeband befestigt. Kleine Klebestreifenstückchen mit einer Markierung für die Druckbohrungsposition wurden mit der klebenden Seite nach oben mit Sensorwachs auf dem Modell positioniert. Wenn die Schale nun aufgelegt wird, kleben die Markierungen an der Schale und die Positionen sind übertragen. An den markierten Positionen wurde nun senkrecht zur Schaleninnenseite von Innen nach Außen durchgebohrt. Um die Bohrung später abdichten zu können wurde die Durchführung als plangesenkte Stufenbohrung ausgeführt in die später ein O-Ring eingesetzt werden kann (durchgehender Durchmesser 0.3mm, Senkungsdurchmesser 4mm). Die Dicke des O-Ring betrug 1.5mm die Tiefe der Senkung 1.3mm. Dabei ist zu beachten, dass die Dicke des zur Montage verwendeten Klebebandes ca. 0.2mm beträgt. Um die Abdichtung zu gewährleisten wurden die O-Ringe zusätzlich dünn mit Sensorwachs bestrichen und in die Senkung gedrückt. Überschüssiges Wachs muss entfernt werden, da es sonst die Bohrung verstopfen kann.

Zusätzlich zu den durchgeführten Druckmessbohrungen ist das Modell mit weiteren Drucksensoren nahe der Vorderkante und auf Ober- und Unterseite der Klappe ausgerüstet. Der vorderste Sensor auf der Oberseite wurde versehentlich bei 2.5%c an Stelle von 0.25%c positioniert. Für die Druckmessung auf der Klappe müssen die Druckröhrchen von außen angebohrt werden. dabei ist darauf zu achten, dass der Draht (soll während der Fertigung das Risiko eines Harzeintrittes reduzieren) vorher aus dem Röhrchen gezogen wird. Sonst droht dieser abzureißen und das Röhrchen zu verstopfen.

Die Röhrchen in der Klappe werden dann über einen flexiblen Schlauch mit den Drucksensoren im Handschuh verbunden (siehe Abbildung 3.15). Neben der Druckinstrumentierung zeigt Abbildung 3.15 auf der linken Seite ebenfalls einen der zur Messung des Klappenwinkels verwendeten Hall-Effekt-Sensoren (Datenblatt siehe Anhang A.11). Die Vertiefungen, in die die Sensoren geklebt wurden sowie die dazugehörigen Kabelkanäle, sind mit dem in Abbildung 3.14 dargestellten Fräsgestell eingebracht wurden.

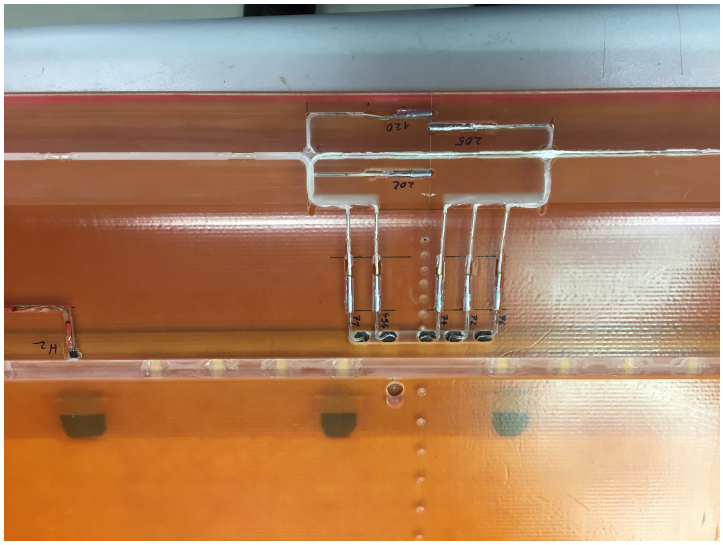

Abbildung 3.15.: Instrumentierte Schale

3.6. Aktuatorik

Für die Realisierung des in Abschnitt 2.2.3 beschriebenen Aktuatorkonzeptes musste das vorhandene Windkanalmodell und dessen Anbindung an den Nickversuchstand im Windkanal modifiziert werden.

Als Verbindungsglied zwischen Modell und Versuchstand dienen die sogenannten Modellbalken an beiden spannweitigen Enden des Modells. Diese können genutzt werden um den Schwerpunkt des Modells mittels Zusatzmassen auf die Rotationsachse zu verschieben, Kabel und Referenzdruckleitungen zu fixieren oder den Anstellwinkel über Abstandsmessungen zu bestimmen. Zur Öffnung der Klappe werden Permanentmagnete unterhalb der Klappe linear verschoben. Diese Translationsbewegung soll mit seitlich am Modell montierten Linearmagneten realisiert werden. Um diese Linearmagnete zu montieren, wurden neue Modellbalken mit entsprechenden Winkelkonsolen konstruiert und gefertigt. Die Konstruktionszeichnungen sind dem Anhang A.15 zu entnehmen. Die Modellbalken sind so konstruiert, dass diese bei einem Anstellwinkel des Modells im Windkanal von etwa 10° horizontal verlaufen.

Die Anker der beiden Linearmagnete werden auf jeder Seite des Modells mit einer Querstange verbunden (Zeichnung siehe Anhang A.16). Diese wird dann mit einer Schubstange mit integrierten Permanentmagneten verbunden. Die Schubstange besteht aus kurzen CFK-Stücken die als Platzhalter zwischen den Magneten dienen. Da die real gefertigten Abstände zwischen den Magneten geringfügig von den durch die Konstruktion vorgegebenen Abständen abweichen können und sich diese Abweichungen aber aufgrund der großen Anzahl von Einzelstücken

aufsummieren können, wurde die Stange auf Basis der real nach der Fertigung der Schalen gemessenen Abstände gefertigt. Dazu wurden auf die Stangenober- und -unterseite je zwei lagen eines dünnen Glasgewebes ($50 g/m^2$) im Handlaminierverfahren auflaminiert. Diese vier Lagen halten die Einzelstücke zusammen und übertragen die Zugkräfte innerhalb der Stange während des Öffnungs- und Schließvorgangs. Auf der Unterseite der Schubstange wurde eine Teflonfolie aufgeklebt um das darunterliegende Modell vor Abrieb zu schützen.
Die Schubstange tritt seitlich im Bereich der Modellbefestigung aus dem Handschuh hervor. Um dies zu ermöglichen wurde der Modellfuß mit einer zusätzlichen Fase versehen (siehe Abbildung 3.16). Eine überschlägige Festigkeitsrechnung unter Berücksichtigung der modifizierten

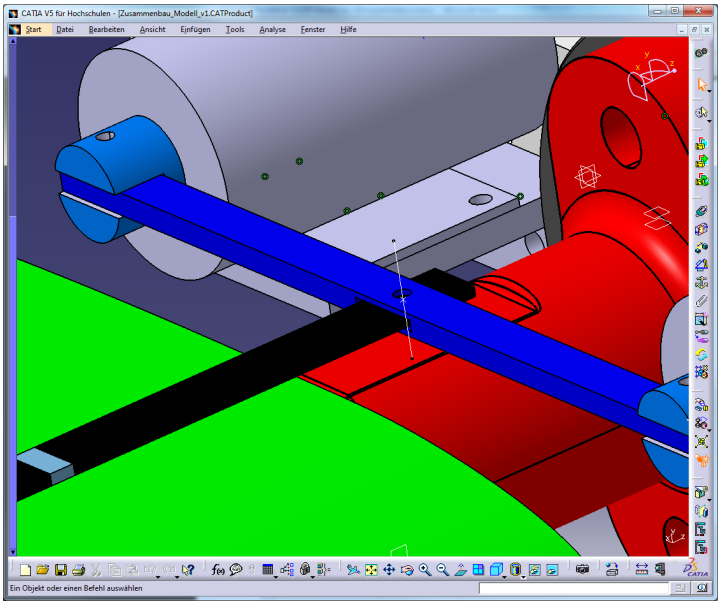

Abbildung 3.16.: Modifikation der Modellhalterung

Geometrie kann im Anhang A.17 gefunden werden.

3.7. Montage auf dem Windkanalmodell

Im Rahmen des Projektes bestand die Anforderung die entwickelte Rückströmklappe als eine Art Nachrüstlösung reversibel auf das schon existierende Windkanalmodell aufzubringen. Die Verwendung einer doppelseitigen Klebefolie schien hier aus mehreren Gründen geeignet.

- Aufgrund der großen Klebefläche reichen bereits moderate Klebfestigkeiten zur sicheren Montage.
- Die Klebefolie stellt einen definierten Abstand der Fügepartner ein.

- Eine Verarbeitung bei Raumtemperatur ist möglich.
- Eine moderate Erwärmung kann evtl. die spätere Demontage erleichtern (fraglich beim final eingesetzten Produkt).
- Die flächige Verklebung wirkt als zusätzliche Abdichtung der Druckmessstellen untereinander.

Trotz dieser Vielzahl an Vorteilen eignet sich nicht jede Klebefolie für den Einsatz im Windkanal. Beim Test eines 20cm breiten Streifens im Windkanal stellte sich der Verwendete Klebefilm als Schwachstelle heraus. Aufgrund der Erwärmung der Kanalluft und des zusätzlichen Wärmeeintrages über die für die Hochgeschwindigkeitsaufnahmen benötigten Scheinwerfer, löste sich eine Ecke des 20cm Handschuhs und musste mit Aluminium-Tape zusätzlich fixiert werden. Ein erneutes Andrücken schaffte zwar kurzzeitig Abhilfe, durch das viskose Verhalten der Klebschicht löste sich der Handschuh unter der konstant wirkenden Kraft jedoch erneut. Eine potentielle Ursache für die Ablösung ist auf die geringe Dicke der verwendeten Klebefolie zurückzuführen. Die Innenseite des Handschuhs hat eine strukturierte Oberfläche. Diese entsteht im Fertigungsprozess durch die Struktur der Trennfolie die den Dummy (während des Ausgießens des Hohlraums mit Harz) umhüllt. Die Oberflächenstruktur und der nur wenig elastische Klebefilm führen dazu, dass es nur einzelne Punktkontakte zwischen Modell und Handschuh gibt.
Um diese Schwierigkeit zu lösen wurden verschiedene Klebefolien beschafft und sowohl im Zugversuch als auch in einem Dauerversuch mit Schälbeanspruchung auf deren Versagensverhalten getestet. Dabei galt es einen Kompromiss zu finden aus :

- maximaler Festigkeit
- Elastizität zum Ausgleich von Unebenheiten in der Oberfläche der Fügepartner
- Kriechverhalten unter andauernder Belastung

Neben diversen am Institut verfügbaren doppelseitigen Klebebändern und -folien wurden folgende vielversprechende Produkte getestet: tesafix® 4965, tesafix® 4970, tesa® ACXplus 7054, 3M Pressure sensitive Tape Scotch® Klebeband (Gewebeklebeband) und 3M Montageband. Für die Verklebung wurde schlussendlich ein doppelseitig klebendes, transparentes Polyesterklebeband mit Acrylatklebmasse (tesafix® 4965) verwendet (Datenblatt siehe Anhang A.10). Diese ca. 0.2mm starke Klebefolie stellte den besten Kompormiss für die oben gelisteten Anforderungen dar. Die Temperaturbeständigkeit des Klebebandes ist für den Versuch von Vorteil,

könnte jedoch beim Entfernen des Handschuhs zu Schwierigkeiten führen.
Auf der Unterseite des Windkanalmodells wird die Oberfläche des unterliegenden Originalmodells verwendet. Am Übergang vom GFK-Handschuh auf das Modell entsteht eine Stufe von ca. 0.5-0.8mm. Diese Kante wurde vor dem Windkanaversuch mit einem essig-vernetzendem Silikon von Hand abgezogen. Die Qualität der Oberfläche und die Gleichmäßigkeit der Fuge über die Profillänge hängt stark vom Geschick des Mitarbeiters ab. Da die Arbeit am eingebauten Modell eine zusätzliche Herausforderung darstellt, sollte diese Arbeit zuvor erfolgen.

A. Anhang

A.1. Paper: Advances in aircraft and spacecraft science (2014), Volume 1 Number 1

Advances in Aircraft and Spacecraft Science, *Vol. 1, No. 1 (2014) 069-091*
DOI: http://dx.doi.org/10.12989/aas.2014.1.1.069

An active back-flow flap for a helicopter rotor blade

Steffen Opitz*[1],Kurt Kaufmann[2a] and Anthony Gardner[2b]

[1]*German Aerospace Center (DLR), Institute of Composite Structures and Adaptive Systems, Lilienthalplatz, 7, 38108 Braunschweig, Germany*
[2]*German Aerospace Center (DLR), Institute of Aerodynamics and Flow Technology, Bunsenstraße, 10, 37073 Göttingen, Germany*

(Received June 18, 2013, Revised August 29, 2013, Accepted November 1, 2013)

Abstract. Numerical investigations are presented, which show that a back-flow flap can improve the dynamic stall characteristics of oscillating airfoils. The flap was able to weaken the stall vortex and therefore to reduce the peak in the pitching moment. This paper gives a brief insight into the method of function of a back-flow flap. Initial wind tunnel experiments were performed to define the structural requirements for a detailed experimental wind tunnel characterization. A structural integration concept and two different actuation mechanisms of a back-flow flap for a helicopter rotor blade are presented. First a piezoelectric actuation system was investigated, but the analytical model to estimate the performance showed that the displacement generated is too low to enable reliable operation. The seond actuation mechanism is based on magnetic forces to generate an impulse that initiates the opening of the flap. A concept based on two permanent magnets is further detailed and characterized, and this mechanism is shown to generate sufficient impulse for reliable operation in the wind tunnel.

Keywords: back-flow flap; active flap; flow control; solid state hinge; helicopter; rotor blade

1. Introduction

If the angle of attack of an airfoil is increased above a critical value, stall occurs. The stall is attended by a decrease of lift, an increase of drag and a change of the aerodynamic pitching moment. In order to reduce these negative effects an observation of birds in flight can inspire a technical solution. In case of stall the top feathers of bird wings begin to lift which delays the decrease in lift and prevents the back-flow, generated by the stall vortex, on the upper airfoil surface. This functional principle can be transferred, and has already been demonstrated for fixed wing aircraft. For helicopters this transfer is even more challenging. The flow field of a helicopter rotor in forward flight is very complex. During each revolution the rotor blades may be subjected to blade vortex interactions, transonic effects, reverse flow and stall. The stall that occurs on the retreating blade has a highly dynamic character and therefore significantly differs from the static stall of airfoils.

Dynamic stall can be controlled using passive devices, including vortex generators and changes in the leading edge contour (Mai *et al.* 2008, Martin *et al.* 2008), but these have disadvantages at

*Corresponding author, Dipl. Ing., E-mail: Steffen.Opitz@dlr.de
[a] Dipl. Ing., E-mail: Kurt.Kaufmann@dlr.de
[b] Ph.D., E-mail: Tony.Gardner@dlr.de

http://www.techno-press.org/?journal=aas&subpage=7 ISSN: 2287-528X (Print), 2287-5271 (Online)

high Mach number and are limited in their control of deep stall. In contrast, active devices including actively retracting vortex generators (LePape *et al.* 2012, Barth *et al.* 2011), which avoid shocks at high Mach number, or air jets (Gardner *et al.* 2012, Weaver *et al.* 2004), which add energy to the flow, can improve the flow control under deep stall conditions.

As part of the DLR project STELAR, alternative methods of influencing the dynamic stall using an active back-flow flap are presently being investigated (Kaufmann *et al.* 2012). In the past back-flow flaps have been tested on gliders as a passive method of reducing stall (Meyer 2000), as freely-hinged spoiler-like flaps on the suction side of the airfoil near the trailing edge. When trailing edge stall occurs, the back-flow lifts the flap and the region of stall can be significantly delayed. Even though the effectiveness of back-flow flaps has been demonstrated in flight experiments with sailplanes, it still has to be investigated whether they are also suited to improve the dynamic stall behavior of helicopter rotor blades (Höfinger 2012). In the past a range of different flap types have been investigated for rotorcraft including slotted leading edges (Carr *et al.* 2001) and droop noses (Martin *et al.* 2003). For vibration and BVI control, trailing edge flaps are preferred (Friedmann *et al.* 2001). Trailing edge flaps have recently been flown on a test helicopter (Ahci-Ezgi *et al.* 2013), showing that both bandwidth and installation problems can be overcome for the implementation of flaps on a real rotor. The presented work focuses on the numerical and experimental investigation of the effectiveness of an active back-flow flap for an oscillating but nonrotating airfoil. The performance of the active flow control system is still unclear for rotary flow and will be studied after the experiments in the nonrotating system.

2. Aerodynamic background and wind tunnel experiments

Dynamic stall is a well-known effect for helicopter airfoils occurring when a pitching airfoil stalls, forming separated flow in a dynamic stall vortex. A lift peak and a negative spike in pitching moment form and then a rapid drop in lift appears as the stall vortex moves downstream. The torsional impulse from the pitching moment peak is often a load-limiting case for the pitch links of the helicopter rotor blades, and high drag is experienced compared to attached flow. The leading-edge stall associated with many helicopter airfoils including the OA209 (Gallot *et al.* 1982) airfoil used for the numerical predictions, is characterized by strong backward flow along the suction side of the airfoil (Mulleners and Raffel 2012). To control dynamic stall of this type, the single dynamic stall vortex should be broken into several smaller vortices and the passage of the vortices should be delayed (Gardner *et al.* 2012). Initial numerical investigations with an actively actuated flap showed promising results.

Fig. 1 shows a comparison between the flow during dynamic stall for M=0.14, R*e*= 920000, $\omega^* = 2\pi fc/v_\infty = 0.1, \alpha = 16 \pm 8°$, at $\alpha = 21°$ on the upstroke, with active and inactive back-flow flap. The computation is performed in 2D using the unstructured DLR-TAU solver and the Spalart-Allmaras turbulence model with the settings of Richter *et al.* 2011. The flap is dynamically actuated to only be deployed during the stalled flow, by using the overset grid (chimera) method with automatic hole cutting. It can be seen that the back-flow flap breaks the main stall vortex into smaller structures, and this results in a reduction in the pitching moment peak by 34% compared to the reference case without actuation, while maintaining the lift during the attached flow (see Fig. 2).

To validate the results of the numerical study, experiments were performed in the 1MG low speed wind tunnel in Göttingen. The experiments were performed with an open test section of 1m

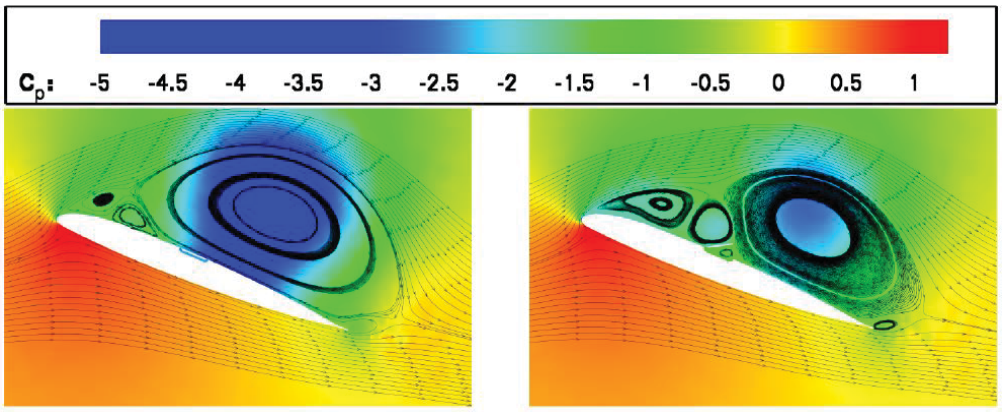

Fig. 1 Comparison of streamlines and pressure for flow without flap actuation (Left) and with flap actuation (Right) for the OA209 airfoil at M=0.14, R*e*= 920000, $\omega^* = 0.1, \alpha = 16 \pm 8°$, at $\alpha = 21°$ on the upstroke (Kaufmann *et al.* 2012)

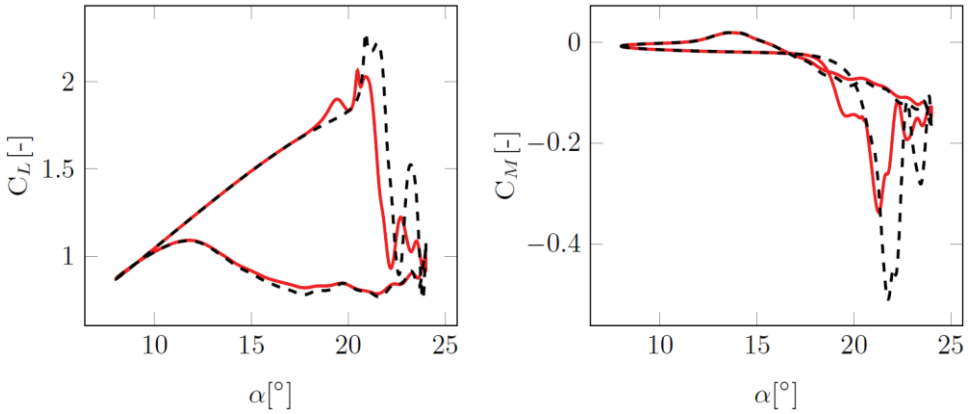

Fig. 2 Comparison of lift (Left) and pitching moment coefficient (Right) for the OA209 airfoil at M=0.14, R*e*= 920000, $\omega^* = 0.1, \alpha = 16 \pm 8°$. The black lines are without flap actuation, and the red lines are with flap actuation (Kaufmann *et al.* 2012)

width and 0.70m height and flow at 50 m/s on a NACA0012 airfoil of 0.3m chord, pitching at $\alpha = 20 \pm 8°$ and f = 3 - 6 Hz: the same conditions as in the CFD above, but with the mean angle increased to compensate for the large blockage of this wind tunnel model.

As seen in Fig. 3, the flap was attached to the suction side of the model with tape, and the deployment of the flap was restrained in angle using cords. The flow was monitored using tufts and a high-speed video camera. For this experiment the model pressures were not monitored. The analysis of the high-speed videos showed that the back-flow flap self-actuated due to the back-flow of the dynamic stall vortex, but that this occurred too late after stall to have an effect on the pitching moment peak due to dynamic stall. Further, the flap self-closed in acceptable time as the flow reattached, and generally was not influenced by the inertial forces due to pitching, at pitching frequencies of up to *f=6Hz*. Unfortunately, the pressure gradient over the flap during

Fig. 3 Passive back-flow flap model in the 1MG at 50 m/s. Flow is from left to right

attached flow caused it to not lie perfectly flat on the airfoil surface, but to stabilize at a minimum angle of around 5-10° to the surface, depending on the flap position. This effect meant that positioning the flap in or close to the suction peak resulted in the flap fully opening even when no separated flow was present. The conclusion was thus that the back-flow flap should have active actuation to open during stall, and active actuation to hold it closed during attached flow.

3. Structural concept

Motivated by the first numerical predictions and the initial wind tunnel experiments the structural realization of such a flap was investigated. Ideally it should be possible to retrofit the back-flow flap to existing blades. Therefore a concept to fit the whole system into a kind of "glove", that can be put over a conventional blade, is pursued. Consequently the resulting limits in the available space will be a major challenge in the design process. Furthermore, the hinge that connects the flap to the blade should be robust enough to enable a reliable deployment at high frequencies without significant friction or wear within the strong centrifugal field of a helicopter rotor. Using composite materials for the flap offers the possibility to integrate functionalities like an actuator or a hinge directly into the structure (Wierach 2012a, Wierach *et al.* 2012b).

3.1 Solid state hinge

The surface of the hinge that connects the flap to the blade should be as smooth as possible to prevent any disturbance of the flow when the flap is not deployed. For this reason conventional hinges, consisting of two hinge leaves, are not suited. Further, those joints rely on the relative movement of two solid bodies. Even though lubricants can reduce the amount of friction that is produced in the contact area between both hinge leaves, high frequency actuation would cause significant wear. For the application on a real helicopter blade the centrifugal forces would make all problems arising with friction and wear even more severe. All these issues can be addressed using a solid state hinge. Solid state hinges generate the relative movement of the rigid parts by elastic deformation of a flexible region. Since they have no moving parts they do not suffer from

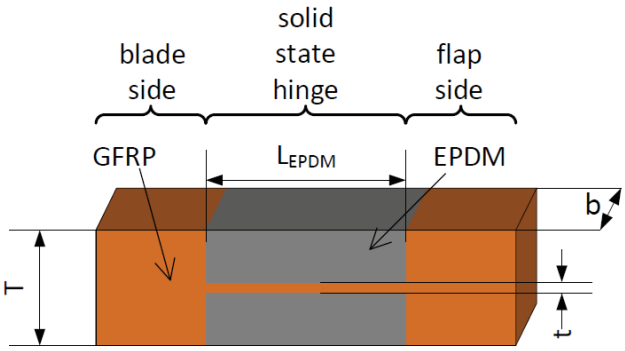

Fig. 4 Principle and dimensions of solid state hinge

friction or wear. The following Fig. 4 depicts the general design and dimensions of the solid state hinge that connects the flap to the blade.

Of course the material in the flexible region must sustain the occurring strains without any plastic deformation. Nevertheless it should have a certain stiffness to prevent large longitudinal strains. As GFRP (Glass Fibre Reinforced Polymer) shows a linear elastic material behavior up to high strains it is a well suited material for this application. Since the fracture strain in fiber direction of a unidirectional GFRP material is higher than transverse to the fiber, the fibers should be oriented in parallel to the neutral axis of the hinge. In this configuration a bending of the hinge does not produce any coupled torsion deformation. The strains that occur due to bending remain small as long as the material is located close to the neutral axis. However due to manufacturing constraints the thickness *t* of the flexible GFRP part of the hinge cannot be arbitrarily small. The hinge is designed to have a symmetric three layer setup. The middle layer GFRP directly connects the flap to the blade. As this thin layer would be quite fragile, it is encapsulated in EPDM (Ethylene Propylene Diene Monomer). The larger distance of the elastomer to the neutral axis, results in bigger strains in the EPDM layers. But as this highly flexible material can easily bear strains of 100% and more, EPDM is an excellent material for this application.

As the degree of freedom in a solid state hinge is realized through an elastic deformation the joint is always characterized by a certain spring characteristic. Consequently an additional force or moment has to be overcome to deploy the flap. For the design process the knowledge of the elastic characteristic of the hinge is needed. For this purpose a simple and fast analytical model to predict the bending stiffness of the 3 layer setup was verified with numerical investigations and finally validated with experimental data. For the analytical prediction of the spring characteristic the bending stiffness of the solid state hinge EI_{SSH} is derived as follows:

$$\frac{EI_{SSH}}{b} = \frac{EI_{GFRP}}{b} + \frac{EI_{EPDM}}{b} \tag{1}$$

$$= E_{GFRP} \cdot \frac{t^3}{12} + E_{EPDM} \cdot \left(\frac{(T - t^3)}{48} + \frac{(T - t) \cdot (T + t)^2}{16} \right) \tag{2}$$

As the stiffness is linearly proportional to the extruded length of the hinge *b* the value EI_{SSH} is normalized to this dimension. For the calculation of the equivalent torsional spring characteristic

c_t, textbook formulas can be used (Grote and Feldhusen (eds) 2012). The inclination angle α_{flap} at the end of a uniform beam with the length L_{EPDM} and the bending stiffness EI_{SSH} that is deformed by a bending moment M_b at the free end can be calculated by:

$$\alpha_{flap} = \frac{M_b \cdot L_{EPDM}}{EI_{SSH}} \tag{3}$$

$$c_t = \frac{M_b}{\alpha_{flap}} \tag{4}$$

$$\frac{c_t}{b} = \frac{EI_{SSH}}{b \cdot L_{EPDM}} \tag{5}$$

In order to verify and validate the analytical estimation of the spring characteristic 4 different configurations of solid state hinges were investigated. A summary of the different designs is given in Table 1.

To adjust the stiffness of the hinge, different design variables can be used. The investigated configurations comprise 2 different thicknesses of the central GFRP layer *t* as well as 2 lengths of the hinges L_{EPDM}. As the GFRP-layer could not be further reduced in thickness (due to manufacturing reasons), configuration 1 had cut outs in the direction of the extruded length *b*. Consequently only 50 % of the hinge area was covered with GFRP. The cut outs were filled with EPDM to prevent any holes allowing pressure equalization between the upper and the lower flap surface. In the analytical and numerical prediction this modification was modeled via a reduction of the elastic modulus of the middle layer according to a simple rule of mixture. Finally all four configurations were manufactured. For the experimental determination of the spring constant c_t a universal testing machine was used. The machine was equipped with a *10N* load cell. The load cell was connected to the flap by a thin sting in such a manner that the movement of the traverse of the testing machine opened the flap while the load cell measured the corresponding string force. The opening angle of the flap as well as the angle between the flap surface and the force was captured in equidistant steps of the traverse position. Therefore a photograph, taken for each step, is post-processed via image processing software. Finally the force component orthogonal to the flap surface is used to calculate the moment at the middle of the solid state hinge. The spring constant is then determined as the linear coefficient between flap angle and moment. Fig. 5 shows the comparison between the analytical and numerical prediction of the spring characteristic and the measured values.

Table 1 Solid state hinge configurations

Configuration no.	t [mm]	T [mm]	L_{EPDM} [mm]	Comment
1	0.125	1.125	10	50% cut out
2	0.125	1.125	10	-
3	0.125	1.125	15	-
4	0.25	1.25	10	-

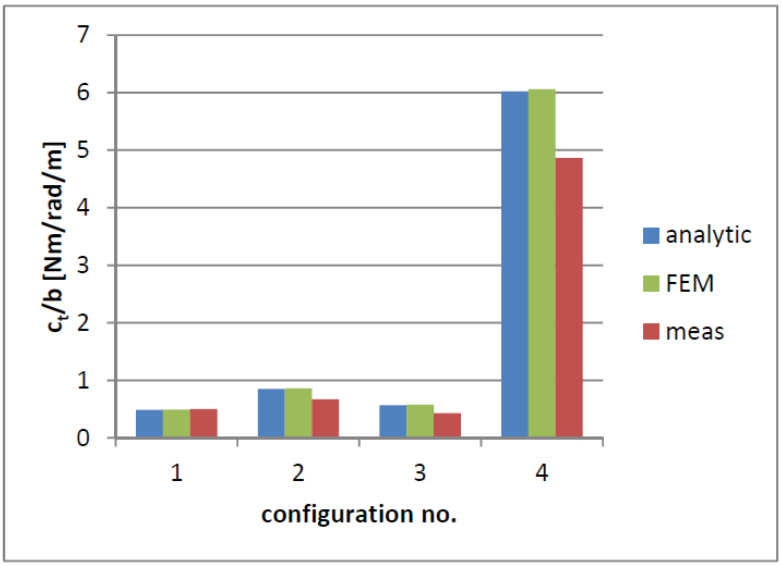

Fig. 5 Comparison of torsional stiffness

While the numerical (FEM) and analytical results (analytic) are in very good agreement (deviation less than 1.5 %), the measured values (meas) only reproduce the trend of the prediction. The deviations are up to 25 %. Analyzing the contributions of GFRP (EI_{GFRP}) and EPDM (EI_{EPDM}) to the total bending stiffness of the hinge (EI_{SSH} see Eq.2), it becomes obvious that the GFRP delivers the major contribution to the bending stiffness as its Young's modulus is about 4500 times higher. For the investigated designs only one or two layers of GFRP-prepreg (preimpregnated fibers) are used. The resulting layer thickness is $\approx 1/8mm$. Due to manufacturing and material deviations this thickness cannot be guaranteed. Micrographs of the manufactured hinges indicated deviations in thickness of a few 100th of a millimeter. Changing the single layer thickness in the analytical and numerical prediction by only $1/100mm$ can bring the deviations down to less than 6 %. Consequently the analytical and the numerical model can be evaluated as sufficiently accurate with respect to the achievable manufacturing accuracy.

3.2 Angle restriction

One outcome of the initial wind tunnel experiments was that a restriction in the opening angle of the flap is needed. Without a limit in the flap opening angle the highly dynamic process caused the flap to flip over. The already investigated spring characteristic of the solid state hinge can only partially improve this behavior. A drawback of the solid state hinge concept is that it is not possible to use a catch like for conventional hinges. The basic idea is to limit the flap angle in a similar manner as already done in the wind tunnel experiments. There a cord was attached to the flap as well as to the blade surface. When the flap opened this string was put under tension and limited the opening angle. This worked for the initial tests but showed significant wear already after a short measurement time. Furthermore the strings were in the flow when the flap was not deployed. This increases the drag and can possibly disturb the natural flow. Consequently a robust restraining mechanism that is integrated into the "glove" and does not disturb the flow is needed.

Fig. 6 shows the basic idea how the angle restraint for the flap with the solid state hinge can be

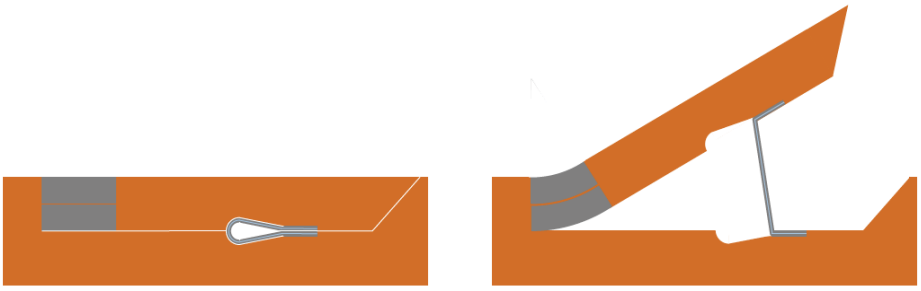

Fig. 6 Principle of flap with solid state hinge and angle restraint (Left: closed, Right: opened)

realized. The restraint mechanism is located underneath the flap in such a manner that the outer surface remains totally smooth if the flap is not deployed. In contrast to the wind tunnel experiments the catch is now a strip that has a certain width in the direction of extrusion (*b*) and no longer a cord. This also guarantees that the strip is always in the same position when the flap is closed. The width of the strip can be designed according to the occurring loads. The maximum opening angle can be set by the proper position and length of the strip. The strip should have almost no bending stiffness but should not elongate significantly to limit the deployment angle to a certain value. Once again a three layer setup of EPDM and glass fibers is identified as an ideal material combination for the strip. Compared to the solid state hinge the bending stiffness of the strip should be reduced significantly, since an actuator would have to overcome this additional stiffness to deploy the flap. For this reason the GFRP material used for the middle layer of the solid state hinge was replaced by a very thin glass fiber fabric ($50 g / m^2$) that was not impregnated with epoxy resin. Hence the elastomer directly embeds the glass fibers in the strip. To reduce the thickness of the strip in stored condition the thickness of the EPDM layers was also decreased. To identify the ideal way to connect the strip, the peel off force between strip and GFRP for different configurations was determined by a customized test in a testing machine.

3.3 Manufacturing concept

One of the major advantages of composite materials is that functionalities like a hinge can be directly integrated in the structure during the manufacturing process. A prerequisite is the selection of compatible raw materials. For the presented back-flow flap a GFRP-prepreg was used for the main structure of the "glove". The matrix is cured at $120°C$. The elastomeric material used for the solid state hinge and for the angle restraint is customized so that it can be vulcanized at the same temperature. This finally allows the combination of cure and vulcanization in one process. Consequently a relatively strong adhesion between both materials can be obtained. As usual for composites the different materials are placed layer by layer on a mold. Here a negative mold was used to guarantee that the outer contour of the airfoil is matched. Numerous separating foils are used to assure that the flap and the angle restraints are only connected in predefined areas which allows that the flap can lift after cure. Due to the integral design and manufacturing concept the glove with solid state hinge and angle restraint can be manufactured in one shot. Fig. 7 gives an impression how the structurally integrated solid state hinge connects the GFRP-flap to the "glove" that is used to retrofit the back-flow flap to an existing blade.

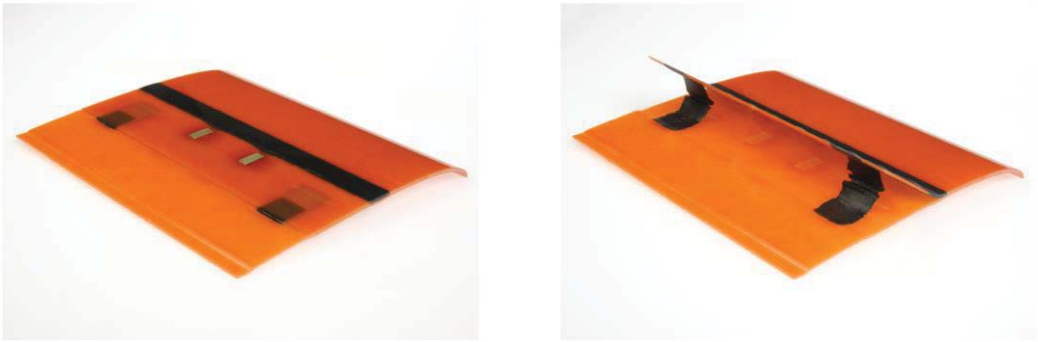

Fig. 7 First structural demonstrator for a GFRP back-flow flap "glove" with solid state hinge and angle restraint (Left: flap closed, Right: flap deployed)

4. Actuation mechanisms

For a reliable operation of the flap an actuation mechanism is intended. To investigate the aerodynamic effect the ideal solution would be an actuator that can directly control the flap deployment angle in the same way as the angle was set during the simulation. Unfortunately such an actuator would have to be quite powerful and once again the limitation in mounting space excludes a lot of the technologically possible solutions. As a compromise between an easy to realize passive flap and a fully active deployable flap the goal is here to develop an actuator that can support the self deployment of the flap by the flow. Such a concept is more likely to be fitted into the "glove". Furthermore the efficient use of system inherent forces will result in quite low energy consumption of the actuation system. In this section of the paper two different approaches for actuation mechanisms that can initiate a flap deployment by the flow are presented and assessed.

4.1 Bending actuator

Composite materials allow integrating different kinds of actuators directly into the structure. In the past mainly piezoelectric actuators were used. Since the strain of those actuators is the response to an electric field, they are easy to operate. The piezoceramics introduce strain into the structure which leads to the desired morphing. Further on those materials have already proven that they can be operated in the centrifugal field of a helicopter rotor (Opitz *et al.* 2010, Wierach *et al.* 2012c). Different types of piezoelectric actuators are available. For the integration into the back-flow flap "glove" especially thin piezo composite actuators are of interest (Wierach 2012d, Wierach 2006). They require only a very limited mounting space and can be integrated even in curved composite parts (Algermissen *et al.* 2011).

The intended operation principle was to integrate a piezo composite actuator directly into the flap (see Fig. 8). The actuator should not be located in the neutral axis of the flap laminate. Consequently the generated strain (see Fig. 8, Middle, red arrow) causes a bending of the flap. This deformation would be used to lift the trailing edge of the flap from the blade surface. The back-flow which develops on the airfoil surface should open the flap. The crucial point of this concept is the assessment of whether the performance of the bending actuator is sufficient to produce a significant flap bending.

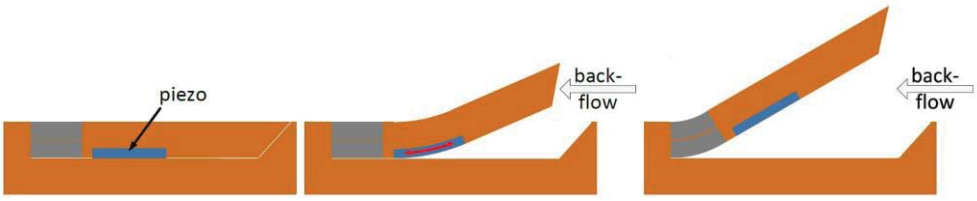

Fig. 8 Principle of flap with piezoelectric bending actuator (Left: closed, Middle: actuator induced bending of the flap, Right: flap fully opened by back-flow)

For the analytical assessment of the bending performance of the integrated actuator, three steps are required.

1. position of neutral axis of the layered setup (fibre composite, piezo composite)
2. bending stiffness of the setup
3. actuator moment

In the following a three layer setup will be investigated since the two layer setup depictedin Fig. 8 can be treated as a special case of this analytical model for the bending (see Fig. 9).

Moreover the largest bending displacement can be achieved with a symmetric three layer setup since the neutral fiber stays in the middle of the central GFRP layer. The assumption of a linear strain distribution over the cross section and a linear stress distribution within each material will be made (see Fig. 10). Where ρ is the curvature radius at position x.

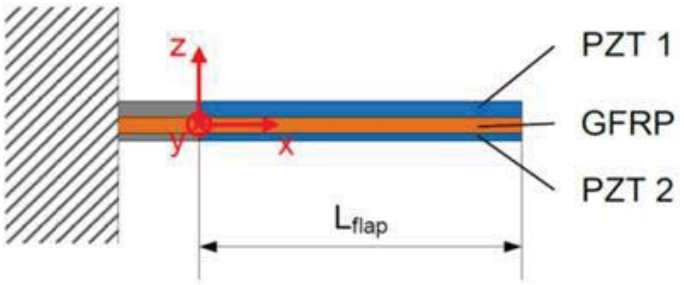

Fig. 9 Principle of piezoelectric bending actuator with three layer setup

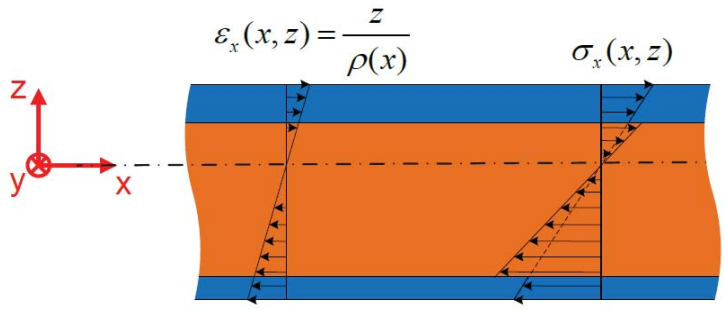

Fig. 10 Bending stress and strain in a piezoelectric bending actuator with three layer setup

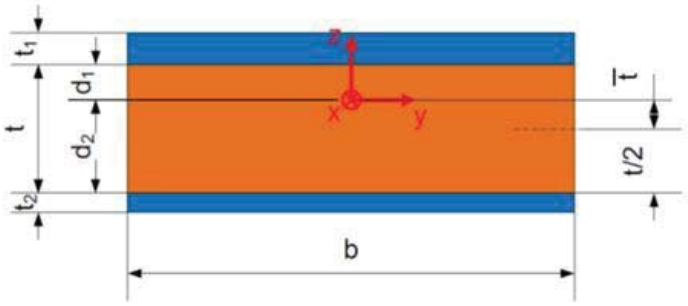

Fig. 11 Cross section of piezoelectric bending actuator with three layer setup

Fig. 11 depicts the cross section of the flap with integrated actuators. For pure bending the neutral fiber of the setup does not elongate. This fact can be used to determine the offset of the neutral axis from the middle of the substrate layer $\bar{t}$.

$$F_L = 0 = \int_{GFRP} \sigma_{GFRP} dA_{GFRP} + \int_{PZT1} \sigma_{PZT1} dA_{PZT1} + \int_{PZT2} \sigma_{PZT2} dA_{PZT2} \tag{6}$$

The assumption of a linear stress-strain relation and that the cross sections remain plain are expressed by the following equation:

$$\sigma = E \cdot \varepsilon = E \cdot \frac{z}{\rho} \tag{7}$$

As the width b of all three integration regions is identical, the substitution of equation 7 into equation 6 leads to an integration over the thickness of the cross section.

$$0 = \int_{-d_2}^{d_1} E_{GFRP} \frac{z}{\rho} b dz + \int_{d_1}^{d_1+t_1} E_{PZT} \frac{z}{\rho} b dz + \int_{-d_2-t_2}^{-d_2} E_{PZT} \frac{z}{\rho} b dz \tag{8}$$

Making two further substitutions within the boundaries of the integral, a single equation with only one unknown ($\bar{t}$) is obtained, that can be easily solved.

$$d_1 = \frac{t}{2} - \bar{t} \tag{9}$$

$$d_2 = \frac{t}{2} + \bar{t} \tag{10}$$

Once the position of the neutral axis is known the bending stiffness with respect to the neutral axis can be determined. The definition of the bending moment as an integral of differential forces with respect to their distance to the neutral axis can be used.

$$M_b = \int z dF = \int z \cdot \sigma \cdot b dz \tag{11}$$

The substitution of σ by Eq. (7) leads to the following equation for the three layer setup.

$$M_b = \int_{-d_2}^{d_1} zE_{GFRP}\frac{z}{\rho}bdz + \int_{d_1}^{d_1+t_1} zE_{PZT}\frac{z}{\rho}bdz + \int_{-d_2-t_2}^{-d_2} zE_{PZT}\frac{z}{\rho}bdz \tag{12}$$

For the simple Euler-Bernoulli beam used in this model the relation between moment and curvature can be expressed as follows:

$$M_b = -EI \cdot w''(x) = EI \cdot \frac{1}{\rho} \tag{13}$$

Consequently the total bending stiffness of the setup ($\overline{EI}$) can be expressed by:

$$\overline{EI} = M_b \cdot \rho = \int_{-d_2}^{d_1} z^2 E_{GFRP} bdz + \int_{d_1}^{d_1+t_1} z^2 E_{PZT} bdz + \int_{-d_2-t_2}^{-d_2} z^2 E_{PZT} bdz \tag{14}$$

For the assessment of the bending moment that can be introduced by the piezoelectric actuators it is possible to estimate the stress that can be generated using the free strain of the actuator in combination with the elastic modulus.

$$\varepsilon_{free} = d_{piezo} \cdot \tilde{\tilde{E}}_{el} \tag{15}$$

$$\sigma_{PZT} = d_{piezo} \cdot \tilde{\tilde{E}}_{el} \cdot E_{PZT} \tag{16}$$

The bending moment generated by the actuators (M_A) can finally be derived through integration

$$M_A = \int_{d_1}^{d_1+t_1} d_{piezo} \cdot \tilde{\tilde{E}}_{el1} \cdot E_{PZT} zbdz + \int_{-d_2-t_2}^{-d_2} d_{piezo} \cdot \tilde{\tilde{E}}_{el2} \cdot E_{PZT} zbdz \tag{17}$$

Even though the proposed analytical model is based on assumptions that limit the accuracy for very thin GFRP-layers, it can still be used to assess the order of magnitude of the displacement that can be achieved at the trailing edge of the flap. For this purpose several configurations were analyzed. The study comprised configurations with one and two piezo composite actuators (2 or 3 layer setup) and various flap thicknesses and materials.

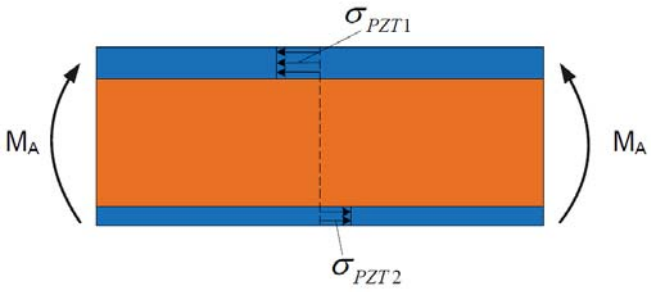

Fig. 12 Moment generated by piezoelectric bending actuator with three layer setup

Table 2 Parameters for bending actuator assessment.

Parameter	Value	Unit
E_{GFRP}	45	GPa
$E_{PZT}=1/s_{33}$	30	GPa
b	1	m
L_{flap}	40	mm
$d_{piezo}=d_{33}$	$425\cdot10^{-12}$	m/V
$t_1=t_2$	0.5	mm
t	0.125	mm
$\tilde{E}_{el1}$	-0.635	kV/mm
$\tilde{E}_{el2}$	2.5	kV/mm

The three layer setup below represents an example configuration with a comparatively good performance. Multilayer piezo composite actuators as described in Wierach 2006 are intended to generate the bending of the flap. The following Table 2 summarizes the model parameters used.

Fig. 13 shows the bending displacement of the flap due to the strain of the piezoelectric actuators. The displacement at the trailing edge of the flap was calculated without any forces from the flow. It can be summarized that the maximum displacement for a flap with a length of 40mm that is fully covered with piezo composite actuators on upper and lower side did not exceed 1.5mm. This relatively small displacement in combination with the experience from initial wind tunnel experiments led to the conclusion that the risk of insufficient actuation authority is too high to further pursue this actuation concept. A second deficit that confirmed this decision is the fact that this actuator is not able to keep the flap closed during attached flow. Consequently alternative actuation mechanisms were investigated.

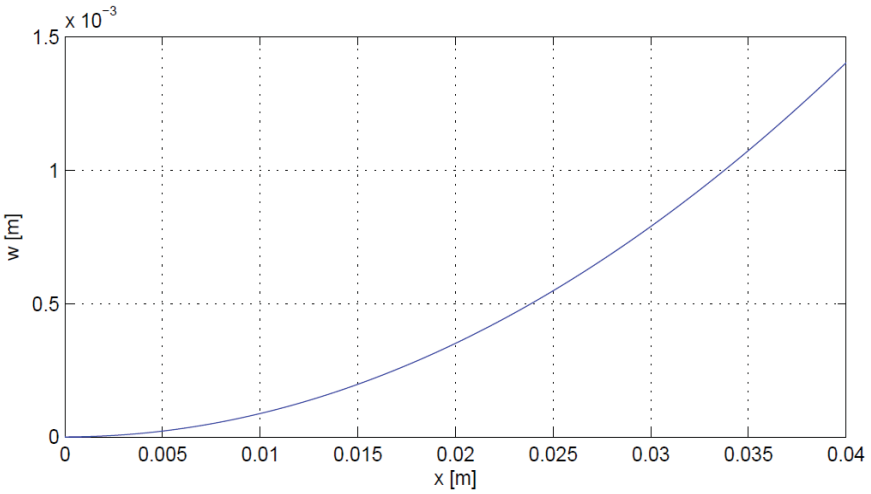

Fig. 13 Bending displacement of flap due to piezocomposite actuators

4.2 Magnetic actuator

Other promising actuation concepts use magnetic forces. As mentioned before the actuator is needed to initiate the deployment of the flap by the flow and not suited to fully deploy the flap against the forces of the flow. Possible concepts rely on the force between:

1. an electro magnet and a ferromagnetic material,
2. an electro magnet with dynamic excitation and a conductive element (eddy current),
3. two permanent magnets,
4. a permanent magnet and an electro magnet with constant excitation,
5. two electro magnets,
6. a permanent magnet and a current (Lorentz force).

Magnetic actuators of category 1 only attract the ferromagnetic material. As the flap has to be pushed away from the blade surface, when deployed, a kinematics is needed that transforms the attraction force into a push motion. Such an actuator would not be able to prevent the deployment of the flap, due to the pressure gradient over the blade surface. Category 2 actuators require large currents and probably cause high electro-magnetic interferences. For the mentioned reasons category 1 and 2 are not further pursued. This paper will focus on actuators of category 3 and 4.

4.2.1 Permanent magnets

A quite simple approach is the deployment of the flap with two permanent magnets. As those cannot be switched on and off, it is necessary to move one of the magnets. The basic principle of operation and the orientation of the magnets can be seen in Fig. 14.
While one neodymium magnet is integrated in the flap during the manufacturing process, the second one can be linearly slid underneath the flap. This motion could be generated by an electromagnet and a push rod at the root of the blade but the detailed design of this mechanism is not the focus of this work. Increasing the number of magnet pairs also increases the force that deploys the flap. In order to predict the forces between the two magnets static finite element calculations were performed. Since the remanent magnetization of the used neodymium magnets is only roughly known the calculations are accompanied by an experimental characterization. The setup can be found in Fig. 15.

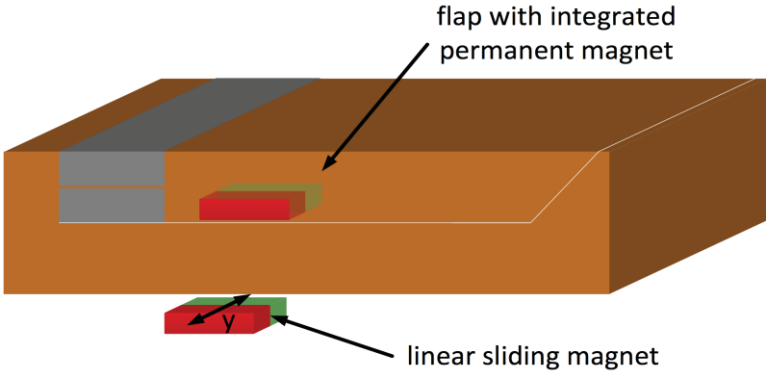

Fig. 14 Principle of flap with integrated permanent magnet

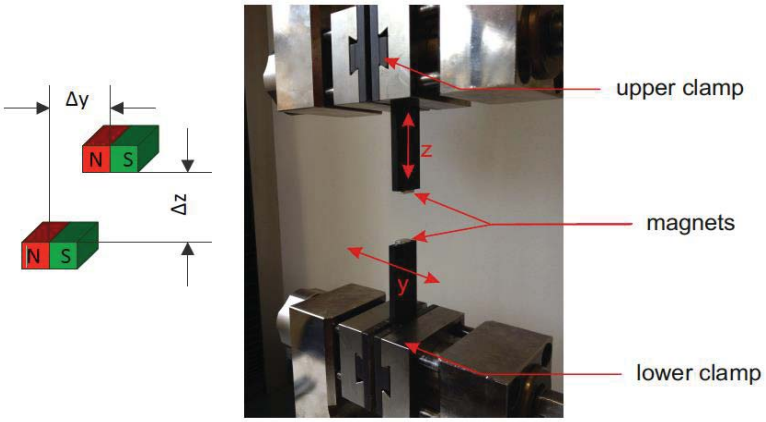

Fig. 15 Setup for the characterization of neodymium magnets

The tests were performed in a universal testing machine. Each of the neodymium magnets was glued to a CFRP (Carbon Fibre Reinforced Polymer) plate in order to have a sufficient distance to all ferromagnetic parts of the machine that could influence the measurement. To characterize the interaction of the two magnets the force in z-direction as a function of Δz was captured for different lateral offsets Δy. As the setup was rather stiff and the range of measured force is low compared to the measurement range of the testing machine, the position of the traverse was used to calculate the gap Δz between the magnets. Furthermore any lateral bending of the CFRP-plates was neglected. Hence the value set for the lateral distance Δy is assumed to stay constant during each measurement. In parallel to the experiment the setup was modeled using the finite element method. To set the remanent magnetization the geometric setup for the point of maximum force within the measurements ($\Delta y = 0$, $\Delta z = 0.5mm$) was simulated.

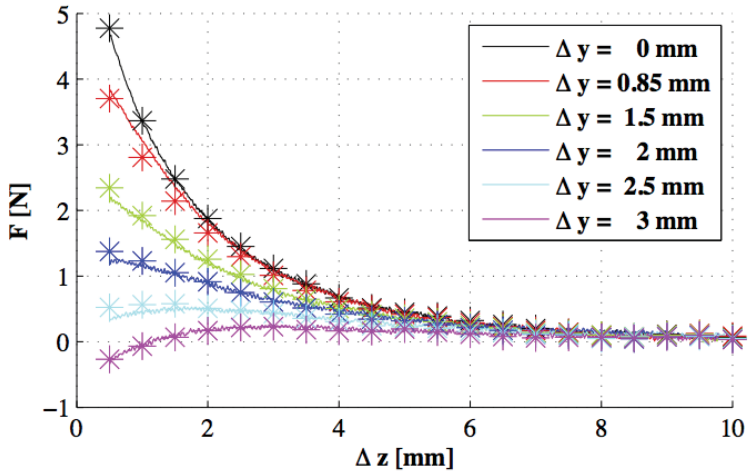

Fig. 16 Results of characterization of neodymium magnets (lines = measurement; markers = FEM prediction)

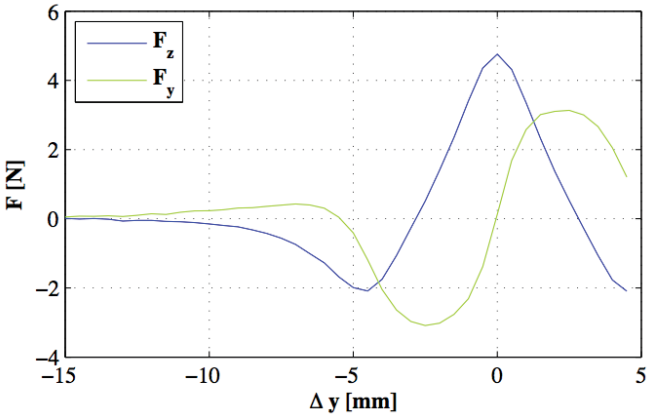

Fig. 17 Prediction of z and y force as a function of lateral offset $\Delta y(\Delta z = 0.5mm)$

At this position the magnetization was varied to match the measured force. Once this value was set, it remained unchanged for all further computations with varying values for Δy and Δz. Fig. 16 depicts the comparison between the measured and the computed characteristics of the magnets.

Looking at these results the following conclusions can be made. The measured results and the finite element prediction are in good agreement. The magnets can generate a maximum force of almost 5N which is quite remarkable for the investigated magnets that have a size of 4.5mm x 10mm x 2mm and a weight of 0.7g. As expected the force rapidly drops when the gap between the magnets gets bigger. There is a small region of lateral distance where the increase of the gap Δz first leads to a slight increase in force until the force drops again (see magenta and turquoise line in Fig. 16). The consequence of this effect will be discussed later on. If the lateral distance between the magnets gets big enough (e.g. $\Delta y = 3mm$) they attract each other. The latter effect can be used to keep the flap closed during attached flow. The finite element computations show that the maximum attraction force F_z occurs at a lateral offset of $\Delta y = 4.5mm$ and has a magnitude of approx. 2N (see Fig. 17).

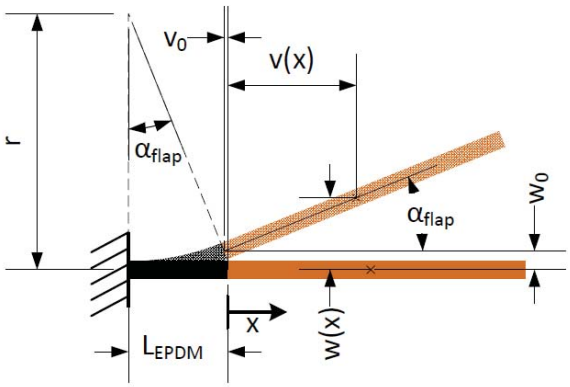

Fig. 18 Kinematics of the back-flow flap

For this estimation of the maximum force the magnet was fixed at the minimum vertical distance of $\Delta z = 0.5mm$. This setup can also be used to estimate the maximum force in y direction F_v that is necessary to slide the magnet underneath the flap. A linear actuator that moves the sliding magnet would have to be able to generate approximately three Newton. When the magnets are directly on top of each other the horizontal force vanishes but it has to be kept is mind that this is an instable state and the magnet tries to move to either horizontal direction.
When the flap opens the motion of the magnet in the flap differs from the so far tested pure increase in vertical offset. To calculate the opening force as a function of the flap angle the kinematics of the flap has to be regarded. Assuming a constant mean moment over the length of the solid state hinge the relative motion of the flap can be described as follows.

$$r = \frac{L_{EPDM}}{\alpha_{flap}} \tag{18}$$

$$v_0 = v(x=0) = r \cdot \sin(\alpha_{flap}) - L_{EPDM} \tag{19}$$

$$w_0 = w(x=0) = r - r \cdot \cos(\alpha_{flap}) \tag{20}$$

$$w(x) = w_0 + x \cdot \cos(\alpha_{flap}) \cdot \tan(\alpha_{flap}) \tag{21}$$

$$v(x) = v_0 + x \cdot \cos(\alpha_{flap}) \tag{22}$$

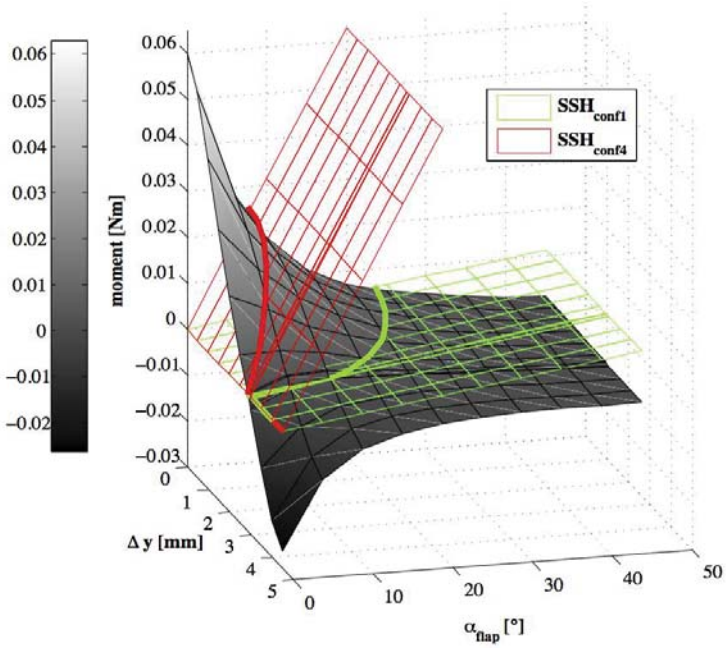

Fig. 19 Work diagram of the actuation mechanism

For a given position x of the center of the magnet the motion with respect to the flap angle can be calculated. This kinematic relation was now used for the finite element simulation to predict the moment at the solid state hinge generated by the magnets according to the flap angle. Equivalent to the characterization of the magnets, that was performed to tune the numerical calculations, the moment that deploys the flap was computed for different lateral distances of the magnets Δy. The results of these computations can be used to generate the work diagram of the actuator. The gray shaded surface in Fig. 19 shows the moment (in the center of the solid state hinge $x=-L_{EPDM}/2$) generated by the actuator as a function of the lateral offset Δy of the magnets and the deployment angle of the flap α_{flap}.

If the characteristics of the load are plotted in the same diagram, the intersection between both surfaces is the line that connects all operating points of the actuator that works against this particular load. For the first shot it is assumed that the magnets only work against the stiffness of the solid state hinge and no aerodynamic forces are present. Within Fig. 19 the load characteristics of a b=30 mm wide strip of two different configurations of the solid state hinge are shown. Choosing designs 1 (SSH_{conf1}) and 4 (SSH_{conf4}) from the above characterized configurations (see Table 1), covers the whole range of investigated hinge stiffnesses. The bold solid lines represent the interconnection of the operation points that result from a certain setting of the lateral distance of the magnets. Negative moments can be used to keep the flap closed.

Due to the nonlinearity of the magnetic forces, the relation between the lateral offset of the magnets and the flap angle is nonlinear too. As already observed in the characterization of the magnets there is a region in lateral offset where the deploying moment increases with an opening of the flap. The consequence of this effect can be analyzed in detail looking at the relation between lateral offset and flap angle for different hinge configurations (see Fig. 20).

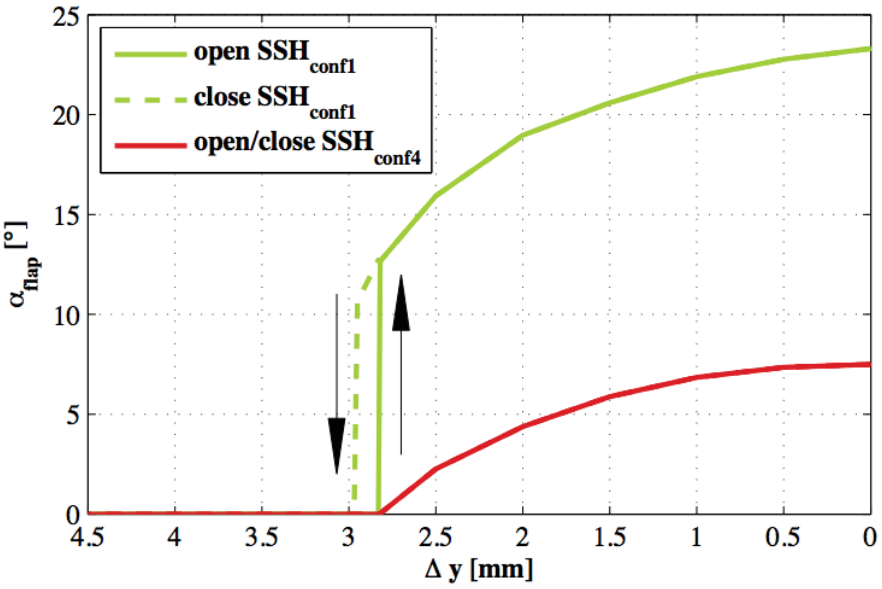

Fig. 20 Flap deployment as a function of the lateral offset Δy for different configurations of the solid state hinge (b=30mm)

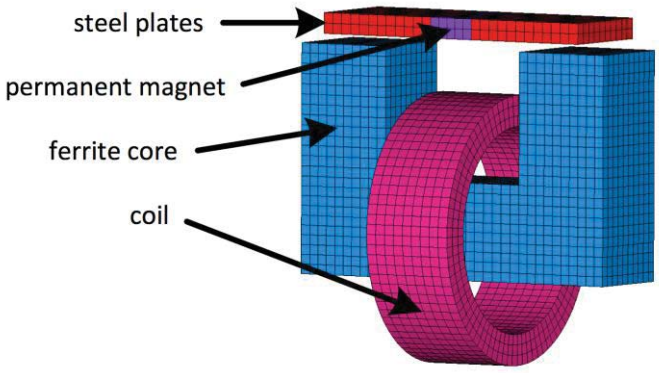

Fig. 21 Setup with permanent and electromagnet

The red line shows the angle of the flap that is connected to the blade via a rather stiff solid state hinge (configuration 4). If the lower, sliding magnet approaches, the flap stays closed until a distance of $\Delta y \approx 2.8mm$. At this point the moment caused by the magnets becomes positive and the flap starts to lift continuously until the maximum angle of $\alpha_{flap} \approx 7.5°$ is reached. In case of a much softer solid state hinge (configuration 1) this behavior changes. In this region of the work diagram the actuator moment becomes bigger with an increase of flap angle. If the stiffness of the solid state hinge is smaller than the slope in the work diagram this leads to an instantaneous deployment of the flap. The angle increases until a new equilibrium state between moment of the magnets and elastic moment to deform the hinge is reached. After this snap opening of the flap the angle can further be increased until $\alpha_{flap} \approx 23°$. When the lateral distance is increased in order to close the flap, it can be observed that the flap also closes instantaneously but not at the same lateral distance as for the opening of the flap. Hence the nonlinear characteristics of the magnets cause a hysteresis in the flap opening behavior that has to be regarded in the development of control laws for the operation of the flap. The instantaneous opening of the flap in combination with the very lightweight flap and low bending stiffness of the solid state hinge allows the deployment of the flap shown in Fig. 7 up to an angle of 30° within only 12.5 ms. This enables an operation in the wind tunnel with airfoil oscillation frequencies up to f=6Hz while matching the control law used in the numerical investigations. Transferring this actuation concept to a rotating blade will be the focus of investigations when the aerodynamic efficiency for the oscillating profile is demonstrated. For this purpose the size and radial position on the blade must be defined by further numerical investigations.

The tools presented so far can be used to investigate further concepts for a magnetic actuation. The design using 2 permanent magnets can serve as benchmark in terms of actuator performance. As it is advantageous to have as few moving components as possible in the centrifugal field of a helicopter rotor, it is self-evident that it would be beneficial to replace the moving magnet by an electromagnet. The challenge is to design the electromagnet that is strong enough to have a comparable performance as the neodymium magnet used so far and that fits into the slim "glove" of the back-flow flap. For the first attempt the constraints in size were neglected and the sliding magnet underneath the flap was replaced by an electromagnet. This simplified setup can be used to investigate the principle interaction between a permanent magnet and an electromagnet. The electromagnet consists of a coil that is wound around a U-shaped ferrite core (see Fig. 21).

Due to the dimensions of a coil that is necessary to generate a comparable magnetic field the poles of the electromagnet will have a larger separation than the poles of the permanent magnets used so far. For this reason thin steel plates with a high magnetic permeability were arranged at both poles of the neodymium magnet. To actuate the back-flow flap the permanent magnet and the steel plates would be integrated into the flap. In a magnetic circuit this part would be the yoke. The ferrite core and the coil are forming the armature and are located within the rotor blade directly underneath the flap. If a permanent magnet is incorporated in the yoke of the magnetic circuit the resulting magnetic flux leads to an attraction of the yoke. No repellent forces can be generated until a magnetic flux with opposite sign is caused by the electric current in the coil that reaches the same level as the flux resulting from the permanent magnet. If the permanent magnet introduces the magnetic flux into the ferrite core, the magnetic resistance that has to be overcome is governed by the air gaps between yoke and armature since the relative permeability of air is at least three orders of magnitude smaller than of the permeability of the core material (steel and ferrite). This situation changes when the flux is generated by the electric current within the coil. The magnetic resistance the coil works against is composed by the air gaps and by the neodymium magnet. As permanent magnets have a relative permeability close to one, the increase in magnetic resistance is quite considerable and can even be higher than the resistance of the air gaps. This results in high current densities needed in the coil to effect a repelling force between armature and yoke. Since the actuator is thought to only generate an opening impulse the current limit within the copper can be elevated. But even for the depicted setup that did not account for any restriction in size of the electromagnet a current density of $30A/mm^2$ resulted in repellent forces that are one order of magnitude lower than the configuration with two permanent magnets. The weight of the depicted solenoid is approx. 70 gram. As several magnets are necessary to operate the flap the additional weight with respect to the sliding neodymium magnet (0.7 gram/magnet) is not acceptable. Therefore this particular setup is not suited for the deployment of the flap and further concepts using electromagnets have to be investigated in future work.

5. Conclusions

This paper presents a structural design concept for a back-flow flap. The development was encouraged by the predicted benefits of initial numerical investigations. Initial wind tunnel experiments have been performed and identified requirements on the structural integration and a possible actuation mechanism. The attachment of the flap via a structurally integrated solid state hinge and an angle restriction mechanism were presented to fulfill these requirements. Further on different actuation concepts were investigated and assessed. It could be shown that a bending actuator that is integrated into the flap probably does not generate enough displacement at the trailing edge of the flap to initiate a reliable deployment of the flap. The combination of two permanent magnets seems to be more promising. The interaction of such an actuator with solid state hinges of different stiffness was elucidated. Finally the general possibility to replace one of the permanent magnets by an electromagnet was investigated. It could be shown that a simple replacement does not result in sufficient actuator performance.

Up to now the actuator only operated against the stiffness of the solid state hinge. In the next step aerodynamic and inertia forces have to be regarded. With these additional loads the number of magnets over the whole length of the wind tunnel model can be determined and the actuator that generates the linear motion of the sliding magnet can be dimensioned. After the manufacturing of

the wind tunnel model a final test campaign will show the effectiveness of the system under wind tunnel conditions.

The challenges that arise under rotating conditions were not in the focus of this paper but had to be kept in mind. After further aerodynamic simulations have identified the radial location of such a flap the transfer of the presented wind tunnel technology to a rotor will be investigated.

References

Mai, H., Dietz, G., Geissler, W., Richter, K., Bosbach, J., Richard, H. and de Groot, K. (2008), "Dynamic stall control by leading edge vortex generators", *J. Am. Helicopter Soc.* **53**(1), 26-36.

Martin, P., Wilson, J., Berry, J., Wong, T., Moulton, M. and McVeigh, M. (2008), "Passive control of compressible dynamic stall", *AIAA 2008-7506*.

LePape, A., Costes, M., Joubert, G., David, F. and Deluc, J.M. (2012), "Experimental study of dynamic stall control using deployable leading-edge vortex generators", *AIAA J*, **50**(10), 2135-2145.

Barth, T., Scholz, P. and Wierach, P. (2011), "Flow control by dynamic vane vortex generators based on piezoceramic actuators", *AIAA J*, **49**(5), 921-931.

Gardner, A.D., Richter K., Mai, H. and Neuhaus, D. (2012), "Experimental control of compressible OA209 dynamic stall by air jets", *38th ERF*, Amsterdam, Sept.

Weaver, D., McAlister, K.W. and Tso, J. (2004), "Control of VR7 dynamic stall by strong steady blowing", *J. Aircraft*, **41**(6), 1404-1413.

Kaufmann, K., Gardner, A.D. and Richter, K. (2012), "Numerical investigations of a back-flow flap for dynamic stall control", *STAB 2012*, *Stuttgart*, Germany, Nov.

Meyer, R.K.J. (2000), "Experimentelle untersuchungen von rückstromklappen auf tragflügeln zur beeinflussung von strömungsablösungen", *Mensch-und-buch-verlag*, Dissertation technische universität Berlin.

Höfinger, M. (2012), "Rotorblatt mit integrierter passiver oberflächenklappe", Deutsches patent DE 10 2010 041 111 A1, Mar.

Carr, L.W., Chandrasekhara, M.S., Wilder, M.C. and Noonan, K.W. (2001), "Effect of compressibility on suppression of dynamic stall using a slotted airfoil", *J. Aircraft*, **38**(2), 296-309.

Martin, P.B., McAlister, K.W., Chandrasekhara, M.S. and Geissler, W. (2003), "Dynamic stall measurements and computations for a VR-12 airfoil with a variable droop leading edge", *American helicopter society 59th annual forum*, Phoenix, Arizona, May.

Friedmann, P.P., de Terlizzi, M. and Myrtle, T.F. (2001), "New developments in vibration reduction with actively controlled trailing edge flaps", *Math. Comput. Model.*, **33**(10-11), 1055-1083.

Ahci-Ezgi, E., Denecke, U., Kuntze-Fechner., Mueller, C. and Pfaller, R. (2013), "Piezo active rotor blade: challenges and solutions", *American helicopter society 69th annual forum*, Phoenix, Arizona, May.

Gallot, J., Vingut, G., De Paul, M.V. and Thibert, J. (1982), "Blade profile for rotary wing of an aircraft", United states patent 4325675, (20.4.1982).

Mulleners, K. and Raffel, M. (2012), "The onset of dynamic stall revisited", *Exp. Fluids*, **52**(3), 779-793, DOI 10.1007/s00348-011-1118-y.

Gardner, A.D., Richter, K. and Rosemann, H. (2012), "Numerical investigation of air jets for dynamic stall control on the OA209 airfoil", *CEAS Aeronaut. J*, **1**(1), 69-82, DOI 10.1007/s13272-011-0002-z.

Richter, K., Le Pape, A., Knopp, T., Costes, M., Gleize, V. and Gardner, A.D. (2011), "Improved two-dimensional dynamic stall prediction with structured and hybrid numerical methods", *J. Am. Helicopter Soc.*, **56**(4), 1-12, DOI 10.4050/JAHS.56.042007.

Wierach, P. (2012a), "Nano-micro-macro", Adaptive, tolerant and efficient composite structures, Research in Aerospace, Wiedemann,M. and Sinapius,M. (eds), Springer-verlag berlin heidelberg 2012, DOI 10.1007/978-3-642-29190-6_2, pp. 17-28.

Wierach, P., Riemenschneider, J., Opitz, S. and Hoffmann, F. (2012b), "Experimental investigation of an

active twist model rotor blade under centrifugal loads", Adaptive, tolerant and efficient composite structures, Research in Aerospace, Wiedemann,M. and Sinapius,M. (eds), Springer-Verlag Berlin Heidelberg 2012, DOI 10.1007/978-3-642-29190-6_32, pp. 391-407.

Grote, K.H. and Feldhusen, J. (2012), "Dubbel: taschenbuch für den Maschinenbau", 23rd edition, Springer-Verlag Berlin Heidelberg 2012.

Opitz, S., Riemenschneider, J., Hoffmann, F. and Schneider, O. (2010), "Measurement of the dynamic tip twist angles of an active twist model scale rotor blade", *36th European Rotorcraft Forum*, Paris, France, Sept.

Wierach, P., Riemenschneider, J., Opitz, S. and Hoffmann, F. (2012c), "Experimental investigation of an active twist model rotor blade under centrifugal loads", Adaptive, tolerant and efficient composite structures, Research in Aerospace, Wiedemann,M. and Sinapius,M. (eds), Springer-verlag berlin heidelberg 2012, ISBN 978-3-642-29189-0.(2012), 391-407.

Wierach, P. (2012d), "Piezocomposite transducers for adaptive structures", Adaptive, tolerant and efficient composite structures, Research in Aerospace, Wiedemann, M. and Sinapius, M. (eds), Springer-Verlag Berlin Heidelberg 2012, DOI 10.1007/978-3-642-29190-6_3, pp. 29-47.

Wierach, P. (2006), "Low profile piezo actuators based on multilayer technology", *Conference proceedings. 17.international conference on adaptive systems and structures*, Taipei, Taiwan, Oct.

Algermissen, S., Keimer, R., Rose, M., Straubel, M., Sinapius, M. and Monner, H.P. (2011), "Smart-structures technology for parallel robots", *J. Intelligent Robot Syst.*, **63**, 547-574, DOI 10.1007/s10846-010-9522-8. ISSN 0921-0296.

EC

Nomenclature

α	Angle of attack [°]
α_{flap}	Flap opening angle [°]
b	Width of flap [m]
c	Airfoil chord [m]
C_D	Drag coefficient
C_L	Lift coefficient
C_M	Pitching moment coefficient
C_P	Pressure coefficient
CFRP	Carbon fiber reinforced polymer
$d_1, d_2, t_1, t_2, \bar{t}$	Parameters of cross section (see Fig. 11) [m]
d_{piezo}	Piezoelectric charge constant [m/V]
ε	Mechanical strain
ε_{free}	Free strain of piezoelectric actuator
$\tilde{\vec{E}}_{el}$	Electric field [V/m]
E_{GFRP}	Elastic modulus of GFRP in x-direction [Pa]
E_{PZT}	Elastic modulus of piezoceramic actuator in x-direction [Pa]
$\overline{EI}$	Total bending stiffness [Nm²]
EI_{EPDM}	Bending stiffness of EPDM layers [Nm²]
EI_{GFRP}	Bending stiffness of GFRP layers [Nm²]
EI_{SSH}	Bending stiffness of solid state hinge [Nm²]
EPDM	Ethylene propylene diene monomer
f	Frequency [Hz]
GFRP	Glass fiber reinforced polymer
L_{EPDM}	Length of solid state hinge [m]
L_{flap}	Length of flap [m]
M	Mach number
M_A	Actuator moment [Nm]
M_b	Bending moment [Nm]
ρ	Curvature radius [m]
r	Solid state hinge curvature radius [m]
Re	Reynolds number based on the model chord
σ	Mechanical stress [Pa]
σ_{PZT}	Mechanical stress generated by the piezoelectric effect [Pa]
t	Thickness of central GFRP-layer [m]
T	Thickness of flap [m]
v_∞	Freestream flow velocity [m/s]
v(x)	x-displacement of the flap at x [m]
v_0	x-displacement of the flap at x=0 [m]
w(x)	z-displacement of the flap at x [m]
w_0	z-displacement of the flap at x=0 [m]
x,y,z	Coordinates in flow direction, breadth and upward [m]
ω^*	Reduced frequency $\omega^*=2\pi fc/v_\infty$

A.2. Paper: CEAS Aeronautical Journal (2014), Volume 5 Number 3

Aerodynamic and structural investigation of an active back-flow flap for dynamic stall control

S. Opitz, A. D. Gardner & K. Kaufmann

CEAS Aeronautical Journal
An Official Journal of the Council of European Aerospace Societies

ISSN 1869-5582
Volume 5
Number 3

CEAS Aeronaut J (2014) 5:279-291
DOI 10.1007/s13272-014-0106-3

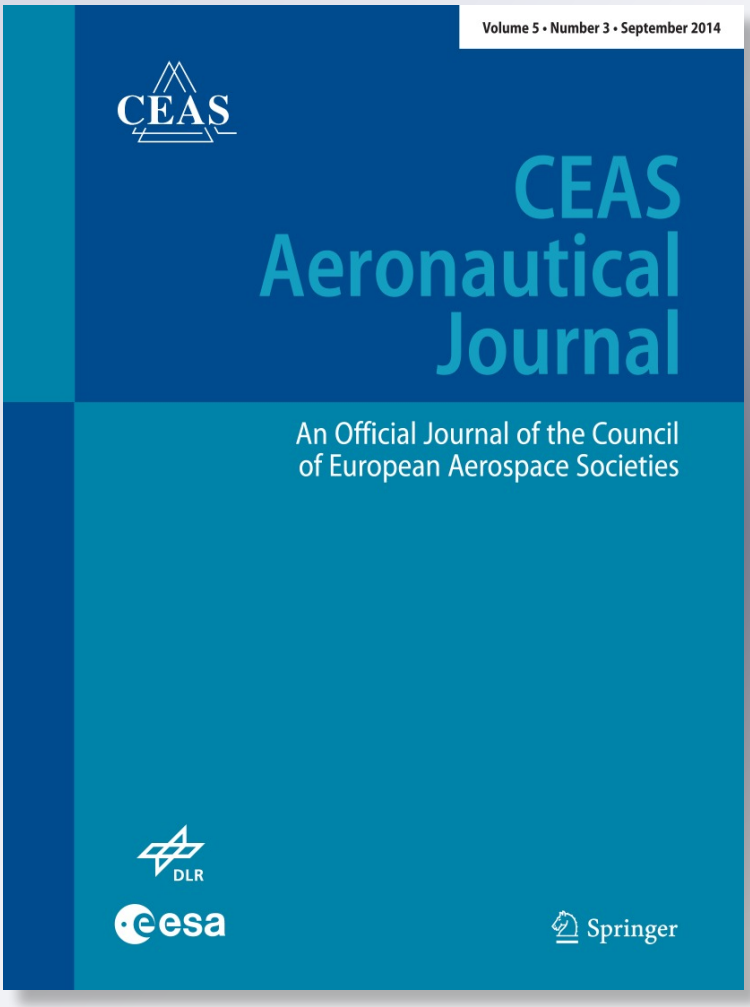

Springer

CEAS Aeronaut J (2014) 5:279–291
DOI 10.1007/s13272-014-0106-3

ORIGINAL PAPER

Aerodynamic and structural investigation of an active back-flow flap for dynamic stall control

S. Opitz · A. D. Gardner · K. Kaufmann

Received: 6 January 2014 / Revised: 11 March 2014 / Accepted: 11 March 2014 / Published online: 29 March 2014

Abstract The design and experimental investigation of a back-flow flap for helicopter dynamic stall control is described. A spoiler-type flap is designed, and shown by CFD to reduce the pitching moment peak during dynamic stall by 34 %. Initial experiments with a passively actuated flap in a low-speed wind tunnel showed that the opening and closing times for the flap due to the aerodynamic forces are sufficiently short and that the flap is not affected by the inertial forces of the model pitching. The experiments showed the need for a flap restraint, and that an active actuation is needed so that the flap angle is sufficient at the time of stall to have a control effect. Initial demonstrators for the structural concept of the active back-flow flap using glass fiber reinforced polymer and a solid state hinge are presented, showing the possibility of fabrication as an after-market add-on.

Keywords Back-flow flap · Active flap · Flow control · Solid state hinge · Helicopter · Rotor blade

List of symbols

α	Angle of attack (°)
c	Airfoil chord (=0.300 m)
C_D	Drag coefficient
C_L	Lift coefficient; mean; peak
C_M	Pitching moment coefficient; peak
C_P	Pressure coefficient
f	Frequency (Hz)
M	Mach number
Re	Reynolds number based on the model chord
ρ_∞	Freestream flow density (kg/m^3)
t	Time (s)
v_∞	Freestream flow velocity (m/s)
ω^*	Reduced frequency: ω^*: $\omega^* = 2\pi fc/v_\infty$
x, y, z	Coordinates in flow direction, breadth and upward (m)
y^+	Dimensionless wall distance

1 Introduction

Dynamic stall is a well-known effect for helicopter airfoils occurring when a pitching airfoil stalls, forming separated flow in a dynamic stall vortex. A lift peak and a negative spike in pitching moment form, then a rapid drop in lift appears as the stall vortex moves downstream. The torsional impulse from the pitching moment peak is a load-limiting case for the pitch links of the helicopter rotor blades. Further, high drag is experienced compared to attached flow. Dynamic stall can be controlled using passive devices, including vortex generators and changes in the leading edge contour [1, 2], but these have disadvantages at high Mach number and are limited in their control of deep stall. In contrast, active devices including actively retracting vortex generators [3], which avoid shocks at high Mach number, or air jets [4, 5], which add energy to the flow, can improve the flow control under deep stall conditions.

This paper is based on a presentation at the 39th European Rotorcraft Forum, September 3–6, 2013, Moscow, Russia.

S. Opitz (✉)
German Aerospace Center (DLR), Institute of Composite Structures and Adaptive Systems, Lilienthalplatz 7, 38108 Braunschweig, Germany
e-mail: Steffen.Opitz@dlr.de

A. D. Gardner · K. Kaufmann
German Aerospace Center (DLR), Institute of Aerodynamics and Flow Technology, Bunsenstrasse 10, 37073 Göttingen, Germany

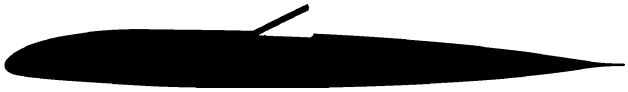

Fig. 1 Back-flow flap geometry

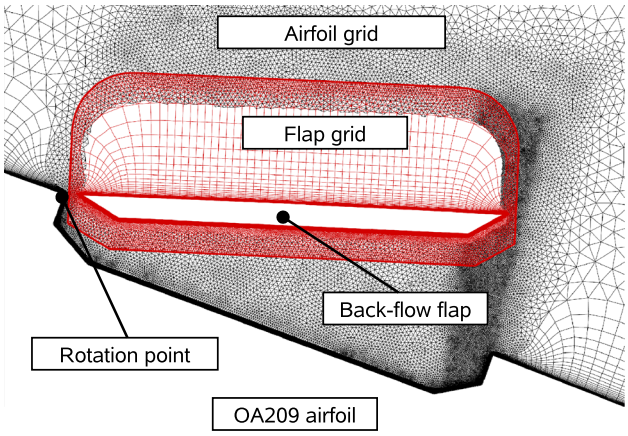

Fig. 2 Chimera grid geometry

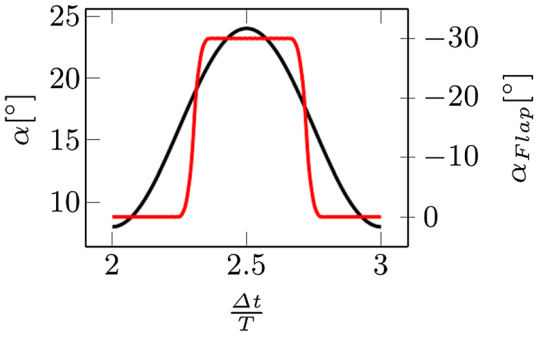

Fig. 3 Angle of attack of the airfoil (*black*) and angle of the flap (*red*) over a pitching period

As part of the DLR project STELAR, alternative methods of influencing the dynamic stall using an active back-flow flap are presently being investigated [6]. The back-flow flap is a spoiler-type split-flap, attached to the suction side of an airfoil. Figure 1 shows an example of a back-flow flap. When closed, the flap lies flush on the surface of the airfoil. The flap has a hinge at its upstream end, and this can either allow flow past, or be sealed. When actuated, the angle of the flap to the airfoil increases, and reverse flow on the rear of the airfoil finds a natural limit, stopping its progression further upstream. A natural analogy is found in the feathers of birds landing, where stall is controlled by the lifting of feathers near the trailing edge of the wing.

In the past, back-flow flaps have been tested on gliders by Meyer et al. [7] as a passive method of reducing stall. These freely hinged spoiler-like flaps were located on the suction side of the airfoil near the trailing edge. When trailing edge stall occurs, the back-flow lifts the flap and the region of stall can be significantly delayed. Meyer et al. showed that a back-flow flap on the top of an airfoil near the trailing edge can increase the lift by 10–18 %. Even though the effectiveness of back-flow flaps has been demonstrated in flight experiments with sailplanes, it still has to be investigated whether they are also suited to improve the dynamic stall behavior of helicopter rotor blades [8].

The leading edge stall associated with many helicopter airfoils including the OA209 [9] airfoil used for the numerical predictions, is characterized by strong backward flow along the suction side of the airfoil [10], and is different from static stall. To control dynamic stall of this type, the single dynamic stall vortex should be broken into several smaller vortices and the passage of the vortices should be delayed [11]. Initial numerical investigations with an actively actuated flap showed promising results.

2 Numerical investigations

Two-dimensional unsteady Reynolds-averaged Navier–Stokes (URANS) computations were undertaken with the DLR TAU code [12]. A dynamic stall test case with a pitching OA209 airfoil and the following parameters is carried out: $M = 0.14$, $\mathrm{Re} = 920{,}000$, $\omega^* = 0.1$, $\alpha = 16 \pm 8°$. Hybrid grids were created with the unstructured grid generator Centaur. A hybrid unstructured grid with triangular and rectangular elements was created with the method of Richter et al. [13], with the boundary layer discretized using 30 rectangular layers. The relative movement between flap and airfoil used the Chimera technique [14]. This technique uses one body fixed grid for the airfoil (black) and one for the flap (red) (Fig. 2). In the overlapping area, the flow information is interpolated between the two grids for each time-step, requiring a strong local mesh refinement in this area. The height of the first prismatic layer and the stretching factor were adjusted to reach a $y^+ \leq 1$ and the boundary layer thickness, respectively. All computations were fully turbulent using the Spalart–Allmaras turbulence model [15]. The URANS computations used 1,000 inner iterations and 2,000 iterations per period as [13]. After two pitching cycles, convergence was reached assuming a maximum difference of 1.5 % between the lift coefficient of the second and third period.

The flap actuation was designed to be a square-wave with rounded corners, so that the flap would be fully open

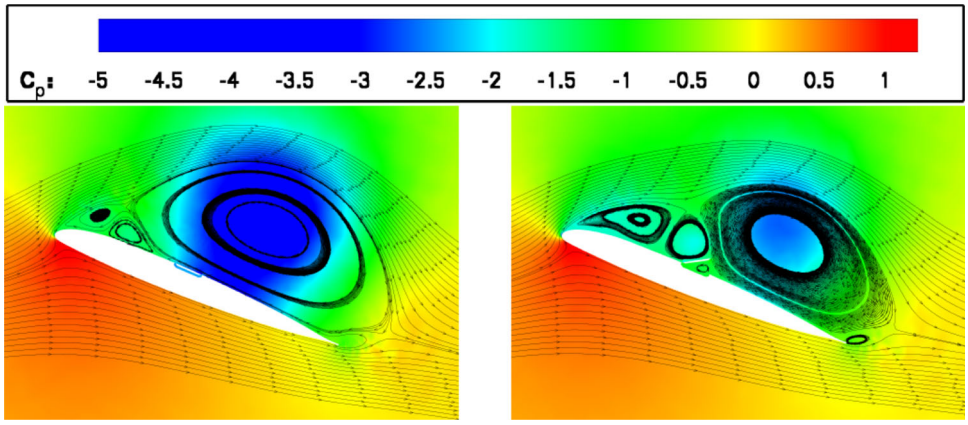

Fig. 4 Comparison of streamlines and pressure for flow without flap actuation (*left*) and with flap actuation (*right*) for the OA209 airfoil at $M = 0.14$, $\mathrm{Re} = 920{,}000$, $\omega^* = 0.1$, $\alpha = 16 \pm 8°$, at $\alpha = 21°$ on the upstroke

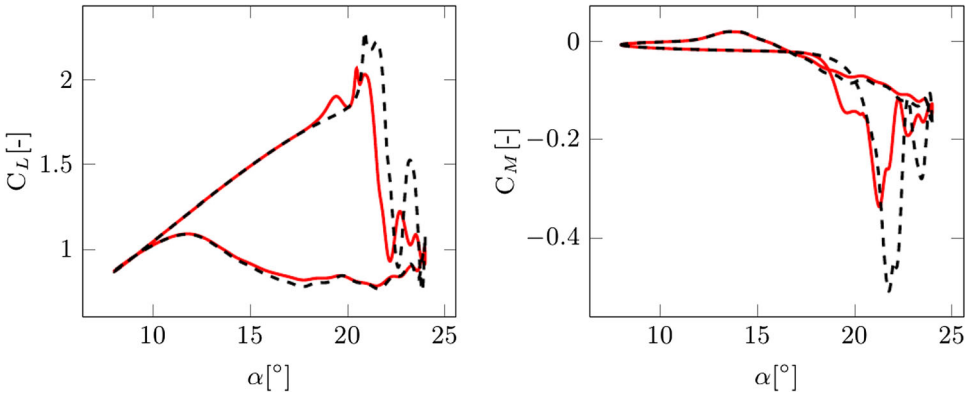

Fig. 5 Comparison of lift (*left*) and pitching moment coefficient (*right*) for the OA209 airfoil at $M = 0.14$, $\mathrm{Re} = 920{,}000$, $\omega^* = 0.1$, $\alpha = 16 \pm 8°$. The *black lines* are without flap actuation, and the *red lines* are with flap actuation

at the moment of leading edge stall, and closed during the separated flow. Figure 3 shows the flap actuation strategy with an open flap only at high angles of attack. Several flap actuation strategies were investigated [16], and this was found to be a good compromise between realizable actuation speeds and correct timing of the flap actuation.

Figure 4 shows a comparison between the flow during dynamic stall for $M = 0.14$, $\mathrm{Re} = 920{,}000$, $\omega^* = 2\pi fc/v_\infty = 0.1$, $\alpha = 16 \pm 8°$, at $\alpha = 21°$ on the upstroke, during the primary peak in pitching moment caused by the dynamic stall with and without flap actuation. In both cases, a large dynamic stall vortex is formed, with an associated low pressure region, which causes both an overshoot in lift, and an increasing pitching moment as the vortex travels towards the trailing edge of the airfoil, as the moment arm increases. The distance between the dynamic stall vortex and the airfoil increases as it moves downstream, decreasing the force due to the region of low pressure, and thus the instant of both maximum lift and minimum pitching moment is usually before the vortex reaches the trailing edge of the airfoil [17]. The flap is dynamically actuated to only be deployed during the stalled flow, and this is the test case found by Kaufmann [16] as the best flap position and actuation prescription studied. The flap actuation starts well before stall, so that at the point of stall the flap is in a position to act on the separated flow. It can be seen in Fig. 4 that the back-flow flap breaks the main stall vortex into smaller structures, and reduces the strength of the pressure minimum contained in the largest vortex. The total size of the separated region is smaller, resulting in less diversion of the flow over the airfoil, and increasing the lift on the airfoil.

Figure 5 shows a comparison between the lift and pitching moment for the airfoil with and without flap actuation. The start of flap actuation at around $\alpha = 18°$ is visible as a bump in the lift in Fig. 5 (left). In the case with flap actuation the lift peak of stall starts at the same time as without flap actuation. The overshoot in lift is reduced with flap actuation, and the strong second lift peak seen without actuation is much less pronounced. After stall, the lift is similar between the two configurations, and the flap closing around $\alpha = 17°$ on the downstroke is not clearly visible in the lift. The reattachment of the flow is at around $\alpha = 10°$ on the downstroke, regardless of the flap actuation.

The pitching moment in Fig. 5 (right) shows an early excursion to negative pitching moment as the flap is actuated, but during the main stall a reduction in the pitching moment peak of 34 % compared to the reference case without actuation is observed. As for the lift, the second peak in the pitching moment is much less

Fig. 6 Passive back-flow flap model in the 1 MG at 50 m/s. Flow is from left to right

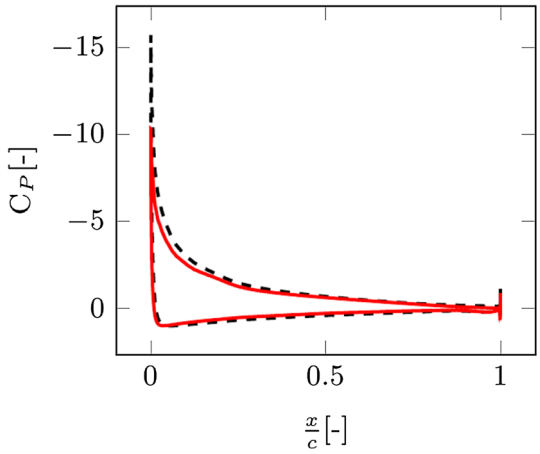

Fig. 7 Pressure distribution on the OA209 airfoil with no flap at $M = 0.14$, Re = 920,000 via CFD. *Red* steady 14, *Black* unsteady 18, upstroke

pronounced when the flap is actuated, and the pitching moments after stall are similar between the cases with and without flap actuation.

3 Experiment with a passively actuated flap

The initial numerical study was done using an actively actuated flap, with a small gap between flap and airfoil, as this was the simplest configuration to use numerically. This investigation left several open questions:

- What is the effect of the true flap geometry, with sealed leading edge?
- Will the passive actuation of the flap through the back-flow after separation be sufficient to open it?
- For attached flow, is the flow sufficient to hold the flap closed against the inertial forces of the model pitching?

To investigate these questions, an initial experiment was performed in the 1 MG low-speed wind tunnel in Göttingen. This tunnel has an open test section of 1 m width and 0.70 m height and flow at 50 m/s was used on a NACA0012 airfoil of 0.3 m chord, pitching at $\alpha = 20 \pm 8°$ and f = 3–6 Hz: the same conditions as in the CFD above, but with the mean angle increased to compensate for the large blockage of this wind tunnel model. As seen in Fig. 6, the flap was attached to the suction side of the model with tape, and the deployment of the flap was restrained in angle using cords. The flow was monitored using tufts and a high-speed video camera, with which the flap deployment and flow direction on the suction surface were monitored. For this experiment, the model pressures were not monitored. In Fig. 6, the model is at high static angle of attack, and the flow on the airfoil is separated. This static separated flow causes a reverse flow on the suction side of the airfoil, which lifts the flap from the surface of the airfoil. The flap angle is restrained by cords, meaning that the opening angle remains constant at the maximum possible angle of attack. Tests without the flap restrained showed that the flap had a continuous unconstrained motion, which depended on the flow condition. In the worst case, the flap increased in angle until it was reversed along the airfoil, after which it fully returned to the closed position, leading to a wildly unsteady flapping motion.

As shown for computational results on a clean OA209 airfoil in Fig. 7, the pressure along the suction side of the airfoil increases monotonically toward the trailing edge. When the flap is on the surface of the airfoil, the pressure under the flap is (roughly) that at the trailing edge of the flap. Since the pressure increases from the front to the back of the flap, this results in a higher pressure under the flap than on top of it, and the flap angle increases. As the flap angle increases, the pressure on the top of the flap increases, and this allows the flap angle to stabilize at a minimum angle of around 5–10° to the surface, depending on the flap position. Perforating the flap resulted in a reduction of this angle, but the results were still unsatisfactory for the surface quality required for normal flight. An extreme example of the effect of a pressure gradient on the flap could be observed by positioning the flap in or close to the suction peak, which resulted in stabilized angles of around 45°, thus having the flap fully opening even when no separated flow was present.

The analysis of the high-speed videos (Fig. 8) showed that the back-flow flap self-actuated due to the back-flow of the dynamic stall vortex. This video was taken with a hand-held camera at 120 frames per second, and thus the inter-framing time is 8.33 ms. In the extracted images,

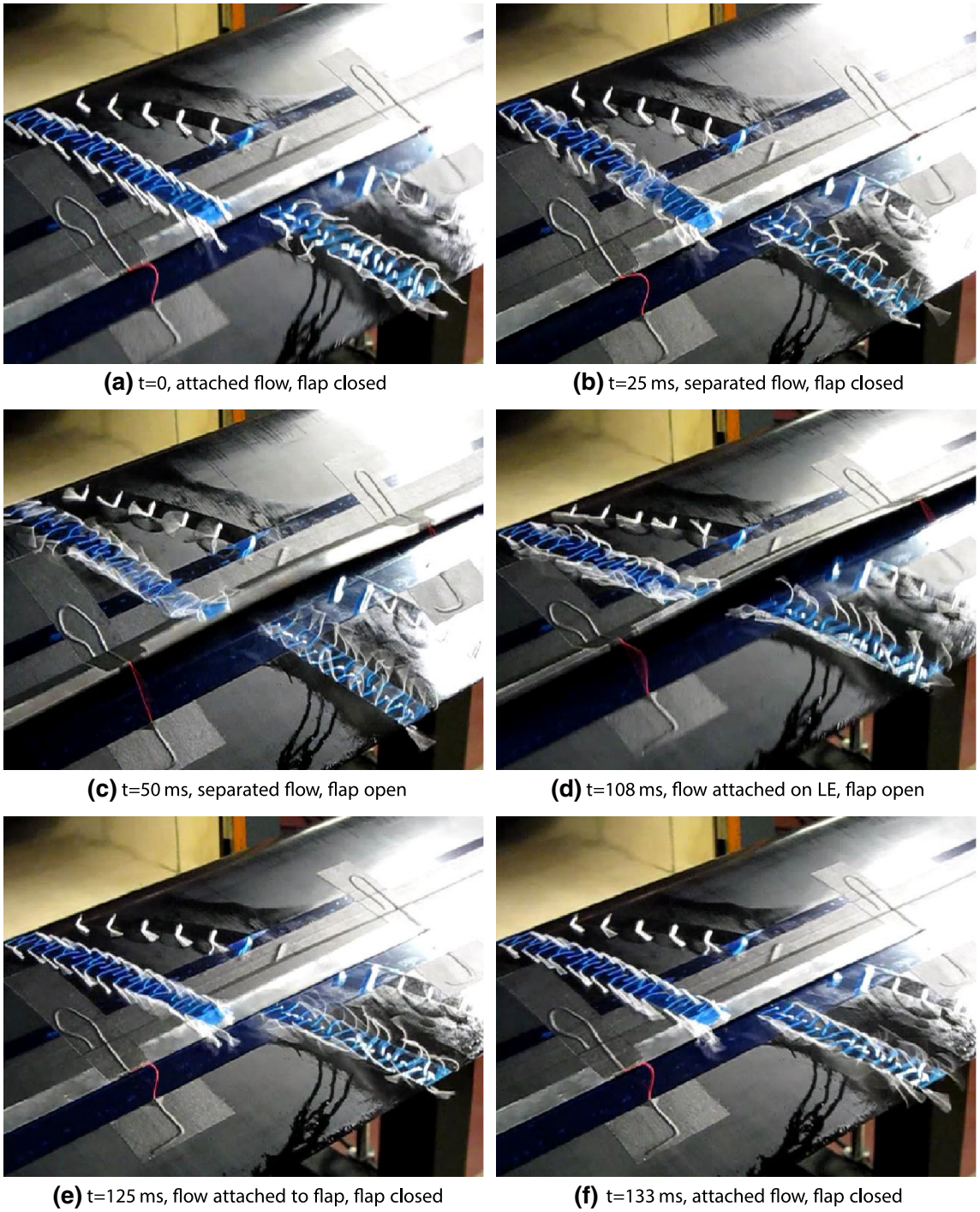

Fig. 8 High-speed video frames of the pitching experiment $\alpha = 20 \pm 8^\circ$ at $f = 6$ Hz, with a flap of length $x/c = 0.10$, with hinge at $x/c = 0.52$, constructed of aluminium plate of thickness 0.5 mm

separation becomes visible through the tuft movement. This movement can be inferred from the blurring of the individual tufts in the still-image. Figure 8a shows the top of the airfoil during pitch-up just before stall. The flow is fully attached, and the flap is lying flat on the surface of the airfoil. Directly behind the flap some tufts are reversed, since there is a small separation on the surface here, due to the residual flap angle in attached flow. In this case, the flap is a strip of 0.5 mm thickness aluminium, with length 30 mm ($x/c = 0.10$). The leading edge of the flap is secured by a length of tape at $x/c = 0.52$, and this is also the hinge point. Due to the tape, there is no flow through the hinge point. Figure 8b shows that the flow is fully separated on the top of the airfoil from around 10 % chord,

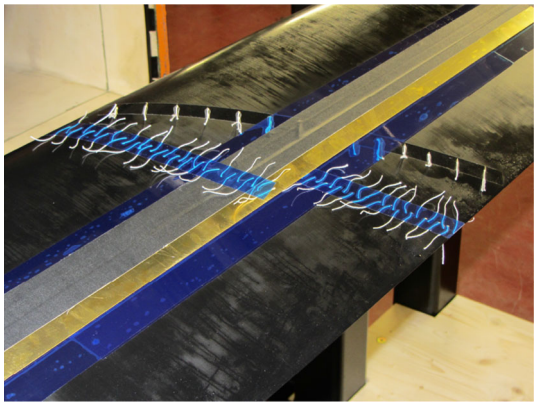

Fig. 9 Flap of 0.6 mm brass for the investigation of effect of flap inertia

with the time for flow separation being around 25 ms. The reverse flow is fully established, but the flap has just started to move away from the static position on the airfoil which it held for attached flow. Although the flap started to actuate immediately after the airfoil stall, it was not fully actuated for around 0.025 s. Figure 8c shows the flap that has reached the position where it is restrained from opening further by the cords. At this pitching condition, this delay is equivalent to a change in angle of attack of $\Delta\alpha = 5°$. If the flap were actuated early enough, this would be a sufficiently short actuation time, but the actuation only starts after the flow separation, and thus the flap is always too late to control the dynamic stall vortex. This suggests that an active flap would be necessary.

If the flap was not restrained by the cords, the back-flow resulted in the flap being completely flipped, until it lay backward on the airfoil surface. Thus, a restraining mechanism to limit the flap maximum angle is necessary. Figure 8d shows the start of flow reattachment. For this airfoil, the flow reattached starting at the leading edge, and in Fig. 8d the tufts at the leading edge of the airfoil are in the direction of flow, indicating attached flow, while the rest of the tufts still indicate separated flow. At this point, the flap starts to close simultaneously with the reattachment of the flow. In Fig. 8e, 17 ms after the start of flow attachment, the flap is fully closed, and the flow downstream of the flap can start to reattach. One camera frame later, in Fig. 8f, the flow was fully attached. The flap self-closed in acceptable time as the flow reattached.

The use of different materials to vary the weight and inertia of the flap (thick flap of brass, thin flap of aluminium), showed that the aerodynamic forces were much larger than the inertial forces (Fig. 9). The pressure distribution from the attached flow counteracted the inertial forces due to pitching, at pitching frequencies of up to $f = 6$ Hz, keeping the flap close to the model surface

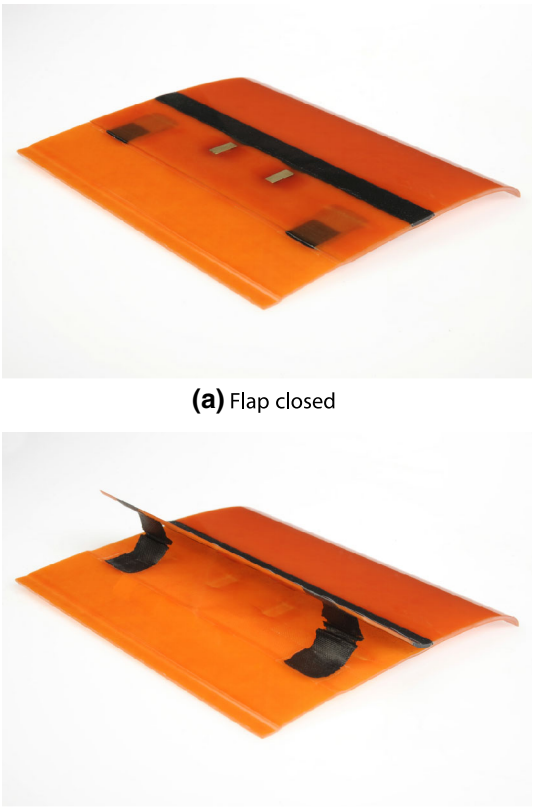

(a) Flap closed

(b) Flap deployed

Fig. 10 First structural demonstrator for a GFRP back-flow flap "glove" (*upper part*) with solid state hinge and angle restraint

during attached flow. Unfortunately, as for the static flow, the pressure gradient over the flap during attached flow caused it to not lie perfectly flat on the airfoil surface, but to stabilize at a minimum angle of around 5–10° to the surface, depending on the flap position. The conclusion was thus that the back-flow flap should have active actuation to open during stall, and active actuation to hold it closed during attached flow.

4 Structural design of the flap

Motivated by the first numerical predictions and the initial wind tunnel experiments, the structural realization of such a flap was investigated. Ideally it should be possible to retrofit the back-flow flap to existing blades. Numerical investigations showed that attaching the hinge and flap as a "bump" on the top of the airfoil always resulted in an unacceptable increase in drag (particularly, at high Mach number), regardless of the flap geometry. Therefore, a concept to fit the whole system into a "glove" of thickness 6 mm, to be attached to the upper side of the rotor blade airfoil was pursued. This restriction on the available space for the flap and actuator is challenging, but realizable. In

contrast to the initial experiments, the back-flow flap should be integrated into the blade surface without steps or gaps. Furthermore, the hinge that connects the flap to the blade should be robust enough to enable a reliable deployment at high frequencies without significant friction or wear within the strong centrifugal field of a helicopter rotor. Using composite materials for the flap offers the possibility of integrating functionalities like an actuator or a hinge directly into the structure [18, 19].

A prerequisite for the integration of these functionalities during the manufacturing process of the composite is the selection of compatible raw materials. For the presented back-flow flap, a GFRP-prepreg (Glass Fiber Reinforced Polymer, pre-impregnated fibers) was used for the main structure of the "glove". The matrix is cured at 120 °C. The elastomeric material used for the solid state hinge and for the angle restraint is customized so that it can be vulcanized at the same temperature. This finally allows the combination of cure and vulcanization in one process. Consequently, a relatively strong adhesion between both materials can be obtained. As usual for composites the different materials are placed layer by layer on a mold. Here, a negative mold was used to guarantee that the outer contour of the airfoil is matched. Numerous separating foils are used to assure that the flap and the angle restraints are only connected in predefined areas which enables the flap to lift after cure. Due to the integral design and manufacturing concept, the glove with solid state hinge and angle restraint can be manufactured in one shot. Figure 10 gives an impression of how the structurally integrated solid state hinge connects the GFRP-flap to the "glove" that is used to retrofit the back-flow flap to an existing blade. The Figure only shows the upper part of the "glove". To prevent any steps in the sensitive leading edge region, the retrofitted structure will be extended to the lower side of the profile.

Within this paper, two different actuation mechanisms will be presented and evaluated, both of which have the potential to operate under the adverse conditions of a helicopter rotor. The first is based on a piezoelectric actuator [18, 20] that is able to bend the back-flow flap and therefore to support the self-actuation of the flap. The second relies on magnetic forces for the deployment of the flap. Both concepts take advantage of integration of the actuator into a back-flow flap that is made of GFRP.

4.1 Solid state hinge

The surface of the hinge that connects the flap to the blade should be as smooth as possible to prevent any disturbance of the flow when the flap is not deployed. For this reason, conventional hinges, consisting of two hinge leaves, are not suited. Further, those joints rely on the relative movement of two solid bodies. Even though lubricants can reduce the amount of friction produced in the contact area between both hinge leaves, high frequency actuation would cause significant wear. For the application on a real helicopter blade, the centrifugal forces would make all problems arising with friction and wear even more severe. All these issues can be addressed using a solid state hinge. Solid state hinges generate the relative movement of the rigid parts by elastic deformation of a flexible region. Since they have no moving parts they do not suffer from friction or wear. Figure 11 depicts the general design and dimensions of the solid state hinge that connects the flap to the blade.

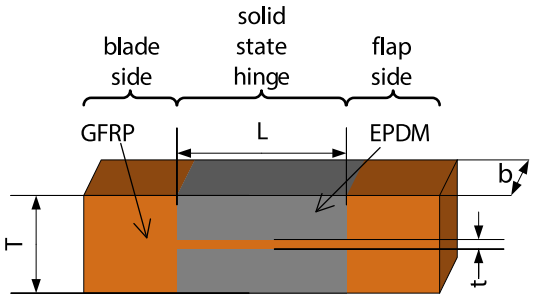

Fig. 11 Principle and dimensions of solid state hinge

The material in the flexible region must sustain the strains occurring without any plastic deformation. Nevertheless, it should have a certain stiffness to prevent large longitudinal strains. As GFRP shows a linear elastic material behavior up to large strains, it is a well-suited material for this application. Since the fracture strain in fiber direction of a unidirectional GFRP material is higher than transverse to the fiber, the fibers should be oriented in parallel to the neutral axis of the hinge. In this configuration, bending of the hinge does not produce a coupled torsion deformation. In principle, the strains due to bending remain small as long as the material is located close to the neutral axis. However, due to manufacturing constraints, the thickness t of the flexible part of the hinge cannot be arbitrarily small. The hinge is designed to have a symmetric three-layer setup. The middle layer GFRP directly connects the flap to the blade. As this thin layer would be quite fragile, it is encapsulated in EPDM (Ethylene Propylene Diene Monomer). The larger distance of the elastomer to the neutral axis, results in bigger strains in the EPDM layers. But as this highly flexible material can easily bear strains of 100 % and more, EPDM is an excellent material for this application.

As the degree of freedom in a solid state hinge is realized through an elastic deformation, the joint is always characterized by a certain spring characteristic. Consequently, an additional force or moment has to be overcome to deploy the flap. For the design process, the knowledge of the elastic characteristic of the hinge is needed. For this

Table 1 Solid state hinge configurations

Config.	t (mm)	T (mm)	L (mm)	Comment
1	0.125	1.125	10	50 % cut out
2	0.125	1.125	10	–
3	0.125	1.125	15	–
4	0.25	1.25	10	–

purpose, a simple and fast analytical model to predict the bending stiffness of the 3-layer setup was verified with numerical investigations and finally validated with experimental data. For the analytical prediction of the spring characteristic, the bending stiffness of the solid state hinge is linearly proportional to the extruded length of the hinge b. For the calculation of the equivalent torsional spring characteristic c_t, textbook formulas can be used [21]. The inclination angle α at the end of a uniform beam with the length L and the bending stiffness EI_{SSH} that is deformed by a bending moment M at the free end can be calculated by:

$$\alpha = \frac{M \cdot L}{EI_{\mathrm{SSH}}} \tag{1}$$

$$c_t = \frac{M}{\alpha} \tag{2}$$

$$\frac{c_t}{b} = \frac{EI_{\mathrm{SSH}}}{b \cdot L}. \tag{3}$$

To verify and validate the analytical estimation of the spring characteristic, four different configurations of solid state hinges were investigated. A summary of the different designs is given in Table 1.

To adjust the stiffness of the hinge, different design variables can be used. The configurations investigated comprise two different thicknesses of the central GFRP layer t as well as two lengths of the hinges L. As the GFRP-layer could not be further reduced in thickness (due to manufacturing constraints), configuration 1 had cut outs in the direction of the extruded length b. Consequently, only 50 % of the hinge area was covered with GFRP. The cut outs were filled with EPDM to prevent any holes allowing pressure equalization between the upper and the lower flap surface. In the analytical and numerical prediction, this modification was modeled via a reduction of the elastic modulus of the middle layer according to a simple rule of mixture. Finally, all four configurations were manufactured. For the experimental determination of the spring constant c_t, a universal testing machine was used. The machine was equipped with a 10 N load cell. The load cell was connected to the flap by a thin sting in such a manner that the movement of the traverse of the testing machine opened the flap, while the load cell measured the corresponding string force. The opening angle of the flap as well as the angle between the flap surface and the force were captured in equidistant steps of the traverse position. Therefore, a photograph, taken for each step, is post-processed via image processing software. Finally, the force component orthogonal to the flap surface is used to calculate the moment at the middle of the solid state hinge. The spring constant is then determined as the linear coefficient between flap angle and moment.

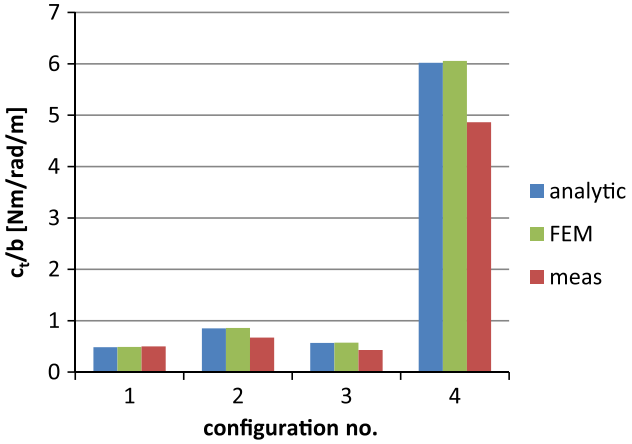

Fig. 12 Comparison of torsional stiffness

Figure 12 shows the comparison between the analytical and numerical prediction of the spring characteristic and the measured values. While the numerical (FEM) and analytical results (analytic) are in very good agreement (deviation less than 1.5 %), the measured values (meas) only reproduce the trend of the prediction. The deviations are up to 25 %. Analysis of the contributions of GFRP and EPDM to the total bending stiffness of the hinge showed that the GFRP delivers the major contribution to the bending stiffness as its Young's modulus is about 4,500 times higher. For the investigated designs, only one or two layers of GFRP-prepreg are used. The resulting layer thickness is approx. 1/8 mm. Due to manufacturing and material deviations, this thickness cannot be guaranteed. Micrographs of the manufactured hinges indicated deviations in thickness of a few 100th of a millimeter. Changing the single layer thickness in the analytical and numerical prediction by only 1/100 mm can bring the deviations down to less than 6 %. Consequently, the analytical and the numerical model can be evaluated as sufficiently accurate with respect to the achievable manufacturing accuracy.

To calculate the opening force as a function of the flap angle, the kinematics of the flap has to be regarded, as shown in Fig. 13. Assuming a constant mean moment over the length of the solid state hinge, the relative motion of the flap can be described as follows.

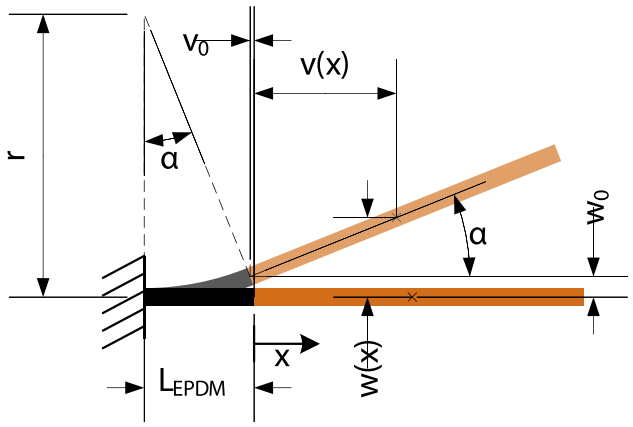

Fig. 13 Kinematics of the back-flow flap

$$r = \frac{L_{\mathrm{EPDM}}}{\alpha} \tag{4}$$

$$v_0 = v(x = 0) = r \cdot \sin(\alpha) - \mathrm{L_{EPDM}} \tag{5}$$

$$w_0 = w(x = 0) = r - r \cdot \cos(\alpha) \tag{6}$$

$$w(x) = w_0 + x \cdot \cos(\alpha) \cdot \tan(\alpha) \tag{7}$$

$$v(x) = v_0 + x \cdot \cos(\alpha). \tag{8}$$

For a given position x of the center of force of an actuator, the motion with respect to the flap angle can be calculated. This kinematic relation was used for the finite element simulation to predict the moment at the solid state hinge generated by the actuators according to the flap angle.

4.2 Angle restriction

One outcome of the initial wind tunnel experiments was that a restriction in the opening angle of the flap is needed. Without a limit in the flap opening angle, the highly dynamic process caused the flap to flip over. The spring characteristic of the solid state hinge can only partially improve this behavior. A drawback of the solid state hinge concept is that it is not possible to use a catch like those available for conventional hinges. The basic idea is to limit the flap angle in a similar manner as already done in the wind tunnel experiments. There, a cord was attached to the flap as well as to the blade surface. When the flap opened, this string was put under tension and limited the opening angle. This worked for the initial tests, but showed significant wear already after a short measurement time. Furthermore, the strings were in the flow when the flap was not deployed. This increases the drag and can possibly disturb the natural flow. Consequently, a robust restraining mechanism that is integrated into the "glove" and does not disturb the flow is needed. Figure 14 shows the basic idea how the angle restraint for the flap with the solid state hinge can be realized.

The restraint mechanism is located underneath the flap in such a manner that the outer surface remains totally smooth if the flap is not deployed. In contrast to the wind tunnel experiments, the catch is now a strip that has a certain width in the direction of extrusion (b) (matched to the loads) and is no longer a cord. This also guarantees that the strip is always in the same position when the flap is closed. The maximum opening angle can be set by the proper position and length of the strip. The strip should have almost no bending stiffness but should not elongate significantly to limit the deployment angle to a certain value. A three-layer setup of EPDM and glass fibers is identified as an ideal material combination for the strip. Compared to the solid state hinge, the bending stiffness of the strip was significantly reduced, since an actuator has to overcome this additional stiffness to deploy the flap. For this reason, the GFRP material used for the middle layer of the solid state hinge was replaced by a very thin glass fiber fabric (50 g/m^2) that was not impregnated with epoxy resin so that the elastomer directly embeds the glass fibers in the strip. To reduce the thickness of the strip in stored condition, the thickness of the EPDM layers was also decreased. To identify the ideal way to connect the strip, the peel-off force between strip and GFRP for different configurations was determined by a customized test in a testing machine.

5 Actuation mechanisms

For a reliable operation of the flap, an actuation mechanism is needed. For the investigation of the aerodynamic effect, the ideal solution would be an actuator that can directly

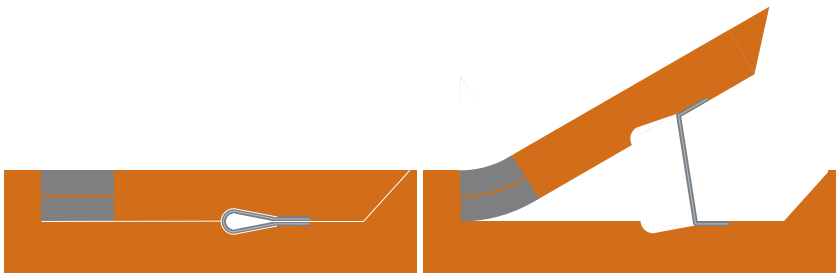

Fig. 14 Principle of flap with solid state hinge and angle restraint (*left* closed, *right* opened)

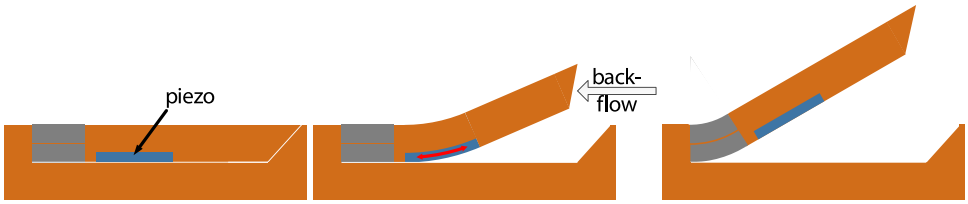

Fig. 15 Principle of flap with piezoelectric bending actuator (*left* closed, *middle* actuator induced bending of the flap, *right* flap fully opened by back-flow)

control the flap deployment angle in the same way as the angle was set during the simulation. Unfortunately, such an actuator would have to be quite powerful and once again the limitation in mounting space excludes a lot of the technologically possible solutions. As a compromise between an easy to realize passive flap and a fully active deployable flap, the goal is here to develop an actuator that can support the self deployment of the flap by the flow. Such a concept is more likely to be fitted into the "glove". Furthermore, the efficient use of system inherent forces will result in quite low energy consumption of the actuation system. In this section of the paper, two different approaches for actuation mechanisms that can initiate a flap deployment by the flow are presented and assessed.

5.1 Bending actuator

Composite materials allow the integration of different kinds of actuators directly into the structure. In the past, mainly piezoelectric actuators were used. Since the strain of those actuators is the response to an electric field, they are easy to operate. The piezo-ceramics introduce strain into the structure which leads to the desired morphing. Further, these materials have already proven that they can be operated in the centrifugal field of a helicopter rotor [19, 22]. Different types of piezoelectric actuators are available. For the integration into the back-flow flap "glove" especially thin piezo-composite actuators are of interest [20, 23]. They require only a very limited mounting space and can be integrated even in curved composite parts [24]. The intended operation principle was to integrate a piezo-composite actuator directly into the flap (see Fig. 15). The actuator should not be located in the neutral axis of the flap laminate. Consequently, the generated strain (see Fig. 15, middle, red arrow) causes a bending of the flap. This deformation would be used to lift the trailing edge of the flap from the blade surface. The back-flow which develops on the airfoil surface should open the flap.

The crucial point of this concept is the assessment of whether the performance of the bending actuator is sufficient to produce a significant flap bending. For the analytical assessment of the bending performance of the integrated actuator, three steps are required.

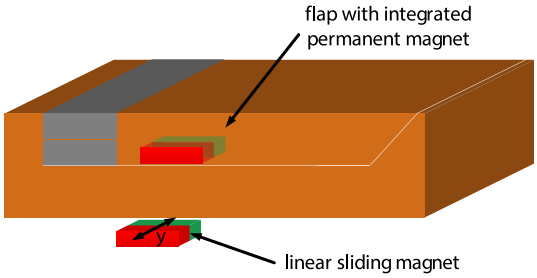

Fig. 16 Principle of flap with integrated permanent magnet

1. position of neutral axis of the layered setup (fiber composite, piezo-composite)
2. bending stiffness of the setup
3. actuator moment

Using an analytical tool based on fundamental mechanics, different designs were evaluated. The study comprised configurations with one and two piezo-composite actuators (two- or three-layer setup) and various flap thicknesses and materials. The displacement at the trailing edge of the flap was calculated without any forces from the flow. It can be summarized that the maximum displacement for a flap with a length of 40 mm did not exceed 1 mm. This relatively small displacement in combination with the experiences from initial wind tunnel experiments led to the conclusion that the risk of insufficient actuation authority is too high to further pursue this actuation concept. A second deficit that confirmed this decision is the fact that this actuator is not able to keep the flap closed during attached flow. Consequently, alternative actuation mechanisms are investigated.

5.2 Permanent magnet

A quite simple approach is the deployment of the flap with two permanent magnets. As those cannot be switched on and off, it is necessary to move one of the magnets. The zero energy requirement to keep the flap closed when not needed make permanent magnets an attractive option. The basic principle of operation and the orientation of the magnets can be seen in Fig. 16.

While one neodymium magnet is integrated in the flap during the manufacturing process, the second one can be

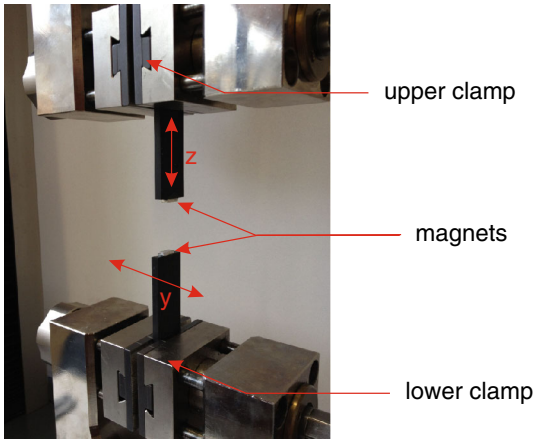

Fig. 17 Setup for the characterization of neodymium magnets

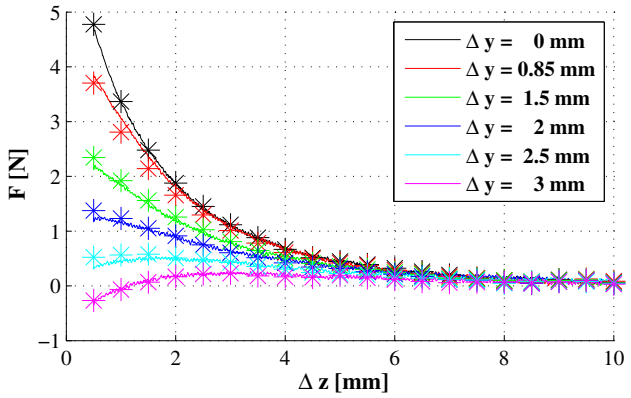

Fig. 18 Results of characterization of neodymium magnets. *Lines* depict measured values and *symbols* FEM values

linearly slid underneath the flap. This motion could be generated by an electromagnet and a push rod at the root of the blade, but the detailed design of this mechanism is not the focus of this work. Increasing the number of magnet pairs also increases the force that deploys the flap. To predict the forces between the two magnets, static finite element calculations were performed. Since the remanent magnetization of the neodymium magnets used is only roughly known, the calculations are accompanied by an experimental characterization.

The tests were performed in a universal testing machine (see Fig. 17). Each of the neodymium magnets was glued to a CFRP (Carbon Fiber Reinforced Polymer) plate to have a sufficient distance to all ferromagnetic parts of the machine that could influence the measurement. To characterize the interaction of the two magnets, the force in z-direction as a function of Δz was captured for different lateral offsets Δy. As the setup was rather stiff and the range of measured force is low compared to the measurement range of the testing machine, the position of the transverse was used to calculate the gap Δz between the magnets. Furthermore, any lateral bending of the CFRP-plates was neglected.

Hence, the value set for the lateral distance Δy is assumed to stay constant during each measurement. In parallel to the experiment, the setup was modeled using the finite element method. To set the remanent magnetization, the geometric setup for the point of maximum force within the measurements ($\Delta y = 0\,mm$, $\Delta z = 0.5$ mm) was simulated. At this position, the magnetization was varied to match the measured value. Once this value was set, it remained unchanged for all further computations with varying values for Δy and Δz. Figure 18 depicts the comparison between the measured and the computed characteristics of the magnets.

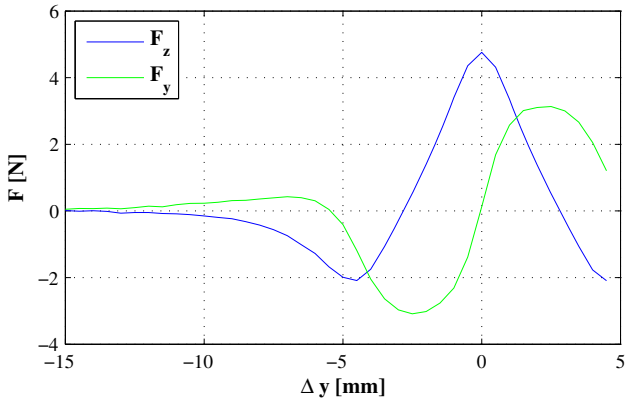

Fig. 19 Prediction of z and y force as a function of lateral offset Δy for constant $\Delta z = 0.5$ mm

Looking at these results, the following conclusions can be made. The measured results and the finite element prediction are in good agreement. The magnets can generate a maximum force of almost 5 N which is quite remarkable for the investigated magnets that have a size of $4.5 \times 10 \times 2$ mm and a weight of 0.7 g. As expected, the force rapidly drops when the gap between the magnets becomes larger. There is a small region of lateral distance where the increase of the gap Δz first leads to a slight increase in force until the force drops again. If the lateral distance between the magnets becomes large enough, they attract each other. The latter effect can be used to keep the flap closed during attached flow. The finite element computations in Fig. 19 show that sufficient attractive and repulsive forces to overcome elastic and aerodynamic forces can be obtained by varying the actuator magnet position in the lateral direction. The maximum attraction force F_z occurs at a lateral offset of $\Delta y = 4.5$ mm and has a magnitude of approx. 2 N.

The tools presented so far can be used to investigate further concepts for a magnetic actuation. The design using two permanent magnets can serve as benchmark in terms of actuator performance. As it is advantageous to have as few moving components as possible in the centrifugal field of a helicopter rotor, it is self-evident that it would be beneficial to replace the moving magnet by an electromagnet. The challenge is to design the electromagnet that is strong enough to have a comparable performance as the neodymium magnet used so far and that fits into the slim "glove" of the back-flow flap. Concepts using electromagnets will be investigated in future work.

6 Conclusion

This paper presents a structural design concept for a back-flow flap. The development was encouraged by the predicted benefits of initial numerical investigations, which showed that with active actuation of a back-flow flap at Mach 0.14, the pitching moment peak could be reduced by 34 %. Initial wind tunnel experiments were performed and showed that although the flap actuation time due to the aerodynamic forces was acceptably short, it actuated too late to control stall. Further, the flap needs to be held closed during attached flow, since the pressure gradient on the rotor blade airfoil causes the flap not to lie flush with the surface. The necessity for an angle restriction to control the unsteady motion of the flap was identified.

The attachment of the flap via a structurally integrated solid state hinge and an angle restriction mechanism were presented to fulfill these requirements, and a demonstrator with integrated hinge and flap in a "glove" to be mounted on an existing rotor blade was presented. Two different actuation concepts were investigated and assessed. It could be shown that a bending actuator that is integrated into the flap does not have enough authority to initiate a reliable deployment of the flap. The combination of two permanent magnets seems to be more promising, with sufficient strength to actuate the flap and to keep it closed during attached flow. The zero energy requirement to keep the flap closed when not needed makes permanent magnets an attractive option.

After the manufacturing of the wind tunnel model, a final test campaign will show the effectiveness of the system under wind tunnel conditions. The challenges that arise under rotating conditions were not in the focus of this paper but had to be kept in mind. After further aerodynamic simulations have identified the radial location of such a flap, the transfer of the presented wind tunnel technology to a rotor will be investigated.

References

1. Mai, H., Dietz, G., Geissler, W., Richter, K., Bosbach, J., Richard, H., de Groot, K.: Dynamic stall control by leading edge vortex generators. J. Am. Helicopter Soc. **53**(1), 26–36 (2008)
2. Martin, P., Wilson, J., Berry, J., Wong, T., Moulton, M., McVeigh, M.: Passive Control of Compressible Dynamic Stall, AIAA Paper, pp. 2008–7506 (2008)
3. LePape, A., Costes, M., Joubert, G., David, F., Deluc, J.-M.: Experimental study of dynamic stall control using deployable leading-edge vortex generators. AIAA J. **50**(10), 2135–2145 (2012)
4. Gardner, A.D., Richter K., Mai, H., Neuhaus, D.: Experimental control of compressible OA209 dynamic stall by air jets. AHS J. 58(4) (2013)
5. Weaver, D., McAlister, K.W., Tso, J.: Control of VR7 Dynamic stall by strong steady blowing. J. Aircr. 41(6) (2004)
6. Kaufmann, K., Gardner, A.D., Richter, K.: Numerical investigations of a back-flow flap for dynamic stall control. In: New results in numerical and experimental fluid mechanics IX, Notes on numerical fluid mechanics and multidisciplinary design, vol. 124, pp. 255–262 (2014)
7. Meyer, R.K.J.: Experimentelle Untersuchungen von Rückstromklappen auf Tragflügeln zur Beeinflussung von Strömungsablösungen. Dissertation, Technische Universität Berlin, Mensch-und-Buch-Verlag (2000)
8. Höfinger, M.: Rotorblatt mit integrierter passiver Oberflächenklappe. Deutsches Patent DE 10 2010 041 111 A1, 22.03.2012 (2012)
9. Gallot, J., Vingut, G., De Paul, M.V., Thibert, J.: Blade profile for rotary wing of an aircraft. United States Patent 4325675, (20.4.1982) (1982)
10. Mulleners, K., Raffel, M.: The onset of dynamic stall revisited. Exp. Fluids **52**(3), 779–793 (2012). doi:10.1007/s00348-011-1118-y
11. Gardner, A.D., Richter, K., Rosemann, H.: Numerical investigation of air jets for dynamic stall control on the OA209 airfoil. CEAS Aeronaut. J. **1**(1), 69–82 (2011). doi:10.1007/s13272-011-0002-z
12. Schwamborn, D., Gardner, A.D., von Geyr, H., Krumbein, A., Lüdeke, H., Stürmer, A.: Development of the TAU-Code for aerospace applications. In: Proceeding of the 50th NAL INCAST (International Conference on Aerospace Science and Technology), Bangalore, India (2008)
13. Richter, K., Le Pape, A., Knopp, T., Costes, M., Gleize, V., Gardner, A.D.: Improved two-dimensional dynamic stall prediction with structured and hybrid numerical methods. AHS J. 56(4) (2011)
14. Schwarz, T.: The overlapping grid technique for the time accurate simulation of rotorcraft flows. In: 31st ERF, Florence, Italy, 13–15 September (2005)
15. Spalart, P.R., Allmaras, S.R.: A one-equation turbulence model for aerodynamic flows. In: AIAA Paper 92–0439, AIAA 30th Aerospace Sciences Meeting and Exhibit, Reno, Jan 6–9 (1992)
16. Kaufmann, K.: Numerische Untersuchung einer Rückstromklappe zur Dynamic Stall-Kontrolle. Diplomarbeit. Uni, Stuttgart IAG (2012)
17. Gardner, A.D., Richter, K.: Influence of rotation on dynamic stall. AHS J. 58(3) (2013)
18. Wierach, P.: Adaptive, tolerant and efficient composite structures, research in aerospace. In: Wiedemann, M., Sinapius, M. (eds.) Nano-Micro-Macro, pp. 17–28. Springer, Berlin (2012). doi:10.1007/978-3-642-29190-6_2
19. Wierach, P., Riemenschneider, J., Opitz, S., Hoffmann, F.: Adaptive, tolerant and efficient composite structures, research in

aerospace. In: Wiedemann, M., Sinapius, M. (eds.) Experimental Investigation of an Active Twist Model Rotor Blade Under Centrifugal Loads, pp. 391–407. Springer, Berlin (2012). doi:10.1007/978-3-642-29190-6_32
20. Wierach, P.: Low profile piezo actuators based on multilayer technology. In: Proceeding of the 17th International Conference on Adaptive Systems and Structures, 2006-10-16–2006-10-19, Taipei, Taiwan (2006)
21. Grote, K.H., Feldhusen, J. (eds.): Dubbel: Taschenbuch für den Maschinenbau, 23rd edn. Springer, Berlin (2012)
22. Opitz, S., Riemenschneider, J., Hoffmann, F., Schneider, O.: Measurement of the dynamic tip twist angles of an active twist model scale rotor blade. In: Proceeding of the 36th European Rotorcraft Forum, 7–9 Sept 2010, Paris (2010)
23. Wierach, P.: Adaptive, tolerant and efficient composite structures, research in aerospace. In: Wiedemann, M., Sinapius, M. (eds.) Piezocomposite Transducers for Adaptive Structures, pp. 29–47. Springer, Berlin (2012). doi:10.1007/978-3-642-29190-6_3
24. Algermissen, S., Keimer, R., Rose, M., Straubel, M., Sinapius, M., Monner, H.P.: Smart-Structures Technology for Parallel Robots. J. Intell. Robotic Syst. 63: 547–574. Springer (2011). doi:10.1007/s10846-010-9522-8. ISSN 0921-0296

A.3. Paper: ERF2015, 41st European Rotorcraft Forum

STRUCTURAL DEMONSTRATION OF AN ACTIVE BACK-FLOW FLAP UNDER WIND TUNNEL CONDITIONS

S. Opitz,
DLR-Institute of Composite Structures and Adaptive Systems, Braunschweig, Germany
A.D. Gardner, C.B. Merz, C.C. Wolf,
DLR-Institute of Aerodynamics and Flow Technology, Göttingen, Germany

Abstract

The paper presents a detailed concept for influencing dynamic stall with a surface integrated active back-flow flap on the upper side of an airfoil. The development of the flap from a basic concept to the final wind tunnel experiment is described. Special attention is paid on the selection of flap size and position, the structural concept, the actuation mechanism and the instrumentation. Further, the manufacturing procedure developed to produce a retrofit solution for an existing wind tunnel model is illustrated. The paper closes with first functional tests of actuation mechanism and instrumentation in the wind tunnel. Finally the results from wind tunnel experiments are used to validate the predicted reduction of the pitching moment peak.

1. INTRODUCTION

Dynamic stall is a well-known effect for helicopter airfoils occurring when a pitching airfoil stalls, forming separated flow in a dynamic stall vortex. A lift peak and a negative spike in pitching moment form and then a rapid drop in lift appears as the stall vortex moves downstream. The torsional impulse from the pitching moment peak is often a load-limiting case for the pitch link rods, and high drag is experienced compared to attached flow. Dynamic stall can be controlled by using passive devices, including vortex generators and changes in the leading edge contour [6, 7], but these have disadvantages at high Mach number and are limited in their control of deep stall. In contrast, active devices include actively retracting vortex generators [5], which avoid shocks at high Mach number, or air jets [11, 12], which add energy to the flow, and thus improve the flow control under deep stall conditions.
The leading-edge stall associated with many helicopter airfoils including the OA209 [1] airfoil used for the numerical predictions, is characterized by strong backward flow along the suction side of the airfoil [9]. To control dynamic stall of this type, the single dynamic stall vortex should be broken into several smaller vortices and the passage of the vortices should be delayed [2].

2. STALL CONTROL WITH A BACK-FLOW FLAP

As part of the DLR project STELAR an alternative method of influencing dynamic stall using an active back-flow flap is presently being investigated [4]. In the past back-flow flaps have been tested on gliders as a passive method of reducing stall [8], as freely-hinged spoiler-like flaps on the suction side of the airfoil near the trailing edge. When trailing edge stall occurs, the back-flow lifts the flap and the region of stall can be significantly delayed. Even though the effectiveness of back-flow flaps has been demonstrated in flight experiments with sailplanes, it still has to be investigated whether they are also suited to improve the dynamic stall behavior of helicopter rotor blades [3].

2.1. Principle of operation

Initial numerical investigations with an actively actuated flap showed promising results. The computation was performed in 2D using the unstructured DLR-TAU solver and the Spalart-Allmaras turbulence model using the settings of Richter et al. [10]. The flap was dynamically actuated to only be deployed during the stalled flow, by using the overset grid (chimera) method with automatic hole cutting. The back-flow flap breaks the main stall vortex into smaller structures, and this results in a reduction in the pitching moment peak of 34 % compared to the reference case without actuation, while maintaining the lift during the attached flow (see Figure 1).

2.2. Findings from first wind tunnel experiment

To gather first experiences, simple wind tunnel experiments were performed with an oscillating 2D airfoil

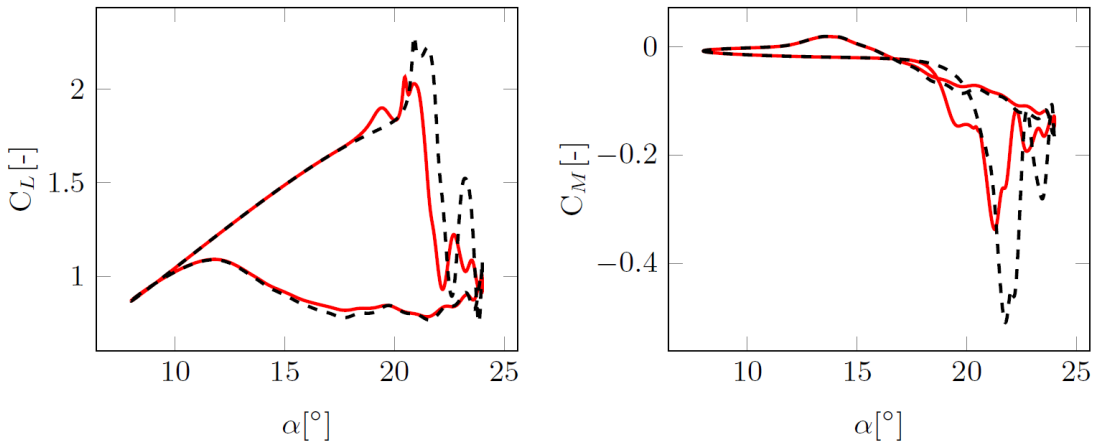

Figure 1: Comparison of lift (left) and pitching moment coefficient (right) for the OA209 airfoil at M=0.14, Re=920000, $\omega^* = 2\,\pi\,f\,c/v_\infty$=0.1, α=16±8°. The black lines are without flap actuation, and the red lines are with flap actuation (image from [4]).

without instrumentation. The model was equipped with a passive back-flow flap and the flow was monitored with tufts and a high-speed video camera (setup see Figure 2). Analyzing the results with passive flaps , it was noted that an existing airfoil could generally be retrofitted with a flow control flap. However, to have reproducible conditions during the

Figure 2: Passive back-flow flap model in the 1MG at 50 m/s. Flow is from left to right (image from [13]).

wind tunnel experiment the back-flow flap approach requires an actuator to hold the flap closed when not needed (e.g. reference cases), and to accelerate the opening of the flap with a pulse of force to guarantee the immediate flap actuation. Further, an angle restriction is needed to limit the flap opening angle, so that the highly dynamic opening of the flap does not cause the flap to flip over lying upside down upstream of the hinge line.

2.3. Basic concept

Summing up the results of the initial numerical investigations and the first wind tunnel experiment a list of requirements for the structure and the actuation mechanism was established. Based upon this list, a concept was developed and presented in detail in [13] and [14]. To prevent any steps or gaps the concept comprises a solid state hinge that connects the flap to a Glassfiber Reinforced Polymer (GFRP) shell that forms the outer model surface. Fiber reinforced elastomers that are highly bendable but do not elongate significantly under tensile loading are intended to limit the flap opening angle.
To provide the opening impulse for the flap the actuation concept uses flap integrated magnets that can be attracted or pushed away by a second set of magnets that moves underneath the GFRP shell. With this approach the flap can be held closed or swiftly opened.
Even though this concept could be shown to be generally feasible there were still a lot of open questions to be answered before the final wind tunnel testing of the back-flow flap. Major points were:

- detailed aerodynamic design (size and position of the flap)
- concept for a retrofit solution of an existing wind tunnel model that is compatible with structure, actuation and instrumentation
- detailed design of actuation mechanism
- instrumentation of the wind tunnel model

These issues will be addressed within this paper, presenting a detailed concept for the retrofit of a wind tunnel model. The paper ends with initial wind tunnel results from the testing of the active back-flow flap.

3. DESIGN OF WIND TUNNEL MODEL

3.1. Aerodynamic design

Computations using the method of Kaufman et al. [4] were performed to estimate the correct size and position of the flap. Therefore the flap size was varied in 3 steps from 5 % chord to 15 % chord. The position of the flap was altered in steps of 10 % chord between 10 % and 70 % of chord. The results of this study are depicted in Figure 3. These computations represent

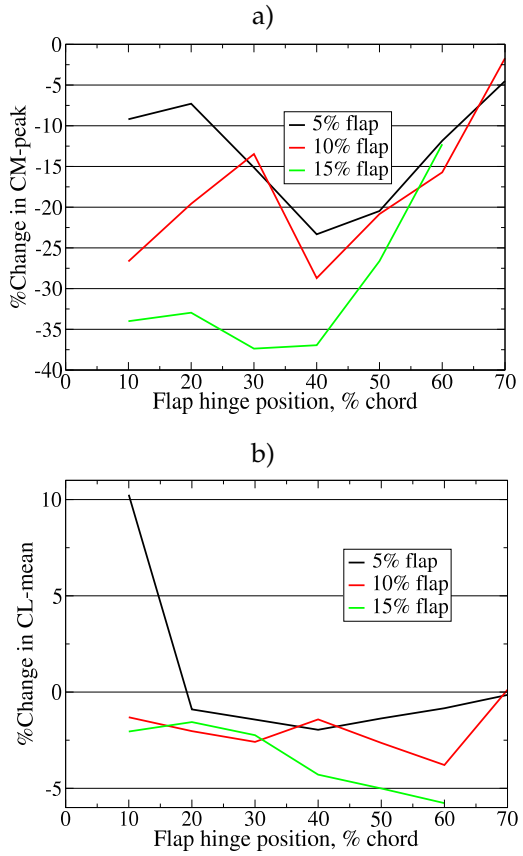

Figure 3: Numerical investigation of the flap size and position, compared to the reference case without a flap, a): Change in pitching moment coefficient peak (Dynamic stall load), b): Change in mean lift coefficient (Hysteresis).

only a rough approximation of the real physics, since they could not model the body-on-body parts of the opening, and always had a gap between the flap and the airfoil. Further, the flap motion which was prescribed in the computations would certainly differ in reality.
Nevertheless some trends can be deduced. In most cases the reduction of the pitching moment peak becomes more effective with increasing flap length. At the same time a larger flap tends to cause a larger reduction of the mean lift coefficient. In contrast to the flaps used to improve the static stall behavior of gliders, positions near the trailing edge do not seem to be effective to reduce the pitching moment peak caused by dynamic stall. For all three investigated flap lengths the best position of the flap appears to be in the range between 30 % and 50 % of chord and tends to be closer to the leading edge for larger flaps. For the two larger flap configurations the mean lift tends to decrease when the flap is shifted towards the trailing edge.
Setting the flap to a length of 15 % chord with hinge position of 30 % chord had the greatest reduction in pitching moment, while not excessively reducing lift. The demonstrator for the basic concept of the solid state hinge and the magnetic actuation concept (see [13]) had an effective flap length of approx. 35 mm which corresponds to approx. 9.5 % chord of the later wind tunnel model. Laboratory tests have shown that in this configuration the actuation mechanism is able to deploy the flap to 30° in approx. 12.5 ms. This opening speed was sufficient to match the prescribed motion that was used in the numerical investigation when the airfoil oscillates with a frequency of 6 Hz.
As the inertia of the flap rises with increasing flap size and consequently reduces the deployment speed, it was decided to realize a flap that extends over 12.5 % of the chord instead of the 15 % that gave the best results in the numerical prediction. Following the best simulated configuration the hinge line of the solid state hinge was placed at 30 % chord. Further on, the decision was made to limit the flap opening angle to a maximum of 30°, to avoid over-opening during the back-flow of the fully separated flow. On the basis of the computations a reduction of the pitching moment peak by 30 % and a loss for $C_{L_{mean}}$ of 2.5 % is expected for this setting.

3.2. Structural design

During the first wind tunnel experiment with passive flaps it was posited that it is possible to equip an existing wind tunnel model with a kind of back-flow flap glove. Such a retrofit solution has multiple advantages. If an adequate concept is found the structure and the instrumentation of an existing model can be used to save costs and to reduce the development time for each tested configuration. Additionally the potential to retrofit existing rotor blades with a back-flow flap can be demonstrated to a certain extent. The first challenge related to a retrofit solution is to find a good compromise between available installation space and size of the model. Increasing the chord length leads to a larger blockage of the wind tunnel and also to a larger flap that might be difficult to deploy in a short time due to its inertia. For this reason the developed glove should be as short and as thin

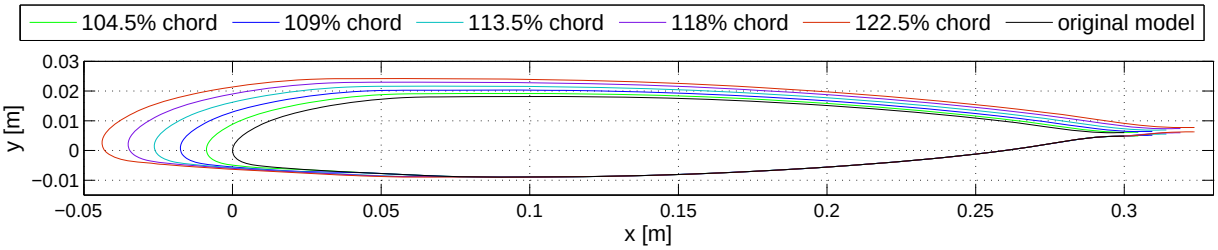

Figure 4: Positioning of the original airfoil of the wind tunnel model within the glove of the back-flow flap for different chord lengths of the modified model.

as possible. To maximize the mounting space available at the upper surface where the flap is installed, it was decided to partially use the lower side of the underlying model. The existing wind tunnel model that is intended to be equipped with the back-flow flap has a chord length of 300 mm. Already knowing the chordwise position and the size of the flap within the retrofit-glove from the aerodynamic design, a small optimization routine was used to place the original airfoil in the enlarged contour of the model with the back-flow flap. This placement was done in a way that a maximum of mounting space is available at the position of the actuation mechanism. The optimization was repeated for increasing chord length of the glove until the distance between new and old airfoil guaranteed a thickness of 5 mm at the position of the flap (see Figure 4). This requirement for a minimum thickness is driven by the size of the neodymium magnets that will be used to actuate the flap. The magnets installed in the flap and the magnets sliding underneath the GFRP-shell have a thickness of 2 mm each. Consequently a minimum of 4 mm thickness is already needed without any structure that incorporates the magnets or friction layers that enable the sliding motion and protect the underlying wind tunnel model. Finally the described optimization procedure resulted in a scale of 1.225 for the glove which is equivalent to a chord length of 367.5 mm (red line in Figure 4).

The basic concept presented in [13] and [14] already demonstrated the general compatibility of an elastomeric angle restriction with the manufacturing process and the actuation mechanism. To guarantee a reliable operation of the flap, the angle restraints for the whole model have to be sized to resist the impulsive opening forces that occur when the back-flow during dynamic stall fully opens the flap. For this purpose customized peel off tests have been performed for different interface designs between angle restraint and GFRP (see Figure 5). The elastomer of the angle restriction is reinforced with a very thin glass fiber fabric. For the connection to the GFRP structure two different configurations were investigated. Configuration 1 connects the restraint via its outer elastomer layer. For configuration 2 the glass fibers of the angle restraint were directly placed on the GFRP. Hence

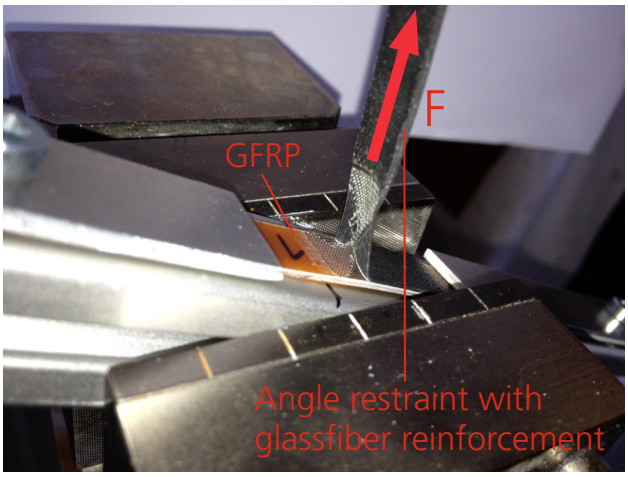

Figure 5: Customized peel off test for the design of the angle restraint

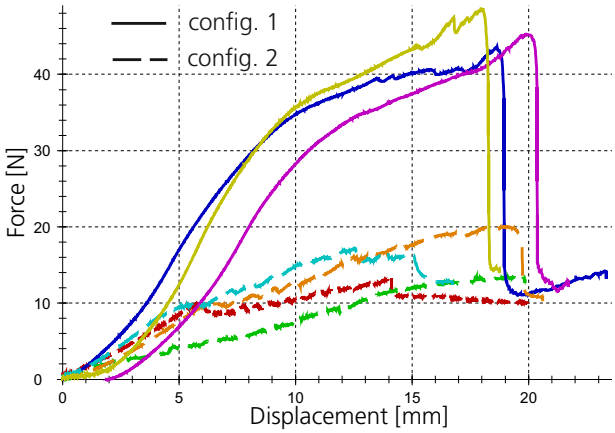

Figure 6: Peel off strength for different configurations of the interface between GFRP and angle restraint (Colors refer to different specimen).

the duromer matrix can infiltrate the glass fiber fabric. The initial intention of this measure was to benefit from the more rigid connection between restraint and GFRP that is formed when the load carrying fibers of the restraint are directly connected to the glove structure. Figure 6 depicts the force carried by the restraints over the displacement of the testing machine for both interface designs.

It is obvious that both configurations have different failure behaviors. Against the expectation all specimen from configuration 2 had a remarkably lower failure load compared to configuration 1. Due to the peel off loading, the rigid connection of the angle restraint leads to a stress concentration at the front of the bond line that causes an early failure in this region. After the first failure the stress concentration moves to the new front of the bond line and consequently causes an successive failure at a low load level. The more flexible interface that connects the glass fiber fabric through an elastomer layer distributes the load over a larger interface area and therefore prevents excessive peel stresses. Consequently higher failure loads are achieved until the initial failure of the interface. Hence configuration 1 was chosen for the final wind tunnel model.
The aerodynamic loads were roughly estimated from the numerical investigations. Finally 8 angle restraints were distributed over the span of the wind tunnel model.

3.3. Actuation

Figure 7 shows the general operation principle for the actuation mechanism of an active back-flow flap presented in [13] and [14]. The mechanism consists of

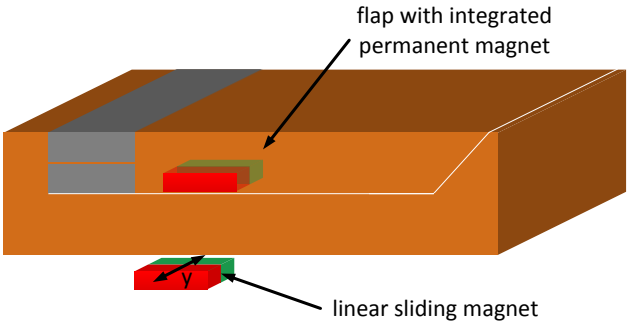

Figure 7: Actuation principle (image from [13]).

two magnets. In previous publications it was demonstrated how a magnet could be integrated into the GFRP-flap. The second, moving magnet and the adjacent actuation mechanism that generates the linear motion were not in the focus of interest so far. In [14] it is shown that the magnetic actuation system can lead to a snap opening of the flap when the bending stiffness of the solid state hinge is small. As the actuation concept allows to keep the flap closed and to deploy it, the bending stiffness of the hinge is preferred to be as small as possible, while still allowing a robust operation of the flap. This enables large opening angles since the restoring moment that has to be overcome by the magnetic forces stays small. The small bending stiffness and the nonlinear magnet forces used to deploy the flap allow the final wind tunnel model to have the same impulsive opening behavior described in [14]. This circumstance already prevents a linear control of the flap angle. Since the flap operation is digital, there is no need to have a linear control of the position of the moving magnets. This makes simple electromechanical solenoids located on both sides of the model an adequate option.
Numerical simulations of the magnetic field between the neodymium magnets in the flap and underneath the GFRP-shell have been used to estimate the repellent and attracting forces for the flap deployment and at the same time the forces that are needed to move a single magnet underneath its counterpart in the flap. Figure 8 shows these forces for a single pair of neodymium magnets. The back-flow flap of the

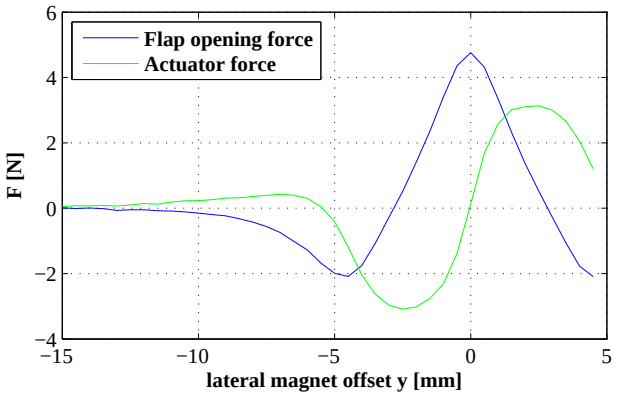

Figure 8: Actuation forces for a single pair of magnets.

wind tunnel model is deployed by 24 pairs of magnets distributed over the span of the model. According to the numerical prediction a force of approx. 75 N is needed to move all magnets in the worst case of a blocked flap that does not deploy.
To comply with the minimum of available mounting space the sliding magnets were integrated into a lightweight fiber composite push rod with a thickness of only 2.2 mm. To ensure a simultaneous motion of all magnet pairs the spacing between the magnets was adjusted to the actual spanwise location of the magnets in the flap after the manufacturing process. as the push rod exits the model in the region of the root attachment (see Figure 9), two electromechanical solenoids were used on both sides of the model. Each electromechanical solenoid is able to generate a pulling force of approximately 40 N when operated in a 25 % duty cycle. Switching to a 10 % duty cycle an increase in the voltage and current to reach forces of up to 55 N per electromechanical solenoid is possible. This leaves enough margin to compensate inertia forces or friction.
The electromechanical solenoids are controlled by a micro-controller that analyzes a sinusoidal signal that represents the pitching angle of the model to allow

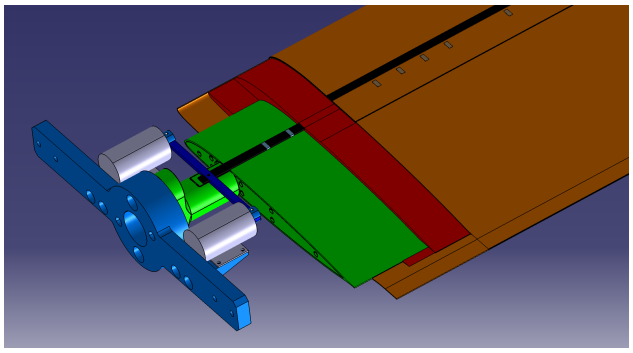

Figure 9: Retrofit-concept (green: original model, orange: GFRP-shell, red: resin, blue: model attachment, gray: electromechanical solenoids, , black: push rod).

the deployment of the flap synchronized to the model motion. The phase angle for the opening of the flap can be set by a potentiometer to tune the timing of the opening to the dynamic stall condition of each measurement point.

3.4. Instrumentation

The main purpose of the investigated back-flow flap is the reduction of the peak in pitching moment when the airfoil dynamically enters stall conditions. Therefore it is necessary to determine the forces and moments acting on the model. One possibility to determine the lift and the pitching moment during dynamic stall is the installation of pressure sensors that are distributed over the chord length of the airfoil on the upper and lower surface of the model. Integrating those pressures over the airfoil surface delivers lift, drag and pitching moment at each time step. The movable flap exhibits a challenge for this method as the orientation of the flap surface has to be regarded during the integration. Further on the pressures at the upper and lower surface of the flap have to be known.

To tackle these challenges the model was equipped with a variety of sensors. A combination of Hall effect sensors and magnets integrated into the flap are used to measure the opening angle of the flap. When the flap opens the integrated magnet moves and the sensor signal changes. A calibration curve is acquired to relate the measured voltage of the hall sensor to an opening angle of the flap.

To enable a measurement of the pressures on the upper and lower surface of the flap, five pressure tubes were integrated into the flap and connected to pressure transducers that are integrated in the rigid part of the glove.

In addition to this instrumentation the pressure sensors from the underlying model are fed through the glove. Small O-rings were used to seal between the glove and the model around each pressure measuring hole. The instrumentation is completed by a set of sensors that allow the measurement of pressures near the leading edge of the glove.

4. MANUFACTURING CONCEPT

The glove is designed to have an upper and a lower shell, that are split along the chord line of the glove profile. The manufacturing of the demonstrator can be divided into several steps and is shown for the upper part of the glove. The main process steps are depicted in Figure 10. First, the outer shell of the wind

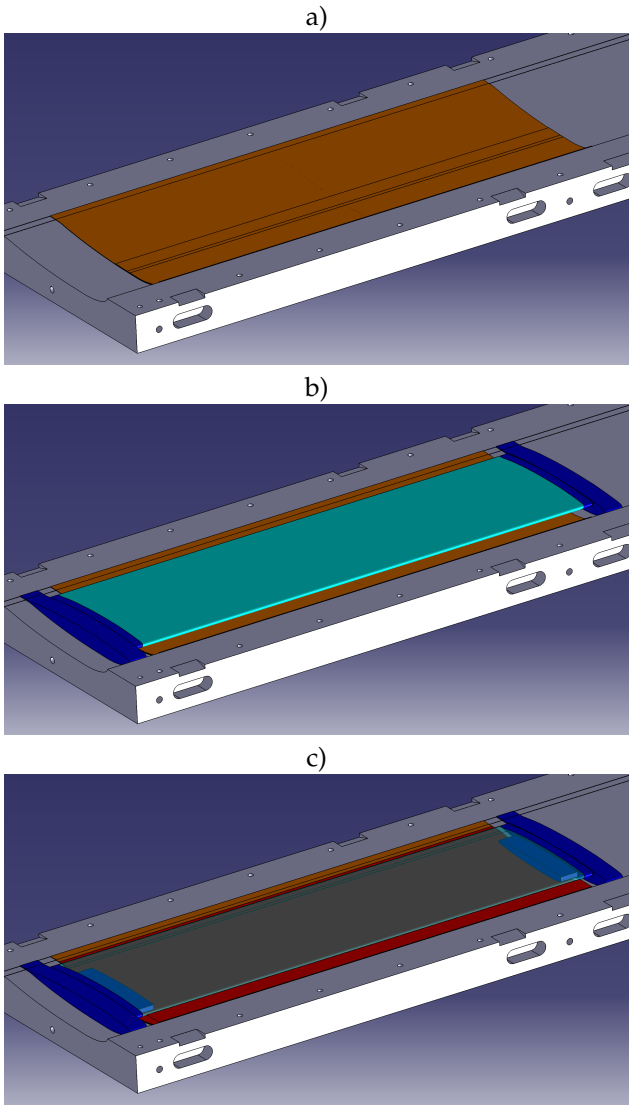

Figure 10: Major manufacturing steps.

tunnel model is manufactured (Figure 10 a)). This part is mainly made of GFRP and has different integrated functionalities. To allow a surface smooth integration of the flap an elastomeric solid state hinge is used to connect the back-flow flap with the GFRP

shell that forms the outer surface of the model. Further, the fiber reinforced elastomers for the limitation of the opening angle are also integrated. Using materials with compatible curing and vulcanization cycles as well as separating foils it was possible to manufacture all GFRP-parts and the hinge in one shot.
The fiber composite shell of the glove also comprises parts of the actuation mechanism and the instrumentation. To allow the integration of permanent magnets (actuation and flap angle measurement) a curing cycle has to be chosen that does not exceed the Curie temperature of the magnetic material.
To prevent the liquid resin from entering the pressure tubes integrated into the flap, both ends were sealed. The end at the trailing edge of the flap was permanently closed with epoxy resin. The other end of the tube is located close to the hinge point of the solid state hinge and is aligned in parallel to the hinge line in order to minimize the motion of the point where the pressure tube is later connected to the transducer via a flexible hose. During manufacturing this end is sealed using a small block of silicon. After the curing cycle the silicon can be removed. The resulting cavity can be used to contain the flexible hose that connects the pressure transducer. Finally a small hole with a diameter of 0.3 mm was drilled through the flap surface into the tube to allow the pressure measurement at this point.
After curing the composite part of the glove, the cavity between the outer shell and the underlying wind tunnel model has to be filled. For this purpose a dummy with the same geometry as the later wind tunnel model (green in Figure 9) was manufactured with a cold setting GFRP laminate. This dummy is depicted in light blue in Figure 10 b). Two positioning guides (dark blue, one on each side) were used to define the relative position between the outer surface of the glove and the dummy of the wind tunnel model. After sealing between the dummy and the GFRP-shell at both spanwise ends, the cavity was filled with a very slow cold setting casting resin (red in Figure 10 c)). This principle is repeated for the lower part of the glove. Afterwards the parting plane of the upper and lower part of the model were milled and the holes for the feed through of the pressure holes to the outer surface of the glove were drilled. The poured resin block can be used to integrate the additional pressure transducers and the Hall effect sensors as well as all kinds of wiring. Finally, the notch that guides the push rod of the actuation mechanism is also milled into the resin.
One of the major intentions for coming up with the retrofit of an existing wind tunnel model was to preserve the functionality of the original model for later investigations. Consequently a solution had to be found to temporarily mount the glove on top of the model. For this purpose different adhesive tapes were experimentally characterized with respect to their ductile behavior. Finally a transparent double-sided self-adhesive tape consisting of a PET backing and a tackyfied acrylic adhesive (tesa® 4965) were selected to mount the glove to the model. The transitions between original wind tunnel model and back-flow flap glove on the lower side of the model were sealed with silicone.

Figure 11: Model in the open test section of the wind tunnel.

5. WIND TUNNEL TESTING

The wind tunnel model with the installed back-flow flap glove is depicted in Figure 11. The model was mounted horizontally in the 1 m wide and 0.75 m high open test section of the 1MG low speed wind tunnel in Göttingen. The airfoil is supported on both sides by bearings, and driven from one side using an electromotor. In the upper picture the actuation mechanism is holding the flap open. As described in section 3.4. the forces on the airfoil were measured using the integration of pressures from the airfoil midline. Additionally a piezoelectric force balance was used as a check of the forces. The pressure integration on the airfoil includes sensors above and below the flap. The flap angle is measured by the Hall-effect sensors and is factored into the force computation. The pressure under the flap is taken to be a constant from the single pressure sensor present there, as an approximately constant pressure was indicated by the CFD computations of [4]. The pressure sensors are differential Kulites, type XCQ-093, which are referenced to the static pressure outside the free jet. To

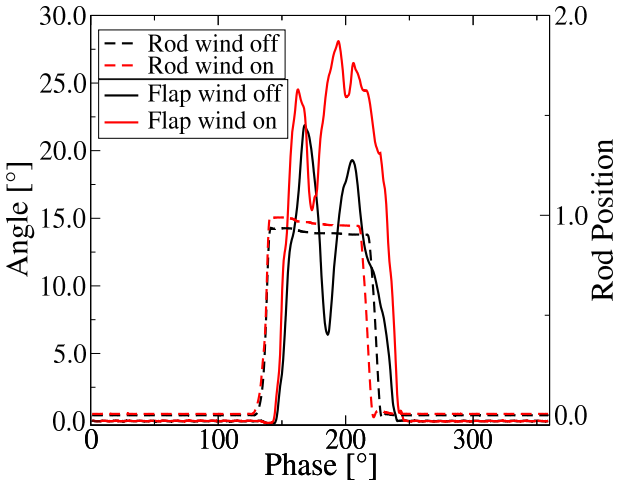

Figure 12: Influence of wind on the flap motion (α=22±8°, f=2.5 Hz, black lines: 0 m/s, red lines: 50 m/s).

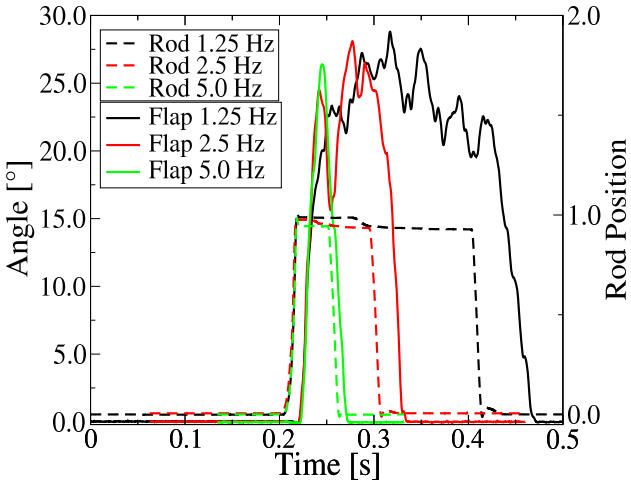

Figure 13: Influence of frequency on the flap motion (α=22±8°, wind speed 50 m/s).

compute C_P, the pressure sensors are referenced to the dynamic pressure as measured by a Prandtl-probe mounted at the nozzle exit. The Prandtl probe is also used to compute the flow speed. The position of the push rod is quantified in the same way as the flap angle using another combination of Hall-effect sensor and magnet. Therefore the permanent magnet was attached to one end of the push rod while the Hall sensor was glued to the model root attachment. The angle of attack of the airfoil is measured using two laser rangefinders, which measure to the flat plate at the bottom of the force balance. The average of the calibrated angles of attack is used.

The flap and its actuation mechanism have already been tested in the laboratory without any aerodynamic forces. Adding wind can have a strong effect on the opening behavior of the flap since the magnetic actuation mechanism exhibits no mechanical connection between push rod and flap. Further on, the whole concept relies on the utilization of the forces generated by the back-flow to fully deploy the flap. Figure 12 shows the opening of the flap with and without wind. Looking on the flap motion without wind it can be seen that the dynamic opening causes a strong oscillation of the flap angle. This is due to the characteristic of the magnetic forces. When the flap opens the repellent force between the two magnets decreases with the square of their mean distance. In the equilibrium state the moment generated by the magnetic forces equals the elastic moment that is needed to deform the solid state hinge. When the flap is dynamically opened the kinetic energy stored in the flap motion leads to an overshoot in flap angle and the flap starts oscillating around this equilibrium. Besides the motion of the flap the diagram also qualitatively shows the motion of the push rod. As expected there is no influence from the wind to the sliding motion of the magnets when the flap opens. Even though the push rod motion indicates a comparable excitation of the flap, operating the flap in the flow of the wind tunnel significantly alters the flap motion (red lines in Figure 12). It can be seen that the flap opening speed is slightly increased by the aerodynamic forces. The oscillation of the flap angle is still visible but less pronounced. After the first cycle of the flap angle oscillation the back-flow developed during dynamic stall fully opens the flap. As the angle restriction has some flexibility (also see Figure 5) the maximum opening angle is rather a soft stop than a hard limit. Comparing the phase shift between the movement of the push rod in "close" position and the reaction of the flap, reveals that the authority of the actuation mechanism to close the flap is limited. This holds especially for large opening angles where the magnetic forces are small. Aerodynamic forces can further delay the closing motion. Principally the flap closes when the flow reattaches and the magnets keep the flap closed.

To investigate the effectiveness of the flap for a large set of operating conditions, the frequency of the model pitching motion was one parameter to be varied. As the flap opening frequency has to match the model motion it has to be investigated how the frequency influences the flap motion. Figure 13 depicts the time histories of the flap angle for different actuation frequencies. In order to compare the opening behavior the curves are shifted so that the push rod motions (into the "open" position) are aligned for all three frequencies. Due to the digital snap-opening behavior of the flap (described in section 3.3.), the slope of the flap angle during opening is independent of the actuation frequency. For slow pitching motions (e.g. 1.25Hz, black line in Figure 13) the stall vortex has

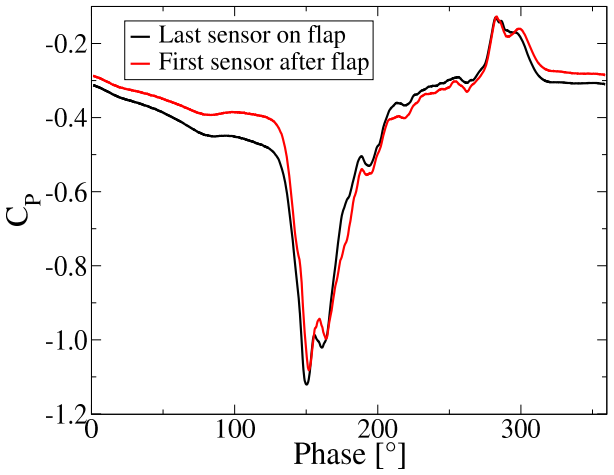

Figure 14: Validation of pressure sensor integration (α=22±8°, f=2.5 Hz, wind speed 50 m/s).

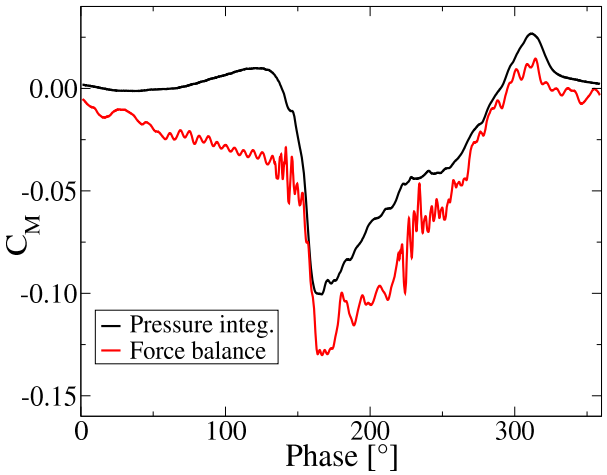

Figure 15: Moment coefficient measured with balance and integration of pressure sensor signals (α=22±8°, f=2.5 Hz, wind speed 50 m/s).

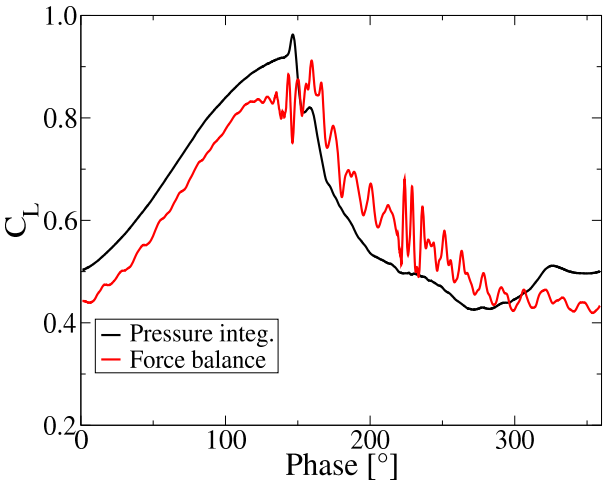

Figure 16: Lift coefficient measured with balance and integration of pressure sensor signals (α=22±8°, f=2.5 Hz, wind speed 50 m/s).

long time to form and the back-flow opens the flap for a long time. During this period the flap angle is oscillating between 20 ° and 28 °. With rising frequency the flap opening period becomes shorter and at 5 Hz it seems that the flap directly closes after the first oscillation cycle. The unsteady flap motion is therefore much less pronounced.

Two tests were performed to check the correctness of the pressure measurement on the flap surface. The first test was executed in the laboratory and addressed the deformation of the flexible hose that was used to connect the pressure tube in the flap to the transducer integrated into the glove. Therefore the measurement hole on the flap surface was closed with tape. It could be confirmed that the small deformation of the flexible hose does not generate a significant pressure signal. The second test was performed in the wind tunnel and clarified that the additional air cavity caused by the rather long pressure tube does not have a major effect on the dynamics of the sensor signal. For this purpose Figure 14 shows the comparison of the signals of a sensor near the trailing edge of the flap (longest pressure tube) and the transducer directly behind the flap. For this experiment the flap was kept closed. Hence there is no deformation of the flexible hose. A flow condition with dynamic stall was chosen for this comparison to have a clear peak in the pressure signals that allows evaluating the slope of the signal and potential phase shifts. From the figure it can be seen that both sensors show very comparable results and no significant delay or damping of the pressure signals is to be expected. The difference in the pressure signals is assumed to be only caused by the chordwise offset of the sensor position.

The motivation for emphasizing the importance of the pressure instrumentation becomes evident when the lift and moment computed from the pressures are compared to the force balance signal. The Figures 15 and 16 show a comparison of moment and lift coefficient determined via force balance and pressure integration. In both cases the signals from the force balance are polluted by strong interferences. Each time the flap is opened or closed the armatures of the electromechanical solenoids swiftly move into a hard stop. Therefore they are generating a strong shock force. The piezoelectric force transducers in the balance are very sensitive to this high frequency excitation. The generated oscillation of the opening and closing of the flap can be clearly recognized at a phase of 130° and 220°.

Another challenge in the post-processing of the force balance signal is the position of the model root attachment relative to the airfoil of the glove. While the original model is connected to the force balance close to the neutral point of the profile there is a sig-

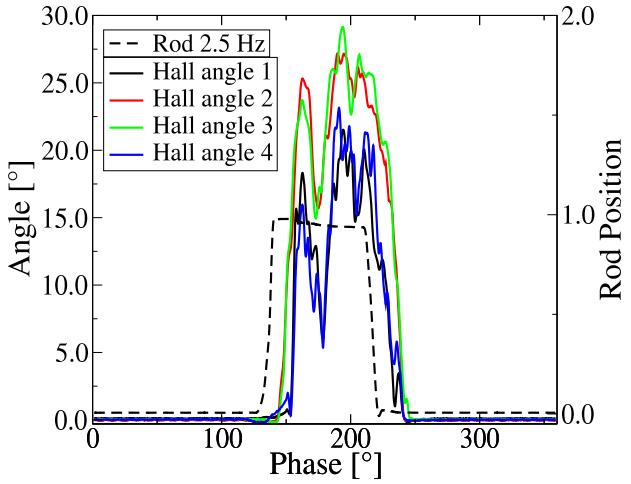

Figure 17: Flap opening angle for different span-wise locations (α=22±8°, f=2.5 Hz, wind speed 50 m/s).

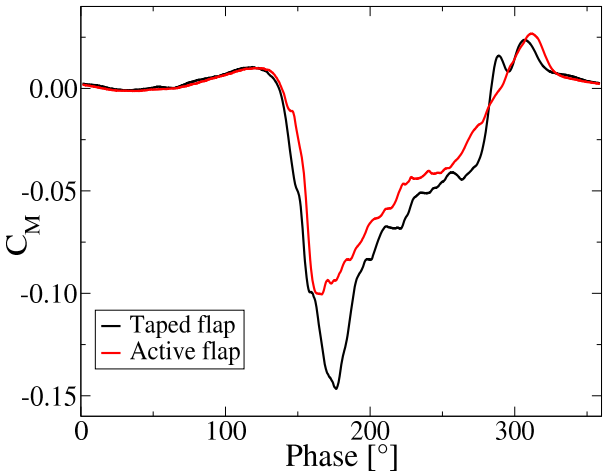

Figure 18: Example result for the influence of the back-flow flap on the pitching moment coefficient (α=22±8°, f=2.5 Hz, wind speed 50 m/s).

nificant chordwise offset between the attachment and the neutral point of the modified airfoil (also see position of original model within the glove in Figure 4). This offset requires a correction of the pitching moment as the lift is generating additional moments.

Since the model is tested in an open test section the force balance measurements are also influenced by edge effects at both spanwise ends of the model. These are the reason for the offset in lift visible in Figure 16.

As a consequence of those difficulties in the post processing of the force balance data the pressure sensor signal will be used to assess the aerodynamic effect of the back-flow flap.

The edge effects at the sides of the model also influence the flap opening. This becomes obvious when the flap angles from the 4 different spanwise positions are compared (see Figure 17). The vortexes rolling up at both sides of the model cause a delay in the flap opening. This can be directly seen in the phase shift of the flap angle from the sensors 1 and 4. The edge effect also prevents the full deployment of the flap at the side of the model. The Hall-effect sensors 2 and 3 are located closer to the airfoil midline. In this region the flap angle becomes significantly higher and the flap begins to open earlier compared to the model ends. The difference in flap angle is an indicator for the flexibility of a GFRP-flap with a thickness of 1 mm, a chord length of approx. 41 mm and a spanwise extension of 1 m. At the same time the similarity of the signals from Hall-effect sensors 1 and 4 as well as from sensors 2 and 3 give a good impression of the symmetry of the flow conditions on both ends of the model.

This paper is not intended to give a detailed insight in the behavior of the flap for a variety of flow conditions. Nevertheless one example result will be

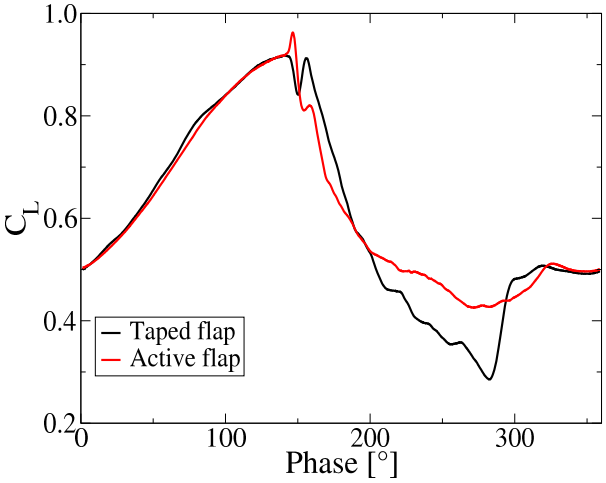

Figure 19: Example result for the influence of the back-flow flap on the lift coefficient (α=22±8°, f=2.5 Hz, wind speed 50 m/s).

presented to prove the effectiveness of the concept. Therefore the model with the flap was tested at a wind speed of 50 m/s. The airfoil was oscillating with an amplitude of 8° around a mean angle of 22° with a frequency of 2.5 Hz causing a pronounced dynamic stall. The related peak in pitching moment can be clearly recognized in Figure 18. In this deep stall condition the magnets were no longer able to keep the flap closed in each cycle. For this reason the flap was closed with tape for the reference measurement without flap actuation. During the experiment the timing for the opening of the flap was set manually to match the onset of the pitching moment peak. An online estimation of the pitching moment from a weighted sum of the pressure sensor signals enabled this procedure. For this flow condition the active back-flow

flap was able to reduce the pitching moment peak by about 32 %. At the same time lift and pitching moment remained almost unchanged until the onset of the dynamic stall.

6. CONCLUSIONS

The paper presents the way from the basic principle of an active back-flow flap to the successful testing in a wind tunnel. The size and position of the flap were determined using numerical simulations. For the structural design of the wind tunnel model a solution that requires a very small mounting space for structure, actuation system and instrumentation has been presented. Based on experimental investigations the interface design for the angle restraint that limits the flap opening angle has been selected. The concepts presented for the actuation and instrumentation were successfully integrated in the manufacturing process. Finally, first wind tunnel results were able to show that the predicted reduction in the pitching moment peak of approx. 30 % can be reached, validating also the results of the numerical simulation. The expected reduction of the mean lift by approx. 2.5 % could not be confirmed by the experimental data. The wind tunnel results even show a small increase in mean lift which is beneficial for the back-flow flap concept but clearly shows the deficits of either the numerical prediction or the wind tunnel setup.

References

[1] Gallot, J., Vingut, G., De Paul, M. V., Thibert, J. “Blade profile for rotary wing of an aircraft", United States Patent 4325675,(20.4.1982).

[2] Gardner, A.D., Richter, K., Rosemann, H., "Numerical investigation of air jets for dynamic stall control on the OA209 airfoil", CEAS Aeronautical Journal, Volume 1, Issue 1, Page 69-82, 2011. DOI 10.1007/s13272-011-0002-z

[3] Höfinger, Marc, “Rotorblatt mit integrierter passiver Oberflächenklappe" Deutsches Patent DE 10 2010 041 111 A1, 22.03.2012.

[4] Kaufmann,K., Gardner, A.D., Richter, K., “Numerical Investigations of a Back-Flow Flap for Dynamic Stall Control", New Results in Numerical and Experimental Fluid Mechanics IX, Notes on Numerical Fluid Mechanics and Multidisciplinary Design, Volume 124, 2014, pp 255-262. DOI: 10.1007/978-3-319-03158-3_26.

[5] LePape, A., Costes, M., Joubert, G., David, F., Deluc, J.-M., “Experimental Study of Dynamic Stall Control Using Deployable Leading-Edge Vortex Generators", AIAA Journal, Vol. 50, No. 10 (2012), pp. 2135-2145.

[6] Mai, H., Dietz, G., Geissler, W., Richter, K., Bosbach, J., Richard, H., de Groot, K., “Dynamic stall control by leading edge vortex generators", J. Am. Helicopter Soc. 53(1), pp26-36 (2008)

[7] Martin, P., Wilson, J., Berry, J., Wong, T., Moulton, M., McVeigh, M., “Passive Control of Compressible Dynamic Stall" AIAA Paper 2008-7506, 2008.

[8] Meyer, R.K.J., “Experimentelle Untersuchungen von Rückströmklappen auf Tragflügeln zur Beeinflussung von Strömungsablösungen. Dissertation Technische Universität Berlin, Mensch-und-Buch-Verlag, 2000.

[9] Mulleners, K., Raffel, M., “The onset of dynamic stall revisited", Experiments in Fluids, Vol. 52, (3), pp 779-793, 2012. DOI 10.1007/s00348-011-1118-y

[10] Richter, K., Le Pape, A., Knopp, T., Costes, M., Gleize, V., Gardner, A.D., “Improved Two-Dimensional Dynamic Stall Prediction with Structured and Hybrid Numerical Methods" Journal of the American Helicopter Society, Volume 56, Issue 4, 2011. doi:10.4050/JAHS.56.042007

[11] Weaver, D., McAlister, K.W., Tso, J., “Control of VR7 Dynamic stall by strong steady blowing", Journal of Aircraft, Vol. 41, No. 6, 2004.

[12] Gardner, A.D., Richter, K., Mai, H., Neuhaus, D., “Experimental Investigation of Air Jets for the Control of Compressible Dynamic Stall", Journal of the American Helicopter Society, Volume 58, Number 4, 2013. DOI: 10.4050/JAHS.58.042001.

[13] Opitz, S., Gardner, A.D., Kaufmann, K., “Aerodynamic and structural investigation of an active back-flow flap for dynamic stall control", CEAS Aeronautical Journal, Vol. 5, No. 3, 2014. pp. 279-291. DOI 10.1007/s13272-014-0106-3

[14] Opitz, S., Gardner, A.D., Kaufmann, K., “An active back-flow flap for a helicopter rotor blade", Advances in Aircraft and Spacecraft Science, Vol. 1, No. 1, 2014, pp. 69-91. DOI: 10.12989/aas.2014.1.1.069.

A.4. Paper: ICAST2015, 26th International Conference on Adaptive Structures and Technologies

ICAST2015: 26th International Conference on Adaptive Structures and Technologies
October 14-16th, 2015, Kobe, Japan

ICAST2015 #058

An active back-flow flap for dynamic stall control - from concept to wind tunnel

Steffen Opitz[1*], Anthony D. Gardner[2], Christoph B. Merz[2] and Christian C. Wolf[2]

[1] Department of Multifunctional Materials, Institute of Composite Structures and Adaptive Systems, DLR (German Aerospace Center), Braunschweig, Germany.
[2] Department of Helicopters, Institute of Aerodynamics and Flow Technology, DLR (German Aerospace Center), Göttingen, Germany.

Abstract

The paper describes the concept, design and realization of a wind tunnel model featuring an active back-flow flap for dynamic stall control. In order to investigate influence of a back-flow flap on the stall behavior of an airfoil with oscillating pitch angle, an existing wind tunnel model is retrofitted with a spoiler-type flap on the upper surface. The presented work starts with the basic idea, describes the aerodynamic and structural design and ends with the first results from the wind tunnel testing. Within the paper special emphasis is given to the magnetic actuation system of the flap. The flap deployment under wind tunnel conditions and the corresponding deformation of the flap are discussed in detail. Finally the influence of the timing of the flap actuation on the flap motion and the aerodynamic performance of the flap will be elucidated.

1. INTRODUCTION

Dynamic stall is a well-known effect for helicopter airfoils occurring when a pitching airfoil stalls, forming separated flow in a dynamic stall vortex. A lift peak and a negative spike in pitching moment form and then a rapid drop in lift appears as the stall vortex moves downstream. The torsional impulse from the pitching moment peak is often a load-limiting case for the pitch links, and high drag is experienced compared to attached flow. Dynamic stall can be controlled by using passive devices, including vortex generators and changes in the leading edge contour [6, 7], but these have disadvantages at high Mach number and are limited in their control of deep stall. In contrast, active devices include actively retracting vortex generators [5], which avoid shocks at high Mach number, or air jets [11, 12], which add energy to the flow, and thus improve the flow control under deep stall conditions.
The leading-edge stall associated with many helicopter airfoils including the OA209 [1] airfoil used for these investigations, is characterized by strong backward flow along the suction side of the airfoil [9]. To control dynamic stall of this type, the single dynamic stall vortex should be broken into several smaller vortexes and the passage of the vortexes should be delayed [2].

2. STALL CONTROL WITH A BACK-FLOW FLAP

As part of the DLR project STELAR an alternative method of influencing dynamic stall using an active back-flow flap is presently being investigated [4]. In the past back-flow flaps have been tested on gliders as a passive method of reducing stall [8], as freely-hinged spoiler-like flaps on the suction side of the airfoil near the trailing edge. When trailing edge stall occurs, the back-flow lifts the flap and the region of stall can be significantly delayed. Even though the effectiveness of back-flow flaps has been demonstrated in flight experiments with sailplanes, it still has to be investigated whether they are also suited to improve the dynamic stall behavior of helicopter rotor blades [3].

* Steffen.Opitz@dlr.de

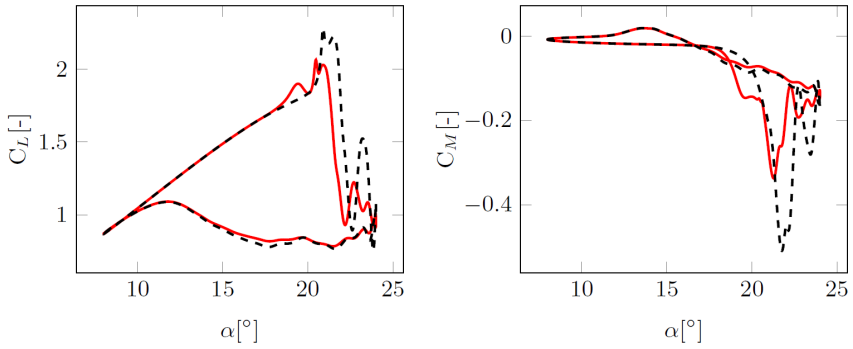

Figure 1. Comparison of lift (left) and pitching moment coefficient (right) for the OA209 airfoil at M=0.14, Re=920000, $\omega^* = 2\,\pi\,f\,c/v_\infty$=0.1, α=16±8°. The black lines are without flap actuation, and the red lines are with flap actuation (image from [4]).

Initial numerical investigations with an actively actuated flap showed promising results. The computation was performed in 2D using the unstructured DLR-TAU solver and the Spalart-Allmaras turbulence model using the settings of Richter et al. [10]. The flap was dynamically actuated to only be deployed during the stalled flow, by using the overset grid (chimera) method with automatic hole cutting. The back-flow flap breaks the main stall vortex into smaller structures, and this results in a reduction in the pitching moment peak of 34 % compared to the reference case without actuation, while maintaining the lift during the attached flow (see Figure 1).
To gather first experiences, simple wind tunnel experiments were performed with an oscillating 2D airfoil without instrumentation. Analyzing the results with passive flaps , it was noted that an existing airfoil could generally be retrofitted with a flow control flap. However, to have reproducible conditions during the wind tunnel experiment the back-flow flap approach requires an actuator to hold the flap closed when not needed (e.g. reference cases), and to accelerate the opening of the flap with a pulse of force to guarantee the immediate flap actuation. Further, an angle restriction is needed to limit the flap opening angle, so that the highly dynamic opening of the flap does not cause the flap to flip over, lying upside down upstream of the hinge line.

Summing up the results of the initial numerical investigations and the first wind tunnel experiment a list of requirements for the structure and the actuation mechanism was established. Based upon this list, a concept was developed and presented in detail in [13] and [14]. To prevent any steps or gaps the concept comprises a solid state hinge that connects the flap to a Glassfiber Reinforced Polymer (GFRP) shell that forms the outer model surface. Fiber reinforced elastomers that are highly bendable but which do not elongate significantly under tensile loading are intended to limit the flap opening angle. To provide the opening impulse for the flap the actuation concept uses flap integrated magnets that can be attracted or pushed away by a second set of magnets that moves underneath the GFRP shell. With this approach the flap can be held closed or swiftly opened.
Even though this concept could be shown to be generally feasible there were still a lot of open questions to be answered before the final wind tunnel testing of the back-flow flap. Major points were the detailed aerodynamic design (size and position of the flap), the detailed design of actuation mechanism and the instrumentation of the wind tunnel model. These issues will be addressed within this paper, presenting a detailed concept for the retrofit of a wind tunnel model. The paper ends with initial wind tunnel results from the testing of the active back-flow flap.

3. DESIGN OF WIND TUNNEL MODEL

3.1 Aerodynamic design

Computations using the method of Kaufman et al. [4] were performed to estimate the correct size and position of the flap. Therefore the flap size was varied in 3 steps from 5 % chord to 15 % chord. The position of the flap was altered in steps of 10 % chord between 10 % and 70 % of chord. The results of this study are depicted in Figure

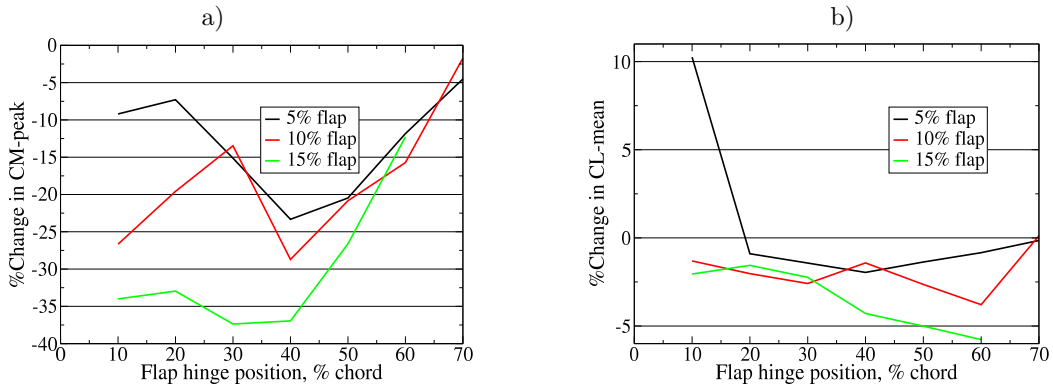

Figure 2. Numerical investigation of the flap size and position, compared to the reference case without a flap, a): Change in pitching moment coefficient peak (Dynamic stall load), b): Change in mean lift coefficient (Hysteresis).

2. These computations represent only a rough approximation of the real physics, since they could not model the body-on-body parts of the opening, and always had a gap between the flap and the airfoil. Further, the flap motion which was prescribed in the computations would certainly differ in reality.
Nevertheless some trends can be deduced. In most cases the reduction of the pitching moment peak becomes more effective with increasing flap length. At the same time a larger flap tends to cause a larger reduction of the mean lift coefficient. In contrast to the flaps used to improve the static stall behavior of gliders, positions near the trailing edge do not seem to be effective to reduce the pitching moment peak caused by dynamic stall. For all three investigated flap lengths the best position of the flap appears to be in the range between 30 % and 50 % of chord and tends to be closer to the leading edge for larger flaps. For the two larger flap configurations the mean lift tends to decrease when the flap is shifted towards the trailing edge.
Setting the flap to a length of 15 % chord with hinge position of 30 % chord had the greatest reduction in pitching moment, while not excessively reducing lift. The demonstrator for the basic concept of the solid state hinge and the magnetic actuation concept (see [13]) had an effective flap length of approx. 35 mm which corresponds to approx. 9.5 % chord of the later wind tunnel model. Laboratory tests have shown that in this configuration the actuation mechanism is able to deploy the flap to 30 ° in approx. 12.5 ms. This opening speed was sufficient to match the prescribed motion that was used in the numerical investigation when the airfoil oscillates with a frequency of 6 Hz. As the inertia of the flap rises with increasing flap size and consequently reduces the deployment speed, it was decided to realize a flap that extends over 12.5 % of the chord instead of the 15 % that gave the best results in the numerical prediction. Following the best simulated configuration the hinge line of the solid state hinge was placed at 30 % chord. Further on, the decision was made to limit the flap opening angle to a maximum of 30 °, to avoid over-opening during the back-flow of the fully separated flow. On the basis of the computations a reduction of the pitching moment peak by 30 % and a loss for $C_{L_{mean}}$ of 2.5 % is expected for this setting.

3.2 Structural design

During the first wind tunnel experiment with passive flaps it was posited that it is possible to equip an existing wind tunnel model with a kind of back-flow flap glove. Such a retrofit solution has multiple advantages. If an adequate concept is found the structure and the instrumentation of an existing model can be used to save costs and to reduce the development time for each tested configuration. Additionally the potential to retrofit existing rotor blades with a back-flow flap can be demonstrated to a certain extent. The first challenge related to a retrofit solution is to find a good compromise between available installation space and size of the model. Increasing the chord length leads to a larger blockage of the wind tunnel and also to a larger flap that might be difficult to deploy in a short time due to its inertia. For this reason the developed glove should be as short and as thin as possible. To maximize the mounting space available at the upper surface where the flap is installed, it was decided to partially use the lower side of the underlying model. The existing wind tunnel model that is intended to be equipped with the back-flow flap has a chord length of 300 mm. Already knowing the chordwise position and the size of the flap

within the retrofit-glove from the aerodynamic design, a small optimization routine was used to place the original airfoil in the enlarged contour of the model with the back-flow flap. This placement was done in a way that a maximum of mounting space is available at the position of the actuation mechanism. The optimization was repeated for increasing chord length of the glove until the distance between new and old airfoil guaranteed a thickness of 5 mm at the position of the flap (see Figure 3). This requirement for a minimum thickness is driven by the size of

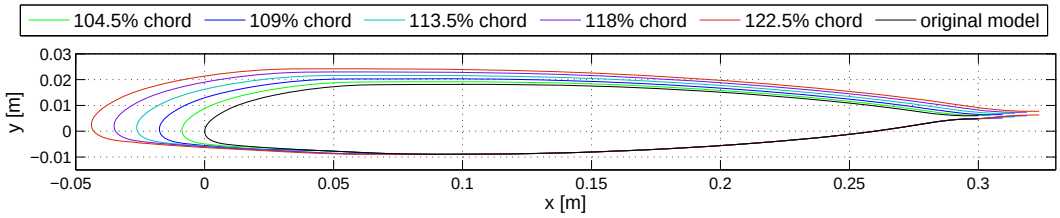

Figure 3. Positioning of the original airfoil of the wind tunnel model within the glove of the back-flow flap for different chord lengths of the modified model.

the neodymium magnets that will be used to actuate the flap. The magnets installed in the flap and the magnets sliding underneath the GFRP-shell have a thickness of 2 mm each. Consequently a minimum of 4 mm thickness is already needed without any structure that incorporates the magnets or friction layers that enable the sliding motion and protect the underlying wind tunnel model. Finally the described optimization procedure resulted in a scale of 1.225 for the glove which is equivalent to a chord length of 367.5 mm (red line in Figure 3).

3.3 Actuation

The left part of Figure 4 shows the general operation principle for the actuation mechanism of an active back-flow flap presented in [13] and [14]. The mechanism consists of two magnets. In previous publications it was

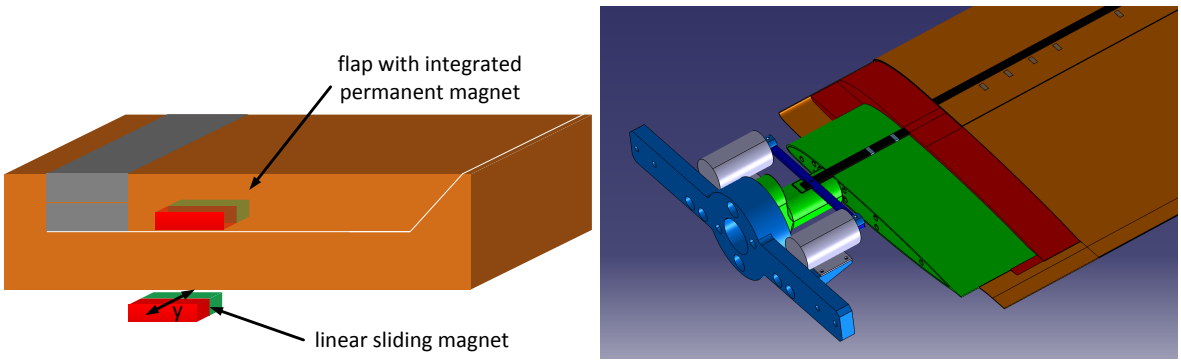

Figure 4. left: Actuation principle (image from [13]) right: Retrofit-concept (green: original model, orange: GFRP-shell, red: resin, blue: model attachment, gray: electromechanical solenoids, , black: push rod).

demonstrated how a magnet could be integrated into the GFRP-flap. The second, moving magnet and the adjacent actuation mechanism that generates the linear motion were not in the focus of interest so far. In [14] it is shown that the magnetic actuation system can lead to a snap opening of the flap when the bending stiffness of the solid state hinge is small. As the actuation concept allows to keep the flap closed and to deploy it, the bending stiffness of the hinge is preferred to be as small as possible, while still allowing a robust operation of the flap. This enables large opening angles since the restoring moment that has to be overcome by the magnetic forces stays small. The small bending stiffness and the nonlinear magnet forces used to deploy the flap allow the final wind tunnel model to have the same impulsive opening behavior described in [14]. This circumstance already prevents a linear control of the flap angle. Since the flap operation is digital, there is no need to have a linear control of the position of the moving magnets. This makes simple electromechanical solenoids located on both sides of the model an adequate

option (see Figure 4, right). To comply with the minimum of available mounting space the sliding magnets were integrated into a lightweight fiber composite push rod with a thickness of only 2.2 mm. To ensure a simultaneous motion of all magnet pairs the spacing between the magnets was adjusted to the actual spanwise location of the magnets in the flap after the manufacturing process. As the push rod exits the model in the region of the root attachment (see Figure 4, right), two electromechanical solenoids were used on both sides of the model.
The back-flow flap of the wind tunnel model is deployed by 24 pairs of magnets distributed over the span of the model. Numerical simulations of the magnetic field between the neodymium magnets in the flap and underneath the GFRP-shell have been used to estimate the repellent and attracting forces for the flap deployment (dashed black line in Figure 5) and at the same time the forces that are needed to move the magnets underneath their counterparts in the flap (solid black line in Figure 5). To switch between attraction and rejection of the flap magnets the push rod

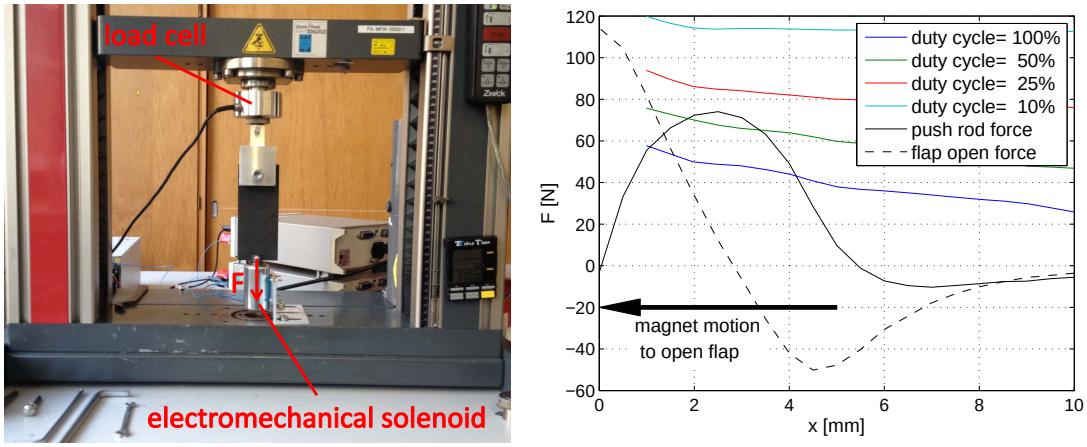

Figure 5. Characterization of electromechanical solenoids (left: test setup, right: maximum solenoid forces for different duty cycles).

has to be moved by approx. 5mm (arrow in Figure 5). According to the numerical prediction a maximum force of approx. 75 N is needed for this movement in the worst case of a blocked flap that does not deploy. To assure a reliable deployment of the flap the force generated by the electromechanical solenoids has to be larger than the push rod force over the whole duration of the push rod motion. Especially for large operating displacements the force of electromagnetic actuators tends to decrease. An adequate geometry of the solenoids armature is needed to overcome this issue. Further on the selection of suited electromechanical solenoids is a trade off between performance and weight. Designing the solenoids to be able to generate a continuous force of 75 N would results in a bulky and heavy actuation system. As these actuators are mounted on an oscillating wind tunnel model the additional mass constitutes an undesirable loading for the motor that drives the oscillation of the model. This additional load can cause restrictions in the maximum pitching frequency or amplitude as well as damages to the model, the drive train or the balance. Form the load characteristic it can be seen that after overcoming the maximum force the push rod force drops to zero and a smaller solenoid would be sufficient to hold the magnets in this position. For this reason it was decided to use smaller and lighter solenoids with a lower continuous force but to operate them at higher power in an intermittent duty. The diagram on the right side of Figure 5 shows the result of the characterization of the forces that can be generated by the electromechanical solenoid for different duty cycles over push rod position. Operating the solenoids at a 25 % duty cycle allows overcoming the push rod force to open the flap. Switching to a 10 % duty cycle an increase in the voltage and current to reach forces of up to 110 N is possible. This leaves enough margin to compensate inertia forces or friction.
The electromechanical solenoids are controlled by a micro-controller that analyzes a sinusoidal signal that represents the pitching angle of the model to allow the deployment of the flap synchronized to the model motion. The phase angle for the opening of the flap can be set by a potentiometer to tune the timing of the opening to the dynamic stall condition of each measurement point.

Figure 6. Model in the open test section of the wind tunnel.

4. WIND TUNNEL TESTING

The wind tunnel model with the installed back-flow flap glove is depicted in Figure 6. The model was mounted horizontally in the 1 m wide and 0.75 m high open test section of the 1MG low speed wind tunnel in Göttingen. The airfoil is supported on both sides by bearings, and driven from one side using an electromotor. In the left picture the actuation mechanism is holding the flap open. The forces on the airfoil were measured using the integration of pressures from the airfoil midline. Additionally a piezoelectric force balance was used as a check of the forces. The pressure integration on the airfoil includes sensors above and below the flap. The flap angle is measured by the Hall-effect sensors and is factored into the force computation. The pressure under the flap is taken to be a constant from the single pressure sensor present there, as an approximately constant pressure was indicated by the CFD computations of [4]. The pressure sensors are differential Kulites, type XCQ-093, which are referenced to the static pressure outside the free jet. To compute C_P, the pressure sensors are referenced to the dynamic pressure as measured by a Prandtl-probe mounted at the nozzle exit. The Prandtl probe is also used to compute the flow speed. The position of the push rod is quantified in the same way as the flap angle using another combination of Hall-effect sensor and magnet. Therefore the permanent magnet was attached to one end of the push rod while the Hall sensor was glued to the model root attachment. The angle of attack of the airfoil is measured using two laser rangefinders, which measure to the flat plate at the bottom of the force balance. The average of the calibrated angles of attack is used. For each measurement point all data was recorded for 40 s with a sampling frequency of 20kHz. The results presented in this paper are averaged over the cycles performed within the measurement period. The flap and its actuation mechanism have already been tested in the laboratory without any aerodynamic forces. Adding wind can have a strong effect on the opening behavior of the flap since the magnetic actuation mechanism exhibits no mechanical connection between push rod and flap. Further on, the whole concept relies on the utilization of the forces generated by the back-flow to fully deploy the flap. Figure 7 shows the flap opening angle measured with a hall sensor located near the mid plane of the model with and without wind (upper diagram) as well as the corresponding motions of the push rod (lower diagram). The shaded area underlaid to each curve depicts the standard deviation as a measure for the cycle to cycle differences. While these deviations are practically invisible for the push rod motion and the flap motion without wind, the amount of arbitrary motion caused by the wind becomes obvious. Looking on the flap motion without wind it can be seen that the dynamic opening causes a strong oscillation of the flap angle. This is due to the characteristic of the magnetic forces. When the flap opens the repellent force between the two magnets decreases with the square of their mean distance. In the equilibrium state the moment generated by the magnetic forces equals the elastic moment that is needed to deform the solid state hinge. When the flap is dynamically opened the kinetic energy stored in the flap motion leads to an overshoot in flap angle and the flap starts oscillating around this equilibrium.
As expected there is no influence from the wind on the push rod motion when the flap opens. Even though the push rod motion indicates a comparable excitation of the flap, operating the flap in the flow of the wind tunnel significantly alters the flap motion (red lines in Figure 7). It can be seen that the flap opening speed is slightly increased by the aerodynamic forces. The oscillation of the flap angle is still visible but less pronounced. After the first maximum of the flap angle oscillation the back-flow developed during dynamic stall supports the deployment of the flap which leads to a significantly higher mean value of the flap opening angle. Comparing the phase shift between the movement of the push rod in the ”closed” position and the reaction of the flap, reveals that the author-

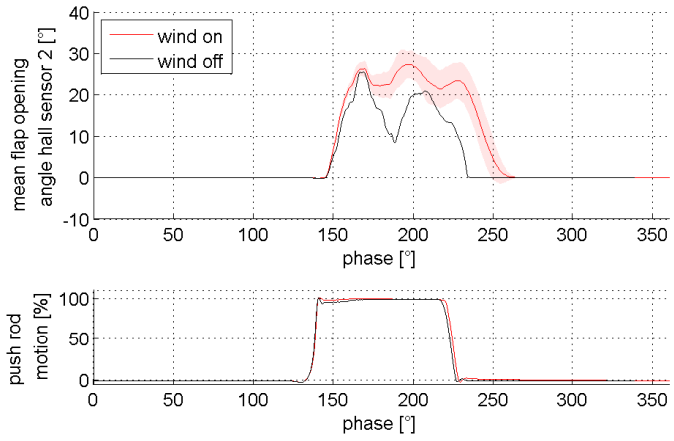

Figure 7. Influence of wind on the flap motion (α=22±8°, f=2.5 Hz, black lines: 0 m/s, red lines: 50 m/s).

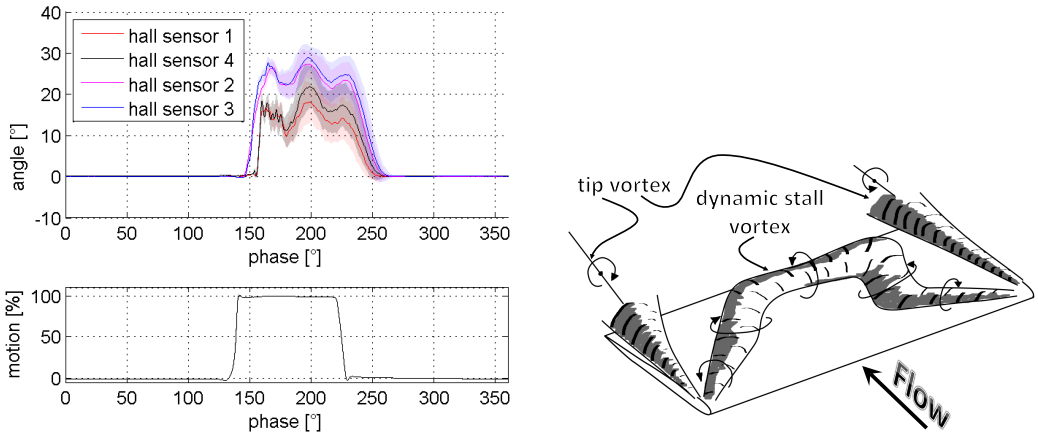

Figure 8. left: Flap opening angle for different span-wise locations (α=22±8°, f=2.5 Hz, wind speed 50 m/s); right: Sketch of vortices on an oscillating finite wing (Figure adapted from [15]).

ity of the actuation mechanism to close the flap is limited. This holds especially for large opening angles where the magnetic forces are small. Aerodynamic forces can further delay the closing motion. Principally the flap closes when the flow reattaches and the magnets keep the flap closed.
Since the model is tested in an open test section the edge effects at the sides of the model also influence the flap opening. This becomes obvious when the flap angles from the 4 different spanwise positions are compared (see Figure 8, left). The similarity of the signals from Hall-effect sensors 1 and 4 as well as from sensors 2 and 3 give a good impression of the symmetry of the flow conditions on both ends of the model. To ease the interpretation of the results a sketch of the typical structure of a dynamic stall vortex that develops on a finite rectangular oscillating wing is depicted in the right part of Figure 8 (adapted from [15]). The illustration shows the dynamic stall vortex with its characteristic "Omega"-shape in the middle of the model and two tip vortexes rolling up at both sides of the model. While the direction of rotation of the Omega vortex supports the flap deployment the tip vortexes push the edges of the flap onto the model surface and cause smaller mean flap opening angle towards both sides of the model. Further on the tip vortexes cause a delay in the flap opening close to the ends of the model. This can be directly seen in the phase shift of the flap angle from the sensors 1 and 4 compared to the sensors 2 and 3 that are located closer to the airfoil midline. The spanwise ends of the flap start to open when the mid region is already almost fully deployed. This difference in flap angle is an indicator for the flexibility of a GFRP-flap with a thickness of 1 mm, a chord length of approx. 41 mm and a spanwise extension of 1 m. A closer look at the signal sequences reveals that in the middle of the model the flap starts oscillating immediately after the snap

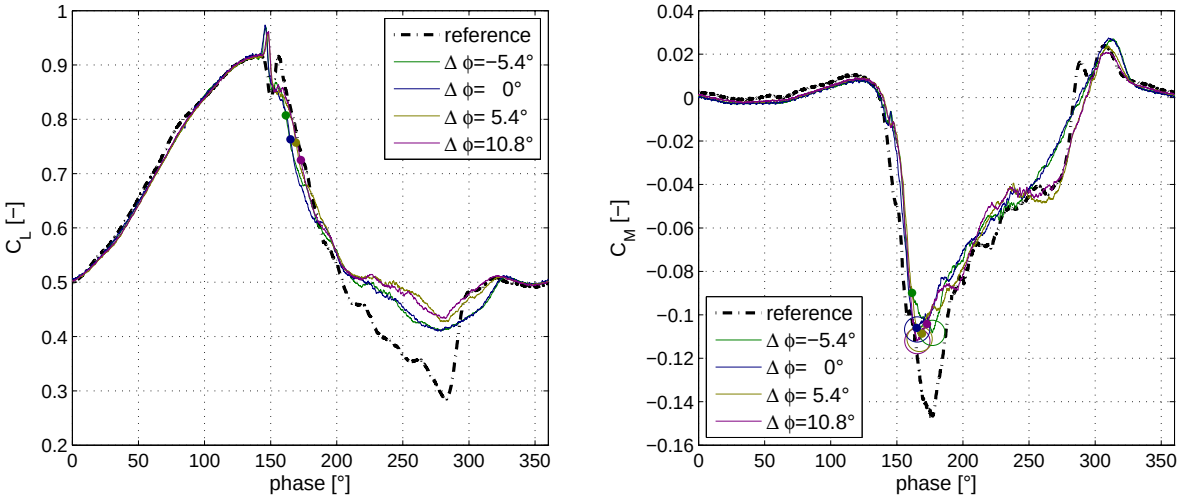

Figure 9. Lift and pitching moment in case of right flap deployment (α=22±8°, f=2.5 Hz, wind speed 50 m/s).

opening. In contrast to that the Hall effect sensors close to the ends of the model indicate that the flap performs higher frequency motions before entering in an equivalent oscillation state. These higher frequency motions are probably caused by the variety of vortexes that are shed from the edges of the model and the edges of the flap itself. The aerodynamic effect of the flap can be evaluated by either using the forces and moments captured by the piezo-electric balance that connects the model to the drive train of the motor or by analyzing the data measured with the integrated pressure sensors. The data from the piezoelectric balance comprises a mixture of the effects from the central stall vortex and the both edge vortexes. As these effects can not be separated in the post-processing the comparability to the initial two-dimensional CFD-computations is very limited. Further on the signal sequences of the forces and moments measured with the balance are polluted by impulsive shock forces. These are generated by the electromechanical solenoids that move into their hard stop when they alter the position of the push rod to trigger the flap opening or closing [16]. Consequently this paper presents the results gathered by pressure instrumentation.

This paper is not intended to give a detailed insight in the behavior of the flap for the whole variety of flow conditions covered by the test matrix of the wind tunnel experiment. As a first result the influence of the timing for the flap opening on the flap motion as well as on the lift and moment coefficient will be investigated. Therefore the model with the flap was tested at a wind speed of 50 m/s. The airfoil oscillated with an amplitude of 8° around a mean angle of 22° with a frequency of 2.5 Hz causing a pronounced dynamic stall. To maintain the readability of the diagrams the standard deviation is not plotted. Nevertheless these results represent the averaged data of approx. 100 cycles. The dotted lines in Figure 9 show the reference for the lift and pitching moment coefficient for a closed flap. The peak in pitching moment caused by the dynamic stall can be clearly recognized in the right diagram. An online estimation of the pitching moment from a weighted sum of the pressure sensor signals enabled to set the timing of the flap opening. In order to get a high reduction in pitching moment peak without disturbing the aerodynamics in the regime of attached flow the flap opening was manually tuned to match the onset of the pitching moment peak. Afterwards the timing was intentionally detuned to investigate the effect of an too early or too late actuation of the flap. The deployment was shifted in 8 steps of Δt= 6 ms in each direction within the oscillation cycle of the model. For a pitching frequency of 2.5 Hz a time step of Δt= 6 ms corresponds to a phase shift of $\Delta\phi$= 5.4 °. To ease the readability of the diagrams the results are presented in three groups. The first one shows the regime of optimal timing of the flap deployment. The second group presents test cases with an early opening of the flap while the third one summarizes the results of a delayed deployment. For each group separate diagrams will illustrate the flap motion and the resulting effect on lift and pitching moment.
Figure 9 shows that for the given measurement point the active back-flow flap can reduce the peak in pitching moment by approx. 28%. Lift and pitching moment remain almost unchanged until the onset of the dynamic stall. Even though the reduction in pitching moment peak is highest for the initial setting of the flap deployment timing the peak size remains in the same range when the timing of the deployment is altered by a small amount.

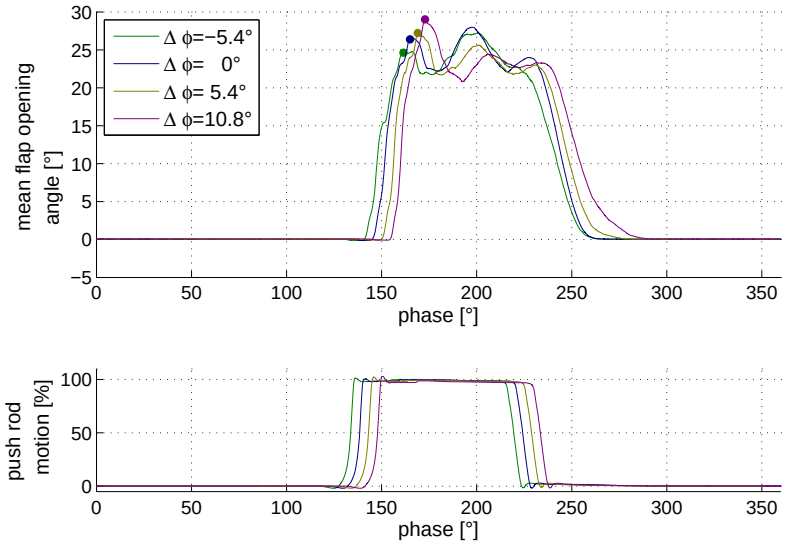

Figure 10. Flap angle in case of right flap deployment (α=22±8°, f=2.5 Hz, wind speed 50 m/s).

This means that to a certain extent the efficiency of the flap is robust and insensitive to any minor jitter in the timing. Comparing the lift with and without flap actuation it can be observed that the flap deployment leads to an increase of the lift in the region of stalled flow. This effect is quite interesting since it was expected to be much less pronounced (see Figure 1). Interpreting the increase in mean lift as another advantage of the back-flow flap it seems to be beneficial to delay the flap deployment by 5 ° to 10 °. Figure 10 depicts the averaged flap motion measured by the two hall sensors close to the airfoil midline. Having a look at the corresponding flap motions reveals that the phase region of increased lift clearly extends the opening period of the flap. The physical effect behind this observation has to be further investigated (e.g. by analyzing the PIV data). For all phase settings the flap angle swiftly increases. The point were the opening angle starts to decrease again is marked in Figure 10 as well as in Figure 9. It seems that the back-flow that supports the deployment is already stronger when the flap is opened at a later instant. The consequence is an increase of the first peak in the flap angle oscillation. For an early opening of the flap the rising edge of the flap opening angle develops a small bump. This effect is much clearer when the second group of measurement points with early opening is analyzed.
Figure 11 depicts the averaged flap opening angle measured by the Hall effect sensors close to the model midline in case of early opening. It can be seen that the stagnation point within the opening process moves to smaller flap angles. This means that the first oscillation starts before the back-flow fully deploys the flap. Until the first peak in the flap angle oscillation the flap always opens with approx. the same speed. In the region of small flap opening angles the driving forces are the repellent forces between the magnets. They determine the opening speed of the flap. The aerodynamic forces are of minor importance for this first part of the opening motion. After the point of first stagnation of the flap angle the opening speed of is significantly reduced. Beyond this point the aerodynamic forces are dominating the flap motion. As stall occurs at approx. 150 ° there is no back-flow that can rapidly deploy the flap. Only the pressure gradient on the upper airfoil surface supports the flap deployment. The pressure gradient from the trailing to the leading edge rises with the angle of attack. This is also supposed to be the reason for the slight increase in angle of the first peak in the flap opening when the flap is activated at a later instant in the oscillation period. The aerodynamic effect of the flap that opens too early is depicted in Figure 12. The point in the opening motion where the aerodynamic forces begin to dominate the flap motion can be recognized in the lift and in the pitching moment signal. In the lift signal the point coincides with the start of the formation of the first bump where the lift curves exceed the lift of the reference case. This bump is also visible in the CFD simulations with prescribed flap motion (see Figure 1) which indicates that the deployment in the simulation is also a little bit to early. Directly after the first oscillation in the flap opening angle the lift drops and stays below the lift of the reference case. At the beginning of the second half of the cycle lift signal is pretty comparable to the measurement points close to the optimal timing. Once again the lift in the region of detached flow is higher than for the reference

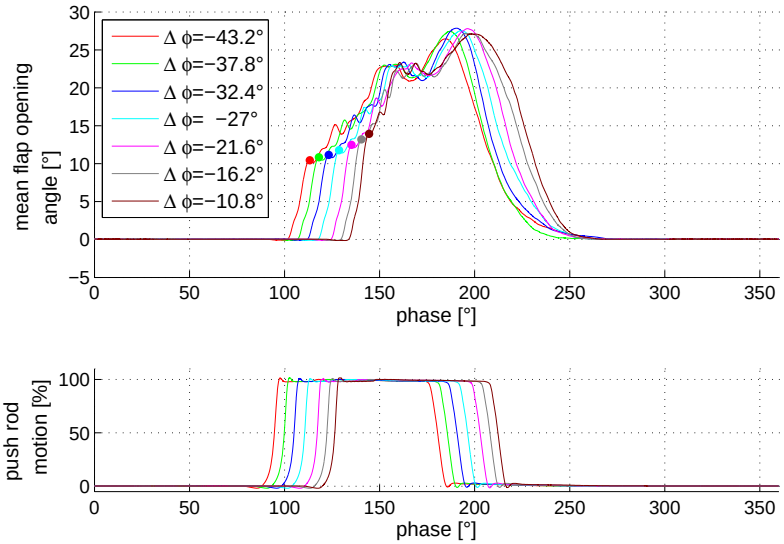

Figure 11. Flap angle in case of early flap deployment (α=22±8°, f=2.5 Hz, wind speed 50 m/s).

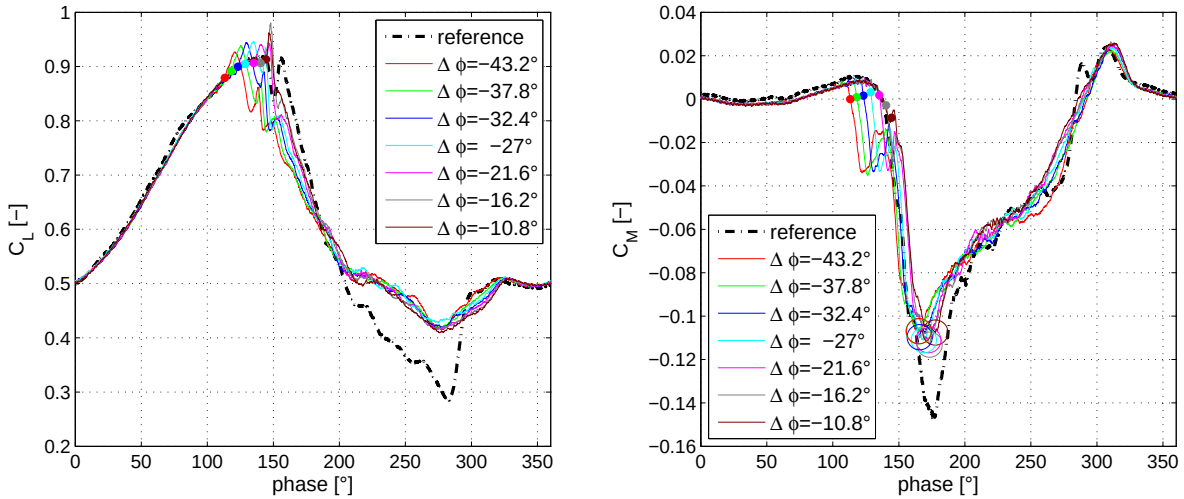

Figure 12. Lift and pitching moment in case of early flap deployment (α=22±8°, f=2.5 Hz, wind speed 50 m/s).

case without flap. Analyzing the pitching moment signal the points marked in the flap motion diagram can be correlated to the first drop in the pitching moment. Even though the early opening of the flap causes this first drop in pitching moment the effect of the back-flow flap in the second half of the cycle and therefore also on the main peak is comparable to the test cases close to the best timing of the flap. Consequently opening the flap to early is not crucial for the reduction of the pitching moment peak but will reduce the mean lift that can be generated over the oscillation cycle.

This picture changes when the flap is deployed too late (see Figure 13). Despite the rapid opening of the flap depicted in Figure 14 both the effect on the pitching moment and the effect on the lift become significantly smaller when the deployment is delayed too much. The activation of the flap gets simply too late to influence the pitching moment peak. Consequently the peak magnitude approaches to that of the reference condition without flap. As already noticed analyzing the test cases with optimal timing, the effect that increases the lift in the region between 200 ° and 300 ° seems to have its origin earlier in the oscillation cycle. This is confirmed by the fact that even

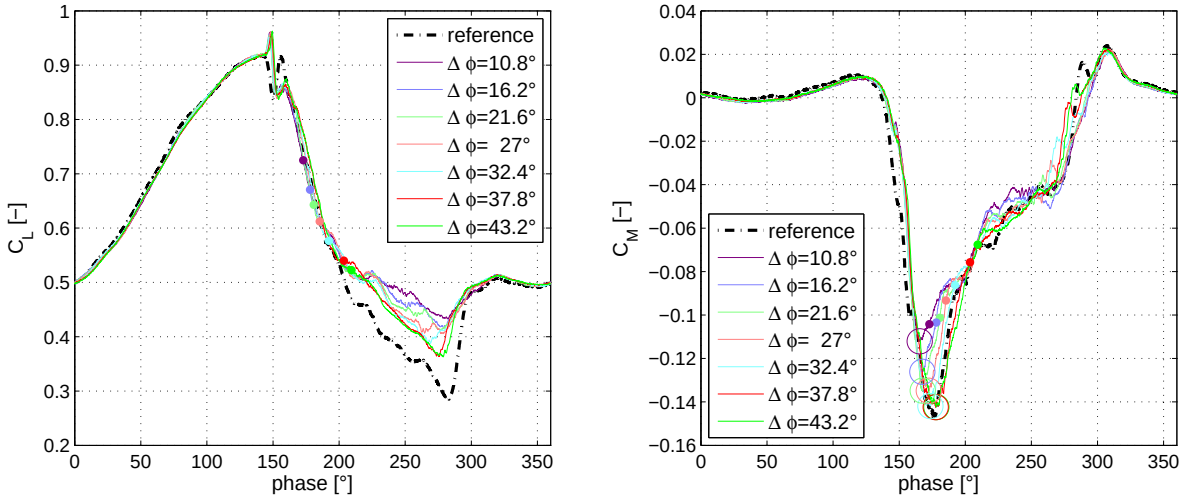

Figure 13. Lift and pitching moment in case of late flap deployment (α=22±8°, f=2.5 Hz, wind speed 50 m/s).

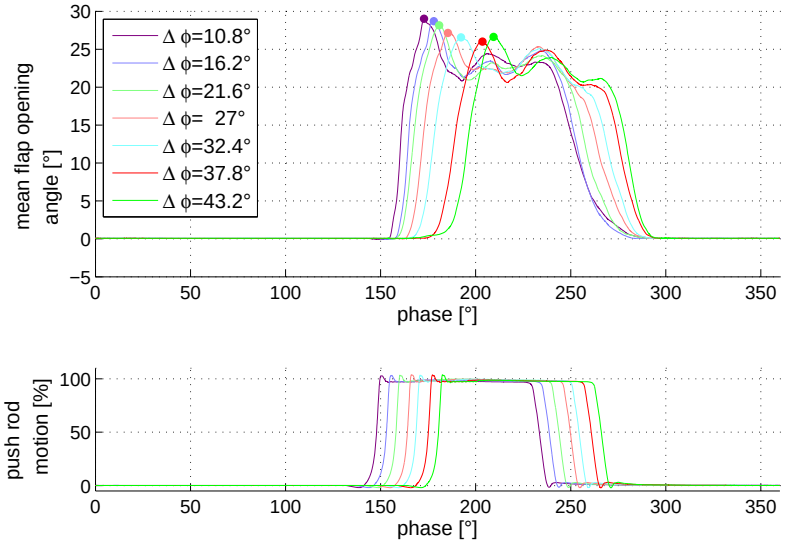

Figure 14. Flap angle in case of late flap deployment (α=22±8°, f=2.5 Hz, wind speed 50 m/s).

though the flap activation with the biggest delay keeps the flap opened for almost the complete phase region with increased lift the effect is much less pronounced than for smaller phase shifts of the opening impulse.

5. CONCLUSIONS

The paper presents the way from the basic principle of an active back-flow flap to the successful testing in a wind tunnel. The size and position of the flap were determined using numerical simulations. For the structural design of the wind tunnel model a solution that requires a very small mounting space for structure and actuation system has been presented. It was demonstrated that electromechanical solenoids can be operated in an intermittent mode to deliver the forces needed to drive the actuation mechanism while keeping the weight of the actuation system small. The effect of the wind on the flap motion was presented as well as the effects of the different vortexes

that are caused by the operation of the model in the open test section of the wind tunnel. Finally, first wind tunnel results were able to show that the predicted reduction in the pitching moment peak of approx. 30 % can be reached, validating also the results of the numerical simulation. The expected reduction of the mean lift by approx. 2.5 % could not be confirmed by the experimental data. The wind tunnel results show an increase in mean lift which is beneficial for the back-flow flap concept but clearly shows the deficits of either the numerical prediction or the wind tunnel setup and needs further investigation. The effect of the timing of the flap actuation was studied in detail. In can be stated that the procedure to determine the optimal phase setting for the flap deployment in the wind tunnel experiment worked reliably. The effects are robust to small changes in the timing. A too early flap actuation mainly causes a decrease in mean lift but has only small effect on the reduction in the pitching moment peak. Deploying the flap too late diminishes the beneficial effects on both lift and pitching moment.

REFERENCES

[1] Gallot, J., Vingut, G., De Paul, M. V., Thibert, J. "Blade profile for rotary wing of an aircraft", United States Patent 4325675,(20.4.1982).

[2] Gardner, A.D., Richter, K., Rosemann, H., "Numerical investigation of air jets for dynamic stall control on the OA209 airfoil", CEAS Aeronautical Journal, Volume 1, Issue 1, Page 69-82, 2011. DOI 10.1007/s13272-011-0002-z

[3] Höfinger, Marc, "Rotorblatt mit integrierter passiver Oberflächenklappe" Deutsches Patent DE 10 2010 041 111 A1, 22.03.2012.

[4] Kaufmann,K., Gardner, A.D., Richter, K., "Numerical Investigations of a Back-Flow Flap for Dynamic Stall Control", New Results in Numerical and Experimental Fluid Mechanics IX, Notes on Numerical Fluid Mechanics and Multidisciplinary Design, Volume 124, 2014, pp 255-262. DOI: 10.1007/978-3-319-03158-3_26.

[5] LePape, A., Costes, M., Joubert, G., David, F., Deluc, J.-M., "Experimental Study of Dynamic Stall Control Using Deployable Leading-Edge Vortex Generators", AIAA Journal, Vol. 50, No. 10 (2012), pp. 2135-2145.

[6] Mai, H., Dietz, G., Geissler, W., Richter, K., Bosbach, J., Richard, H., de Groot, K., "Dynamic stall control by leading edge vortex generators", Journal of the American Helicopter Society, Volume 53, Number 1, pp26-36 (2008)

[7] Martin, P., Wilson, J., Berry, J., Wong, T., Moulton, M., McVeigh, M., "Passive Control of Compressible Dynamic Stall" AIAA Paper 2008-7506, 2008.

[8] Meyer, R.K.J., "Experimentelle Untersuchungen von Rückströmklappen auf Tragflügeln zur Beeinflussung von Strömungsablösungen. Dissertation Technische Universität Berlin, Mensch-und-Buch-Verlag, 2000.

[9] Mulleners, K., Raffel, M., "The onset of dynamic stall revisited", Experiments in Fluids, Vol. 52, (3), pp 779-793, 2012. DOI 10.1007/s00348-011-1118-y

[10] Richter, K., Le Pape, A., Knopp, T., Costes, M., Gleize, V., Gardner, A.D., "Improved Two-Dimensional Dynamic Stall Prediction with Structured and Hybrid Numerical Methods", Journal of the American Helicopter Society, Volume 56, Issue 4, 2011. doi:10.4050/JAHS.56.042007

[11] Weaver, D., McAlister, K.W., Tso, J., "Control of VR7 Dynamic stall by strong steady blowing", Journal of Aircraft, Vol. 41, No. 6, 2004.

[12] Gardner, A.D., Richter, K., Mai, H., Neuhaus, D., "Experimental Investigation of Air Jets for the Control of Compressible Dynamic Stall", Journal of the American Helicopter Society, Volume 58, Number 4, 2013. DOI: 10.4050/JAHS.58.042001.

[13] Opitz, S., Gardner, A.D., Kaufmann, K., "Aerodynamic and structural investigation of an active back-flow flap for dynamic stall control", CEAS Aeronautical Journal, Vol. 5, No. 3, 2014. pp. 279-291. DOI 10.1007/s13272-014-0106-3

[14] Opitz, S., Gardner, A.D., Kaufmann, K., "An active back-flow flap for a helicopter rotor blade", Advances in Aircraft and Spacecraft Science, Vol. 1, No. 1, 2014, pp. 69-91. DOI: 10.12989/aas.2014.1.1.069.

[15] Coton, F.N., Galbraith, R.A.McD., "An examination of dynamic stall on an oscillating rectangular wing", AIAA Paper 2003-3675, 2003.

[16] Opitz, S., Gardner, A.D., Merz, C.B., Wolf C.C., "Structural demonstration of an active back-flow flap under wind tunnel conditions", 41st European Rotorcraft Forum, Munich, Germany, 1-4 Sept, 2015

A.5. Charakterisierung der Anbindung der Winkelbegrenzung

Prüfverfahren: Einfacher Zugversuch

Projektname	:	Stelar	Prüfmaschine	:	Zwick Z005
Auftraggeber	:	S. Opitz	Kraftaufnehmer	:	5kN
Kostenträger	:	1111111	Letzte Kalibrierung	:	09.10.2012
Probenlaufplan-Nr	:	2013-000	Wegaufnehmer	:	Traverse / cross head
Prüfer	:	C. Westphal	Probenhalter	:	10kN Schraub
Prüfdatum	:	10.04.2013	Prüfklima	:	23°C / 50% r. F.
Prüfnorm	:	o.N.	Konditionierung	:	23°C / 50% r. F.
Serienbezeichnung	:	Feststoffgelenk Steffen Opitz			

Prüfgeschwindigkeit	:	6 mm/min	Freie Länge	:	76,0 mm

Ergebnisse

Nr	t_{mess} mm	w mm	P_u N	Lfd.-Nr.
1	1,00	10	13,4	1-1
3	1,00	10	13,5	1-2
7	1,00	10	43,6	1-3
8	1,00	10	20,1	2-1
9	1,00	10	45,3	2-2
10	1,00	10	17,2	3-1
11	1,00	10	48,6	3-2

Statistik

Serie n = 7	t_{mess} mm	w mm	P_u N
$\bar{x}$	1,00	10	28,8
s	0,00	0,000	16,1
ν	0,00	0,00	56,04

Bemerkung:
Versuch 1-1: Versagen Anbindung 1
Versuch 1-2: Versuch Anbindung 2 versagen zu lassen - Versuch wurde gestoppt
Versuch 1-3: Anbindung 1 getrennt - EPDM im unteren Spannwerkzeug eingespannt - spontaner Rissfortschritt bei Übergang auf Anbindungsart 1
Versuch 2-1: Versagen Anbindung 1
Versuch 2-2: Anbindung 1 getrennt - EPDM im unteren Spannwerkzeug eingespannt - spontaner Rissfortschritt bei Übergang auf Anbindungsart 1
Versuch 3-1: Versagen Anbindung 1
Versuch 3-2: Anbindung 1 getrennt - EPDM im unteren Spannwerkzeug eingespannt - spontaner Rissfortschritt bei Übergang auf Anbindungsart 1

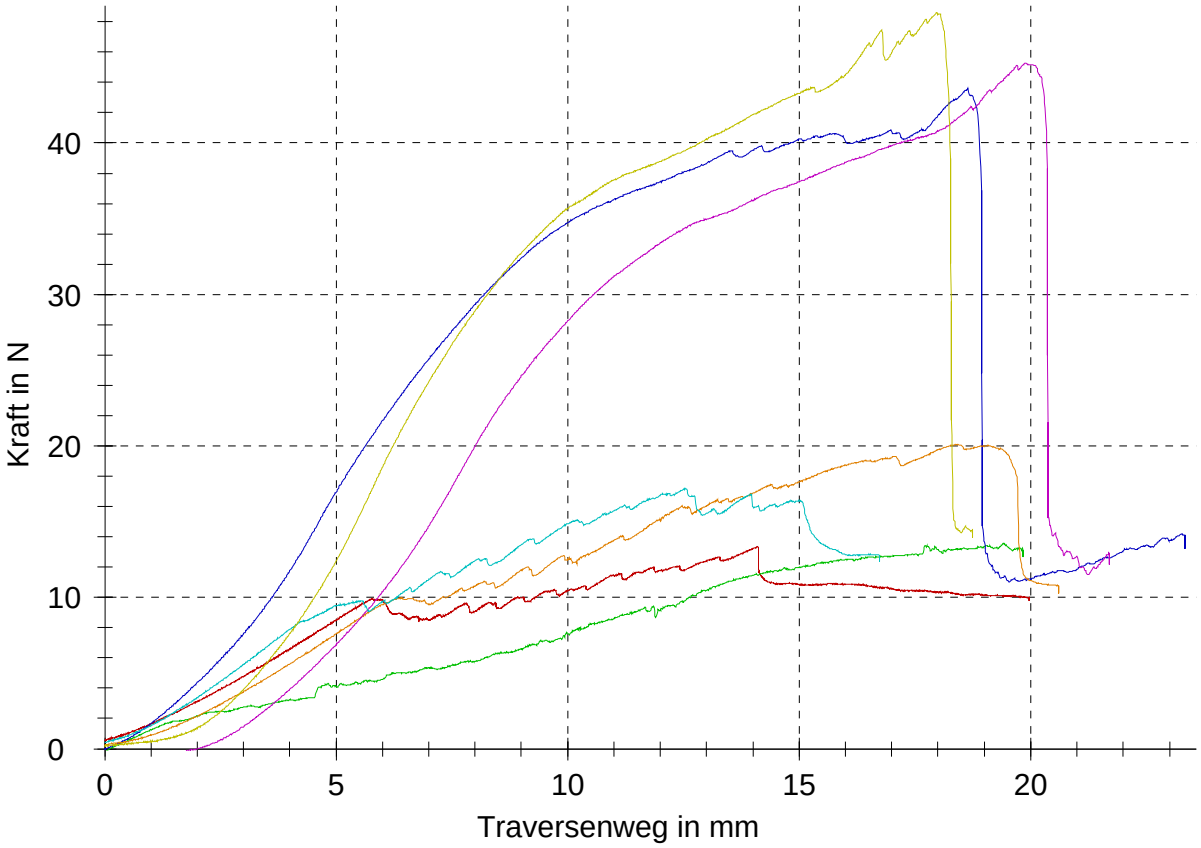
Kraft in N
0
10
20
30
40
0
5
10
15
20
Traversenweg in mm

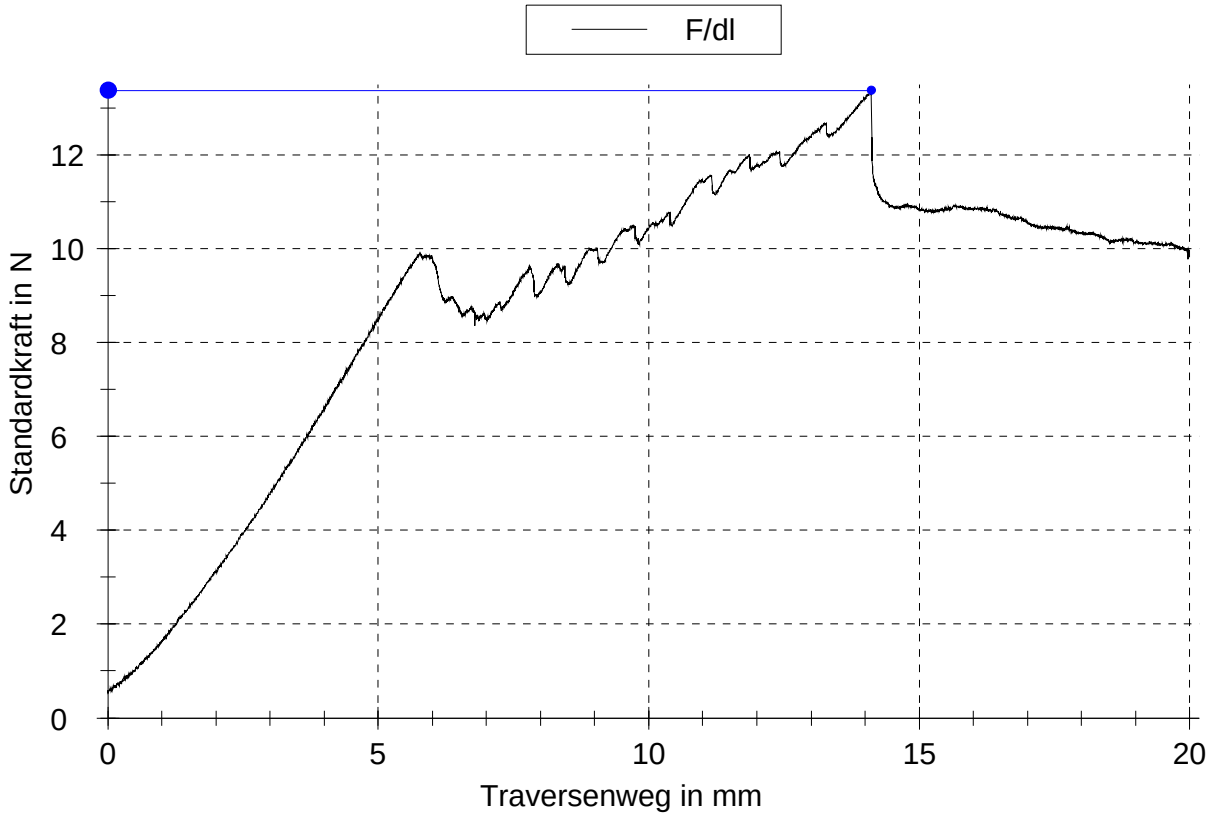
F/dl
Standardkraft in N
0
2
4
6
8
10
12
0
5
10
15
20
Traversenweg in mm

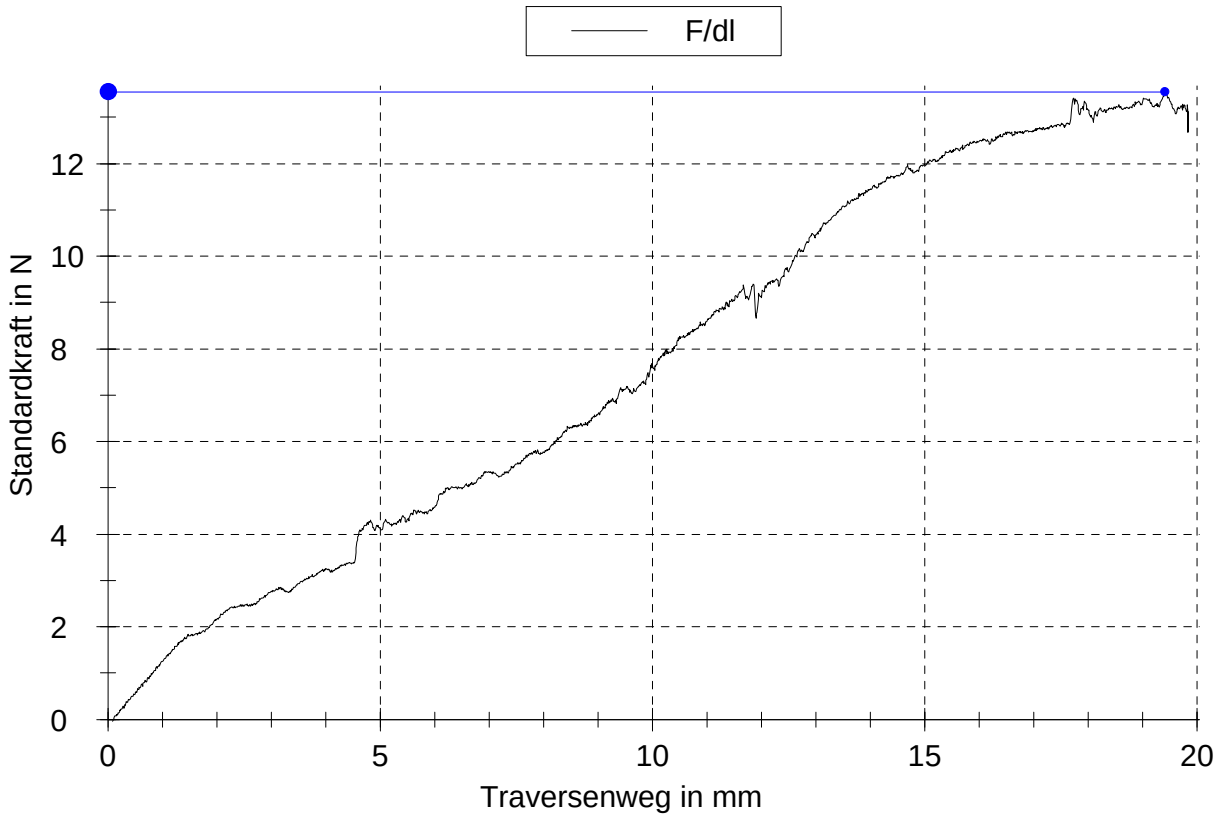
F/dl
Standardkraft in N
0
2
4
6
8
10
12
0
5
10
15
20
Traversenweg in mm

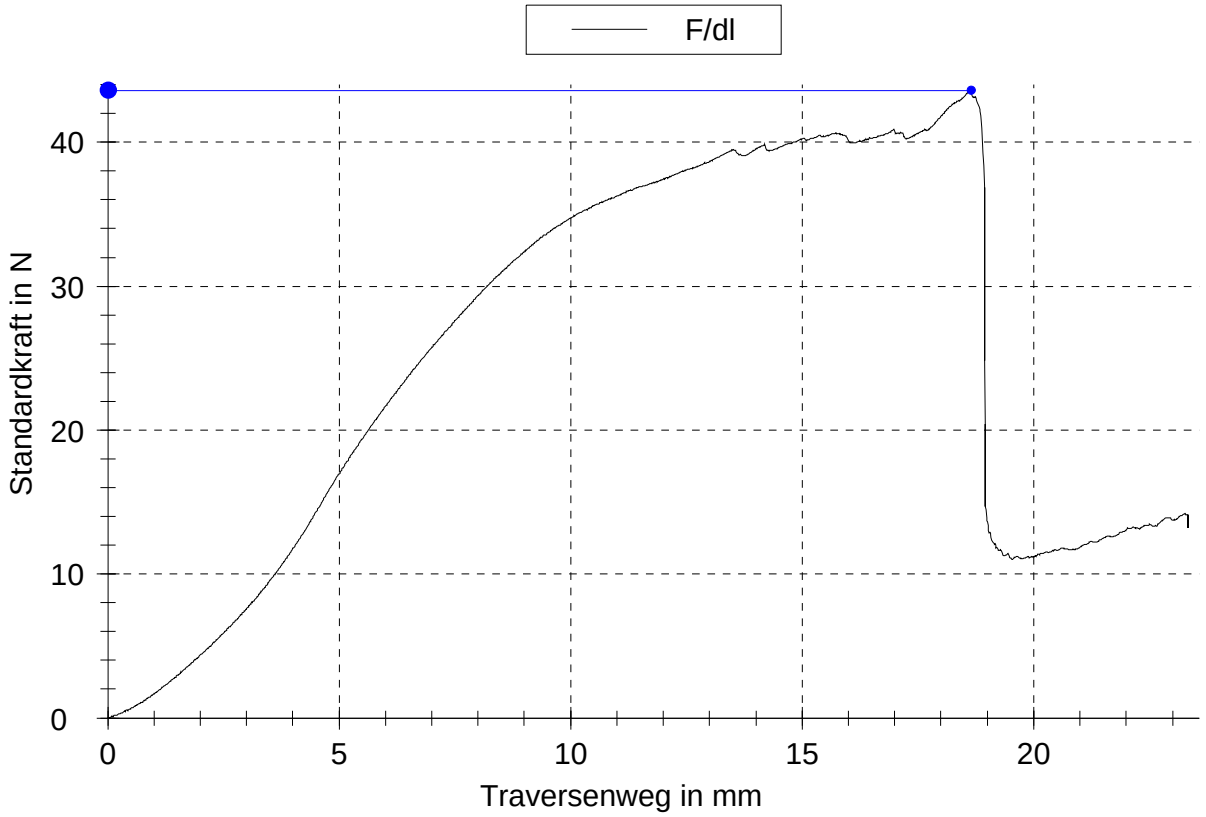
F/dl
Standardkraft in N
0
10
20
30
40
0
5
10
15
20
Traversenweg in mm

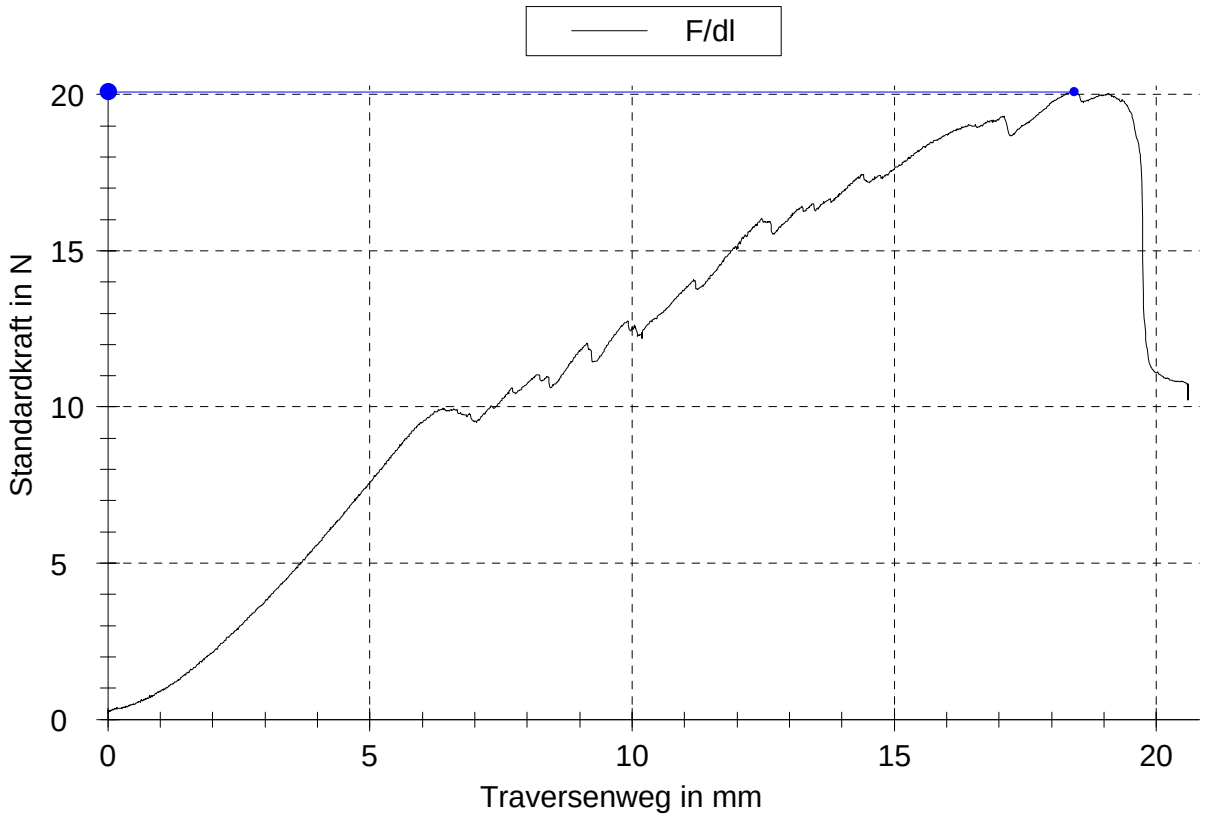
F/dl
Standardkraft in N
0
5
10
15
20
0
5
10
15
20
Traversenweg in mm

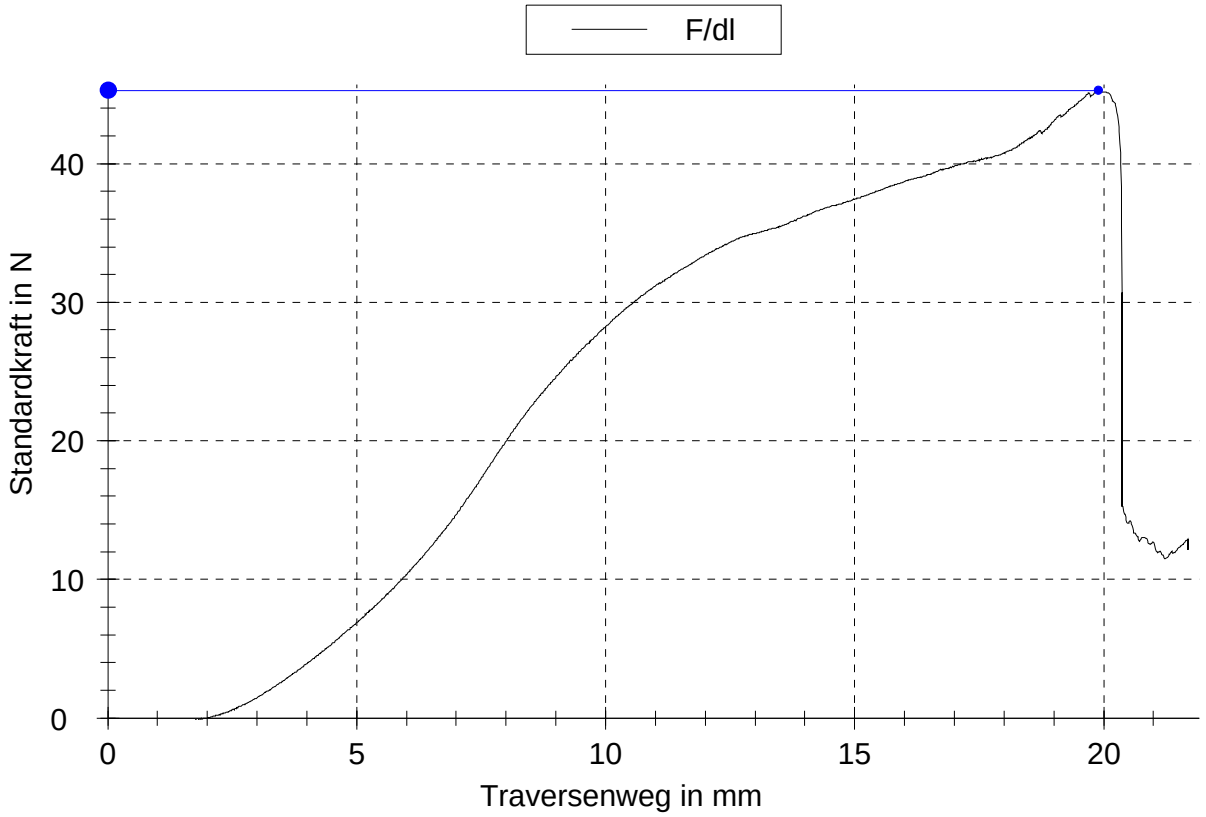
F/dl
Standardkraft in N
0
10
20
30
40
0
5
10
15
20
Traversenweg in mm

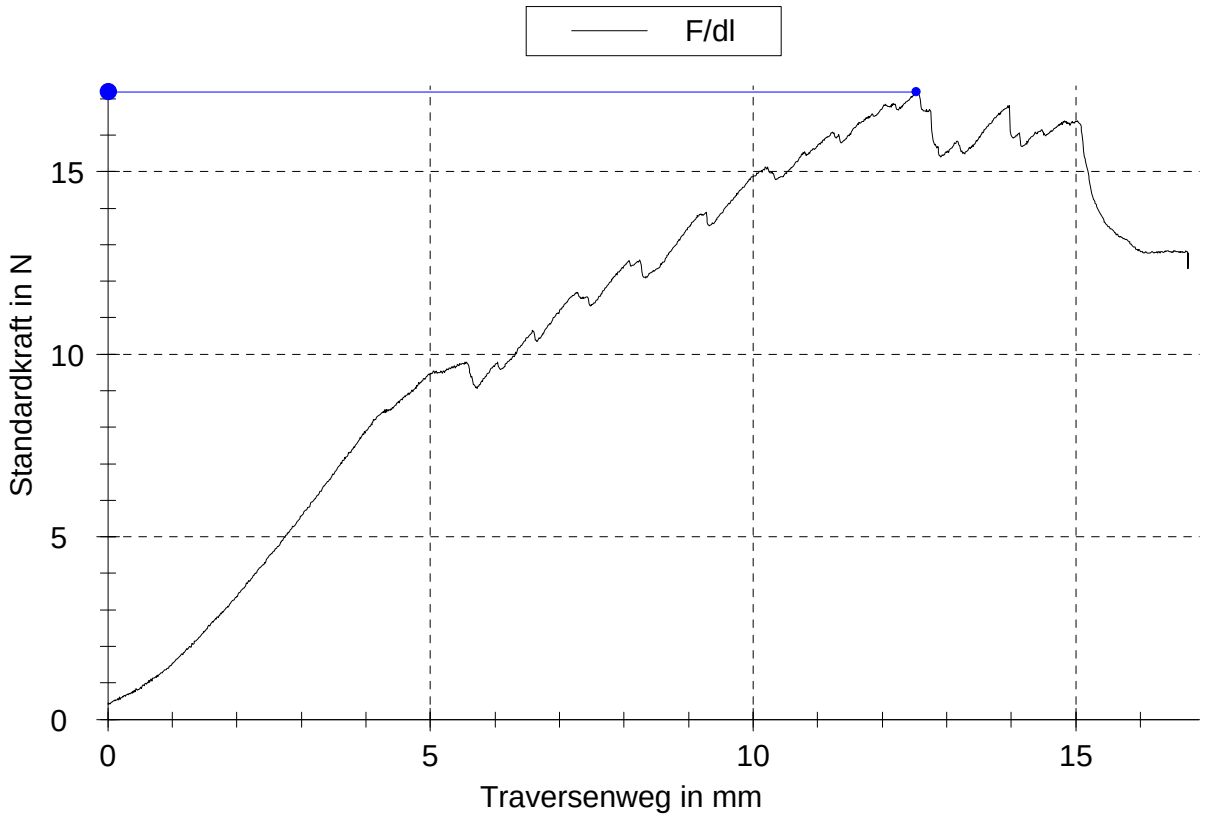
F/dl
Standardkraft in N
0
5
10
15
0
5
10
15
Traversenweg in mm

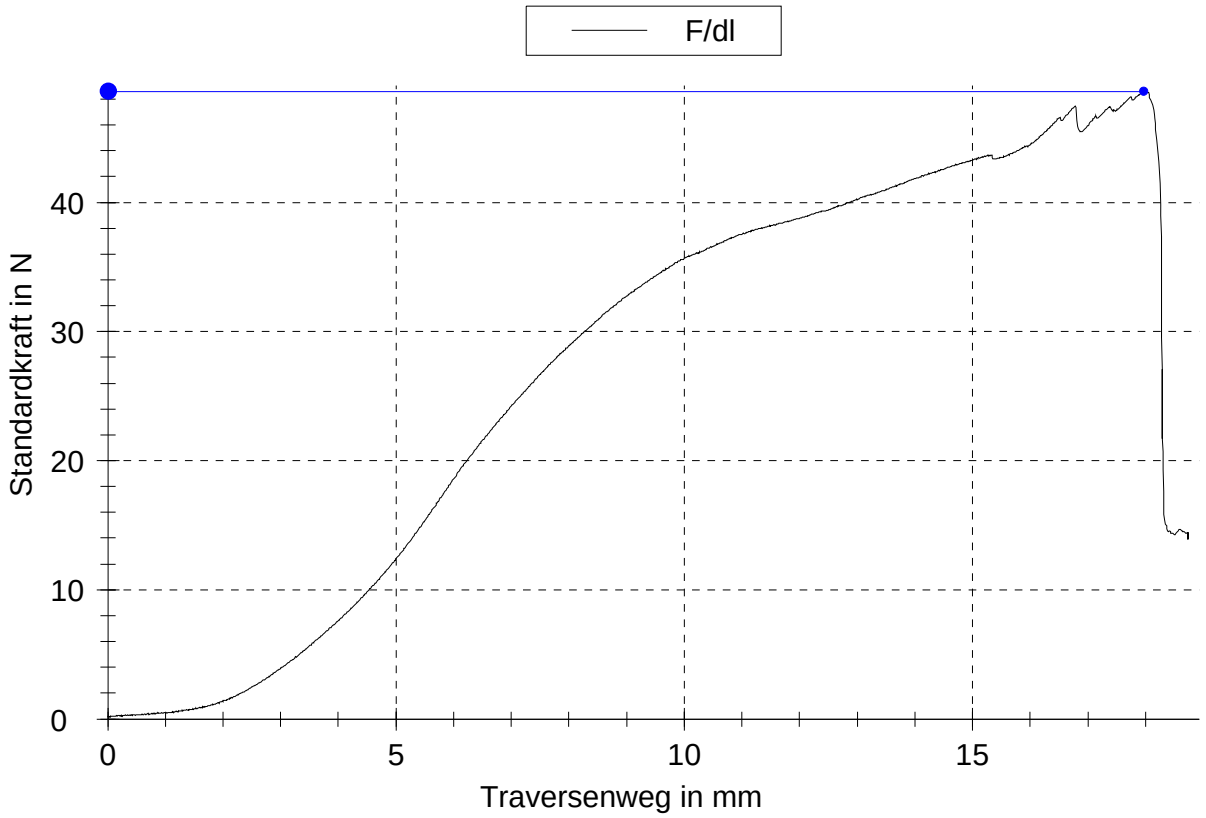
F/dl
Standardkraft in N
0
10
20
30
40
0
5
10
15
Traversenweg in mm

A.6. Life Data Sheet des Windkanalmodells

Life Data Sheet

- Diese Akte ist am Bauteil mitzuführen -

Programm / Projekt: STELAR

Windkanalmodell Rückströmklappe

Kurzkennung:

STELAR-Modell

Kostenträger:	2380619
Geplantes Abschlussdatum:	31.12.2015
Erstellt:	10.03.2015, S. Opitz Datum, Projektleiter
Geprüft:	10.03.2015, S. Opitz Datum, Fertigung

Durchlaufplan

	Datum			Durchgeführte Arbeiten am Bauteil	
Nr.	Beginn	Ende	Name	Protokolle und Anlagen sind dem LDS anzuhängen	Stempel
1	12.02.2015		Opitz / Braun	Zuschnitt Prepreg (Cutter)	+
2	20.02.2015		Opitz	Vorbereitung Druckmessröhrchen	+
3	24.02.2015		Braun	Zuschnitt EPDM (Cutter)	
4	24.02.2015		Braun	Zuschnitt der Trennfolien (Cutter)	+
5	26.02.2015		Braun / Dullo	Vorbereitung Winkelbegrenzung	+
6	10.03.2015		Braun	Säubern und Eintrennen der Form	+
7	11.03.2015		Opitz	Zuschnitt der Glasfaser	+
8	11.03.2015		Opitz	Oberseite: Ablage von Prepreg und EPDM, Integration der Magnete, Druckmessröhrchen und Winkelbegrenzungen	+
9	11.03.2015		Opitz	Unterseite: Ablage von Prepreg	+

Inhaltsverzeichnis

1 Allgemeine Informationen

Nachrüstung eines bestehenden Windkanalmodells mit einer Rückströmklappe zur Untersuchung des Einflusses auf Dynamic Stall.

2 Werkstoffdaten

Eingesetzte Werkstoffe: Prepreg Hexply913, EPDM, Neodymmagnete, Teflonisiertes Abrweißgewebe

3 Fertigung

Fertigungsort: DLR Braunschweig
Fertigungsart: Prepreg
Fertigungsanlagen: Autoklav, Säge

3.1 Mitgeltende Dokumente

Zuschnitte siehe:

\Stelar\Form\Zuschnitte_Cutter\Zuschnitte_Komplett.CatDrawing

3.2 Plattengeometrie und Schnittplan für Proben

Legeplan oben:

1.) Legen der Klappe 212,36mm von der Hinterkante Lage 1
2.) Legen Zusatz 0° Lage Druckrohr L1.5
3.) Ablage Lagen 2 und 3
    Ab Lage 2 Nutzen der Röhrchen als Abstandhalter zwischen den Einzelzuschnitten. Überprüfen der Ausschnitte für die Magnete
4.) Legen des 1.EPDM Steifen vor der Klappe. Einzelne Rowings in 0° auf das EPDM legen
5.) Legen der Lagen 1-3 vor dem EPDM
6.) 90° Lage (Lage 4) legen
7.) Legen der Zusatzlagen 90° im Bereich der Druckröhrchen L4.5
8.) Legen der Lagen 5-6 der Klappe
9.) Ablegen einzelner Rowings in 0° Richtung im Bereich des EPDM
10.) Ablegen des EPDM-Streifen
11.) Ablegen der Lagen 5-7 vor dem EPDM
12.) Einlegen der Druckröhrchen
13.) Legen der Zusatzlage 0° im Bereich der Druckröhrchen L6.5
14.) Einlegen der Magnete
15.) Legen der Lage 7 der Klappe
16.) Abdecken der Magnete mit dünnem Glasfasergewebe
17.) Ablegen der Trennfolie mit Aussparung für die Winkelbegrenzungen
18.) Kurzen UD Streifen über die Anbindung des EPDM legen
19.) Ablegen der Winkelbegrenzungen (gefaltet mit Trennfolie)
20.) Kurzen UD Streifen unter die Anbindung des EPDM legen
21.) TEILWEISE abdecken der Winkelbegrenzung
22.) Ablegen der kompletten Lagen 8-15
23.) Teflonisiertes Abreisgewebe
24.) Saugglas
25.) Vakuumsack

Legeplan unten:

1.) Legen der Lagen 1-8 unten Vorn
2.) Legen der Lagen 1-8 unten Hinten
3.) Teflonisiertes Abreisgewebe
4.) Saugglas
5.) Vakuumsack

3.3 Ablage der Lagen und Ausrichtung

Oberseite:

Lfd. Nr.	Bezeichnung	Orientierung [°]	Fertigung	Kontrolle
1	Klappe 1	0		
2	Klappe 1.5	0		
3	Klappe 2-1	45		
4	Klappe 2-2	45		
5	Klappe 2-3	45		
6	Klappe 2-4	45		
7	Klappe 2-5	45		
8	Klappe 3-1	-45		
9	Klappe 3-2	-45		
10	Klappe 3-3	-45		
11	Klappe 3-4	-45		
12	Klappe 3-5	-45		
13	EPDM 1	-		
14	VK 1	0		
15	VK 2-1	45		
16	VK 2-2	45		
17	VK 2-3	45		
18	VK 3-1	-45		
19	VK 3-2	-45		
20	VK 3-3	-45		
21	Klappe 4-1	90		
22	Klappe 4-2	90		
23	Klappe 4-3	90		
24	Klappe 4-4	90		
25	Klappe 4.5	90		
26	Klappe 5-1	-45		
27	Klappe 5-2	-45		
28	Klappe 5-3	-45		
29	Klappe 5-4	-45		
30	Klappe 5-5	-45		
31	Klappe 6-1	45		
32	Klappe 6-2	45		
33	Klappe 6-3	45		
34	Klappe 6-4	45		
35	Klappe 6-5	45		
36	EPDM 2	-		
37	VK 5-1	-45		
38	VK 5-2	-45		
39	VK 5-3	-45		
40	VK 6-1	45		
41	VK 6-2	45		

42	VK 6-3	45		
43	VK 7	0		
44	Klappe 6.5	0		
45	Klappe 7	0		
46	Komplett 8-1	0		
47	Komplett 8-2	0		
48	Komplett 9-1	45		
49	Komplett 9-2	45		
50	Komplett 9-3	45		
51	Komplett 9-4	45		
52	Komplett 10-1	-45		
53	Komplett 10-2	-45		
54	Komplett 10-3	-45		
55	Komplett 10-4	-45		
56	Komplett 11-1	90		
57	Komplett 11-2	90		
58	Komplett 11-3	90		
59	Komplett 11-4	90		
60	Komplett 12-1	90		
61	Komplett 12-2	90		
62	Komplett 12-3	90		
63	Komplett 12-4	90		
64	Komplett 13-1	-45		
65	Komplett 13-2	-45		
66	Komplett 13-3	-45		
67	Komplett 13-4	-45		
68	Komplett 14-1	45		
69	Komplett 14-2	45		
70	Komplett 14-3	45		
71	Komplett 14-4	45		
72	Komplett 15-1	0		
73	Komplett 15-2	0		

Unterseite:

Lfd. Nr.	Bezeichnung	Orientierung [°]	Fertigung	Kontrolle
1	UV 1	0		
2	UV 2-1	45		
3	UV 2-2	45		
4	UV 2-3	45		
5	UV 3-1	-45		
6	UV 3-2	-45		
7	UV 3-3	-45		
8	UV 4-1	90		
9	UV 4-2	90		
10	UV 4-3	90		
11	UV 4-4	90		

12	UV 5-1	90		
13	UV 5-2	90		
14	UV 5-3	90		
15	UV 5-4	90		
16	UV 6-1	-45		
17	UV 6-2	-45		
18	UV 6-3	-45		
19	UV 7-1	45		
20	UV 7-2	45		
21	UV 7-3	45		
22	UV 8	0		
23	UH 1	0		
24	UH 2-1	45		
25	UH 2-2	45		
26	UH 2-3	45		
27	UH 3-1	-45		
28	UH 3-2	-45		
29	UH 3-3	-45		
30	UH 4-1	90		
31	UH 4-2	90		
32	UH 4-3	90		
33	UH 4-4	90		
34	UH 5-1	90		
35	UH 5-2	90		
36	UH 5-3	90		
37	UH 5-4	90		
38	UH 6-1	-45		
39	UH 6-2	-45		
40	UH 6-3	-45		
41	UH 7-1	45		
42	UH 7-2	45		
43	UH 7-3	45		
44	UH 8	0		

3.4 Prozessierung Autoklav

Programm Nr.: 18 (großer Autoklav)

Härtungszyklus: HexPly 913: 30min 90°C, 3h 125°C, 6bar und Vakuum während des kompletten Prozesses

Ist-Datensatz abgespeichert: _____

4 Bemerkungen

Kap.	Bemerkung	Name	Datum

A.7. Datenblatt: EPDM

Faserverstärkte Kunststoffe – Kautschuk – Verbund

Sie erhalten eine 0,5 mm starke, kalandrierte Rohgummiplatte der Mischung AA6CFZ die für den direkten Verbund zu Epoxy-Prepregs geeignet ist. Vinylester- und Polyesterharze sind ebenfalls möglich.
Die Lagerung bei Raumtemperatur ist möglich, aber auch eine Kühlung ist unschädlich. Bitte die Rolle möglichst hängend lagern, um Druckstellen oder ein erschwertes Lösen von der Folie zu vermeiden.

Die gelieferte Mischung entspricht einer Standardausführung. Sie kann in vielen Eigenschaften wie beispielsweise Farbe, Fließverhalten, Härte, Dämpfungs- und Vulkanisationsverhalten Ihren Anforderungen entsprechend modifiziert werden.

Verarbeitungshinweise:

1. Konfektion

Die kalandrierte Rohgummiplatte kann wie Prepreg eingelegt, aufgedoppelt und drapiert werden.
Innerhalb der t_{10} fließt das Material unter dem Außendruck in die gewünschte Form und kann dabei auch komplexe Konturen abformen. Deshalb muss die Elastomermasse nur grob konfektioniert werden.

2. Härtung

Der Zutritt von Luftsauerstoff während der Härtung inhibiert die Vernetzung und führt zu einer untervernetzten und klebrigen Oberflächen. Die Verarbeitungsbedingungen wurden für eine Vernetzung mit Mitteltemperatur-Epoxi-Prepregs optimiert.

Vulkanisationsbedingungen / Härtezeiten der Mischung AA6CFZ

Temperatur [℃]	Druck absolut [bar]	Verarbeitungszeit oder Fließzeit t_{10} [min]	Aushärtezeit t_{90} [min]
110	1,4	9,0	115
120	2,0	4,2	64
130	2,7	3,3	20
140	3,6	0,8	7,3
150	4,8	0,3	3,8

Die angegebenen Härtezeiten sind Mindestangaben. Längere Härtezyklen sind unkritisch.

Um Porosität im Elastomer zu vermeiden sollte nach bisheriger Erfahrung der in der Tabelle angegebene minimale Gesamtdruck eingehalten werden. Dabei sind der Druck im Vakuumsack und der äußere Druck, z.B. durch Autoklaven, zu addieren.

Viel Erfolg bei ihren Versuchen.

Stand 12/2008

TECHNISCHES DATENBLATT
TECHNICAL DATA SHEET

Mischung	***Compound:***	**AA6CFZ** (Entwicklungsbezeichnung SAA1052/70)			
Spezifikation:	***Specification:***	**Keine / none**			
Firma:	***Company:***				
Vulkanisationsbed.	*Vulcanisation Conditions*	Probekörper	Ring R1	15 Min / min	140 ℃
		Test specimen	Stab S2 *Dumbbell*	10 Min / min	140 ℃
Temperbedingungen	*Post Curing Conditions*			**0 Std. / h**	℃
Prüfmerkmale	***Properties***		**Einheiten** ***Units***	**Soll – Werte** ***Desired val.***	**Ist – Werte** ***Actual value***
Reißfestigkeit (S2)	*Tensile Strength (S2)*	DIN 53504	MPa		8,1
Reißdehnung (S2)	*Elongation at break (S2)*	DIN 53504	%		310
Spannungswert 50%	*Modulus 50% (S2)*	DIN 53504	MPa		1,6
Spannungswert 100%	*Modulus 100% (S2)*	DIN 53504	MPa		2,3
Spannungswert 200%	*Modulus 200% (S2)*	DIN 53504	MPa		4,3
Spannungswert 300%	*Modulus 300% (S2)*	DIN 53504	MPa		7,9
Härte (R1)	*Hardness (R1)*	DIN 53505	Shore A	64+-5	64
Rückprallelastizität	*Rebound Resilience (R1)*	DIN 53512	%		54
Weiterreißwiderstand	*Tear strength* (S2)	DIN ISO 34-1	N/mm		8,1
Dichte (R1)	*Specific Gravity (R1)*	DIN 53479	kg /dm^3	1,04+-0,02	1,04
Abrieb	*Abrasion*	DIN ISO 4649	mm^3		138
Druckverformungsrest	*Compression Set* 72 h RT	DIN ISO 815	%		17
Druckverformungsrest	*Compression Set* 22 h 70℃	DIN ISO 815	%		22
Druckverformungsrest	*Compression Set* 22 h 100℃	DIN ISO 815	%		29
Beständigkeit gegen Heißluft	***Resistance against hot air***	**DIN 53508**		**Zeit : 14 Tage** ***Time: Days***	**Temp. 120℃**
Reißfestigkeit	*Tensile Strength*	DIN 53504	MPa		7,7
Reißfestigkeitsänderung	*Change in tensile strength*	DIN 53504	%		-4,8
Reißdehnung	*Elongation at break*	DIN 53504	%		270
Reißdehnungsänderung	*Change in elongation at break*	DIN 53504	%		-12,9
Spannungswert 50%	*Modulus 50% (S2)*	DIN 53504	MPa		1,8
Spannungswert 100%	*Modulus 100% (S2)*	DIN 53504	MPa		2,6
Spannungswert 200%	*Modulus 200% (S2)*	DIN 53504	MPa		4,8
Härte	*Hardness*	DIN 53505	Shore A		69
Härteänderung	*Hardness change*	DIN 53505	Shore A		+5

Datum *Date:* *22.07.10* Unterschrift *Sign:* *Jens Schaube*

KRAIBURG GROUP
Gummiwerk KRAIBURG GmbH & Co. KG
Teplitzer Str. 20
84478 Waldkraiburg / Germany

Fon + 49 (0) 8638 / 61- 0
Fax + 49 (0) 8638 / 61- 310
info@kraiburg.de
www.kraiburg-kautschuk.de

Handelsregister Traunstein HRA 8626
PhG.: Gummiwerk KRAIBURG Verwaltungs GmbH
Handelsregister Traunstein HRB 16108
Sitz Waldkraiburg, GF: Helmut Esefeld

A.8. Datenblatt: GFK

HexPly® 913

125°C curing epoxy matrix

Product Data

Description

HexPly 913 is a proven modified epoxy matrix with a low temperature cure cycle which exhibits outstanding environmental resistance, whilst retaining good hot/wet mechanical performance. This versatile matrix system can be processed using a wide range of techniques according to the application and is capable of co cure with epoxy film adhesives.

HexPly 913 is a highly successful matrix used extensively in the aerospace industry for primary aircraft structures and helicopter blades.

Benefits and Features

- Exceptional environmental resistance
- Controlled minimum viscosity giving easy processing
- Capable of being processed by various techniques
- Good tack and drape characteristics
- Long shelf life and out life at room temperature
- Compatible with Redux 312 and 335K adhesive films

Resin Matrix Properties

Rheology

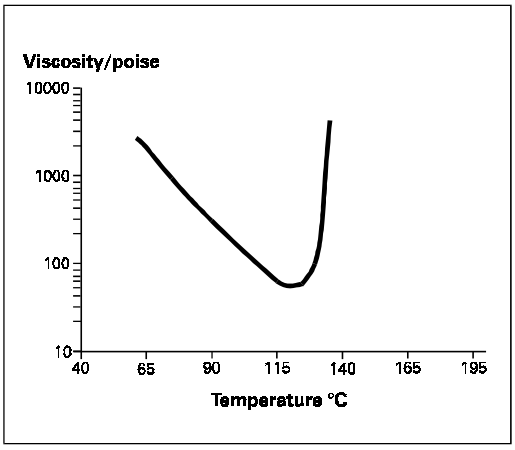

Gel Time

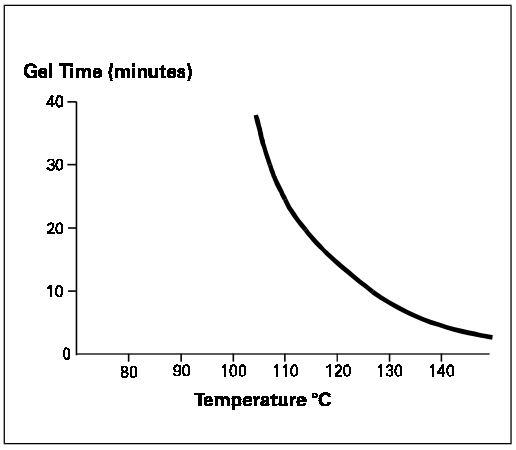

HexPly® 913 *Product Data*

Cured Matrix Properties (cured at 125°C)

		Method
Tensile strength	65.5 MPa	ISO R527 type 1
Tensile modulus	3.39 GPa	ISO R527 type 1
Cured density	1.23 g/cm^3	

Prepreg Curing Conditions

60 mins at 125°C and 700kN/m^2 (7 bar) pressure. Heat up rate 2°C to 8°C.

Alternative cure cycles:

Temperature °C	Time (Min)
140	40
150	20
160	10

Components up to 3 mm thick can be cured without a dwell in the schedule provided that the heat-up rate is not more than 5°C/minute. A dwell period is necessary in the heat-up to avoid the occurrence of a resin exotherm (usually 80 - 100°) but the dwell period will depend on the mass and type of tool.

Prepreg Storage Life

- Tack Life @ 23°C 30 days
- Guaranteed Shelf Life @ -18°C 12 months
- Storage conditions.

HexPly 913 prepregs should be stored as received in a cool dry place or in a refrigerator. After removal from refrigerator storage, prepreg should be allowed to reach room temperature before opening the polythene bag, thus preventing condensation. (A full reel in its packaging can take up to 48 hours).

Precautions for Use

The usual precautions when handling uncured synthetic resins and fine fibrous materials should be observed, and a Safety Data Sheet is available for this product. The use of clean disposable inert gloves provides protection for the operator and avoids contamination of material and components.

Important

All information is believed to be accurate but is given without acceptance of liability. Users should make their own assessment of the suitability of any product for the purposes required. All sales are made subject to our standard terms of sale which include limitations on liability and other important terms.

Publication FTA054b (Oct 2002)

For further information, please contact your nearest sales office, or visit our website at **www.hexcelcomposites.com**

Australia
Suite 2, 86 Grimshaw Street
Greensborough, Victoria 3088
Tel: **61** 3 9432 7100
Fax: **61** 3 9432 7200

Austria
Industriestrasse 1
A-4061, Pasching
Tel: **43** (0)7229 7720
Fax: **43** (0)7229 772299

Belgium
Rue Trois Bourdons, 54
B-4840 Welkenraedt
Tel: **32** 87 307 411
Fax: **32** 87 882 895

Brazil
Av. J. Guilhermino, 474/72
S.J.Campos, SP 12210-130
Tel: **55** 12 3941 2242
Fax: **55** 12 3923 1186

China
Room B707, Yin Hai Bldg.
250 Cao Xi Rd
Shanghai 200233
Tel: **86** 21 6483 6741/2
Fax: **86** 21 6483 6744

France
ZI La Plaine, B.P.27 Dagneux
01121 Montluel CEDEX
Tel: **33** (0)4 72 25 26 27
Fax: **33** (0)4 72 25 27 30

Germany
Postfach 1560
21655 Stade
Tel: **49** 4141 7879-00
Fax: **49** 4141 7879-01

Italy
Via San Cristoforo, 44
21047 Saronno (VA)
Tel: **39** 02 96709082
Fax: **39** 02 9600809

Japan - *Joint Venture*
DIC - Hexcel Limited
Room 603, Santsu-Mori Bldg.
2-22-1 Nishi - Shimbashi
Minato-Ku, Tokyo 105
Tel: **81** 3 5401 0271
Fax: **81** 3 5401 0270

Spain
Bruselas, 10 - 16
Polig. Ind. “Ciudad de Parla”
28980 Parla, Madrid
Tel: **34** 91 664 4900
Fax: **34** 91 698 4914

United Kingdom
Duxford, Cambridge
CB2 4QD
Tel: **44** (0)1223 833141
Fax: **44** (0)1223 838808

USA
11711 Dublin Blvd.
Dublin, CA 94568-2832
Tel: **1** 925 551 4900
Fax: **1** 925 828 9202

USA
101 East Ridge Drive, Suite 102
Danbury, CT 06810
Tel: **1** 203 798 8311
Fax: **1** 203 798 8161

USA
42705 Grand River
Suite 201
Novi, MI 48375
Tel: **1** 248 344 8688
Fax: **1** 248 305 9760

USA
2350 Airport Freeway, Suite 550
Bedford, TX 76022-6027
Tel: **1** 817 315 3939
Fax: **1** 817 571 8629

USA
16310 NE 80th Street, Suite 102
Redmond, WA 98052
Tel: **1** 425 558 4400
Fax: **1** 425 861 5847

A.9. Datenblatt: Gießharz

Poxy-Systems®

Technische Daten

Epoxyd-Gießharzsystem "wasserklar"

Zweikomponentiges klares, farbloses Epoxydharzsystem

Beschreibung

- **Sehr gute UV-Beständigkeit**
- **Hochtransparente Komponenten**
- **Polierfähige, harte Oberfläche**
- **Sehr gute Schlagzähigkeit**
- **Auch in dünnen Schichten völlig klebefrei härtend**
- **Für transparente Beschichtungen sehr gut geeignet**
- **Eignet sich ebenfalls als Laminerharzsystem mit sehr langer Topfzeit**

Die Reaktivität des Systems wurde erhöht, so dass sich daraus auch die Ansatzgröße bzw. die Gießmenge verringert. Pro Guss können 500 g Ansatz ohne Einfallen der Oberfläche vergossen werden. Bei größeren Ansätzen sind Schichten bis zu 50 mm möglich.
Wie bei allen Reaktionsharzsystemen begrenzt die auftretende Reaktionswärme (Exothermie) die mögliche, zu vergießende Menge: Oftmals kann auch eine verringerte Härtungstemperatur (z.B. nachts in einem Raum unter 20 °C Umgebungstemperatur) einer zu großen Exothermie entgegenwirken .

Verarbeitung

Harz und Härter werden bei Raumtemperatur (20 °C - 25 °C) für ca. 2 Minuten homogenisiert. Nach dem Mischen läßt man die Mischung ca. 20 Minuten ruhen.
Lassen Sie den frischen Verguß für 48 Stunden auf einer ebenen Fläche stehen. Bitte nicht berühren und nicht bewegen.

Ausgabe 06/2010, Änderungen vorbehalten

Epoxyd-Gießharz "wasserklar"

Modifiziertes, niedrigviskoses Epoxydharz

Beschreibung

- **Epoxyd-Gießharz für Härter "wasserklar"**

Anwendungsgebiet

Reaktivverdünntes Epoxydharz, das universell für die verschiedensten Anwendungen kalthärtender Epoxydharz-Systeme eingesetzt werden kann.

Einzelpackungen: 2,25 kg - 200 kg Bestell-Nr. 107 106-X, Arbeitspackungen: (siehe Härter)

Epoxyd-Gießharz "wasserklar"	Einheit	Wert
Lieferform	-	flüssig
Farbzahl	Gardener	< 2
Dichte bei 23 °C	g/cm³	1,14 ± 0,01
Viskosität bei 23 °C	mPas	950 ± 100
Epoxydwert	100 g/Äquivalent	0,578
Epoxydäquivalent	g/Äquivalent	173 ± 10
Brechungsindex DIN 51 423-2	-	1,553 ± 0,001
Lagerung (originalverpackt)	Monate	min. 12

Ausgabe 06/2010, Änderungen vorbehalten

Härter "wasserklar"

Beschreibung

- **Härter für Epoxyd-Gießharz "wasserklar"**
- **Mischungsverhältnis: 100 : 37 Gewichtsteile Harz : Härter**
- **Verarbeitungszeit ca. 5 Stunden**
- **Aushärtezeit ca. 24—48 Stunden**

Anwendungsgebiet

Sehr nierigviskoser Härter mit langer Verarbeitungszeit, geringer Exothermie sowie guter Lichtbeständigkeit.

Einzelpackungen: 835 g - 200 kg Bestell-Nr. 107 111-X, Arbeitspackungen: 310 g Gebinde Bestell-Nr. 107 102-1, 685 g Gebinde Bestell-Nr. 107 102-2, 1,37 kg Gebinde Bestell-Nr. 107 102-3

Härter "wasserklar"	Einheit	Wert
Lieferform	-	flüssig
Farbzahl	Gardener	< 1
Dichte bei 23 °C	g/cm³	0,95
Viskosität bei 23 °C	mPas	15
Aminäquivalent	g/Äquivalent	61
Brechungsindex DIN 51 423-2	-	1,4470 ± 0,0008
Lagerung (originalverpackt)	Monate	min. 12

Ausgabe 06/2010, Änderungen vorbehalten

A.10. Datenblatt: Klebefolie

tesafix® 4965

Temperaturbeständiges doppelseitiges Klebeband

PRODUKTINFORMATION

Produktbeschreibung

tesafix® 4965 ist ein doppelseitig klebendes, transparentes Polyesterklebeband mit Acrylatklebmasse. Es ist mit einer roten Folie abgedeckt. tesafix® 4965 zeichnet sich durch gute Klebkraft auf verschiedenen Kunststoffen wie ABS und sogar EPDM aus, da es sehr beständig gegen Weichmacher ist.
tesafix® 4965 ist UL-gelistet unter MH/18055.

Hauptanwendungen

- Für Montage von ABS-Teilen in der KFZ-Industrie.
- Zum selbstklebend Ausrüsten von Gummi und EPDM-Profilen.
- Leistenverklebung in der Möbelindustrie.
- Verschließen von Isolierrohrschalen.
- Display- (z.B. für Handys) und Schilderverklebung.
- Ausrüstung von Bleiprofilen.
- Cabrioverdeckverklebung.
- Endlosverklebung von Alu-Blechen.

Technische Daten

Trägermaterial	PET-Film	Klebmasse	modifiziertes Acrylat
Farbe	transparent	Reißdehnung	50 %
Dicke	205 µm	Reißkraft	20 N/cm

Klebkraft auf

Stahl (initial)	11.5 N/cm	Stahl (nach 14 Tagen)	11.8 N/cm
ABS (initial)	10.3 N/cm	ABS (nach 14 Tagen)	12 N/cm
Aluminium (initial)	9.2 N/cm	Aluminium (nach 14 Tagen)	10.6 N/cm
PC (initial)	12.6 N/cm	PC (nach 14 Tagen)	14 N/cm
PE (initial)	5.8 N/cm	PE (nach 14 Tagen)	6.9 N/cm
PET (initial)	9.2 N/cm	PET (nach 14 Tagen)	9.5 N/cm
PP (initial)	6.8 N/cm	PP (nach 14 Tagen)	7.9 N/cm
PS (initial)	10.6 N/cm	PS (nach 14 Tagen)	12 N/cm
PVC (initial)	8.7 N/cm	PVC (nach 14 Tagen)	13 N/cm

Eigenschaften

Temp.beständigkeit kurzfr.	200 °C	Chemikalienbeständigkeit	+
Temp.beständigkeit langfr.	100 °C	Weichmacherbeständigkeit	+
Anfassklebkraft	+	Statische Scherfestigkeit bei 23°C	+
Alterungsbeständigkeit (UV)	++	Statische Scherfestigkeit bei 40°C	+
Feuchtigkeitsbeständigkeit	++	Anfassklebkraft	+

Bewertung innerhalb des relevanten tesa® Sortiments: ++ sehr gut, + gut, o mittel, - niedrig

Für aktuelle Information zu diesem Produkt besuchen Sie http://l.tesa.com/?ip=04965

tesa SE
Ein Beiersdorf Unternehmen

tesa SE
Postfach 57 02 62
D-22771 Hamburg
Deutschland
Tel: 040-4909 3400
Fax: 0180-234 3520
www.tesa.de

tesa GmbH
Laxenburger Str. 151
A-1100 Wien
Österreich
Tel: 01-614 00 295
Fax: 01-614 00 363
www.tesa.at

tesa tape Schweiz AG
Industriestrasse 19
CH-8962 Bergdietikon
Schweiz
Tel: 044-744 34 44
Fax: 044-744 32 22
www.tesa.ch

tesafix® 4965

Temperaturbeständiges doppelseitiges Klebeband

PRODUKTINFORMATION

Weitere Informationen

Trennpapier-/Trennfolie-Varianten:
PV0 rote MOPP-Folie (80µm; 72g/m²)
PV1 braunes Trennpapier (71µm; 82g/m²)

Für aktuelle Information zu diesem Produkt besuchen Sie http://l.tesa.com/?ip=04965

tesa SE
Ein Beiersdorf Unternehmen

tesa SE
Postfach 57 02 62
D-22771 Hamburg
Deutschland
Tel: 040-4909 3400
Fax: 0180-234 3520

www.tesa.de

tesa GmbH
Laxenburger Str. 151
A-1100 Wien
Österreich
Tel: 01-614 00 295
Fax: 01-614 00 363

www.tesa.at

tesa tape Schweiz AG
Industriestrasse 19
CH-8962 Bergdietikon
Schweiz
Tel: 044-744 34 44
Fax: 044-744 32 22

www.tesa.ch

A.11. Datenblatt: Hall-Effekt-Sensor

TAPE PACKING OPTIONS

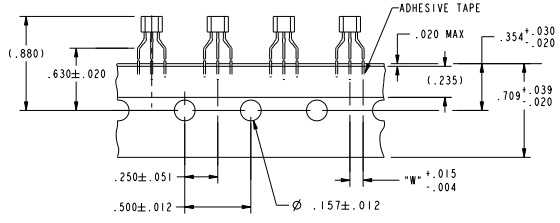

TAPE DIMENSIONS

TAPE STYLE

AMMOPACK STYLE "T2" /12/14

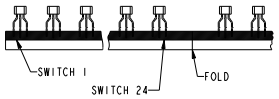

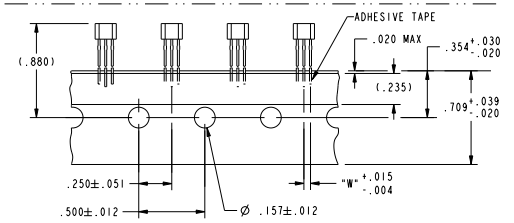

TAPE DIMENSIONS

AMMOPACK STYLE "T3" /12/14

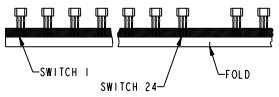

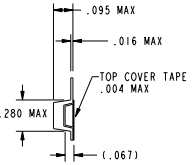

TAPE DIMENSIONS

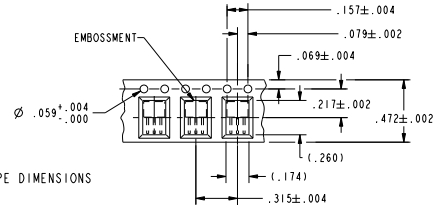

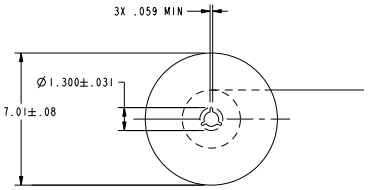

DIRECTION OF FEED FROM REEL

TAPE STYLE "P" /15

NOTES
/1 CENTERLINE OF HALL CELL
/2 THE + MAGNETIC FLUX IS IN THE DIRECTION SHOWN (THIS ASSUMES THE CONVENTION THAT THE DIRECTION OF THE EXTERNAL FLUX OF A MAGNET IS FROM THE NORTH TO THE SOUTH POLE OF THE MAGNET)
3 - THE DEVICE CANNOT BE DAMAGED BY MAGNETIC OVERDRIVE
4 - OUTPUT TYPE - RATIOMETRIC
5 - LEADS MUST BE ADEQUATELY SUPPORTED DURING ANY FORMING/SHEERING OPERATION TO ASSURE THAT THE LEADS ARE NOT STRESSED WITHIN THE PLASTIC
6 - PCB WAVE SOLDERING GUIDELINES ARE AS FOLLOWS: 250°C PEAK FOR 10 S MAX OR 260° C PEAK FOR 5 S MAX.
/7 BURRS ARE ALLOWED ONLY IF FULL LENGTH OF LEADS WILL PASS THROUGH Ø.023 HOLE.
/8 LEAD REFERENCE DIMENSIONS DO NOT INCLUDE SOLDER THICKNESS
/8 DIMENSION REFERS TO THE LOCATION OF LEAD CENTERLINES AS THE EXIT THE PLASTIC PACKAGE
9 - SOME COMBINATIONS OF BASIC LISTING AND PACKAGE OPTIONS MAY NOT BE AVAILABLE
/10 ABSOLUTE MAXIMUM RATINGS ARE THE EXTREME LIMITS THE DEVICE WILL MOMENTARILY WITHSTAND WITHOUT DAMAGE TO THE DEVICE. ELECTRICAL AND MAGNETIC CHARACTERISTICS ARE NOT GUARANTEED IF THE RATED VOLTAGE AND/OR CURRENTS ARE EXCEEDED NOR WILL THE DEVICE NECESSARILY OPERATE AT ABSOLUTE MAXIMUM RATINGS
/11 LEAD STRAIGHTNESS MAY BE DETERIORATED ON SOME UNITS BY BULK PACKAGING. APPLICATIONS HAVING A CRITICAL LEAD STRAIGHTNESS REQUIREMENT SHOULD USE A TAPE PACKAGING OPTION
/12 AMMOPACK STYLE "T2" & "T3". 24 SWITCHES BETWEEN FOLDS, SKIP 1 SPACE AT FOLD. MAY BE REFERRED TO AS "FAN FOLD"
/13 MOLDED PART DIMENSIONS DO NOT INCLUDE FLASH. FLASH IS LIMITED TO .005 MAX
/14 TAPE AND AMMOPACK PER EIA-468
/15 POCKET TAPE PER EIA-481

CATALOG LISTING	TAPE STYLE	DIM "L"	DIM "W"	COMMENTS /11
SS495A	NONE	.590	.050	BULK - 1000/BAG
SS495A-T2	T2	.590	.100	5000/BOX
SS495A-T3	T3	.590	.050	5000/BOX
SS495A-S	NONE	.125	.050	BULK - 1000/BAG
SS495A-SP	P	.125	.050	1000/PACKET TAPE AND REEL
SS495AI	NONE	.590	.050	BULK - 1000/BAG
SS495AI-T2	T2	.590	.100	5000/BOX
SS495AI-T3	T3	.590	.050	5000/BOX
SS495AI-S	NONE	.125	.050	BULK - 1000/BAG
SS495AI-SP	P	.125	.050	1000/PACKET TAPE AND REEL
SS495A2	NONE	.590	.050	BULK - 1000/BAG
SS495A2-S	NONE	.125	.050	BULK - 1000/BAG
SS495A2-SP	P	.125	.050	1000/PACKET TAPE AND REEL
SS495A2-T2	T2	.590	.100	5000/BOX
SS495A2-T3	T3	.590	.050	5000/BOX
SS495A-L	NONE	.735	.050	BULK - 1000/BAG
SS495AI-L	NONE	.735	.050	BULK - 1000/BAG
SS495A2-L	NONE	.735	.050	BULK - 1000/BAG
SS495B	NONE	.590	.050	BULK - 1000/BAG
SS495B-T2	T2	.590	.100	5000/BOX
SS495B-T3	T3	.590	.050	5000/BOX
SS495B-S	NONE	.125	.050	BULK - 1000/BAG
SS495B-SP	P	.125	.050	1000/PACKET TAPE AND REEL

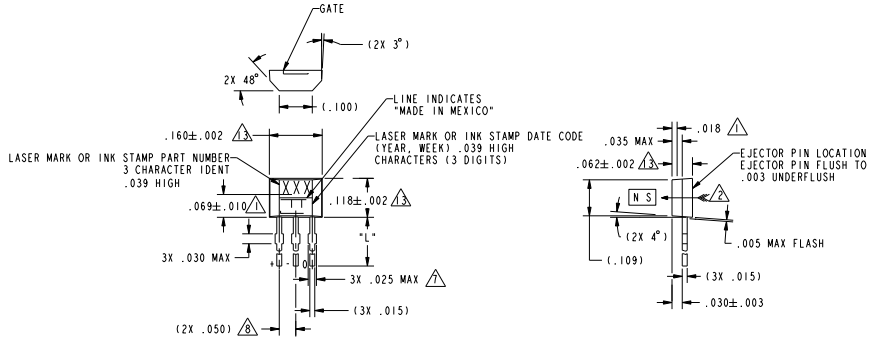

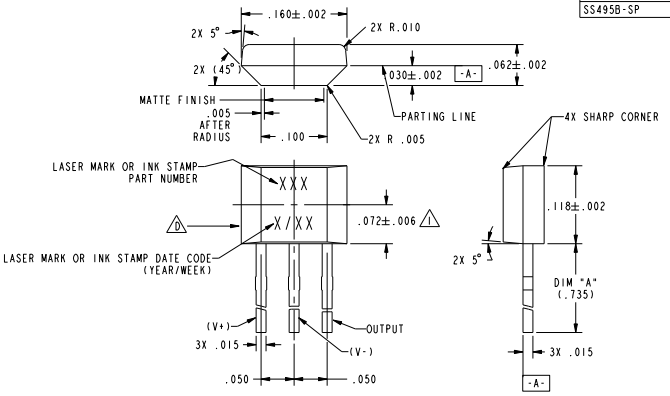

LEAD STYLES L ONLY
SCALE 10:1

OPTIONAL SURFACE MOUNT LEAD STYLE

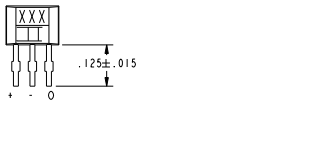

CAUTION ELECTROSTATIC SENSITIVE DEVICES DO NOT OPEN IN AN ELECTROSTATIC FREE WORK AREA
ESD SENSITIVITY: CLASS 3

ANSI Y14.5M-1982 APPLIES

FED. MFG. CODE 91929
MICRO SWITCH a Honeywell Division

MINIATURE RATIOMETRIC LINEAR HALL EFFECT SENSOR

CATALOG LISTING
SS495 SERIES CHART 1

THIRD ANGLE PROJECTION
SCALE 5:1
DO NOT SCALE PRINT
UNLESS OTHERWISE SPECIFIED TOLERANCES ARE
ONE PLACE (.0) +.030
TWO PLACE (.00) +.015
THREE PLACE (.000) +.005
ANGLES +2°
WEIGHT

MSS495 SERIES CHART 1 PAGE 5 OF 5 RELEASE NO. PR-21283 REVISIONS 41 ISSUE CHECK
REVISIONS C 0034535 RDE 26 OCT 07
PTC/CAD 20 DRAWN C S L 12 APR 02 CHECK SAV 4 APR 02 CHECK

CHARACTERISTICS ARE AT Vs=5.00 WITH 4.7K OUTPUT TO MINUS WITH TA= -40°C TO +125°C UNLESS OTHERWISE SPECIFIED

SS495A

MSS495 SERIES CHART 1

PARAMETER	CONDITIONS	MIN	TYP	MAX	UNITS
SENSITIVITY	TA = 25°C	3.00	3.125	3.25	mV/GAUSS
NULL	TA = 25°C	2.425	2.50	2.575	VOLTS
SUPPLY CURRENT	TA = 25°C		7	8.7	mA
OUTPUT CURRENT SOURCE	Vs > 4.5	1mA	1.5mA		
SINK	Vs > 4.5	.6mA	1.5mA		
SINK	Vs > 5.0	1mA	1.5mA		
RESPONSE TIME			3µS		
OUTPUT VOLTAGE SWING					
VOM -	-B APPLIED	.4	.2		VOLTS
VOM +	+B APPLIED	Vs -.4	Vs -.2		VOLTS
B LIMITS FOR LINEAR	-B MAX	-600	-670		GAUSS
OPERATION	+B MAX	+600	+670		GAUSS
Vnull DRIFT	B = 0, TA = 25°C TO 125°C	-.06		+.06	% /°C
Vnull DRIFT	B = 0, TA = -125°C TO +150°C	-.08		+.08	% /°C
SENSITIVITY DRIFT	TA=+25°C TO +150°C	-.01		+.05	% /°C
SENSITIVITY DRIFT	TA=-40°C TO +25°C	0		+.06	% /°C
LINEARITY	B = -600 TO +600	0	-1.0	-1.5	% OF SPAN
SUPPLY VOLTAGE	-40°C TO +125°C	4.5	5.0	10.5	VOLTS
OPERATING TEMP	SEE MAX TEMPERATURE CHART	-40		+150	°C

BLOCK DIAGRAM CURRENT SINKING OR SOURCING OUTPUT

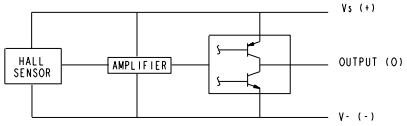

ABSOLUTE MAXIMUM CHARACTERISTICS ⚠10

CHARACTERISTIC	SYMBOL	TEST CONDITION	MIN	MAX	UNITS
SUPPLY VOLTAGE	Vcc		-0.5	11	V
OUTPUT VOLTAGE	Vout		-0.5	11	V
OUTPUT CURRENT	Iout	SOURCE OR SINK		10	mA
TEMPERATURE	TA	OPERATING	-55	150	°C
	Ts	STORAGE (Vcc=0)	-55	165	°C

NULL SHIFT VERSUS TEMPERATURE

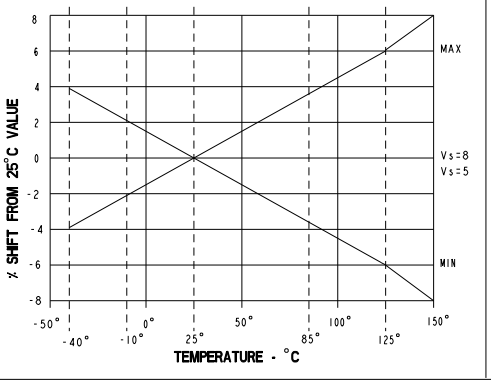

RATIO OF Vnull TO Vs

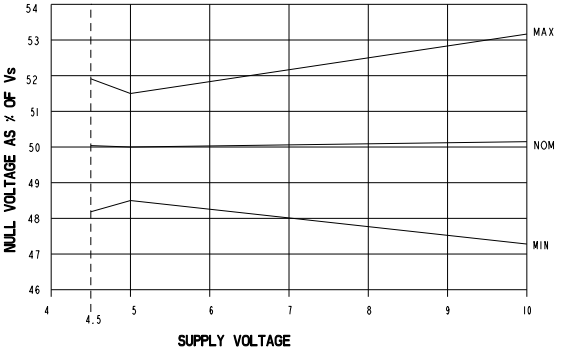

SENSITIVITY SHIFT VERSUS TEMPERATURE

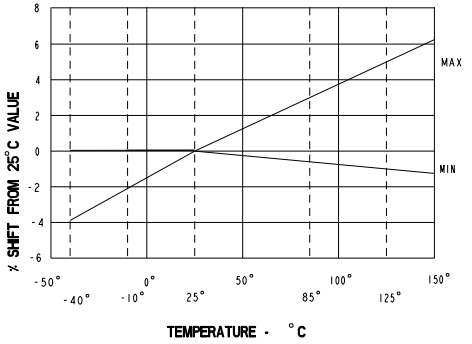

SENSITIVITY/V VERSUS Vs
(mV/GAUSS/VOLT)

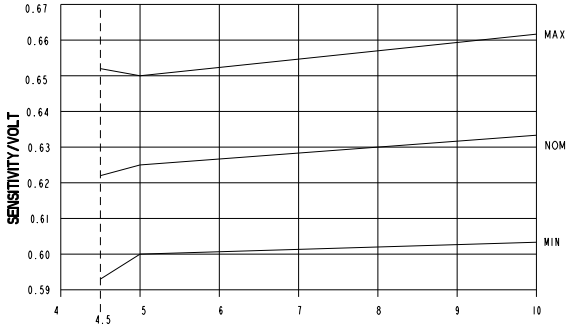

LINEARITY VERSUS Vs
END POINT OF SPAN METHOD

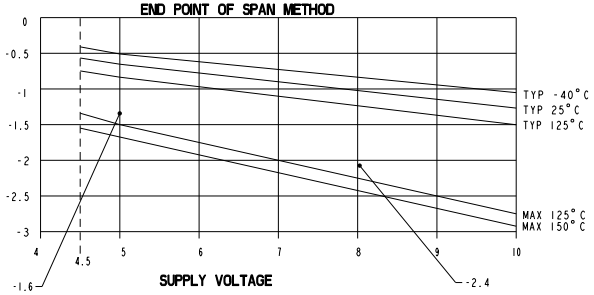

TRANSFER CHARACTERISTICS AT Vs=5.0 VDC

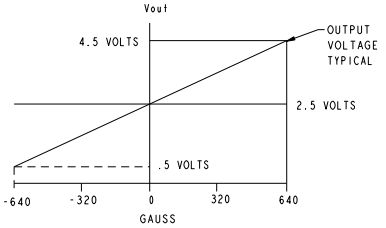

SUPPLY CURRENT VERSUS TEMPERATURE

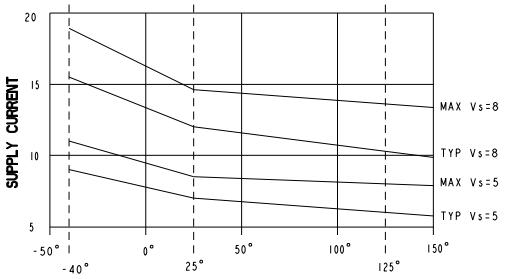

TYPICAL FREQUENCY RESPONSE
RL=33k PARALLEL WITH 100pF

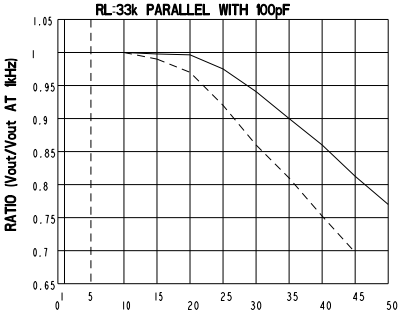

MAXIMUM ALLOWABLE AMBIENT TEMPERATURE

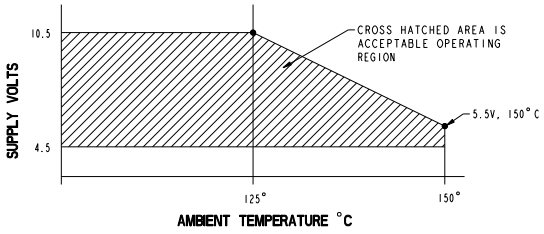

CAUTION ELECTROSTATIC SENSITIVE DEVICES
ESD SENSITIVITY: CLASS 3

ANSI Y14.5M-1982 APPLIES

FED. MFG. CODE 01929

MICRO SWITCH a Honeywell Division

MINIATURE RATIOMETRIC LINEAR HALL EFFECT SENSOR

CATALOG LISTING: SS495 SERIES CHART 1

THIRD ANGLE PROJECTION

SCALE NONE

DO NOT SCALE PRINT

UNLESS OTHERWISE SPECIFIED TOLERANCES ARE

ONE PLACE	(.0)	+.030
TWO PLACE	(.00)	+.015
THREE PLACE	(.000)	+.005
ANGLES		+2°

WEIGHT

MSS495 SERIES CHART 1 PAGE 2 OF 5 RELEASE NO. PR-21283 REVISIONS

ISSUE K4 DRAWING NO. 00-0000 CHECK

REVISIONS C 0034535 ECO 25 OCT 07

PTC/CAD 120 DRAWN C S L 12 APR 02 CHECK SAV 4 APR 02 CHECK

CHARACTERISTICS ARE AT Vs=5.00 WITH 4.7K OUTPUT TO MINUS WITH TA= -40°C TO +125°C UNLESS OTHERWISE SPECIFIED

SS495A1

PARAMETER	CONDITIONS	MIN	TYP	MAX	UNITS
SENSITIVITY	TA = 25° C	3.031	3.125	3.219	mV/GAUSS
NULL	TA = 25° C	2.425	2.50	2.575	VOLTS
SUPPLY CURRENT	TA = 25° C		7	8.7	mA
OUTPUT CURRENT SOURCE	Vs > 4.5	1mA	1.5mA		
SINK	Vs > 4.5	.6mA	1.5mA		
SINK	Vs > 5.0	1mA	1.5mA		
RESPONSE TIME			3µS		
OUTPUT VOLTAGE SWING					
VOM -	-B APPLIED	.4	.2		VOLTS
VOM +	+B APPLIED	Vs -.4	Vs -.2		VOLTS
B LIMITS FOR LINEAR	-B MAX	-600	-670		GAUSS
OPERATION	+B MAX	+600	+670		GAUSS
Vnull DRIFT	B = 0, TA = 25°C TO 125°C	-.04		+.04	% / °C
Vnull DRIFT	B = 0, TA = +125°C TO +150°C	-.08		+.08	% /°C
SENSITIVITY DRIFT	TA=+25° C TO +150° C	-.01		+.05	% /°C
SENSITIVITY DRIFT	TA=-40° C TO +25° C	0		+.06	% /°C
LINEARITY	B = -600 TO +600	0	-1.0	-1.5	% OF SPAN
SUPPLY VOLTAGE	-40°C TO +125°C	4.5	5.0	10.5	VOLTS
OPERATING TEMP	SEE MAX TEMPERATURE CHART	-40		+150	° C

BLOCK DIAGRAM CURRENT SINKING OR SOURCING OUTPUT

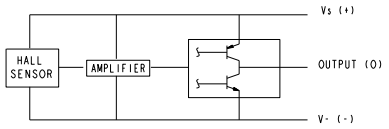

ABSOLUTE MAXIMUM CHARACTERISTICS ⚠1

CHARACTERISTIC	SYMBOL	TEST CONDITION	MIN	MAX	UNITS
SUPPLY VOLTAGE	Vcc		-0.5	11	V
OUTPUT VOLTAGE	Vout		-0.5	11	V
OUTPUT CURRENT	Iout	SOURCE OR SINK		10	mA
TEMPERATURE	TA	OPERATING	-55	150	°C
	Ts	STORAGE (Vcc=0)	-55	165	°C

NULL SHIFT VERSUS TEMPERATURE

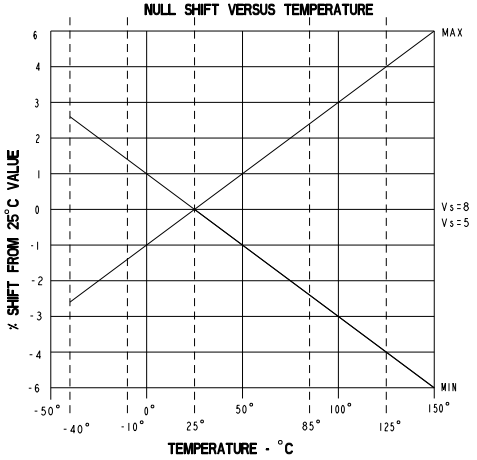

RATIO OF Vnull TO Vs

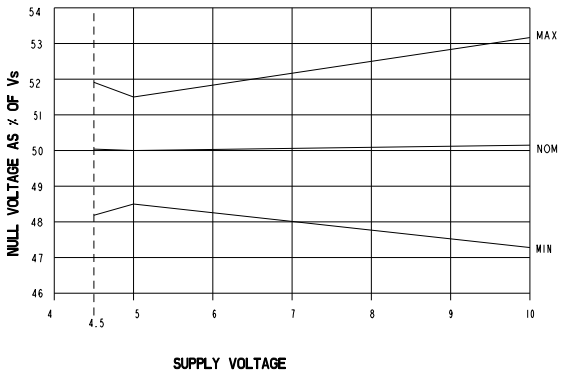

SENSITIVITY SHIFT VERSUS TEMPERATURE

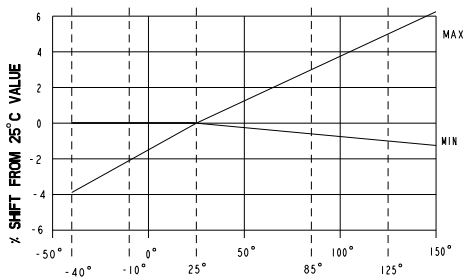

SENSITIVITY/V VERSUS Vs (mV/GAUSS/VOLT)

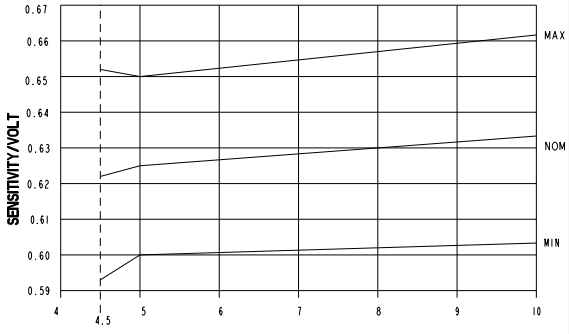

LINEARITY VERSUS Vs END POINT OF SPAN METHOD

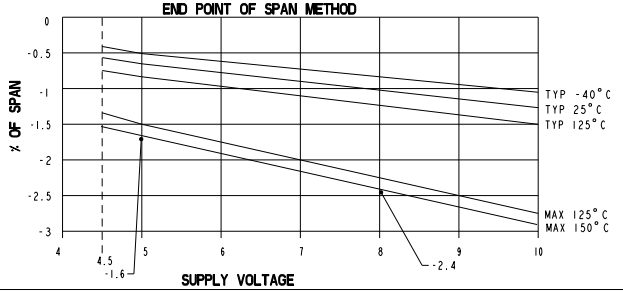

TRANSFER CHARACTERISTICS AT Vs = 5.0 VDC

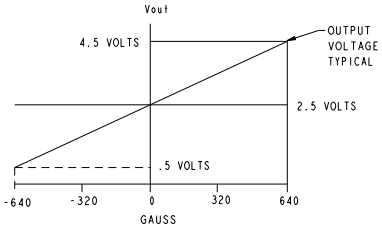

SUPPLY CURRENT VERSUS TEMPERATURE

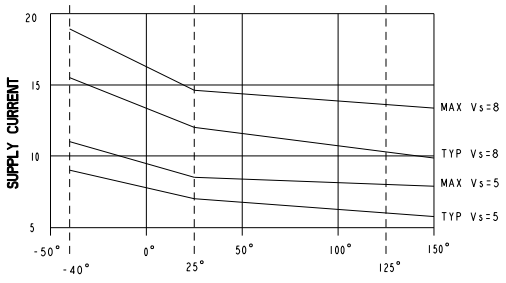

TYPICAL FREQUENCY RESPONSE RL=33k PARALLEL WITH 100pF

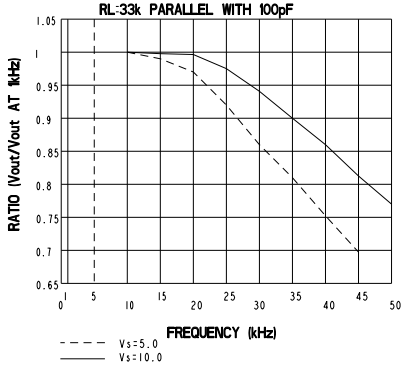

MAXIMUM ALLOWABLE AMBIENT TEMPERATURE

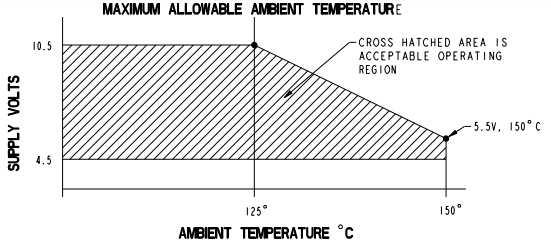

CAUTION ELECTROSTATIC SENSITIVE DEVICES DO NOT OPEN OR HANDLE EXCEPT AT A STATIC FREE WORKSTATION

ESD SENSITIVITY: CLASS 3

ANSI Y14.5M-1982 APPLIES

FED. MFG. CODE 01929

MICRO SWITCH a Honeywell Division

MINIATURE RATIOMETRIC LINEAR HALL EFFECT SENSOR

CATALOG LISTING: SS495 SERIES CHART 1

THIRD ANGLE PROJECTION

SCALE NONE

DO NOT SCALE PRINT

UNLESS OTHERWISE SPECIFIED TOLERANCES ARE

ONE PLACE	(.0)	+.030
TWO PLACE	(.00)	+.015
THREE PLACE	(.000)	+.005
ANGLES		+2°

WEIGHT

M SS495 SERIES CHART 1 | PAGE 3 OF 5 | RELEASE NO. PR-21283 | ISSUE 14 | REVISIONS C 9034535 | DRAWN C S LIS APR 02 | CHECK SAV 5 APR 02 | CHECK | PTC/CAD 20

CHARACTERISTICS ARE AT Vs:5.00 WITH 4.7K OUTPUT TO MINUS WITH TA: -40°C TO +125°C UNLESS OTHERWISE SPECIFIED

SS495A2

SS495 SERIES CHART 1

PARAMETER	CONDITIONS	MIN	TYP	MAX	UNITS
SENSITIVITY	TA = 25°C	2.969	3.125	3.281	mV/GAUSS
NULL	TA = 25°C	2.400	2.50	2.600	VOLTS
SUPPLY CURRENT	TA = 25°C		7	8.7	mA
OUTPUT CURRENT SOURCE	Vs > 4.5	1mA	1.5mA		
SINK	Vs > 4.5	.6mA	1.5mA		
SINK	Vs > 5.0	1mA	1.5mA		
RESPONSE TIME			3µS		
OUTPUT VOLTAGE SWING					
VOM -	-B APPLIED	.4	.2		VOLTS
VOM +	+B APPLIED	Vs -.4	Vs -.2		VOLTS
B LIMITS FOR LINEAR	-B MAX	-600	-670		GAUSS
OPERATION	+B MAX	+600	+670		GAUSS
Vnull DRIFT	B = 0, TA = 25°C TO 125°C	-.07		+.07	% /°C
Vnull DRIFT	B = 0, TA = +125°C TO +150°C	-.08		+.08	% /°C
SENSITIVITY DRIFT	TA=+25°C TO +150°C	-.02		+.06	% /°C
SENSITIVITY DRIFT	TA=-40°C TO +25°C	-.01		+.07	% /°C
LINEARITY	B = -600 TO +600	0	-1.0	-1.5	% OF SPAN
SUPPLY VOLTAGE	-40°C TO +125°C	4.5	5.0	10.5	VOLTS
OPERATING TEMP	SEE MAX TEMPERATURE CHART	-40		+150	°C

BLOCK DIAGRAM CURRENT SINKING OR SOURCING OUTPUT

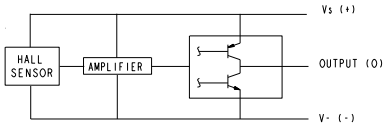

ABSOLUTE MAXIMUM CHARACTERISTICS (1)

CHARACTERISTIC	SYMBOL	TEST CONDITION	MIN	MAX	UNITS
SUPPLY VOLTAGE	Vcc		-0.5	11	V
OUTPUT VOLTAGE	Vout		-0.5	11	V
OUTPUT CURRENT	Iout	SOURCE OR SINK		10	mA
TEMPERATURE	TA	OPERATING	-55	150	°C
	Ts	STORAGE (Vcc=0)	-55	165	°C

NULL SHIFT VERSUS TEMPERATURE

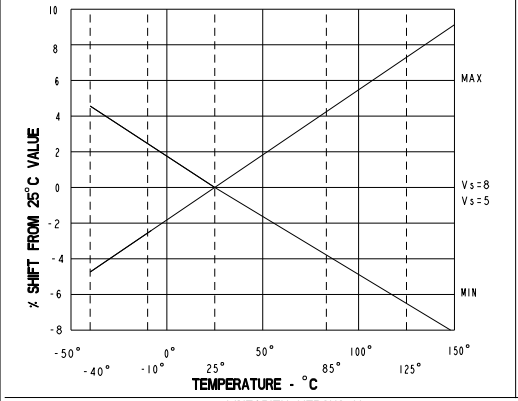

RATIO OF Vnull TO Vs

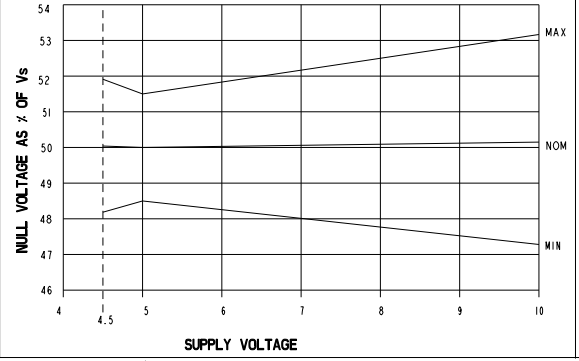

SENSITIVITY SHIFT VERSUS TEMPERATURE

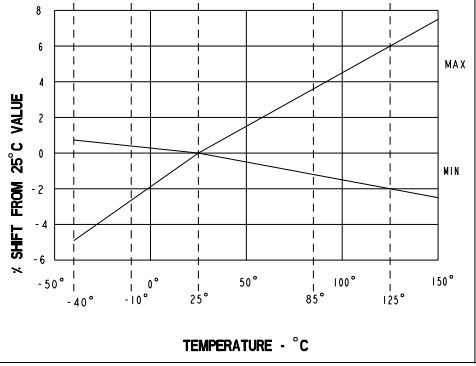

SENSITIVITY/V VERSUS Vs (mV/GAUSS/VOLT)

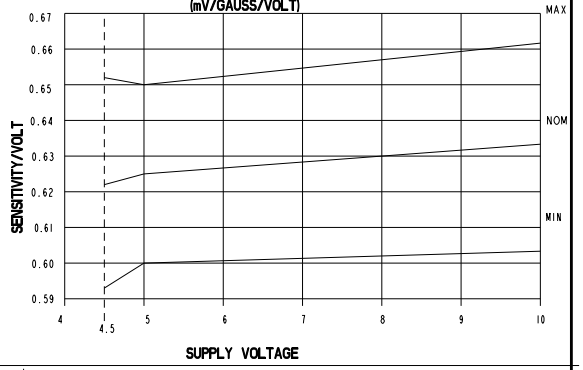

LINEARITY VERSUS Vs END POINT OF SPAN METHOD

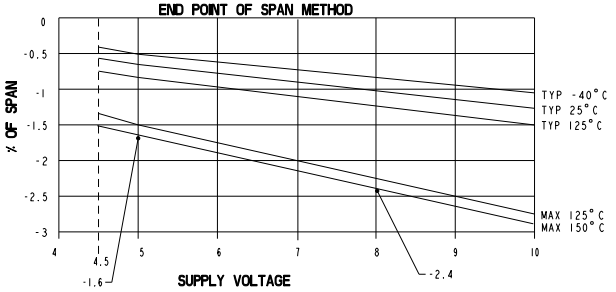

TRANSFER CHARACTERISTICS AT Vs : 5.0 VDC

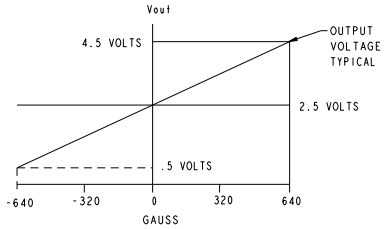

SUPPLY CURRENT VERSUS TEMPERATURE

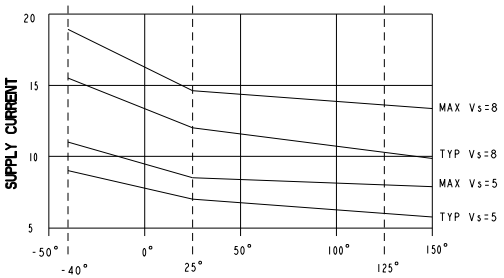

TYPICAL FREQUENCY RESPONSE RL : 33k PARALLEL WITH 100pF

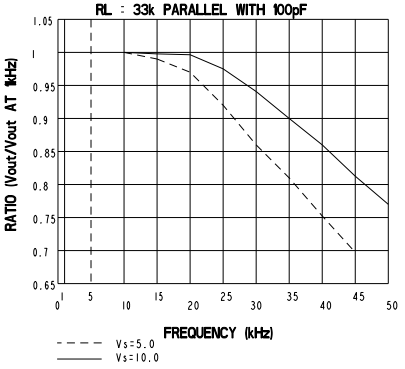

MAXIMUM ALLOWABLE AMBIENT TEMPERATURE

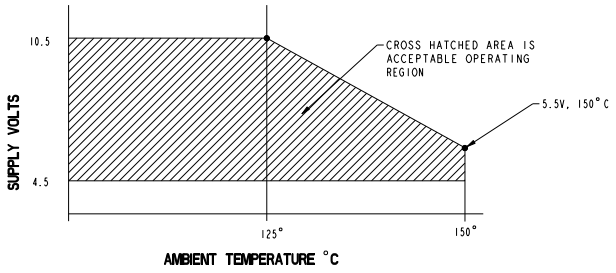

ESD SENSITIVITY: CLASS 3

ANSI Y14.5M-1982 APPLIES

FED. MFG. CODE 01929

MICRO SWITCH a Honeywell Division

MINIATURE RATIOMETRIC LINEAR HALL EFFECT SENSOR

CATALOG LISTING: SS495 SERIES CHART 1

THIRD ANGLE PROJECTION

SCALE NONE

DO NOT SCALE PRINT

UNLESS OTHERWISE SPECIFIED TOLERANCES ARE

ONE PLACE	(.0) +.030
TWO PLACE	(.00) +.015
THREE PLACE	(.000) +.005
ANGLES	+2°

WEIGHT

SS495 SERIES CHART 1 | PAGE 4 OF 5 | RELEASE NO. PR-22532 | DRAWING NUMBER 14 | ISSUE | REVISIONS C 0034535 ADE 26 OCT 07 | CHECK | SAV 5 APR 02 CHECK | C S L 15 APR 02 CHECK | DRAWN | PTC/CAD 20

CHARACTERISTICS ARE AT Vs=5.00 WITH 4.7K OUTPUT TO MINUS WITH TA: -40°C TO +125°C UNLESS OTHERWISE SPECIFIED

SS495B

SS495 SERIES CHART 1

PARAMETER	CONDITIONS	MIN	TYP	MAX	UNITS
SENSITIVITY	TA = 25°C	2.875	3.125	3.375	mV/GAUSS
NULL	TA = 25°C	2.35	2.50	2.650	VOLTS
SUPPLY CURRENT	TA = 25°C		7	8.7	mA
OUTPUT CURRENT SOURCE	Vs > 4.5	1mA	1.5mA		
SINK	Vs > 4.5	.6mA	1.5mA		
SINK	Vs > 5.0	1mA	1.5mA		
RESPONSE TIME			3µS		
OUTPUT VOLTAGE SWING					
VOM -	-B APPLIED	.4	.2		VOLTS
VOM +	+B APPLIED	Vs -.4	Vs -.2		VOLTS
B LIMITS FOR LINEAR	-B MAX	-600	-670		GAUSS
OPERATION	+B MAX	+600	+670		GAUSS
Vnull DRIFT	B = 0, TA = 25°C TO 125°C	-.08		+.08	% /°C
Vnull DRIFT	B = 0, TA = +125°C TO +150°C	-.08		+.08	% /°C
SENSITIVITY DRIFT	TA=+25° C TO +150° C	-.02		+.08	% /°C
SENSITIVITY DRIFT	TA=-40° C TO +25° C	-.02		+.08	% /°C
LINEARITY	B = -600 TO +600	0	-1.0	-1.5	% OF SPAN
SUPPLY VOLTAGE	-40° C TO +125° C	4.5	5.0	10.5	VOLTS
OPERATING TEMP	SEE MAX TEMPERATURE CHART	-40		+150	°C

BLOCK DIAGRAM CURRENT SINKING OR SOURCING OUTPUT

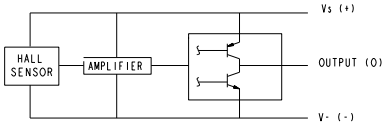

ABSOLUTE MAXIMUM CHARACTERISTICS ⚠10

CHARACTERISTIC	SYMBOL	TEST CONDITION	MIN	MAX	UNITS
SUPPLY VOLTAGE	Vcc		-0.5	11	V
OUTPUT VOLTAGE	Vout		-0.5	11	V
OUTPUT CURRENT	Iout	SOURCE OR SINK		10	mA
TEMPERATURE	TA	OPERATING	-55	150	°C
	Ts	STORAGE (Vcc=0)	-55	165	°C

NULL SHIFT VERSUS TEMPERATURE

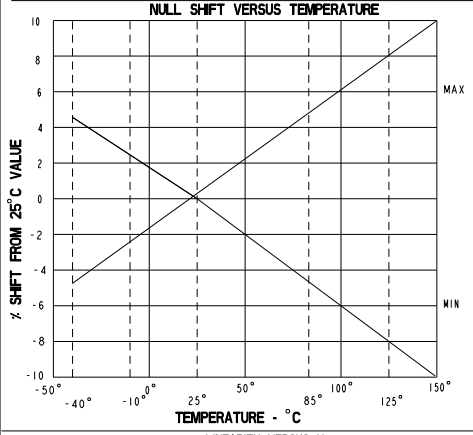

RATIO OF Vnull TO Vs

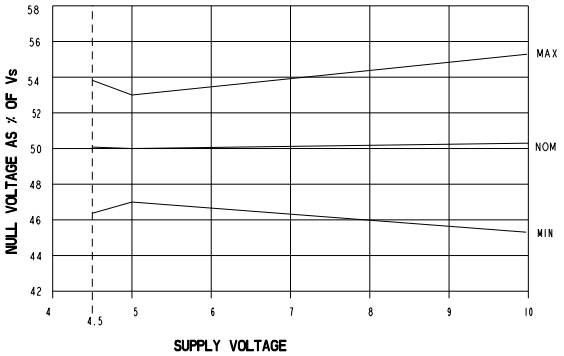

SENSITIVITY SHIFT VERSUS TEMPERATURE

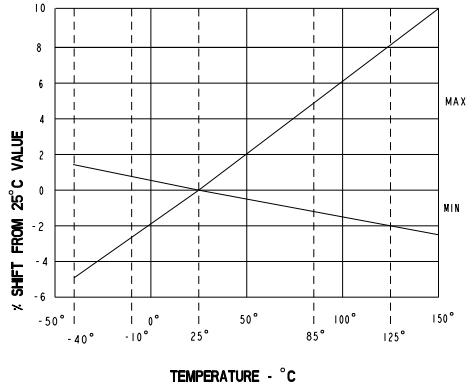

SENSITIVITY/V VERSUS Vs (mV/GAUSS/VOLT)

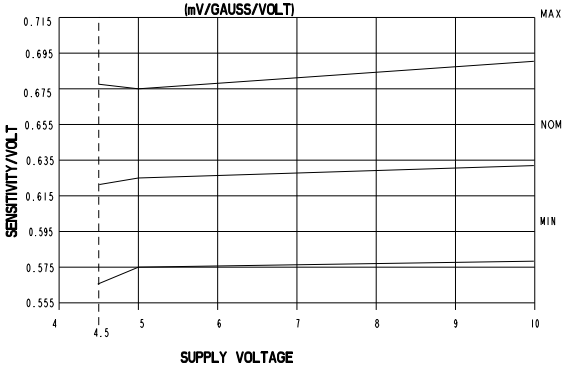

LINEARITY VERSUS Vs END POINT OF SPAN METHOD

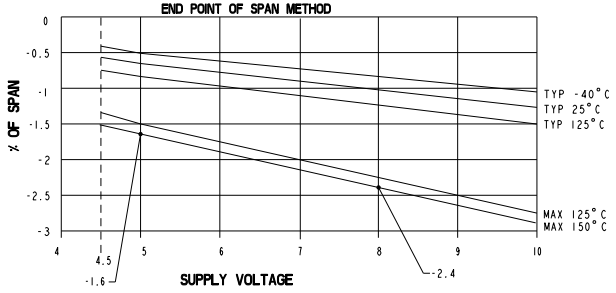

TRANSFER CHARACTERISTICS AT Vs = 5.0 VDC

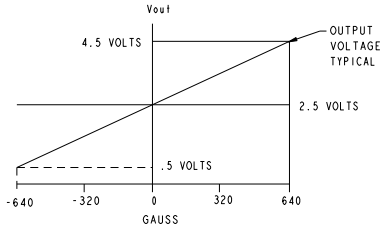

SUPPLY CURRENT VERSUS TEMPERATURE

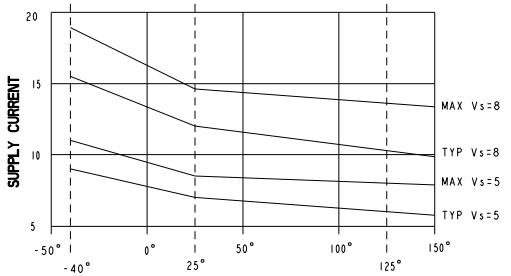

TYPICAL FREQUENCY RESPONSE RL = 33k PARALLEL WITH 100pF

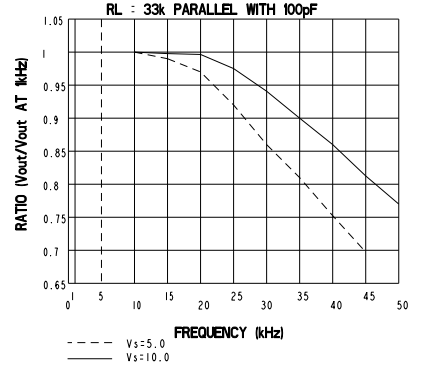

MAXIMUM ALLOWABLE AMBIENT TEMPERATURE

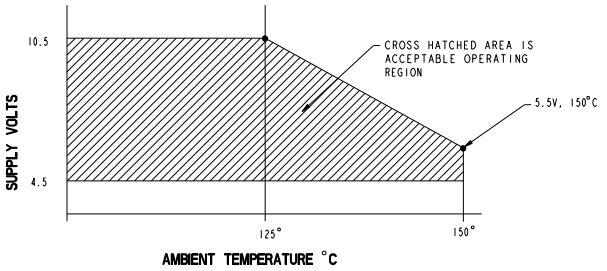

ESD SENSITIVITY: CLASS 3

ANSI Y14.5M-1982 APPLIES

FED. MFG. CODE 01929

MICRO SWITCH a Honeywell Division

MINIATURE RATIOMETRIC LINEAR HALL EFFECT SENSOR

CATALOG LISTING: SS495 SERIES CHART 1

THIRD ANGLE PROJECTION

SCALE NONE

DO NOT SCALE PRINT

UNLESS OTHERWISE SPECIFIED TOLERANCES ARE

ONE PLACE (.0) +.030

TWO PLACE (.00) +.015

THREE PLACE (.000) +.005

ANGLES +2°

WEIGHT

SS495 SERIES CHART 1 PAGE 3 OF 5 RELEASE NO. PR-21063 REVISIONS

DRAWING NUMBER 14

ISSUE

REVISIONS C 0034535 ROE 26 OCT 07

PTC/CAD 20 DRAWN C S L 15 APR 02 CHECK SAV 5 APR 02 CHECK

A.12. Datenblatt: Magnetsteller

LINEARMAGNET
Zylindermagnet

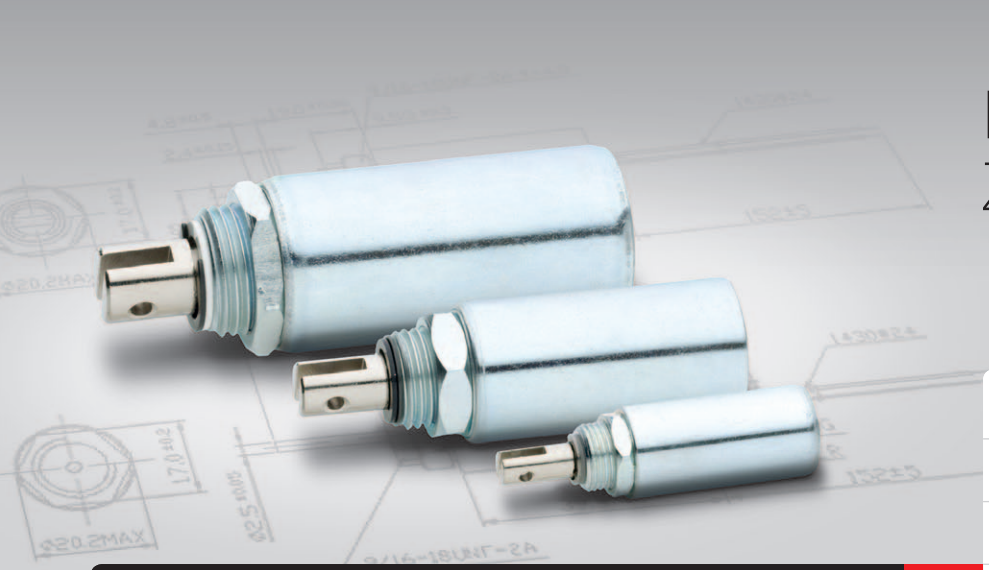

- Einbau über Montageplatte
- übersteuerbar
- extrem robust

ITS-LZ 3869

Bauform

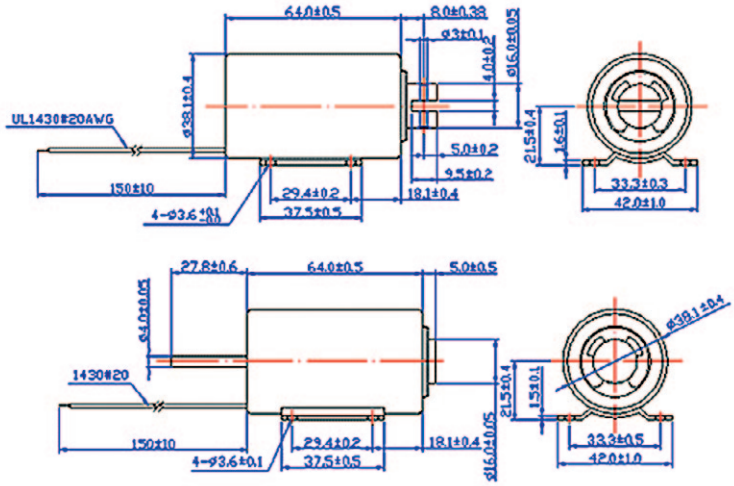

Kraft-Weg-Diagramm (N/mm)

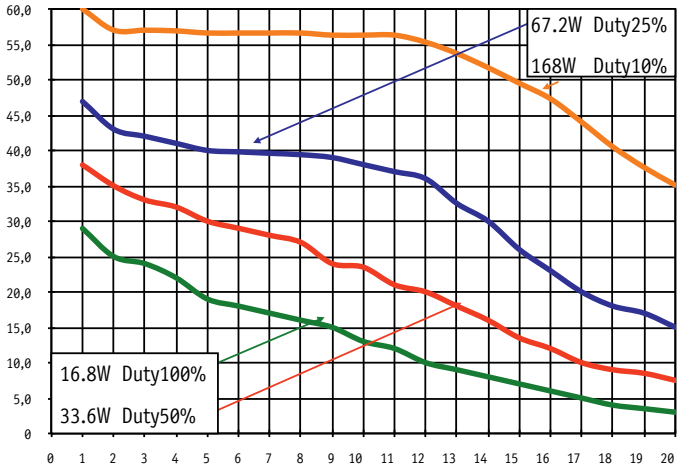

Beschreibung

Durch Ihre geschlossene Bauform haben diese einen höheren Wirkungsgrad als Bügelmagnete.

Sie können in rauer Umgebung eingesetzt werden, da das Gehäuse sehr stabil und unempfindlich ist.

Zylindermagnet, klein.
Hub 20 – 30 mm. Gewicht: 500,0 g

Spulendaten

Relative ED (Prozent)	100	50	25	10
Max. Leistung (Watt)	16,8	33,6	67,2	168
Max. ED (Sekunden)	∞	420	100	25

Magnetausführungen

Varianten:
- Zugmagnet
- Druckmagnet mit Rückholfeder

Spannungen:
- 12 VDC (standard)
- 24 VDC (standard)
- weitere Spannungsvarianten auf Anfrage

Sonderanfertigungen

Sie wollen diesen Standardmagneten abändern (z.B. Abmessungen, Kräfte usw...) dann senden Sie uns einfach dieses Formular: Checkliste (PDF, 390 kB)

RED MAGNETICS®
POWERED BY INTERTEC

Intertec Components GmbH
Fachabteilung: Red Magnetics
Erdinger Straße 45
85356 Freising
Deutschland

Kontakt:
Telefon: 0049-(0)8161-9913-0
Telefax: 0049-(0)8161-9913-20
E-Mail: service@red-magnetics.com
Info: www.red-magnetics.com

A.13. Datenblatt: MOSFET

International
IOR Rectifier

AUTOMOTIVE MOSFET

PD - 94758

IRF540Z
IRF540ZS
IRF540ZL

HEXFET® Power MOSFET

Features

- Advanced Process Technology
- Ultra Low On-Resistance
- 175°C Operating Temperature
- Fast Switching
- Repetitive Avalanche Allowed up to Tjmax

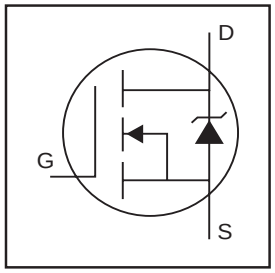

V_{DSS} = 100V

$R_{DS(on)}$ = 26.5mΩ

I_D = 36A

Description

Specifically designed for Automotive applications, this HEXFET® Power MOSFET utilizes the latest processing techniques to achieve extremely low on-resistance per silicon area. Additional features of this design are a 175°C junction operating temperature, fast switching speed and improved repetitive avalanche rating . These features combine to make this design an extremely efficient and reliable device for use in Automotive applications and a wide variety of other applications.

TO-220AB
IRF540Z

D^2Pak
IRF540ZS

TO-262
IRF540ZL

Absolute Maximum Ratings

	Parameter	Max.	Units
I_D @ T_C = 25°C	Continuous Drain Current, V_{GS} @ 10V (Silicon Limited)	36	A
I_D @ T_C = 100°C	Continuous Drain Current, V_{GS} @ 10V	25	
I_{DM}	Pulsed Drain Current ①	140	
P_D @T_C = 25°C	Power Dissipation	92	W
	Linear Derating Factor	0.61	W/°C
V_{GS}	Gate-to-Source Voltage	± 20	V
$E_{AS\ (Thermally\ limited)}$	Single Pulse Avalanche Energy②	83	mJ
E_{AS} (Tested)	Single Pulse Avalanche Energy Tested Value ⑥	120	
I_{AR}	Avalanche Current ①	See Fig.12a, 12b, 15, 16	A
E_{AR}	Repetitive Avalanche Energy ⑤		mJ
T_J	Operating Junction and	-55 to + 175	°C
T_{STG}	Storage Temperature Range		
	Soldering Temperature, for 10 seconds	300 (1.6mm from case)	
	Mounting Torque, 6-32 or M3 screw ⑦	10 lbf•in (1.1N•m)	

Thermal Resistance

	Parameter	Typ.	Max.	Units
$R_{\theta JC}$	Junction-to-Case	—	1.64	°C/W
$R_{\theta CS}$	Case-to-Sink, Flat Greased Surface ⑦	0.50	—	
$R_{\theta JA}$	Junction-to-Ambient ⑦	—	62	
$R_{\theta JA}$	Junction-to-Ambient (PCB Mount) ⑧	—	40	

10/31/03

Electrical Characteristics @ T_J = 25°C (unless otherwise specified)

	Parameter	Min.	Typ.	Max.	Units	Conditions
$V_{(BR)DSS}$	Drain-to-Source Breakdown Voltage	100	—	—	V	V_{GS} = 0V, I_D = 250µA
$\Delta V_{(BR)DSS}/\Delta T_J$	Breakdown Voltage Temp. Coefficient	—	0.093	—	V/°C	Reference to 25°C, I_D = 1mA
$R_{DS(on)}$	Static Drain-to-Source On-Resistance	—	21	26.5	mΩ	V_{GS} = 10V, I_D = 22A ③
$V_{GS(th)}$	Gate Threshold Voltage	2.0	—	4.0	V	V_{DS} = V_{GS}, I_D = 250µA
gfs	Forward Transconductance	36	—	—	V	V_{DS} = 25V, I_D = 22A
I_{DSS}	Drain-to-Source Leakage Current	—	—	20	µA	V_{DS} = 100V, V_{GS} = 0V
		—	—	250		V_{DS} = 100V, V_{GS} = 0V, T_J = 125°C
I_{GSS}	Gate-to-Source Forward Leakage	—	—	200	nA	V_{GS} = 20V
	Gate-to-Source Reverse Leakage	—	—	-200		V_{GS} = -20V
Q_g	Total Gate Charge	—	42	63		I_D = 22A
Q_{gs}	Gate-to-Source Charge	—	9.7	—	nC	V_{DS} = 80V
Q_{gd}	Gate-to-Drain ("Miller") Charge	—	15	—		V_{GS} = 10V ③
$t_{d(on)}$	Turn-On Delay Time	—	15	—		V_{DD} = 50V
t_r	Rise Time	—	51	—		I_D = 22A
$t_{d(off)}$	Turn-Off Delay Time	—	43	—	ns	R_G = 12 Ω
t_f	Fall Time	—	39	—		V_{GS} = 10V ③
L_D	Internal Drain Inductance	—	4.5	—		Between lead,
					nH	6mm (0.25in.)
L_S	Internal Source Inductance	—	7.5	—		from package
						and center of die contact
C_{iss}	Input Capacitance	—	1770	—		V_{GS} = 0V
C_{oss}	Output Capacitance	—	180	—		V_{DS} = 25V
C_{rss}	Reverse Transfer Capacitance	—	100	—	pF	f = 1.0MHz
C_{oss}	Output Capacitance	—	730	—		V_{GS} = 0V, V_{DS} = 1.0V, f = 1.0MHz
C_{oss}	Output Capacitance	—	110	—		V_{GS} = 0V, V_{DS} = 80V, f = 1.0MHz
C_{oss} eff.	Effective Output Capacitance	—	170	—		V_{GS} = 0V, V_{DS} = 0V to 80V ④

Source-Drain Ratings and Characteristics

	Parameter	Min.	Typ.	Max.	Units	Conditions
I_S	Continuous Source Current	—	—	36		MOSFET symbol
	(Body Diode)				A	showing the
I_{SM}	Pulsed Source Current	—	—	140		integral reverse
	(Body Diode) ①					p-n junction diode.
V_{SD}	Diode Forward Voltage	—	—	1.3	V	T_J = 25°C, I_S = 22A, V_{GS} = 0V ③
t_{rr}	Reverse Recovery Time	—	33	50	ns	T_J = 25°C, I_F = 22A, V_{DD} = 50V
Q_{rr}	Reverse Recovery Charge	—	41	62	nC	di/dt = 100A/µs ③
t_{on}	Forward Turn-On Time	Intrinsic turn-on time is negligible (turn-on is dominated by LS+LD)				

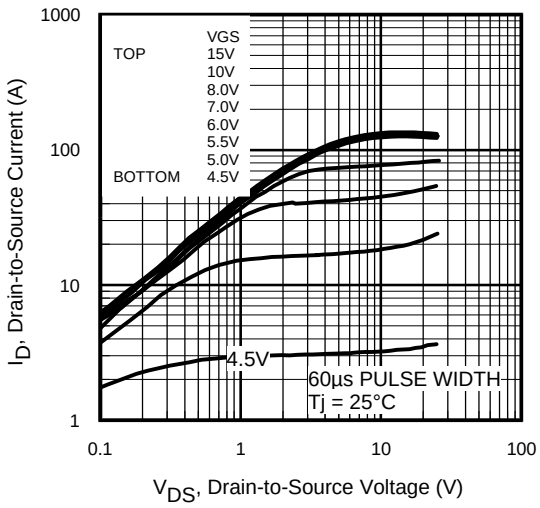

Fig 1. Typical Output Characteristics

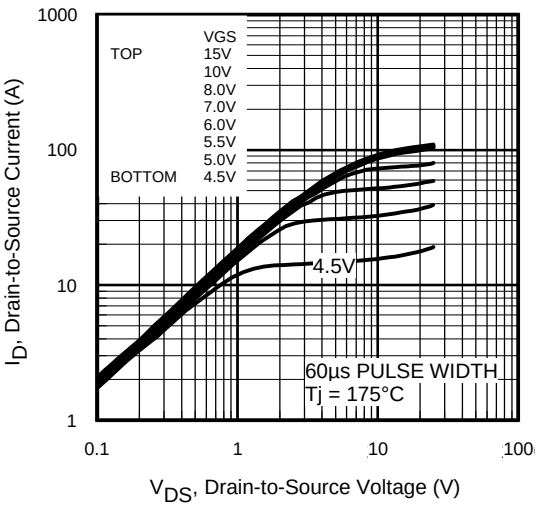

Fig 2. Typical Output Characteristics

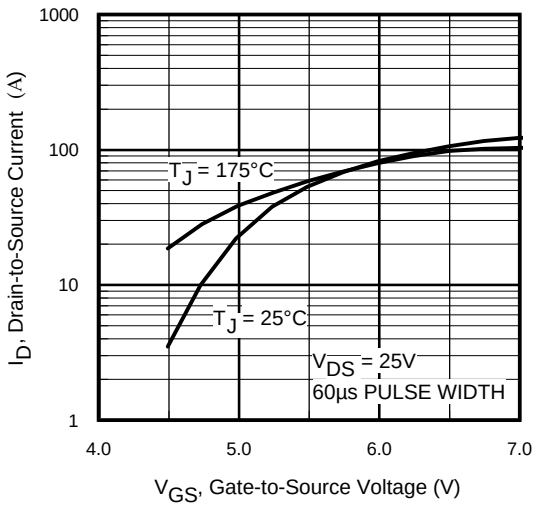

Fig 3. Typical Transfer Characteristics

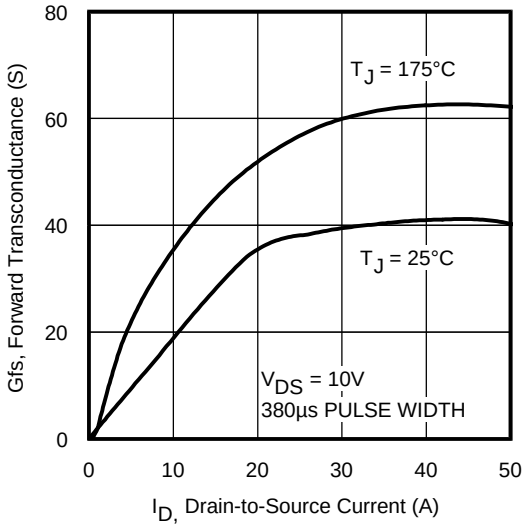

Fig 4. Typical Forward Transconductance Vs. Drain Current

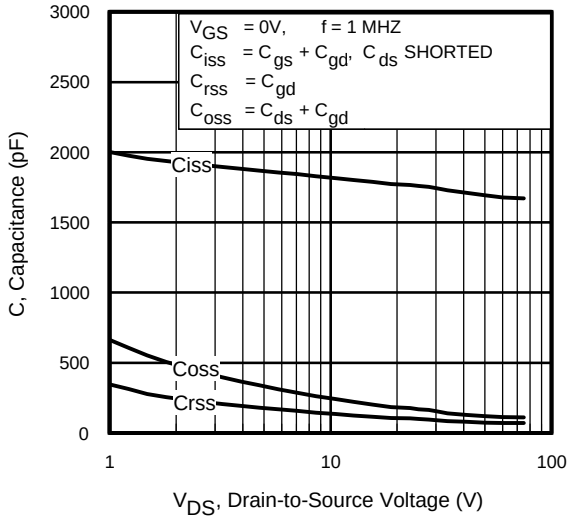

Fig 5. Typical Capacitance Vs. Drain-to-Source Voltage

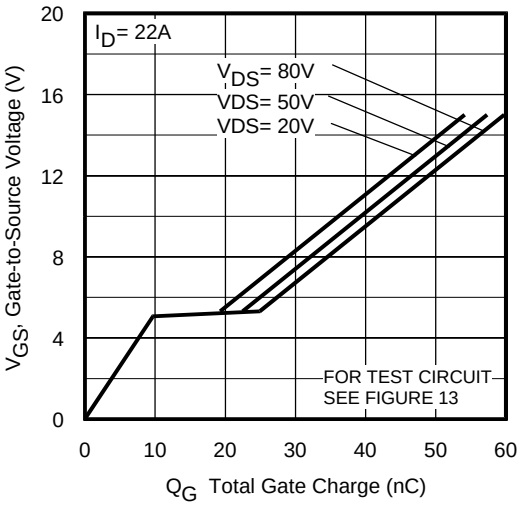

Fig 6. Typical Gate Charge Vs. Gate-to-Source Voltage

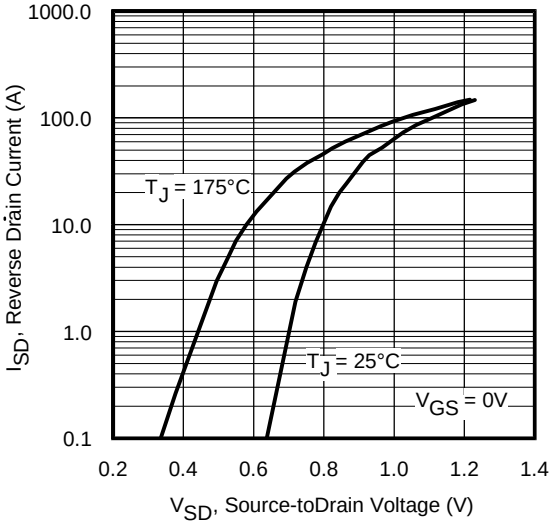

Fig 7. Typical Source-Drain Diode Forward Voltage

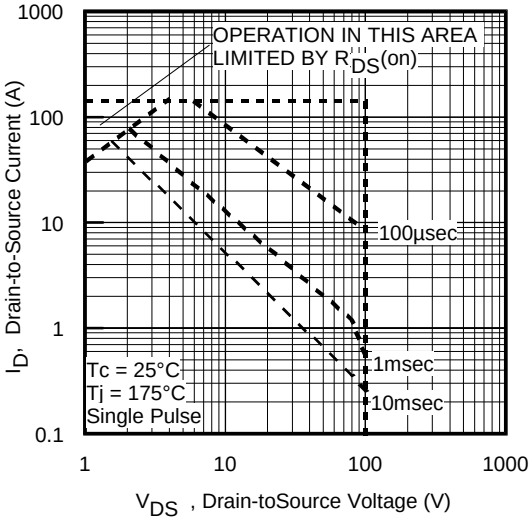

Fig 8. Maximum Safe Operating Area

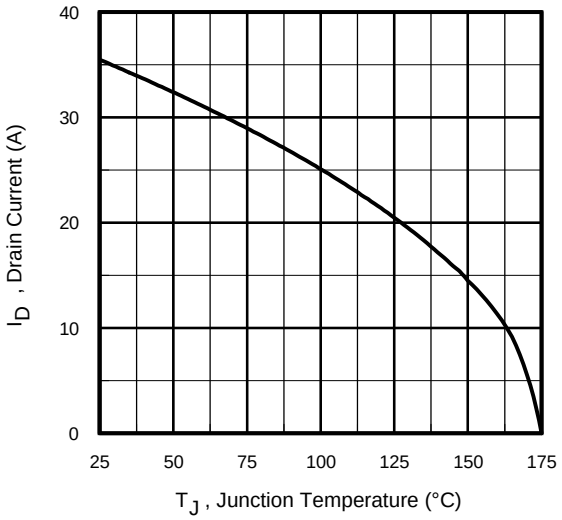

Fig 9. Maximum Drain Current Vs. Case Temperature

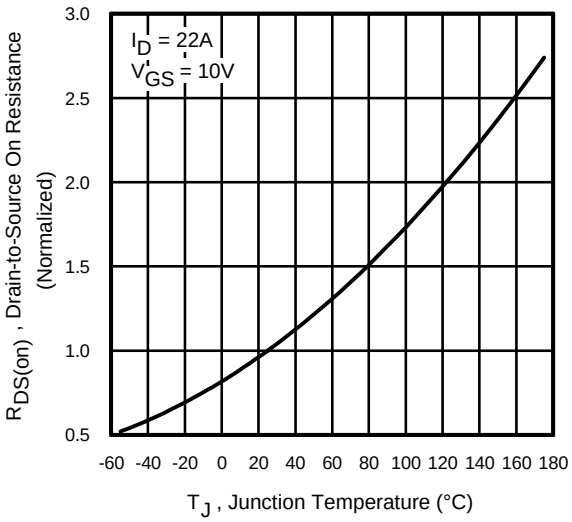

Fig 10. Normalized On-Resistance Vs. Temperature

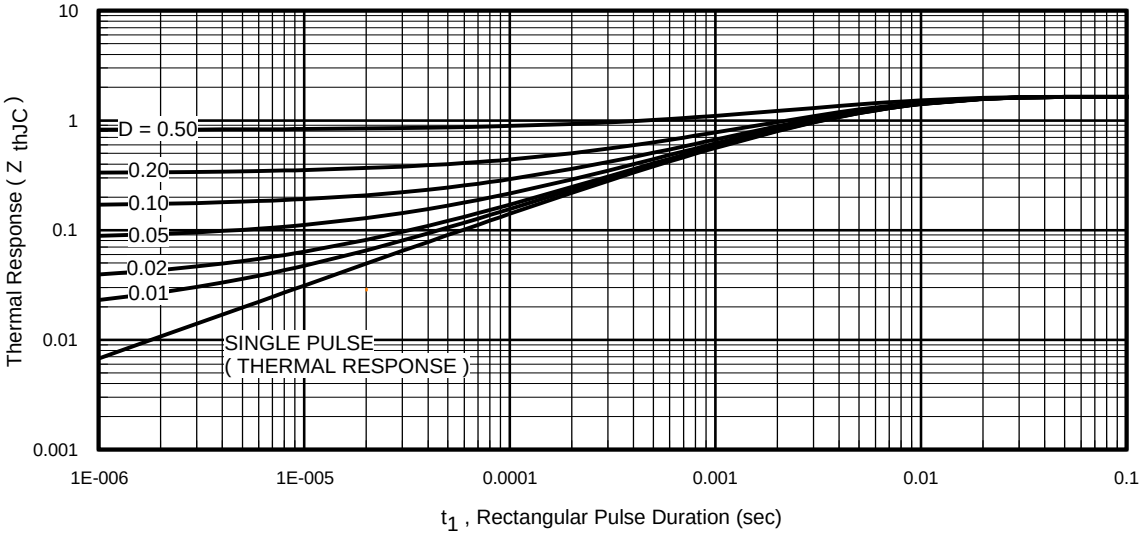

Fig 11. Maximum Effective Transient Thermal Impedance, Junction-to-Case

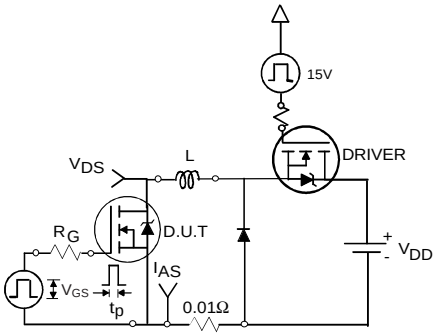

Fig 12a. Unclamped Inductive Test Circuit

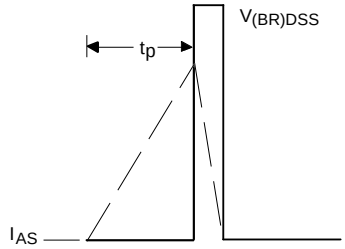

Fig 12b. Unclamped Inductive Waveforms

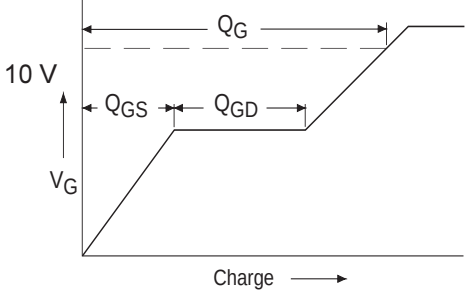

Fig 13a. Basic Gate Charge Waveform

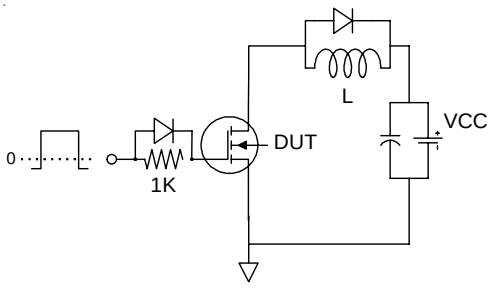

Fig 13b. Gate Charge Test Circuit

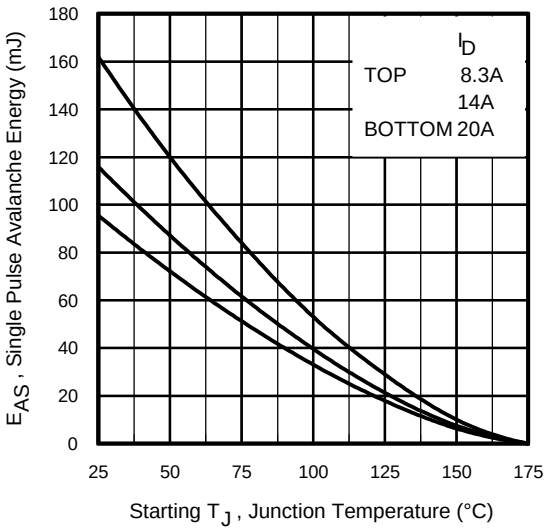

Fig 12c. Maximum Avalanche Energy Vs. Drain Current

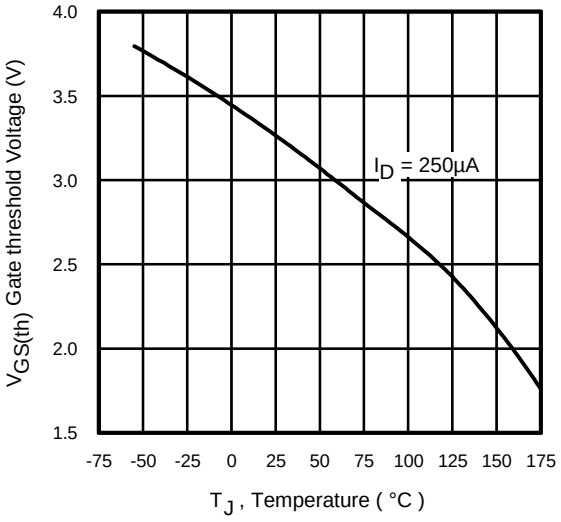

Fig 14. Threshold Voltage Vs. Temperature

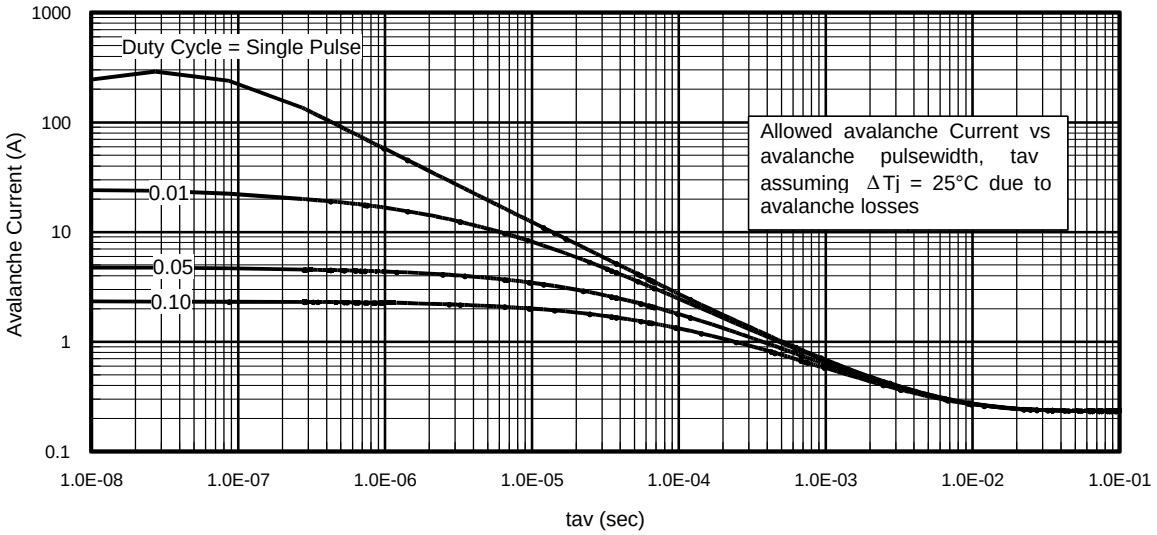

Fig 15. Typical Avalanche Current Vs.Pulsewidth

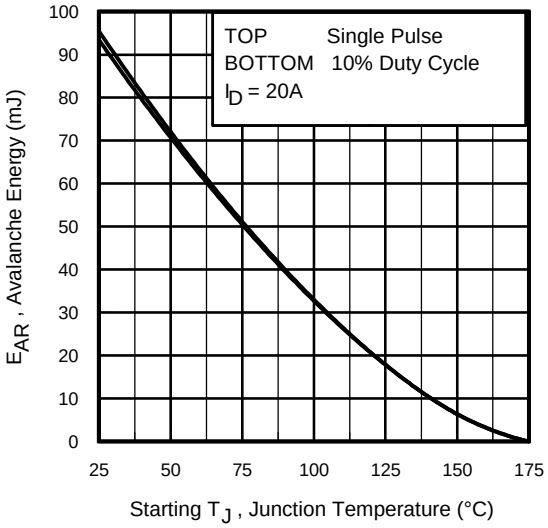

Fig 16. Maximum Avalanche Energy Vs. Temperature

Notes on Repetitive Avalanche Curves , Figures 15, 16:
(For further info, see AN-1005 at www.irf.com)

1. Avalanche failures assumption:
   Purely a thermal phenomenon and failure occurs at a temperature far in excess of T_{jmax}. This is validated for every part type.
2. Safe operation in Avalanche is allowed as long asT_{jmax} is not exceeded.
3. Equation below based on circuit and waveforms shown in Figures 12a, 12b.
4. $P_{D\ (ave)}$ = Average power dissipation per single avalanche pulse.
5. BV = Rated breakdown voltage (1.3 factor accounts for voltage increase during avalanche).
6. I_{av} = Allowable avalanche current.
7. ΔT = Allowable rise in junction temperature, not to exceed T_{jmax} (assumed as 25°C in Figure 15, 16).
   t_{av} = Average time in avalanche.
   D = Duty cycle in avalanche = $t_{av} \cdot f$
   $Z_{thJC}(D, t_{av})$ = Transient thermal resistance, see figure 11)

$$P_{D\ (ave)} = 1/2\ (\ 1.3 \cdot BV \cdot I_{av}) = \Delta T / Z_{thJC}$$
$$I_{av} = 2\Delta T / [1.3 \cdot BV \cdot Z_{th}]$$
$$E_{AS\ (AR)} = P_{D\ (ave)} \cdot t_{av}$$

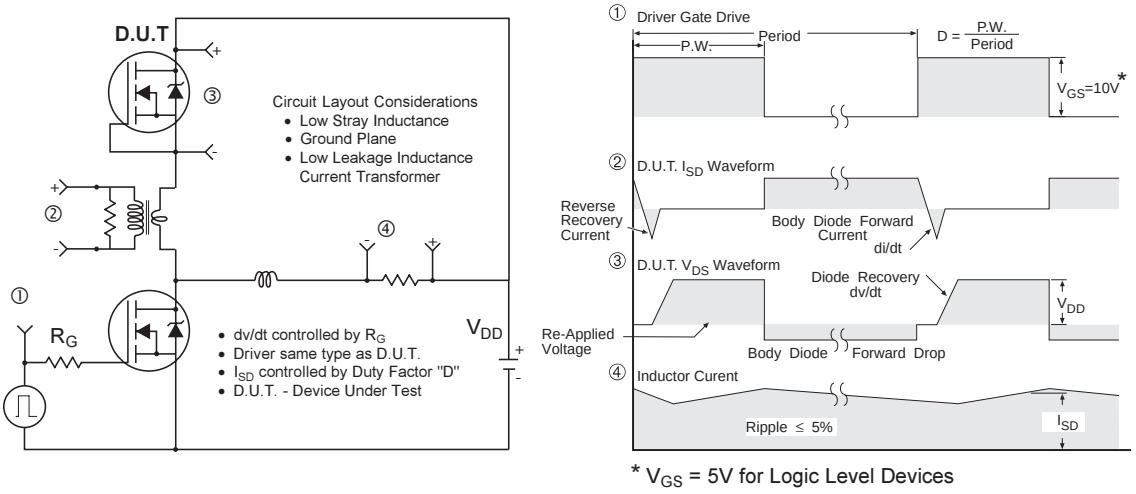

Fig 17. Peak Diode Recovery dv/dt Test Circuit for N-Channel HEXFET® Power MOSFETs

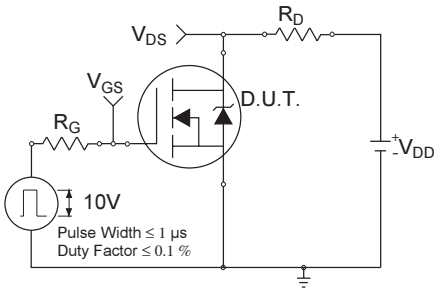

Fig 18a. Switching Time Test Circuit

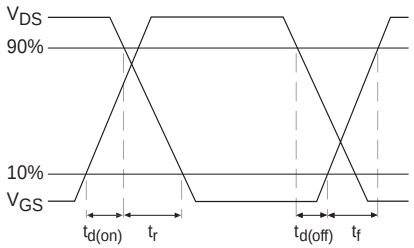

Fig 18b. Switching Time Waveforms

TO-220AB Package Outline

Dimensions are shown in millimeters (inches)

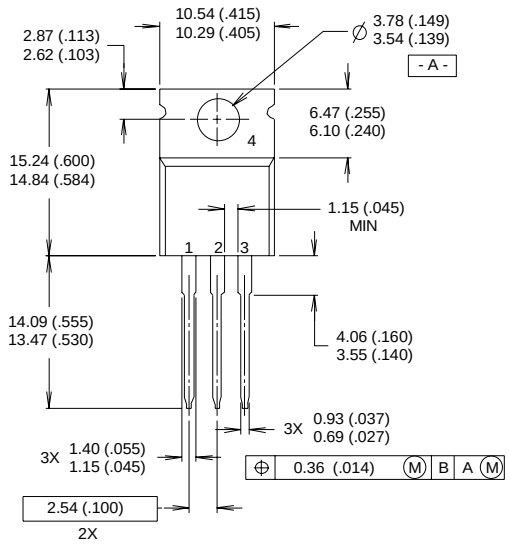

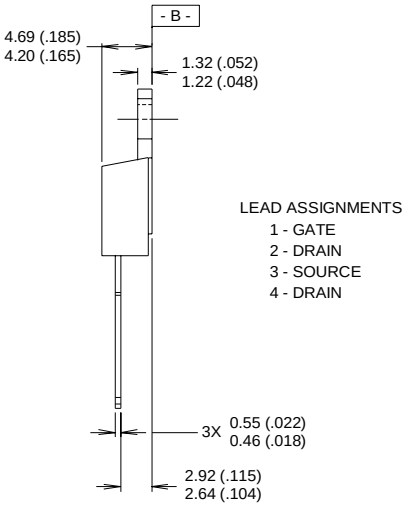

NOTES:

1 DIMENSIONING & TOLERANCING PER ANSI Y14.5M, 1982.
2 CONTROLLING DIMENSION : INCH
3 OUTLINE CONFORMS TO JEDEC OUTLINE TO-220AB.
4 HEATSINK & LEAD MEASUREMENTS DO NOT INCLUDE BURRS.

TO-220AB Part Marking Information

EXAMPLE: THIS IS AN IRF1010
LOT CODE 1789
ASSEMBLED ON WW 19, 1997
IN THE ASSEMBLY LINE "C"

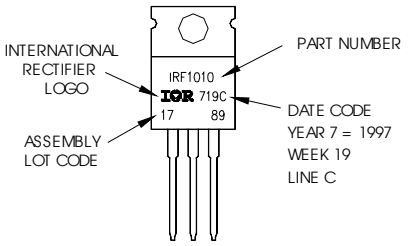

For GB Production

EXAMPLE: THIS IS AN IRF1010
LOT CODE 1789
ASSEMBLED ON WW 19, 1997
IN THE ASSEMBLY LINE "C"

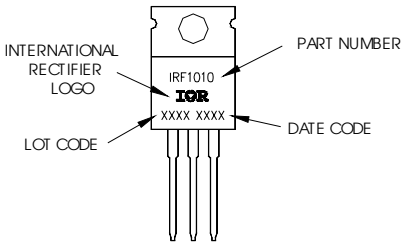

International
IOR Rectifier

D²Pak Package Outline

Dimensions are shown in millimeters (inches)

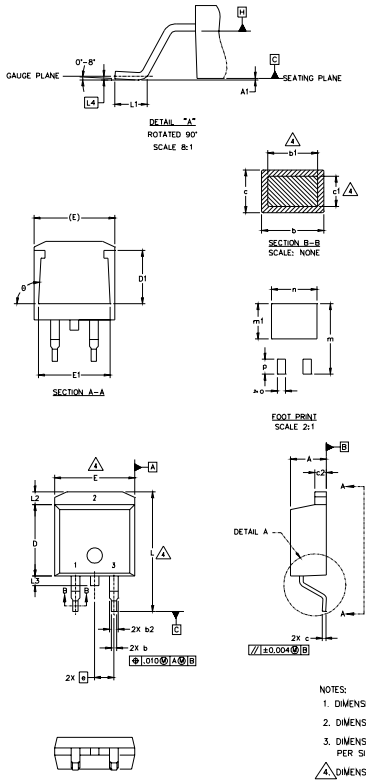

SYMBOL	DIMENSIONS				NOTES
	MILLIMETERS		INCHES		
	MIN.	MAX.	MIN.	MAX.	
A	4.06	4.83	.160	.190	
A1		0.127		.005	
b	0.51	0.99	.020	.039	
b1	0.51	0.89	.020	.035	4
b2	1.14	1.40	.045	.055	
c	0.43	0.63	.017	.025	
c1	0.38	0.74	.015	.029	4
c2	1.14	1.40	.045	.055	
D	8.51	9.65	.335	.380	3
D1	5.33		.210		
E	9.65	10.67	.380	.420	3
E1	6.22		.245		
e	2.54 BSC		.100 BSC		
L	14.61	15.88	.575	.625	
L1	1.78	2.79	.070	.110	
L2		1.65		.065	
L3	1.27	1.78	.050	.070	
L4	0.25 BSC		.010 BSC		
m	17.78		.700		
m1	8.89		.350		
n	11.43		.450		
o	2.08		.082		
p	3.81		.150		
θ	90°	93°	90°	93°	

LEAD ASSIGNMENTS

HEXFET	IGBTs, CoPACK	DIODES
1.– GATE	1.– GATE	1.– ANODE *
2.– DRAIN	2.– COLLECTOR	2.– CATHODE
3.– SOURCE	3.– EMITTER	3.– ANODE

* PART DEPENDENT.

NOTES:
1. DIMENSIONING AND TOLERANCING PER ASME Y14.5M–1994
2. DIMENSIONS ARE SHOWN IN MILLIMETERS [INCHES].
3. DIMENSION D & E DO NOT INCLUDE MOLD FLASH. MOLD FLASH SHALL NOT EXCEED 0.127 [.005"] PER SIDE. THESE DIMENSIONS ARE MEASURED AT THE OUTMOST EXTREMES OF THE PLASTIC BODY.
4. DIMENSION b1 AND c1 APPLY TO BASE METAL ONLY.
5. CONTROLLING DIMENSION: INCH.

D²Pak Part Marking Information

EXAMPLE: THIS IS AN IRF530S WITH
LOT CODE 8024
ASSEMBLED ON WW 02, 2000
IN THE ASSEMBLY LINE "L"

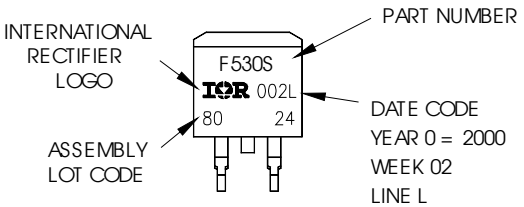

For GB Production

EXAMPLE: THIS IS AN IRF530S WITH
LOT CODE 8024
ASSEMBLED ON WW 02, 2000
IN THE ASSEMBLY LINE "L"

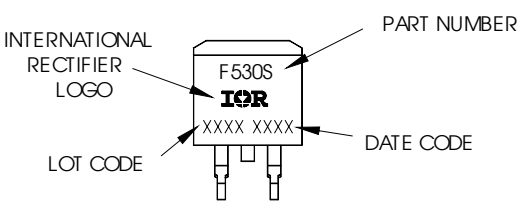

TO-262 Package Outline

Dimensions are shown in millimeters (inches)

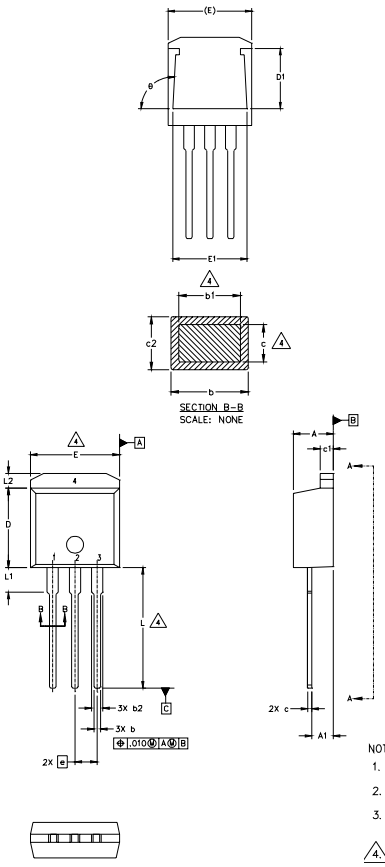

SYMBOL	DIMENSIONS				NOTES
	MILLIMETERS		INCHES		
	MIN.	MAX.	MIN.	MAX.	
A	4.06	4.83	.160	.190	
A1	2.03	2.92	.080	.115	
b	0.51	0.99	.020	.039	
b1	0.51	0.89	.020	.035	4
b2	1.14	1.40	.045	.055	
c	0.38	0.63	.015	.025	4
c1	1.14	1.40	.045	.055	
c2	0.43	.063	.017	.029	
D	8.51	9.65	.335	.380	3
D1	5.33		.210		
E	9.65	10.67	.380	.420	3
E1	6.22		.245		
e	2.54 BSC		.100 BSC		
L	13.46	14.09	.530	.555	
L1	3.56	3.71	.140	.146	
L2		1.65		.065	

LEAD ASSIGNMENTS

HEXFET	IGBT
1.– GATE	1- GATE
2.– DRAIN	2- COLLECTOR
3.– SOURCE	
4.– DRAIN	

NOTES:

1. DIMENSIONING AND TOLERANCING PER ASME Y14.5M–1994
2. DIMENSIONS ARE SHOWN IN MILLIMETERS [INCHES].
3. DIMENSION D & E DO NOT INCLUDE MOLD FLASH. MOLD FLASH SHALL NOT EXCEED 0.127 [.005"] PER SIDE. THESE DIMENSIONS ARE MEASURED AT THE OUTMOST EXTREMES OF THE PLASTIC BODY.
4. DIMENSION b1 AND c1 APPLY TO BASE METAL ONLY.
5. CONTROLLING DIMENSION: INCH.

TO-262 Part Marking Information

EXAMPLE: THIS IS AN IRL3103L
LOT CODE 1789
ASSEMBLED ON WW 19, 1997
IN THE ASSEMBLY LINE "C"

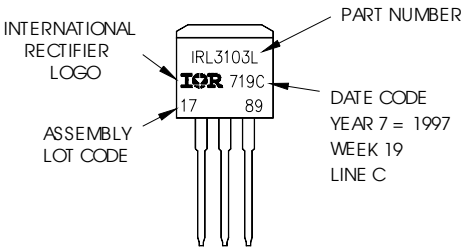

D²Pak Tape & Reel Information

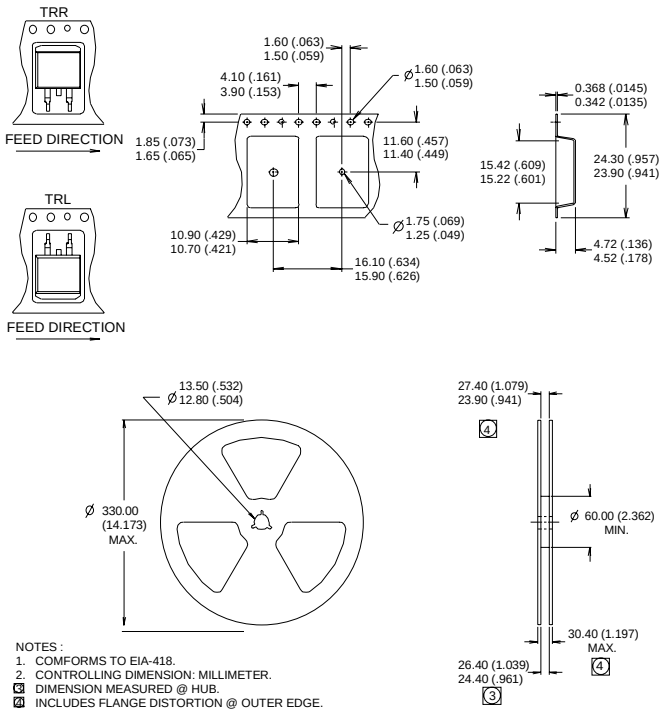

Notes:

① Repetitive rating; pulse width limited by max. junction temperature. (See fig. 11).

② Limited by T_{Jmax}, starting T_J = 25°C, L = 0.46mH R_G = 25Ω, I_{AS} = 20A, V_{GS} =10V. Part not recommended for use above this value.

③ Pulse width ≤ 1.0ms; duty cycle ≤ 2%.

④ C_{oss} eff. is a fixed capacitance that gives the same charging time as C_{oss} while V_{DS} is rising from 0 to 80% V_{DSS} .

⑤ Limited by T_{Jmax} , see Fig.12a, 12b, 15, 16 for typical repetitive avalanche performance.

⑥ This value determined from sample failure population. 100% tested to this value in production.

⑦ This is only applied to TO-220AB pakcage.

⑧ This is applied to D²Pak, when mounted on 1" square PCB (FR-4 or G-10 Material). For recommended footprint and soldering techniques refer to application note #AN-994.

TO-220AB package is not recommended for Surface Mount Application.

Data and specifications subject to change without notice.
This product has been designed and qualified for the Automotive [Q101]market.
Qualification Standards can be found on IR's Web site.

International
IOR Rectifier

IR WORLD HEADQUARTERS: 233 Kansas St., El Segundo, California 90245, USA Tel: (310) 252-7105
TAC Fax: (310) 252-7903
Visit us at www.irf.com for sales contact information. 10/03

A.14. Ansteuerung der Rückströmklappe

```
#include <avr/io.h>
#include <stdlib.h>
#include <stdint.h>
#ifndef F_CPU
/* Definiere F_CPU, wenn F_CPU nicht bereits vorher definiert
   (z. B. durch Übergabe als Parameter zum Compiler innerhalb
   des Makefiles). Zusätzlich Ausgabe einer Warnung, die auf die
   "nachträgliche" Definition hinweist */
#warning "F_CPU war noch nicht definiert, wird nun mit 8000000 definiert"
#define F_CPU 8000000UL     /* 8 Mhz */
#endif
#include <util/delay.h>     /* in älteren avr-libc Versionen <avr/delay.h>
#include <avr/interrupt.h>


void ADC_Init(uint8_t mux) {

  uint16_t result;

  ADMUX = mux;  // Kanal waehlen
  ADMUX |= (0<<ADLAR);
  ADMUX |= (0<<REFS1) | (0<<REFS0); // externe Referenz == VCC , mißt also

  ADCSRA = (1<<ADEN) | (1<<ADPS1) | (1<<ADPS0) | (1<<ADPS2);    // Frequenz
                              // setzen auf 128 (1) und ADC aktivieren (1)
                              //Samplingfrequenz 125kHz
  ADCSRA |= (0<<ADFR);      //single conversion mode

  /* nach Aktivieren des ADC wird ein "Dummy-Readout" empfohlen, man liest
     also einen Wert und verwirft diesen, um den ADC "warmlaufen zu lassen"
  ADCSRA |= (1<<ADSC);                // eine ADC-Wandlung
  while ( ADCSRA & (1<<ADSC) ) {
     ;     // auf Abschluss der Konvertierung warten
  }
  result = ADCW;  // ADCW muss einmal gelesen werden,
                  // sonst wird Ergebnis der nächsten Wandlung
                  // nicht übernommen.
}

//A/D Wandlung durchführen
uint16_t ReadChannel(uint8_t mux)
{

  uint8_t i;
  uint16_t result;

  ADMUX= (ADMUX & ~(0x1F)) | (mux & (0x1F));

  /* Eigentliche Messung - Mittelwert aus x aufeinanderfolgenden Wandlungen
  result = 0;
  for( i=0; i<1; i++ )
  {
    ADCSRA |= (1<<ADSC);            // eine Wandlung "single conversion"
    while ( ADCSRA & (1<<ADSC) ) {
      ;   // auf Abschluss der Konvertierung warten
    }
    result += ADCW;         // Wandlungsergebnisse aufaddieren
  }
  //ADCSRA &= ~(1<<ADEN);             // ADC deaktivieren (2)

  //result /= 1;                     // Summe durch x teilen = arithm. Mitt


  return result;
}


void long_delay_ms(uint16_t ms)
{
    for(; ms>0; ms--) _delay_ms(1);
}
```

```
int main(void){

// Deklaration Variablen
uint16 t V act=0;
uint16 t V min=0;
uint16_t V_max=0;
uint16_t V trig=100;
double time until open=0;
double open time=0;
double time until close=0;
double close time=0;
double time until idle=0;
uint16 t half cycle_tics=0;
uint16_t count=0;
double cycle_time_ms=0;

// Setzen der Data Direction Register (input oder output)
DDRB=0b00111111;
DDRC=0b11111110;
DDRD=0b10111111;

// Initialisieren ADC
ADC_Init(0);

// Definition Parameter Klappenbewegung

#define shift phase 50
#define close_phase 90


#define open period 36
#define close_period 36
#define idle_gap 10


//Initialisierung von Timer1 (16bit)
  TCCR1B = 0b00000101; // Prescaler 1024


//Definition Parameter zum Programmablauf
#define init_time 10000         // Initialisierungszeit in ms bei Delay=1ms

//Initialisierung zum Bestimmen von Maximum. Minimum und Frequenz
#define peak_range 20

//TCNT1H= 0b00000000;
//TCNT1L= 0b00000000;
//for( count=0; count<35000; count++ )
//{
V_act=ReadChannel(0);
//}
//count=TCNT1;
//PORTD=count;

while(V act < V trig){                  // Warten bis irgendwas beim Signal
    V_act=ReadChannel(0);
}
V_min=V_act;//+peak_range;
V_max=V_act;//-peak_range;


//PORTD=4;
// delay ms(1000);
//PORTD=2;
// delay ms(1000);
//PORTD=1;
// delay ms(1000);
//PORTD=0;

//while(act time<init time){
for( count=0; count<init_time; count++ )            // Max_Zähler/increment
```

```
{
    V_act=ReadChannel(0);
    //PORTD=0;
    if(V_act>V_max){
        V_max=V_act;
    }
    if(V_act>V_max-peak_range){
        TCNT1H= 0b00000000;
        TCNT1L= 0b00000000;
        //PORTD=8;
    }
    if(V_act<V_min){
        V_min=V_act;
    }
    if(V_act<V_min+peak_range){
        half_cycle_tics=TCNT1;
        //PORTD=4;
    }
    _delay_us(375);         //weniger als eine ms da andere Operationen in
}


cycle_time_ms=half_cycle_tics*2*0.1285;

time until open=cycle time ms*shift phase/360;
open time=cycle time ms*open period/360;
time until close=cycle time ms*(close phase-open_period)/360;
close time=cycle time ms*close period/360;
time until idle=cycle time ms*(360-close_phase-close_period-shift_phase-idl
//time until open=cycle time_ms/4;
//open time=cycle time ms/4;
//time until close=cycle time_ms/4;
//close_time=cycle_time_ms/5;


ADCSRA &= ~(1<<ADEN);                   // ADC deaktivieren damit analoger Comp
SFIOR |= (1<<ACME);                     //Auswahl des negativen Comparator über
ADMUX &= ~((1<<MUX3)|(1<<MUX2)|(1<<MUX1)|(1<<MUX0));
ACSR &= ~(1<<ACD);                      // Comparator anschalten
ACSR &= ~(1<<ACBG);                     // keine feste bandgap reference voltag
ACSR &= ~(1<<ACIE);                     // keinen Interrupt auslösen
ACSR &= ~(1<<ACIC);                     // nicht für Timer/Counter1 nutzen
ACSR &= ~((1<<ACIS1)|(1<<ACIS0));       // 00== Interrupt on toggle output (tri
//ACSR |= ((1<<ACIS1)|(1<<ACIS0));      // 11== Interrupt on rising edge
//ACSR |= (1<<ACIS1);                   // 10==faling edge
//ACSR &= ~(1<<ACIS0);                  // 10==faling edge

while(1){


if(ACSR & (1 << ACI)){
long_delay_ms(time_until_open);
//PORTD=0b00000011;                 // Schwarz,Blau
PORTD |=  ((1<<PD1)|(1<<PD0));
long delay ms(open time);
//PORTD=0b00000000;
PORTD &= ~((1<<PD1)|(1<<PD0));
long delay ms(time until_close);
//PORTD=0b00001100;                 // Rot, Gelb
PORTD |=  ((1<<PD3)|(1<<PD2));
long delay ms(close_time);
//PORTD=0b00000000;
PORTD &= ~((1<<PD3)|(1<<PD2));
long_delay_ms(time_until_idle);}else{
}

ACSR |= (1<<ACI);                       // zurücksetzen des interrupt flag bits
//ACSR &= ~(1<<ACI);
}

return 0;
}
```

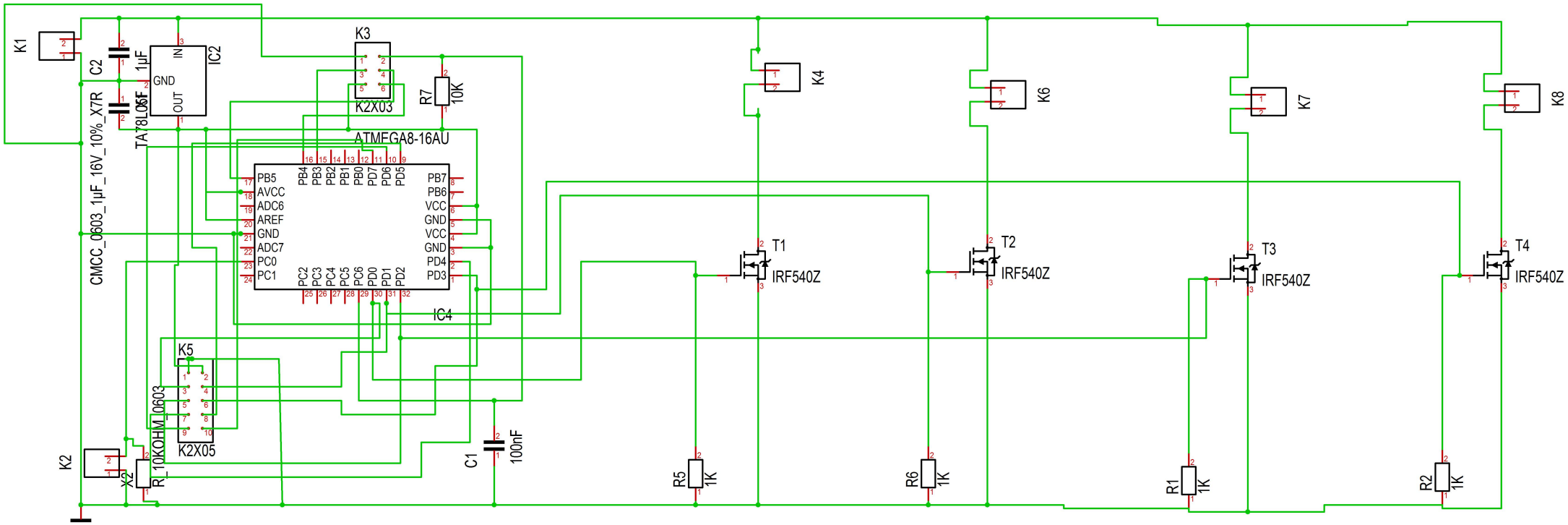
K1
C2
1µF
CMCC_0603_1µF_16V_10%_X7R
IC2
GND
IN
OUT
TA78L05F
K3
K2X03
R7
10K
ATMEGA8-16AU
PB5
AVCC
ADC6
AREF
GND
ADC7
PC0
PC1
PB4
PB3
PB2
PB1
PB0
PD7
PD6
PD5
PB7
PB6
VCC
GND
VCC
GND
PD4
PD3
PC2
PC3
PC4
PC5
PC6
PD0
PD1
PD2
IC4
K4
K6
K7
K8
T1
T2
T3
T4
IRF540Z
K5
K2X05
K2
X1
R_10KOHM_0603
C1
100nF
R5
1K
R6
1K
R1
1K
R2
1K

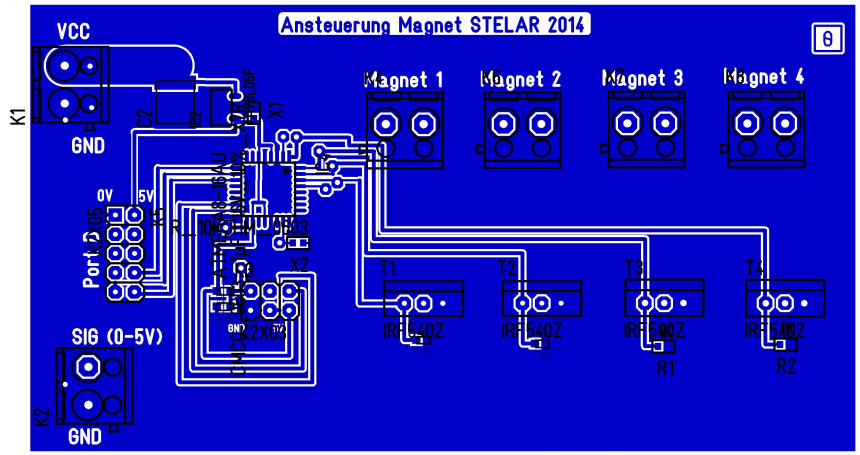
Ansteuerung Magnet STELAR 2014
VCC
GND
SIG (0-5V)
GND
Magnet 1
Magnet 2
Magnet 3
Magnet 4
T1
T2
T3
T4
R1
R2
K1
K2
X1
X2
0V
5V

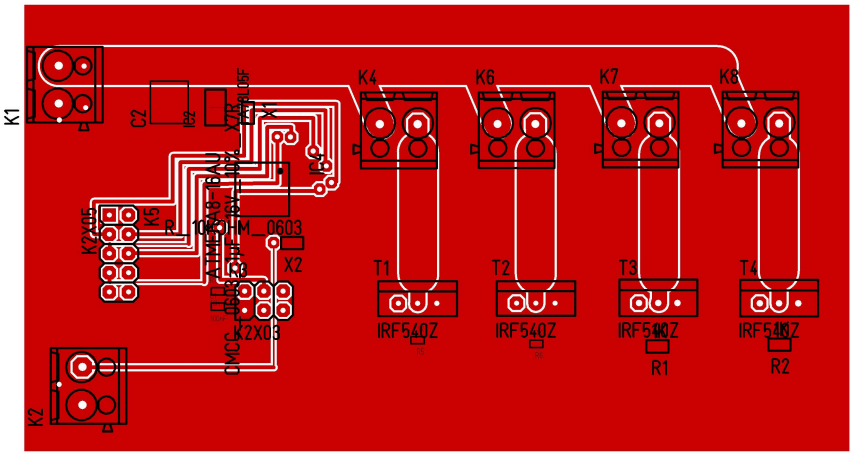
K1
C2
K4
K6
K7
K8
X1
K5
K2X05
0603
X2
K2X03
T1
T2
T3
T4
IRF540Z
IRF540Z
IRF540Z
IRF540Z
R1
R2
K2

A.15. Konstruktion der Modellbalken

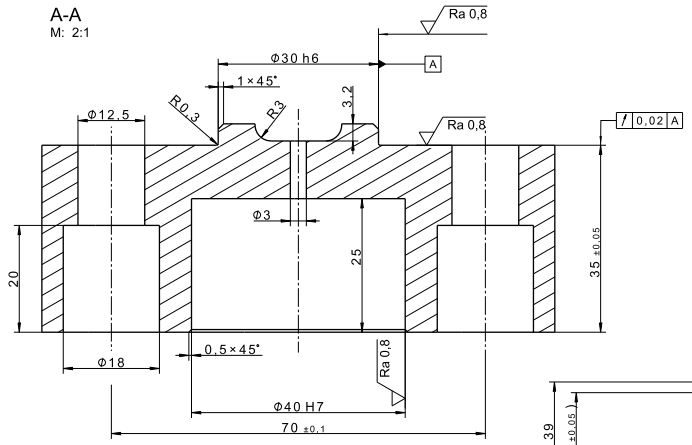

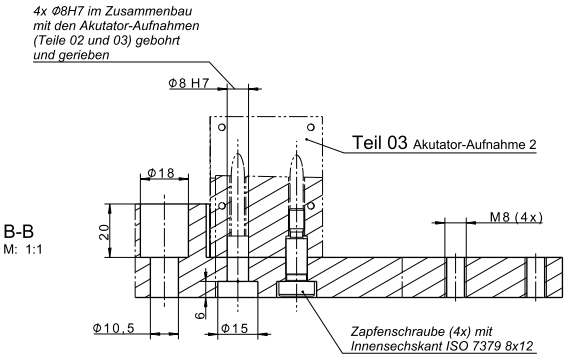

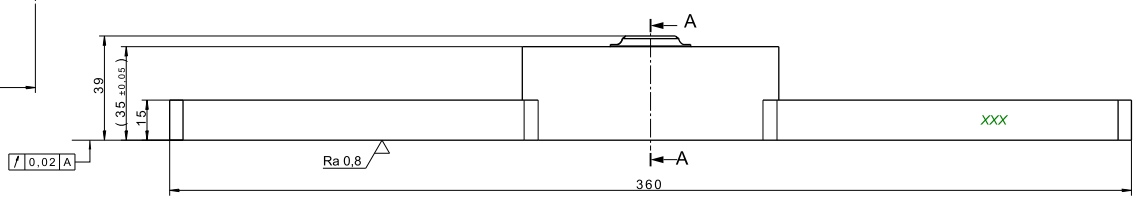

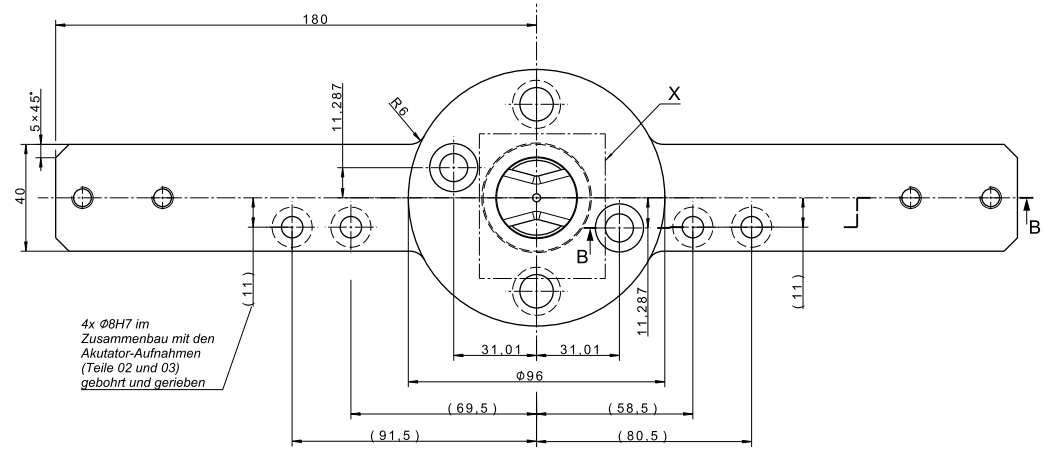

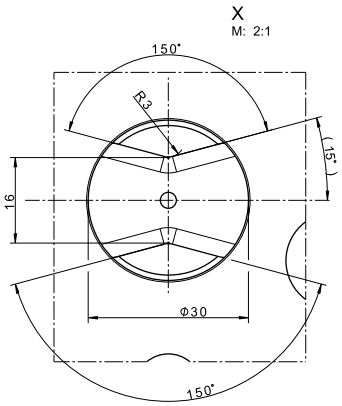

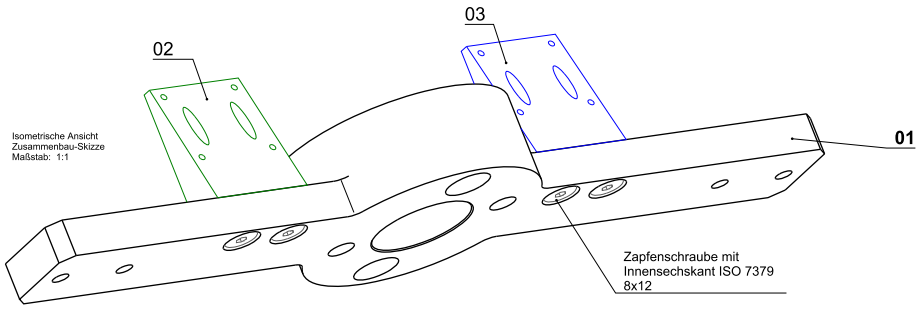

Anmerkung:

Bohrungen für Pass-Schrauben (4x Φ8H7) im Zusammenbau mit den Aktuator-Aufnahmen, Teile 02 und 03, gebohrt und gerieben

XXX Platz für Bauteilkennzeichnung

Kanten ISO 13715 -0,3 +0,5

Ra 3,2 (Ra 0,8)

40 H7	40,000	40,025
8 H7	8,000	8,015
Passmaß	Mindestmaß	Höchstmaß

NUR ZUR INFORMATION

Teil-Nr.: 01	Stückzahl: .	Maße ohne Toleranzangabe nach DIN ISO 2768 - mH	Oberflächen nach DIN ISO 1302	Werkstoff Materialnr.: EN AW-7075 3.4365	Gewicht: 0,989kg
		Datum / Name		Bearbeitung: Stelar Modellbalken	Maßstab: .
		Gezeichnet: 25.04.2014 Drescher			
		Kontrolliert: 2014 S. Opitz			
		Genehmigt:		Balken	
		DLR Deutsches Zentrum für Luft- und Raumfahrt e.V. in der Helmholtz-Gemeinschaft		Zeichnungsnummer: GO-038-673-05-01-01	
Index Datum Änderung Name		Systemhaus Technik, Region Nord Standort Braunschweig		Ersatz für:	Ersetzt durch:
ISO/E				Handschriftl. Änderung bzw. Eintragung auf der Zeichnung	Blatt 01 von 01

ÄNDERUNGEN SIND NUR ÜBER CAD-CATIA ZULÄSSIG! powered by SHT CATIA V5R20 - Zeichnung Format A1

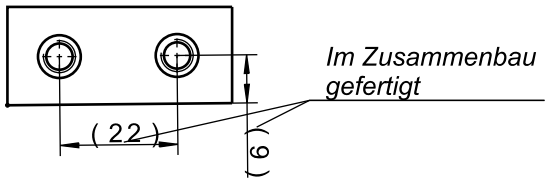

Anmerkung:

Bohrungen für Pass-Schrauben (2x ⌀8H7) im Zusammenbau mit dem Balken, Teil 01, gebohrt und gerieben

Schräge Fläche nach NC-Datei gefertigt

XXX Platz für Bauteilkennzeichnung

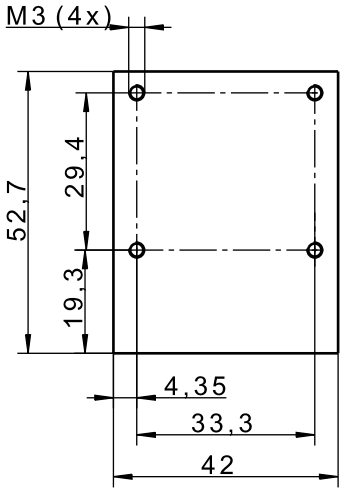

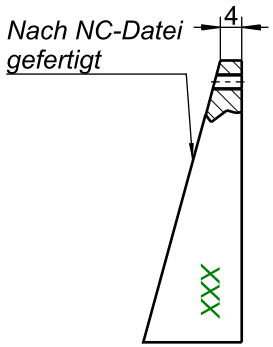

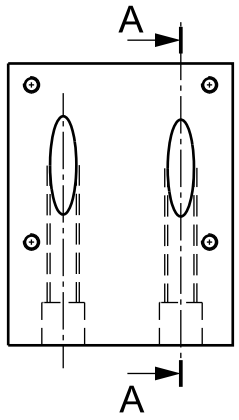

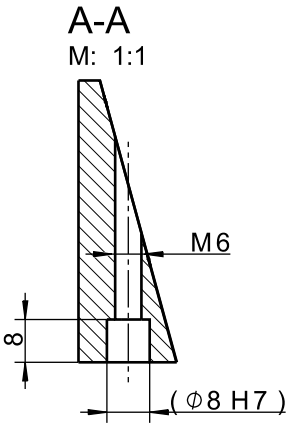

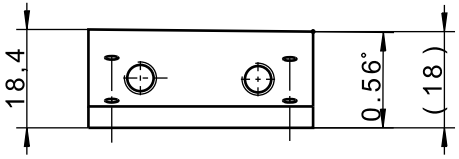

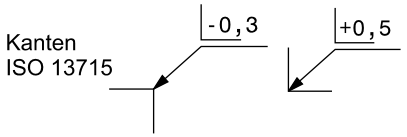

Ra 3,2

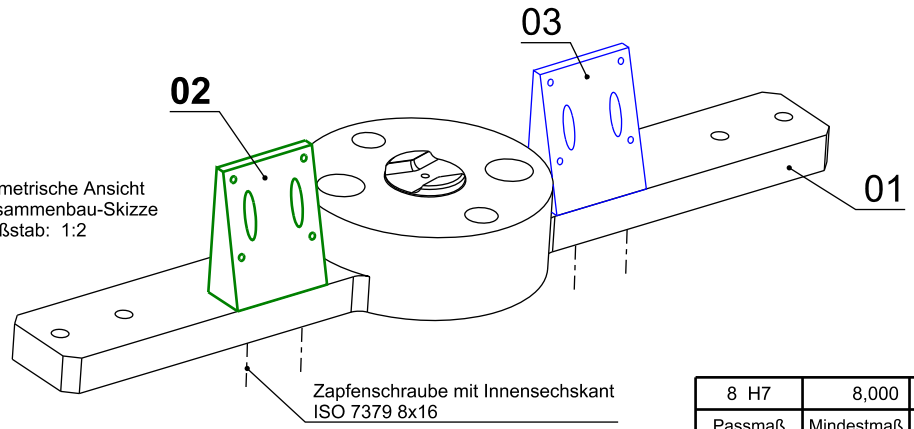

8 H7	8,000	8,015
Passmaß	Mindestmaß	Höchstmaß

NUR ZUR INFORMATION

Teil-Nr.: 02	Stückzahl: .	Maße ohne Toleranzangabe nach DIN ISO 2768 - m H	Oberflächen nach DIN ISO 1302	Werkstoff / Material-Nr. EN AW-7075 3.4365	Gewicht .
			Datum / Name	Benennung Stelar Modellbalken	Maßstab 1:1
		Gezeichnet	25.04.2014 Drescher		
		Konstruiert	2014 S. Opitz		
		Geprüft	. .		
		Genehmigt	. .	Aktuator-Aufnahme 1	
Index Datum Änderung Name				Zeichnungsnummer: GO-038-673-05-01-02	
ISO/E		DLR Deutsches Zentrum für Luft- und Raumfahrt e.V. in der Helmholtz-Gemeinschaft Systemhaus Technik, Region Nord Standort Braunschweig		Ersatz für . / Erstellt aus .	
				Handschriftl. Änderung bzw. Eintragung auf der Zeichnung / SmarTeam Stand .	Blatt 01 von 01

ÄNDERUNGEN SIND NUR ÜBER CAD-CATIA ZULÄSSIG! powered by SHT

CATIA V5R20 - Zeichnung Format A3

Anmerkung:

Bohrungen für Pass-Schrauben (2x ⌀8H7) im Zusammenbau mit dem Balken, Teil 01, gebohrt und gerieben

Schräge Fläche nach NC-Datei gefertigt

XXX Platz für Bauteilkennzeichnung

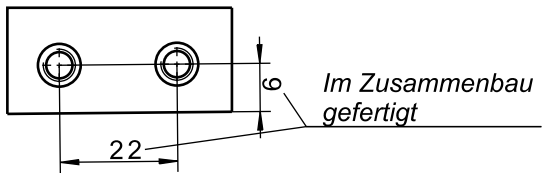

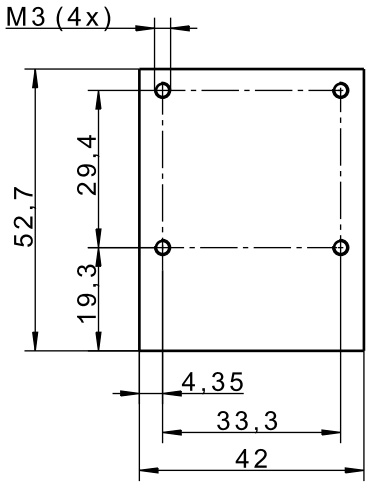

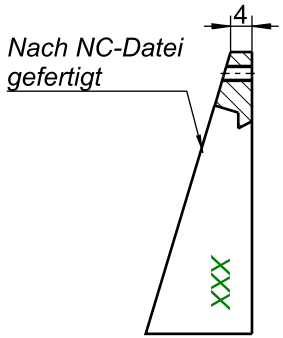

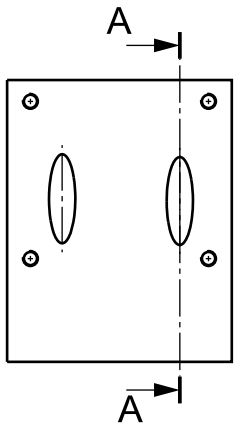

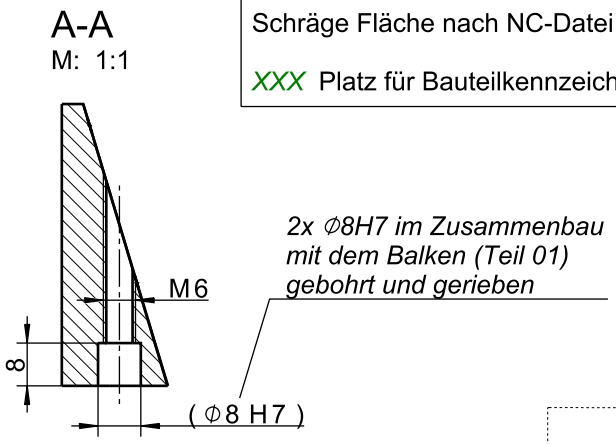

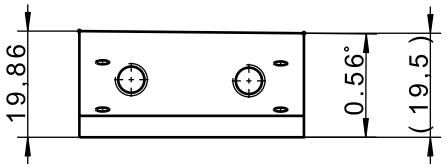

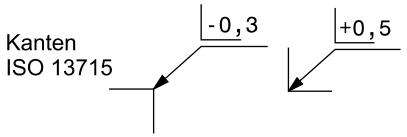

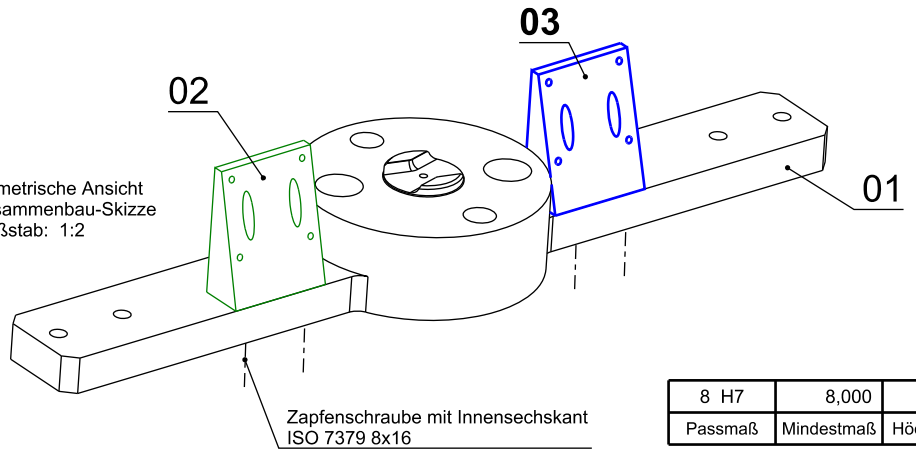

8 H7	8,000	8,015
Passmaß	Mindestmaß	Höchstmaß

NUR ZUR INFORMATION

Teil-Nr.: 03	Stückzahl: .	Maße ohne Toleranzangabe nach DIN ISO 2768 - m H	Oberflächen nach DIN ISO 1302
Werkstoff / Material-Nr.	EN AW-7075 3.4365	Gewicht: .	
Gezeichnet: 25.04.2014 Drescher	Konstruiert: 2014 S. Opitz	Geprüft: .	Genehmigt: .
Benennung	Stelar Modellbalken	Maßstab: 1:1	
Aktuator-Aufnahme 2			
Zeichnungsnummer: GO-038-673-05-01-03			
Ersatz für: .	Erstellt aus: .		
Index / Datum / Änderung / Name			
ISO/E	DLR Deutsches Zentrum für Luft- und Raumfahrt e.V. in der Helmholtz-Gemeinschaft; Systemhaus Technik, Region Nord, Standort Braunschweig	Handschriftl. Änderung bzw. Eintragung auf der Zeichnung	SmarTeam Stand: .
		Blatt 01 von 01	

ÄNDERUNGEN SIND NUR ÜBER CAD-CATIA ZULÄSSIG! powered by SHT

CATIA V5R20 - Zeichnung Format A3

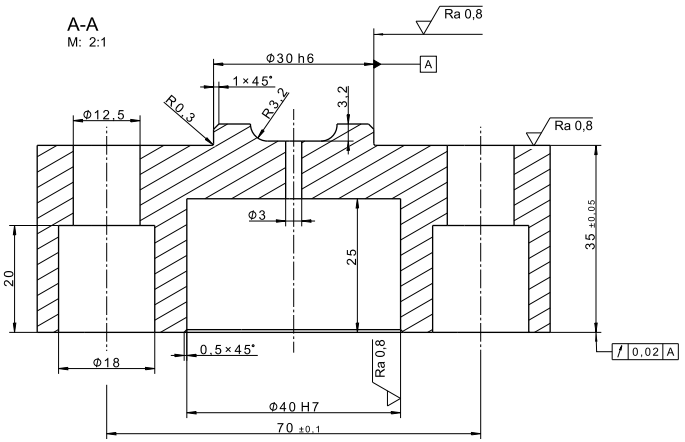

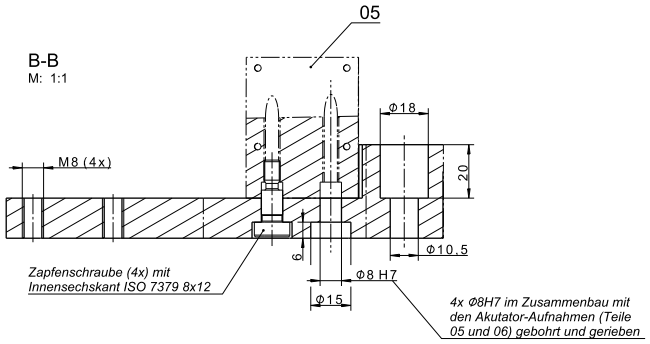

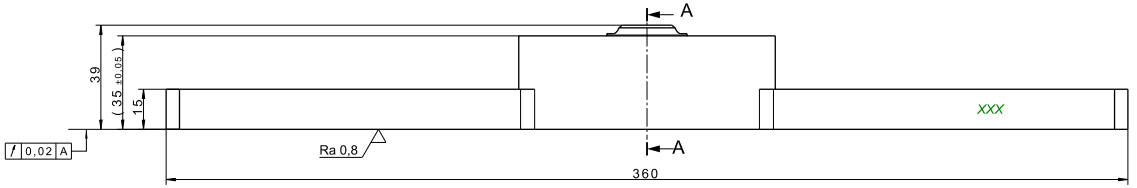

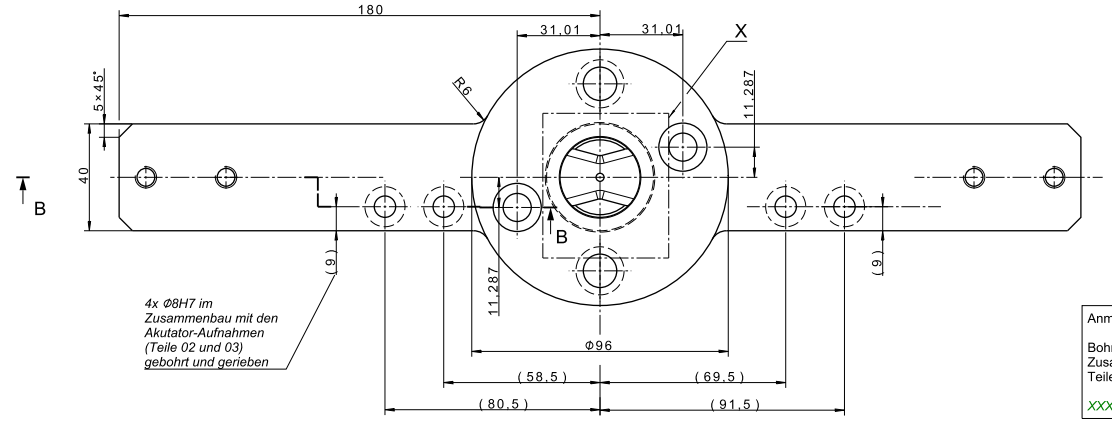

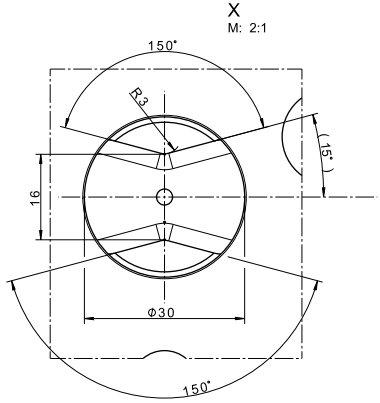

Isometrische Ansicht
Zusammenbau-Skizze
Maßstab: 1:1

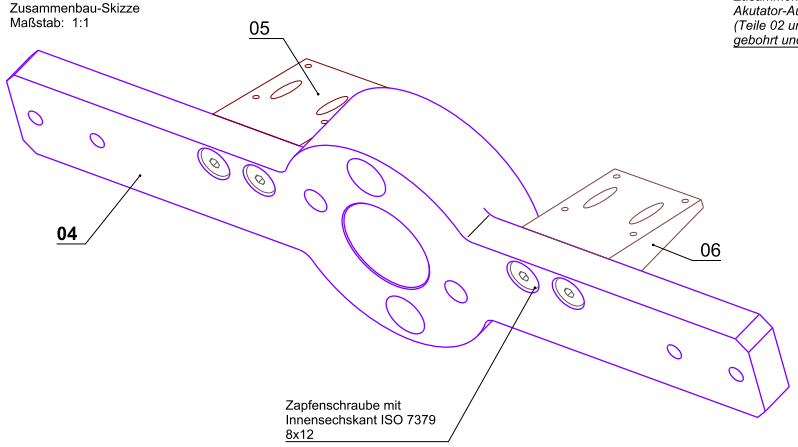

Anmerkung:

Bohrungen für Pass-Schrauben (4x Φ8H7) im Zusammenbau mit den Aktuator-Aufnahmen, Teile 05 und 06, gebohrt und gerieben

XXX Platz für Bauteilkennzeichnung

Kanten ISO 13715 -0,3 +0,5

Ra 3,2 (Ra 0,8)

40 H7	40,000	40,025
8 H7	8,000	8,015
Passmaß	Mindestmaß	Höchstmaß

NUR ZUR INFORMATION

Teil-Nr.: 04	Stückzahl: .	Maße ohne Toleranzangabe nach DIN ISO 2768 - mH	Oberflächen nach DIN ISO 1302	Werkstoff Materialnr.: EN AW-7075 3.4365	Gewicht: 0,989kg
		Datum / Name		Bearbeitung: Stelar	Maßstab: .
		Gezeichnet: 25.04.2014 Drescher		Modellbalken	
		Konstruiert: 2014 S. Opitz		Balken	
		Geprüft:			
		Genehmigt:		Zeichnungsnummer: GO-038-673-05-01-04	
Index / Datum / Änderung / Name		Deutsches Zentrum für Luft- und Raumfahrt e.V. in der Helmholtz-Gemeinschaft		Ersatz für:	Ersetzt durch:
ISO/E		Systemhaus Technik, Region Nord Standort Braunschweig		Handschrift. Änderung bzw. Eintragung auf der Zeichnung	Blatt 01 von 01

ÄNDERUNGEN SIND NUR ÜBER CAD-CATIA ZULÄSSIG! powered by SHT CATIA V5R20 - Zeichnung, Format A1

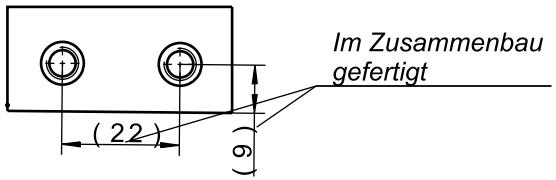

Anmerkung:

Bohrungen für Pass-Schrauben (2x ⌀8H7) im Zusammenbau mit dem Balken, Teil 04, gebohrt und gerieben

Schräge Fläche nach NC-Datei gefertigt

XXX Platz für Bauteilkennzeichnung

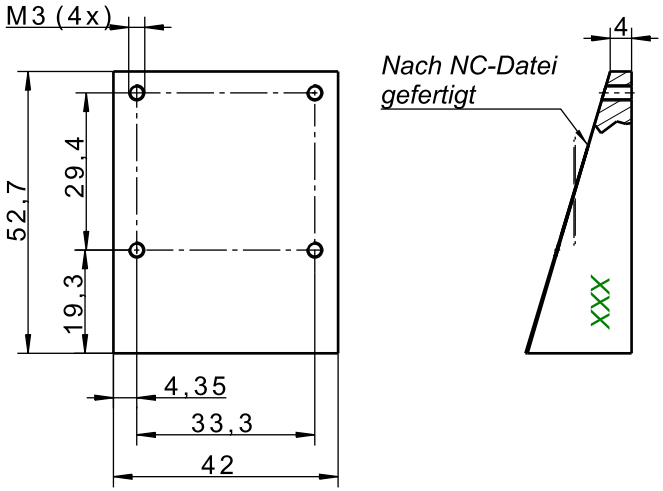

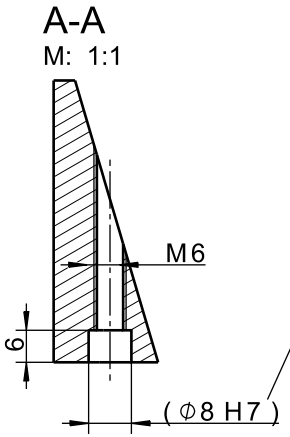

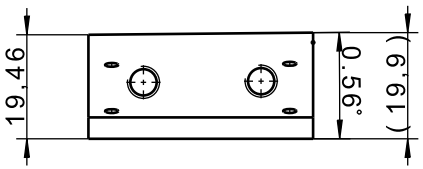

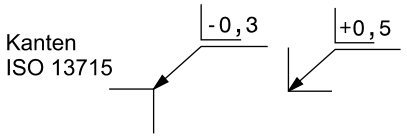

Ra 3,2

NUR ZUR INFORMATION

Isometrische Ansicht
Zusammenbau-Skizze
Maßstab: 1:2

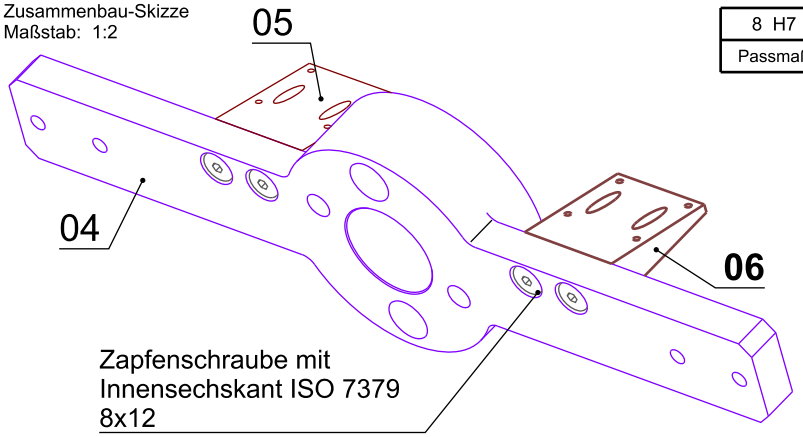

8 H7	8,000	8,015
Passmaß	Mindestmaß	Höchstmaß

Teil-Nr.: 06	Stückzahl: .	Maße ohne Toleranzangabe nach DIN ISO 2768 - m H	Oberflächen nach DIN ISO 1302
Werkstoff / Material-Nr.: EN AW-7075 3.4365	Gewicht: .		
		Datum	Name
Gezeichnet		25.04.2014	Drescher
Konstruiert		2014	S. Opitz
Geprüft		.	.
Genehmigt		.	.
Benennung: Stelar Modellbalken	Maßstab: 1:1		
Aktuator-Aufnahme 4			
Zeichnungsnummer: GO-038-673-05-01-06			
Ersatz für: .	Erstellt aus: .		
Handschriftl. Änderung bzw. Eintragung auf der Zeichnung	SmarTeam Stand: .	Blatt 01 von 01	

Index | Datum | Änderung | Name

ISO/E

DLR Deutsches Zentrum für Luft- und Raumfahrt e.V. in der Helmholtz-Gemeinschaft

Systemhaus Technik, Region Nord
Standort Braunschweig

ÄNDERUNGEN SIND NUR ÜBER CAD-CATIA ZULÄSSIG! powered by SHT

CATIA V5R20 - Zeichnung Format A3

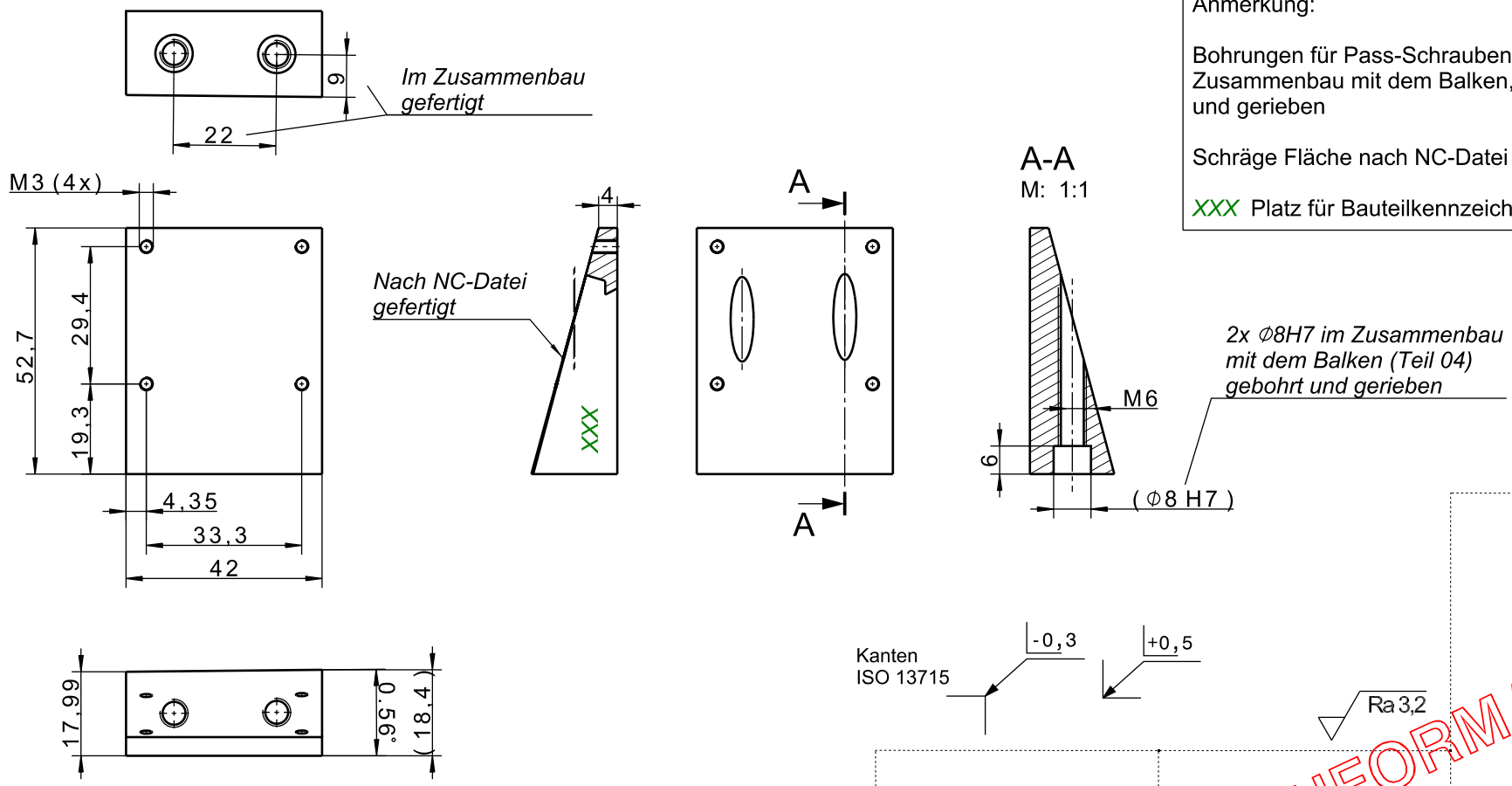

Anmerkung:

Bohrungen für Pass-Schrauben (2x Φ8H7) im Zusammenbau mit dem Balken, Teil 04, gebohrt und gerieben

Schräge Fläche nach NC-Datei gefertigt

XXX Platz für Bauteilkennzeichnung

Kanten ISO 13715 -0,3 +0,5

Ra 3,2

Isometrische Ansicht
Zusammenbau-Skizze
Maßstab: 1:2

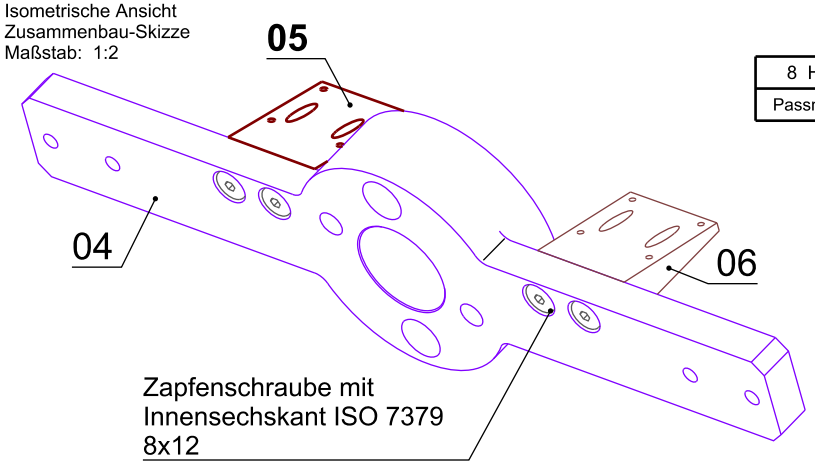

8 H7	8,000	8,015
Passmaß	Mindestmaß	Höchstmaß

Teil-Nr.:	05	Stückzahl:	.
Maße ohne Toleranzangabe nach DIN ISO 2768 - m H		Oberflächen nach DIN ISO 1302	
Werkstoff Material-Nr.	EN AW-7075 3.4365	Gewicht	.
	Datum	Name	
Gezeichnet	25.04.2014	Drescher	
Konstruiert	2014	S. Opitz	
Geprüft	.	.	
Genehmigt	.	.	
Benennung	Stelar Modellbalken	Maßstab	1:1
	Aktuator-Aufnahme 3		
Zeichnungsnummer:	GO-038-673-05-01-05		
Ersatz für .		Erstellt aus .	
Handschriftl. Änderung bzw. Eintragung auf der Zeichnung		SmarTeam Stand .	Blatt 01 von 01

Index | Datum | Änderung | Name

ISO/E

DLR Deutsches Zentrum für Luft- und Raumfahrt e.V. in der Helmholtz-Gemeinschaft

Systemhaus Technik, Region Nord
Standort Braunschweig

ÄNDERUNGEN SIND NUR ÜBER CAD-CATIA ZULÄSSIG! powered by SHT

CATIA V5R20 - Zeichnung Format A3

A.16. Konstruktion der Querstange

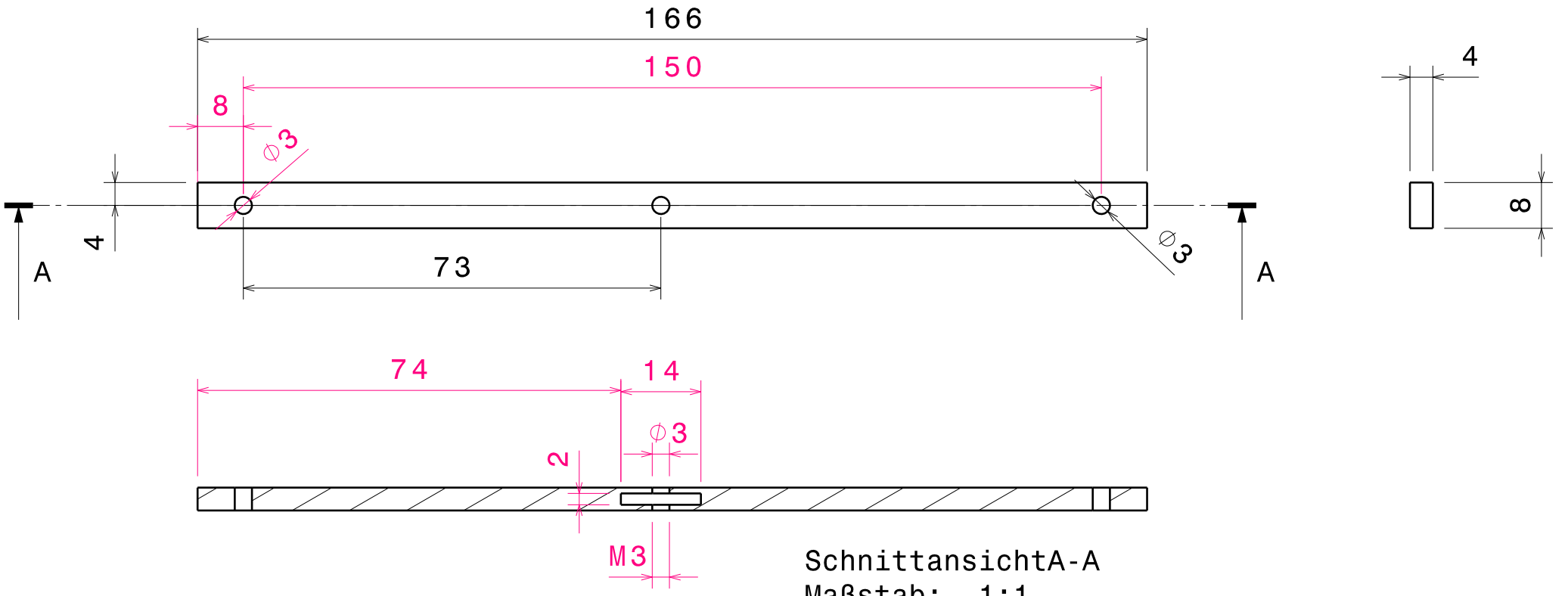

SchnittansichtA-A
Maßstab: 1:1

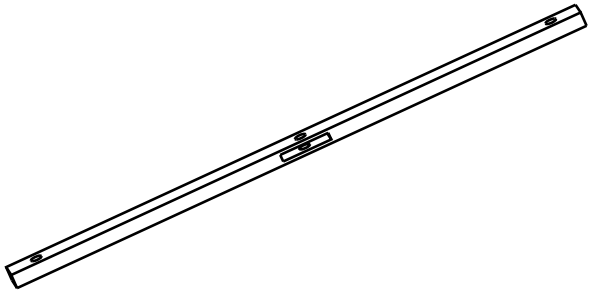

1	Querstange	2	_ NORM _	01	_ Muster _	_ DIM _	_ 999 _
Position	Benennung	Stk.	Zeichnungsnr., Norm	Index	Werkstoff	Rohmass	Gewicht [kg]

Allgemeintoleranz NORM EN 22768 m		Name	Datum	DLR - FA Institut für Faserverbundleichtbau und Adaptronik
	gezeichnet	S. Opitz	14.07.2014	Zeichnungsname: Querstange
Projektion	2D-Dateiname	Querstange.CATDrawing		
Maßstab 1:1	3D-Dateiname	Querstange.CATPart		Zeichnungs-Nr.: 1 Index: 01

A.17. Festigkeit des Modellfuß

Festigkeit Modellfuß OA209 Modell

Zu modifizierendes Bauteil im Ausgangzustand:

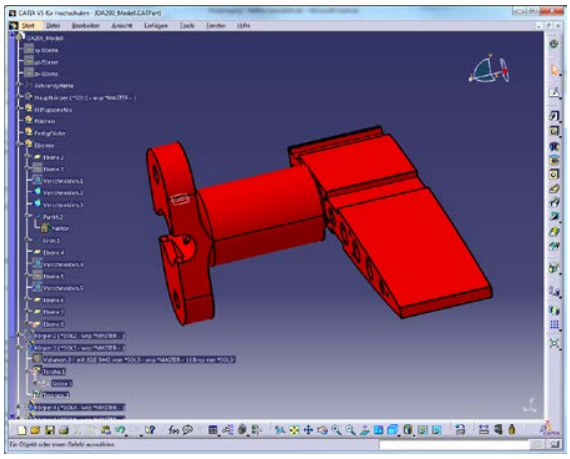

Schubstange zum Öffnen der Klappe würde mit dem Schaft kollidieren:

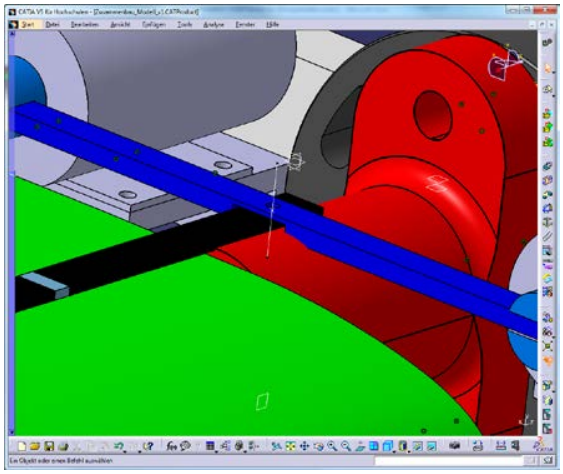

Lösungsvorschlag: Anbringen einer kleinen Fase:

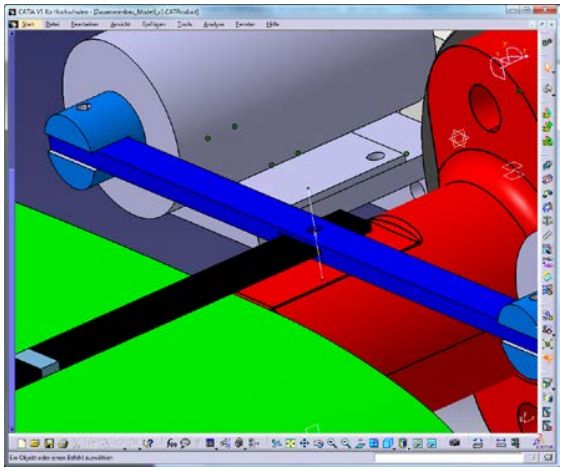

Zusammenstellung der Wichtigsten Querschnittsdaten:

Querschnitt Schaft ohne Fase:

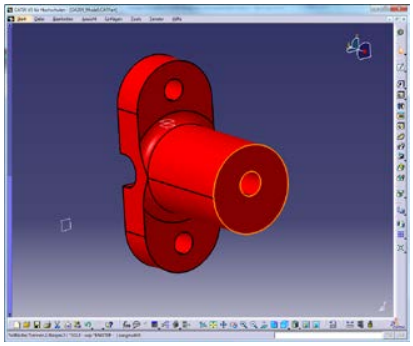

Fläche: $A_{ohne\ Fase}$=0,001162m²

Minimales Flächenträgheitsmoment: $I_{min\ ohne\ Fase}$= 1,243e-007m^4

Randfaserabstand (konservativ geschätzt da leichte Asymmetrie): $e_{min\ ohne\ Fase}$= 0,021m

Maximales Flächenträgheitsmoment: $I_{max\ ohne\ Fase}$= 1,249e-007e-007m^4

Randfaserabstand (Symmetrie): $e_{max\ ohne\ Fase}$= 0,02m

Querschnitt Schaft mit Fase:

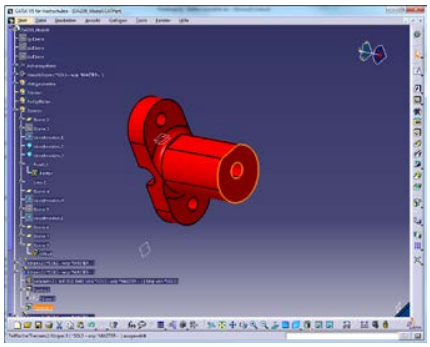

Fläche: A_{Fase}= 0,001139m² (Reduktion: 1,98%)

Minimales Flächenträgheitsmoment: $I_{min\ Fase}$= 1,159e-007m^4 (Reduktion: 6,75%)

Randfaserabstand (konservativ geschätzt etwas mehr Asymmetrie): $e_{min\ Fase}$= 0,023m

Maximales Flächenträgheitsmoment: $I_{max\ Fase}$= 1,246e-007m^4 (Reduktion: 0,24%)

Randfaserabstand (Symmetrie): $e_{max\ Fase}$= 0,02m

Querschnitt im Bereich des Rippenanschlusses:

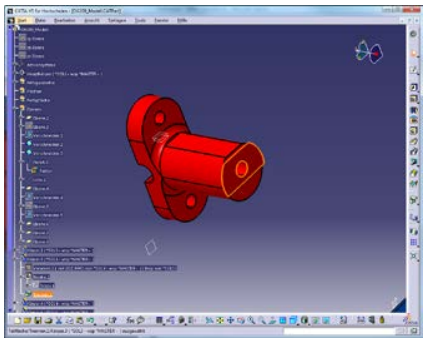

Fläche: A_{Rippe}= 7,797e-004m²

Maximales Flächenträgheitsmoment: $I_{max\ Rippe}$= 1,106e-007m^4

Randfaserabstand (Symmetrie): $e_{max\ Rippe}$= 0,02m

Minimales Flächenträgheitsmoment: $I_{min\ Rippe}$= 3,447e-008m^4

Randfaserabstand (im besten Fall→geringste Spannungen): $e_{min\ Rippe}$= 0,011m

<u>Betrachtung verschiedener Belastungsfälle</u>

Querkraft / Schub:

Verlauf konstant in diesem Bereich da keine nennenswerten Kräfte

$\tau_{max}=F/A_{min}$

➔ Dimensionierend ist der Querschnitt mit der geringsten Fläche (Rippenanschluss)

Ohne Fase:

$\tau_{ohne\ Fase}/\tau_{Rippe}=A_{Rippe}/A_{ohne\ Fase}$= 0,67

Mit Fase:

$\tau_{ohne\ Fase}/\tau_{Rippe}=A_{Rippe}/A_{Fase}$= 0,68

Fazit Schub: Die Spannungen im Bereich des Rippenanschlusses sind ca. 1,5 mal so groß. Die Fase ändert daran nichts.

Längskraft:

Tritt quasi nur durch Modellbiegung auf (sekundärer Effekt) ist konstant in dem Bereich

$\sigma_{max}=F/A_{min}$

➔ Dimensionierend ist der kleinste Querschnitt (Rippenanschluss)

➔ Weitere Betrachtungen äquivalent zu Schub

Torsion:

Torsionsmomentverlauf ist konstant in diesem Bereich, leichte aber zu vernachlässigende Zunahme aufgrund der Eigenträgheit des Modellfuß (geringer Abstand zur Rotationsachse)

$\tau_{max}= M_t/W_t=M_t/(I_t/r_{max})$

Querschnitt ohne Fase (Kreisring):

$r_{max}= 0,021$

$D_i= 0,011m$

$D_a= 0,04m$

$I_{t\ ohne\ Fase}=\pi/32*(D_a^4-D_i^4)= 2,5e\text{-}7\ m^4$

$W_{t\ ohne\ Fase}= 1,19e\text{-}5m^3$

Querschnitt mit Fase (Kreisring; konservativ: Verminderung des Außendurchmessers um Fasenhöhe):

$r_{max}= 0,023$

$D_i= 0,011m$

$D_a= 0,038m$

$I_{t\ Fase}=\pi/32*(D_a^4-D_i^4)= 2,03e\text{-}\ m^4$ (Reduktion <19%)

$W_{t\ Fase}= 8,84e\text{-}6m^3$

Querschnitt Anbindung der Rippe (Annäherung als Rechteck):

	Querschnitt	I_t		W_t		Bemerkungen				
10	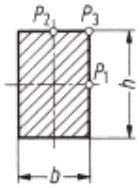	$c_1 h b^3 = c_1 n b^4$		$c_2 h b^2 = c_2 n b^3$		Voraussetzung: $h/b = n \geq 1$ τ_{max} in P_1 In P_2: $\tau_2 = c_3 \tau_{max}$ In P_3: $\tau_3 = 0$				
		$n=h/b$	1	1,5	2	3	4	6	8	10	∞
		c_1	0,141	0,196	0,229	0,263	0,281	0,298	0,307	0,312	0,333
		c_2	0,208	0,231	0,246	0,267	0,282	0,299	0,307	0,312	0,333
		c_3	1,000	0,858	0,796	0,753	0,745	0,743	0,743	0,743	0,743

(Quelle: Dubbel)

b= 0,022m

h= 0,04m

h/b≈ 2 →c_1= 0,229 ; c_2= 0,246

$I_t = c_1 * h * b^3$= 9,75e-8m^4

$W_{t\ Rippe}$= 4,76e-6m^3

Verhältnis der Schubspannungen in Folge von Torsion in den beiden Querschnitten:

Ohne Fase:

$\tau_{ohne\ Fase}/\tau_{Rippe} = (M_t/W_{t\ ohne\ Fase})/(M_t/W_{t\ Rippe}) = W_{t\ Rippe}/W_{t\ ohne\ Fase}$= 0,4

Mit Fase:

$\tau_{Fase}/\tau_{Rippe} = (M_t/W_{t\ Fase})/(M_t/W_{t\ Rippe}) = W_{t\ Rippe}/W_{t\ Fase}$= 0,53

Fazit Torsion: Die größten Schubspannungen treten im Anschluss der letzten Rippe auf. Durch die Fase werden die Spannungen im Schaft etwas größer bleiben jedoch etwa halb so groß sie die Schubspannungen im Rippenanschluss.

Biegung:

Zunahme des Biegemomentes zur Einspannung möglich, worst case (Hebelarm wird maximal): Konzentration aller Kräfte in einem Punkt in der Mitte des Modells d.h. linearer Anstieg des Biegemomentes bis zur Einspannung

Geometrie:

$L/2$= 576mm — Halbe Länge des Modells

L_{Fase}= 41mm — minimaler Abstand Schaft mit Fase zur Einspannung (größter möglicher Momentenunterschied im Vergleich zum Schaft/Rippe-Übergang)

L_{Rippe}= 80mm — Abstand Übergang Rippe/Schaft zur Einspannung

Maximale Momentenüberhöhung am Ende des Bereichs mit Fase

$M_{max}=L/2*F$

$M_{Rippe}=(L/2-L_{Rippe})*F$

$M_{Fase}=(L/2-L_{Fase})*F$

$M_{Fase}/M_{Rippe}=(L/2-L_{Fase})/(L/2-L_{Rippe})= 1.08$ → das Moment an der Fase kann maximal 8% größer sein als beim Übergang der Rippe zum Schaft

Betrachtung minimales Flächenträgheitsmoment (Schlagbiegung):

$\sigma_{Fase}/\sigma_{Rippe} = (M_{Fase}*e_{min\ Fase}/I_{min\ Fase})/(M_{Rippe}*e_{min\ Rippe}/I_{min\ Rippe}) =$

$= M_{Fase}/M_{Rippe}\ (e_{min\ Fase}/I_{min\ Fase})/(e_{min\ Rippe}/I_{min\ Rippe}) =$

$= 1,08*0,62 = 0,67$ (ohne Fase: 0,57)

Betrachtung maximales Flächenträgheitsmoment (Schwenkbiegung):

$\sigma_{Fase}/\sigma_{Rippe} = (M_{Fase}*e_{max\ Fase}/I_{max\ Fase})/(M_{Rippe}*e_{max\ Rippe}/I_{max\ Rippe}) =$

$= M_{Fase}/M_{Rippe}\ (e_{max\ Fase}/I_{max\ Fase})/(e_{max\ Rippe}/I_{max\ Rippe}) =$

$= 1,08*0,89 = 0,96$ (ohne Fase: 0,95)

Fazit Biegung: Die größten Biegespannungen treten immer im Bereich des Überganges Schaft/Rippe auf. Im Fall der Schlagbiegung kommt es zu einem leichten Anstieg der Spannungen im Bereich der Fase. Diese sind ähnlich wie bei der Torsion jedoch trotzdem ca. 1,5 mal kleiner als im Bereich des Übergangs. Auf die Spannungen in Folge von Schwenkbiegung hat die Fase nur einen untergeordneten Effekt. Für diese Belastung sollte auch die Verbindung zwischen Rippe und Schaft noch mit ausreichender Sicherheit dimensioniert sein.

Generelle Bemerkung:

Das Material, das durch die Fase in der Nähe des Profils abgetragen wird, kann keine Lasten aufnehmen, da es sich um eine freie Kante handelt. Ab welchem Abstand vom Profil das durch die Fase entfallende Material mitträgt, ist schwer zu sagen. Auch an dieser Stelle ist die obige Abschätzung der Reduktion der Festigkeit konservativ da dort immer alles Material zu 100% trägt. Trotz stets konservativer Modellannahmen besteht kein Indiz dafür, dass die Fase die Sicherheit des Modells beeinflusst. Dimensionierend ist in jedem Fall die Anbindung von der Rippe an den Schaft.